NUI Galway
OÉ Gaillimh

Combined Experimental Testing and Numerical Modelling of a Novel Vertical Axis Tidal Turbine

A thesis submitted to the National University of Ireland, Galway

as fulfilment of the requirements for the Degree of Doctor of Philosophy

By

Brian A. Mannion B.Eng. (Mech) (2014)

November 2018

Research Supervisors: Dr Stephen Nash and Prof Sean Leen

Civil and Mechanical Engineering, National University of Ireland, Galway

DEDICATION

This work is dedicated to parents, John and Patricia.

Thank you for all your help and continued

support.

Abstract

This research presents a study of a novel vertical axis tidal turbine (VATT) – the GKinetic turbine – using experimental testing of scale devices and numerical modelling. The primary aims of the thesis were: (1) to assess the mechanical power extraction performance of the turbine via experimental testing and (2) to develop a hydrodynamic model capable of predicting the power performance. During the process of numerical model development, two different modelling techniques were assessed for their suitability for modelling of VATTs: (1) the computationally-efficient blade element momentum theory (BEMT) approach and (2) the more computationally-intensive Reynolds-averaged Navier Stokes (RANS) approach. The former was developed by the author in MATLAB while the latter used the commercial computational fluid dynamics (CFD) code, ANSYS Fluent.

The GKinetic turbine incorporates two novel design features; a mechanism for accelerating the inflows to its twin turbines and a blade pitch control mechanism to implement variable pitching. This research is the first detailed research study of the device and since the device is novel, the research is also novel and significantly advances the knowledge-base concerning the device.

Experimental testing of the turbine was conducted at various scales. 1:40 and 1:20 scale devices were tested under controlled conditions in a recirculating flume and a 1:10 scale device was subsequently tested under controlled conditions in the field using tow-testing. The device was shown to be capable of accelerating the free-stream velocity by a factor of 2 and achieved a peak mechanical efficiency of 40 %. Following the 1:10 scale tests, a structural analysis of some of the device components was undertaken and recommendations for improved design were made; some of these recommendations have since been incorporated in subsequent iterations of the device.

A BEMT design tool has been developed for prediction of the hydrodynamic performance of high solidity and highly loaded VATTs. The model utilises a graphical approach from the literature for determining induction factors, rather than the more common iterative approach. The research is significant as VATTs typically have a higher solidity than wind turbines, thus the iterative approach for determining

induction factors, which is more suited to low solidity rotors will generally, not be valid. This is the first time that the graphical approach for determining induction factors has been implemented in a VATT model. The model also incorporates modifications to correct for processes such as dynamic stall, flow expansion and finite aspect ratio blades. The model reproduced measured peak power coefficient values to within 6.4 % for a low solidity case, and to within 27 % for a high solidity case.

2D and 3D CFD models of a 3-bladed VATT were developed to assess the accuracy of RANS models in prediction of power performance and near-wake properties. The turbine models were developed using the sliding mesh technique and model performance was assessed using the results of experimental tow tank testing from the literature. The primary aim of the research was to determine the suitability of the sliding mesh technique for modelling of standard VATTs before applying the technique to the more complex GKinetic turbine. A blockage correction approach was trialled for 2D models and shown to significantly improve model accuracy. The CFD methodology developed allowed the 3D model to accurately model the power performance curve and turbine near-wake velocities. An additional novelty of this research is the use of the Transitional SST turbulence model, which, to the author's knowledge, has not yet been used in 3D modelling of vertical axis tidal turbines.

A 2D CFD model of the GKinetic turbine was developed using a nested sliding mesh technique. The model includes the flow accelerating mechanism and the variable blade pitching facilitated by the nested sliding meshes. Model performance was assessed by comparison with measured data for mechanical power and near-wake velocities from the undertaken 1:20 scale experimental tests. The model was used to investigate various aspects of the current device setup including the number of turbine blades, the benefits of variable versus fixed pitch blades, shaft sizing, the location of the turbine relative to the bluff body and the effect of blade chord-length. The results of the design study will inform future development of the device.

Acknowledgements

First and foremost, I would like to thank, my primary supervisor, Dr Stephen Nash for his invaluable assistance and direction throughout the course of this research. Furthermore, he provided me with the necessary support and encouragement, without which the completion of this PhD would not have been possible.

I would also like to thank my co-supervisor Prof Seán Lean for committing his time and support to the project, and whose input was invaluable particularly in the area of design.

My gratitude is owed to Dr Ciaran Kennedy for his advice and direction at the early stages of this project.

I am grateful to GKinetic for allowing me to work on their exciting tidal project and to help further their device towards commercial scale.

I would like to thank the NUI Galway technical staff for their support throughout the undertaking of this research, particularly Mr Pat Kelly, Mr Bonaventure Kennedy, Mr Dermot McDermott, Mr Edward Killcullen, Mr Colm Walsh and Mr William Kelly.

Furthermore, I would like to thank the members of my Graduate Research Committee, Prof Padraic O'Donoghue, Prof Michael Hartnett and Dr Jamie Goggins for their advice throughout this research.

I would like to thank my friends and colleagues in NUIG, particularly, Shane, Paddy, Enda, Dermot, Conor, Donnacha, Tarek, Raydo, Guillermo and the wider PhD research group. Thanks also to all the lads outside of college.

To my parents John and Patricia for your love, support and for everything you have done to get me this far and for helping me get through whatever obstacle I have faced, I am eternally grateful. To my brothers Ollie, John, and Damien, thanks for keeping me sane throughout this time, a great bunch of lads. Thanks to Ollie for his engineering insight and for helping to revise this thesis.

And finally, thanks to Niamh for providing me with a welcome distraction from the stresses of PhD life, and for her support and perseverance with me.

Table of Contents

Table of Figures

Table of Tables

Nomenclature

Symbol	Definition	Unit
U_∞	Ambient/Free-stream Velocity	m/s
α	Angle of Attack	deg (∘)
ϕ	Any Scalar	
A	Area	m^2
AR	Aspect Ratio	
Q_{avg}	Average Torque	Nm
a	Axial Induction Factor	
θ	Azimuthal Position	deg (∘)
F_B	Bearing Force	N
AR	Blade Aspect Ratio	
$C_{x,BET}$	Blade Element Force Coefficient	
L_B	Blade Length	m
ΩR	Blade Tip Speed	m rad/s
F_1, F_2, F_3	Blending Functions	
h	Camber Height	m
x, y, z	Cartesian Coordinates	m
$\Delta\theta$	Change in Azimuthal Position	deg (∘)
Δt	Change in Time/Time-Step	s
ΔQ	Change in Torque	Nm
c	Chord Length	m
$Re_{\theta c}$	Critical Reynolds Number	
ρ	Density	Kg/m^3
y^+	Dimensionless Wall Distance	
y	Distance or Deflection	m
V_d	Downstream-stream Velocity	m/s
C_D	Drag Coefficient	
F_D	Drag Force	N
μ	Dynamic Viscosity	$N\ m/s^2$
V_e	Equilibrium Velocity	m/s
$\tilde{c}$	Equivalent Chord Length	m

F	Force	N
C_{x}	Force Coefficient	
u_{τ}	Friction Velocity	m/s
∇	Gradient	
g	Gravity	m/s^2
V_a	Induced Velocity	m/s
Q_i	Instantaneous Torque	Nm
γ	Intermittency	
∇^2	Laplacian	
C_{L}	Lift Coefficient	
F_{L}	Lift Force	N
Ma	Mach Number	
m	Mass	kg
$\dot{m}$	Mass Flow Rate	kg/s
$\tau_{\max}$	Maximum In-Plane Shear Stress	MPa
$M_{\max}$	Maximum Shaft Bending Moment	Nm
P_{mech}	Mechanical Power	W
M	Moment	Nm
C_{m}	Moment Coefficient	
I	Moment of Inertia	m^4
$C_{x,MOM}$	Momentum Force Coefficient	
ω_{N}	Natural Frequency	Rad/s
C_{N}	Normal Coefficient	
F_{N}	Normal Force	N
N_{B}	Number of Blades	
N_{tubes}	Number of Stream-tubes	
$C_{\mathrm{P}max}$	Peak Power Coefficient	
ν	Poisson's Ratio	
J	Polar 2nd Moment of Area	m^4
P_{avail}	Power Available for Extraction Based on Device Area	W
C_{P}	Power Coefficient	

P, p	Pressure	Pa
σ_1, σ_2	Principle Stresses	MPa
V_{rec}	Recovered Velocity	m/s
α_{ref}	Reference Angle of Attack	deg (∘)
V_{rel}	Relative Velocity	m/s
Re	Reynolds Number	
ω_i	Shaft Critical Speed	Rad/s
d	Shaft Diameter	m
τ	Shear Stress	MPa
C_{f}	Skin Friction Coefficient	
σ_{solid}	Solidity	
ω	Specific Turbulent Dissipation Rate	1/s
α_{SS}	Static Stall Angle	deg (∘)
ε	Strain	
β	Stream-tube Angle	deg (∘)
F_{x}	Stream-wise Force	N
σ	Stress	MPa
C_{T}	Tangential Coefficient	
F_{T}	Tangential Force	N
T	Thrust	N
$\dot{\alpha}$	Time Derivative Angle of Attack	deg (∘)
t	Time/Time-Step	s
λ, TSR	Tip Speed Ratio	
Q	Torque	Nm
C_{Q}	Torque Coefficient	
$\overline{Re}_{\theta t}$	Transition Momentum Thickness Reynolds Number	
$Re_{\theta t}$	Transition onset Reynolds Number	
D	Turbine Diameter	m
T_1, T_2	Turbine Identification Numbers	
R	Turbine Radius	m
Ω	Turbine Rotational Velocity	Rad/s

T_I	Turbulence Intensity	%
μ_{t}	Turbulent Eddy Viscosity	N m/s^2
k	Turbulent Kinetic Energy	m^2/s^2
ε	Turbulent Rate of Dissipation	m^2/s^3
V_u	Upstream Velocity	m/s
u, v, w	Velocities	m/s
σ_{VMS}	Von Mises Stress	MPa
ζ	Vorticity	1/s
V_w	Wake Velocity	m/s
τ_{w}	Wall Shear Stress	MPa
σ_{y}	Yield Strength	MPa
τ_{y}	Yield Strength in Shear	MPa
E	Young's Modulus	GPa

Abbreviation	Definition
$ADCP$	Acoustic Doppler Current Profiler
ADV	Acoustic Doppler Velocimetry
BEM	Blade Element Theory
$BEMT$	Blade Element Momentum Theory
CFD	Computational Fluid Dynamics
CS	Control Surface
CV	Control Volume
DES	Detached Eddy Simulation
DNS	Direct Numerical Simulation
$DMST$	Double Multiple Stream-tube
DS	Dynamic Stall
$EMEC$	European Marine Energy Centre
FOS	Factor of Safety
FAR	Finite Aspect Ratio
FE	Flow Expansion

GHT	Gorlov Helical Turbine
$HATT$	Horizontal Axis Tidal Turbine
HAT	Horizontal Axis Turbine
$HAWT$	Horizontal Axis Wind Turbine
IEC	International Electrotechnical Commission
LES	Large Eddy Simulation
LDV	Laser Doppler Velocimetry
$LCOE$	Levelised Cost of Electricity
LST	Lucid Spherical Turbine
$MaREI$	Marine and Renewable Energy Ireland
MCT	Marine Current Turbines
MRF	Moving Reference Frame
$NACA$	National Advisory Committee for Aeronautics
$PISO$	Pressure-Implicit with Splitting of Operators
PLC	Programmable Logic Controller
RPM	Revolutions per Minute
$RANS$	Reynolds Averaged Navier-Stokes
$RMSE$	Root Mean-Squared Error
RDD	Rotating Domain Diameter
RD	Rotor Diameter
SFI	Science Foundation Ireland
SIMPLE	Semi-Implicit Method for Pressure-Linked Equations
SIMPLEC	Semi-Implicit Method for Pressure-Linked Equations-Consistent
SST	Shear-Stress Transport
$SEAI$	Sustainable Energy Authority of Ireland
TEC	Tidal Energy Converter
TVR	Turbulence Viscosity Ratio
UTS	Ultimate Tensile Strength
$\mathrm{UNH-RVAT}$	University of New Hampshire Reference Vertical Axis Turbine
$URANS$	Unsteady Reynolds Averaged Navier-Stokes
UDF	User Defined Function

$VATT$	Vertical Axis Tidal Turbine
VAT	Vertical Axis Turbine
$VAWT$	Vertical Axis Wind Turbine
$2D$	Two-Dimensional
$3D$	Three-Dimensional

Chapter 1. Introduction

Fossil fuels (coal, oil and natural gas) have long been the linchpin of the energy production sector. However, the finite nature of these fuels, their impending depletion and the adverse environmental effects of their use (particularly greenhouse gas emissions and climate change) has led to the realisation by world leaders, that carbon-dense fossil fuels can no longer be solely used to meet the world's energy requirements. As a result, much focus has been given to exploring and developing clean renewables. In December 2015, the Paris Climate Agreement [1] was ratified by almost all heads of state around the world. The agreement aims to keep global warming below 2^{o} C, with more ambitious goals set every five years. This presents major difficulties for society as every facet of a developed/developing economy relies on fossil fuels for electricity production, transport and heating. For example, in recent years, countries in the Asian-Pacific region have seen substantial growth in their economies resulting in a significant increase in CO_2 emissions for the region, as reported by BP [2] and shown in Figure 1.1.

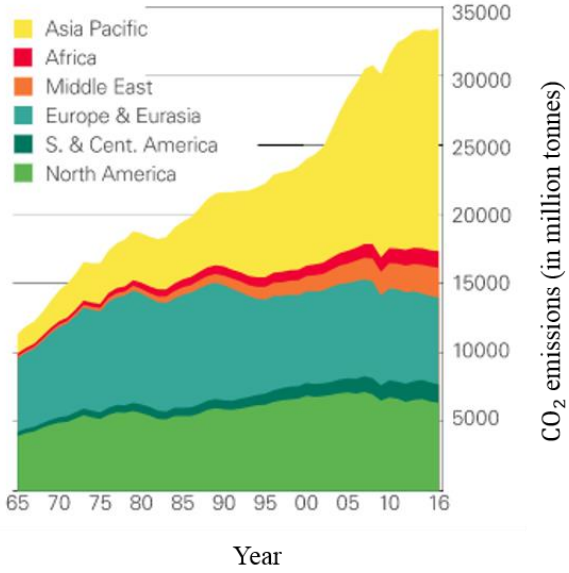

Figure 1.1: 50-year trends (1966 to 2016) for global CO_2 emissions (in million tonnes) per geographical region [2].

As part of the Paris agreement, every country involved must set and meet targets with the aim of reducing climate change. Since the primary cause of climate change is

greenhouse gases arising from the combustion of fossil fuels, these targets effectively aim to limit the use of fossil fuels. The EU has set out clear targets for 2020, 2030 and 2050 [3]. The 2020 targets are a 20 % reduction in greenhouse gases in comparison to 1990 levels and 20 % of total energy consumption to be from renewable energy. This will be followed by targets for 2030 of 40 % reduction in greenhouse gases and 27 % of total energy consumption from renewable sources. The long-term goal, to be realised by 2050, is to reduce total greenhouse gas emissions across all EU countries by 80 to 95 % of 1990 levels and to turn the EU into a highly energy efficient, low carbon economy. To meet these ambitious targets, a gradual transition away from fossil fuel dependent energy generation is required. Several alternative renewable energy resources have been identified, such as wind, solar, tidal, wave, and biomass. It is doubtful that any one of these technologies will single-handedly replace fossil fuels; rather, it is envisaged that a combination of these technologies coupled with improvements in energy storage technology and smart grid integration can lead to a cleaner more robust and reliable energy production system.

1.1 The Move to Renewables

Progress has been made in the reduction of fossil fuel consumption worldwide. Figure 1.2 shows the worldwide trends in primary energy consumption from 1966 to 2016. Oil consumption has been falling steadily for many years, and in 2016, coal consumption at 28.1 % of total global energy consumption, was at its lowest level since 2004. In contrast, renewable energy production has seen steady growth in recent years, increasing by 14.1 % in 2016, with wind and solar energy leading the renewable energy market. Despite its recent growth, renewable energy still only accounts for 4 % of the primary energy consumption globally [2].

In the short term, renewable energy can be used to provide competition for fossil fuel energy generation, to the benefit of the end user with a reduced levelised cost of energy (LCOE). Going forward, competition within renewable technologies will lead to each technology striving for the highest of efficiencies, maintaining a low LCOE and achieving a clean, green environment. An additional benefit of developing a mature renewable energy industry is job creation.

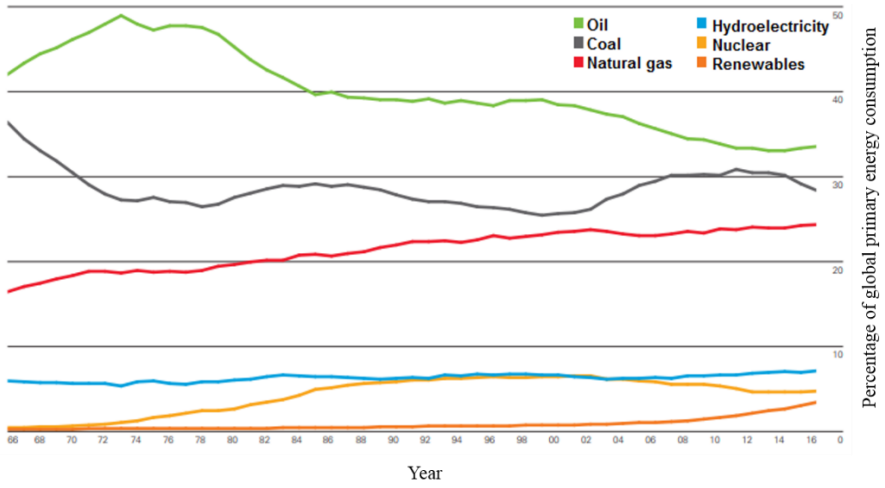

Figure 1.2: 50-year trends (1966 to 2016) for energy resource shares of total global primary energy consumption percentage [2].

1.2 Tidal Energy

Tidal energy exploits the natural rise and fall of oceanic waters caused primarily by the action of the gravitational fields of the moon and sun on the earth [4]. Ocean currents generated as a result of differences in tidal water levels are often magnified by coastal topographical features, such as headlands, inlets and straits, when water is forced through narrow channels. There are two methods for extracting power from tidal waters: (1) using tidal barrages and (2) using tidal stream devices.

A tidal barrage is a dam usually constructed across a river or estuary, which allows water to flow through tunnels in the dam as the tide goes in and out. The dam captures the water through the use of sluice gates, trapping water at high tide and releasing it through low head turbines when sufficient pressure head has developed on the outgoing tide. The highest tidal range in the world occurs at the Bay of Fundy; tidal barrages are not new and have been used most notably in France (the 240 MW La Rance Barrage which was commissioned in 1966 [5]). The two main types of turbines used are the Francis turbine and the Kaplan turbine, both of which are shown in Figure 1.3. The Francis turbine (Figure 1.3 (a)) is a mixed flow turbine; flow enters radially but leaves the turbine axially. It is a medium head turbine. The Kaplan turbine (Figure 1.3 (b)) is an axial flow, low head turbine. Although tidal barrage technology is well established, barrages are impractical in many cases due to their significant environmental impact (changes to the tidal regime and resulting impacts on flora and fauna) and sizeable financial costs, such as in the case of the proposed Severn Barrage.

One of the most significant impediments is that there are very few suitable sites. Tidal barrages generally require large tidal ranges in excess of 5 m, which are not very common. However, in the UK it is estimated that tidal barrages have the potential to generate 45 GW, with a further 14 GW from tidal lagoons [5].

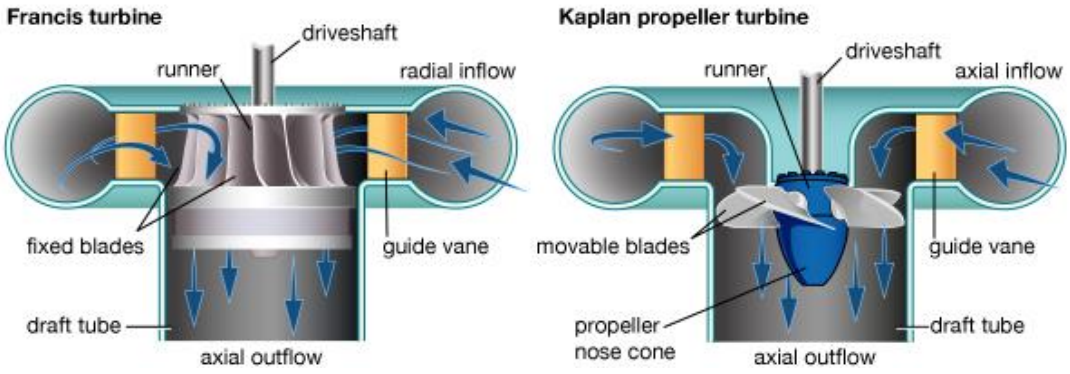

Figure 1.3: Two most commonly used tidal barrage devices: (a) Francis turbine, and (b) Kaplan turbine [6].

In contrast with barrages, tidal stream devices are used to exploit the kinetic energy in tidal currents and are quite similar to wind turbines (see Figure 1.4). Due to the higher density of water (approximately 800 times that of air), tidal turbine blades can be shorter and rotate slower than wind turbines, whilst delivering a similar amount of power. To increase the flow and power output from the turbine, shrouds can be used around the blades to streamline and concentrate the flow towards the rotors, such as the one used by OpenHydro.

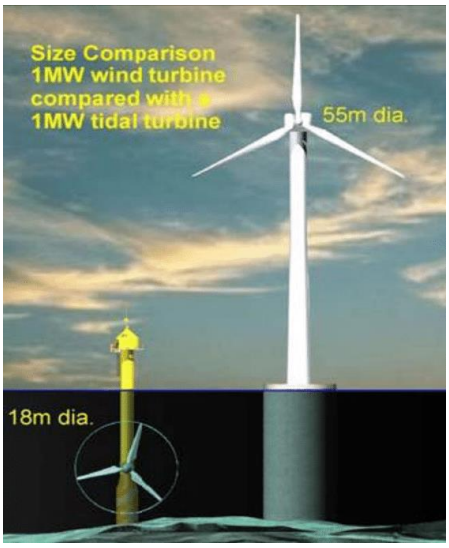

Figure 1.4: Tidal turbine comparison to a wind turbine [7].

To date, tidal resources available globally have been underutilised in regards to power generation. The estimates of the global potential for power generation vary, but it is widely agreed that tidal stream energy capacity could exceed 120 GW globally; this equates to 150 TWh per year of economically exploitable resource [8]. Figure 1.5 shows a world map of the most energetic tidal stream resources shown in red, with areas of interest for deployment sites circled.

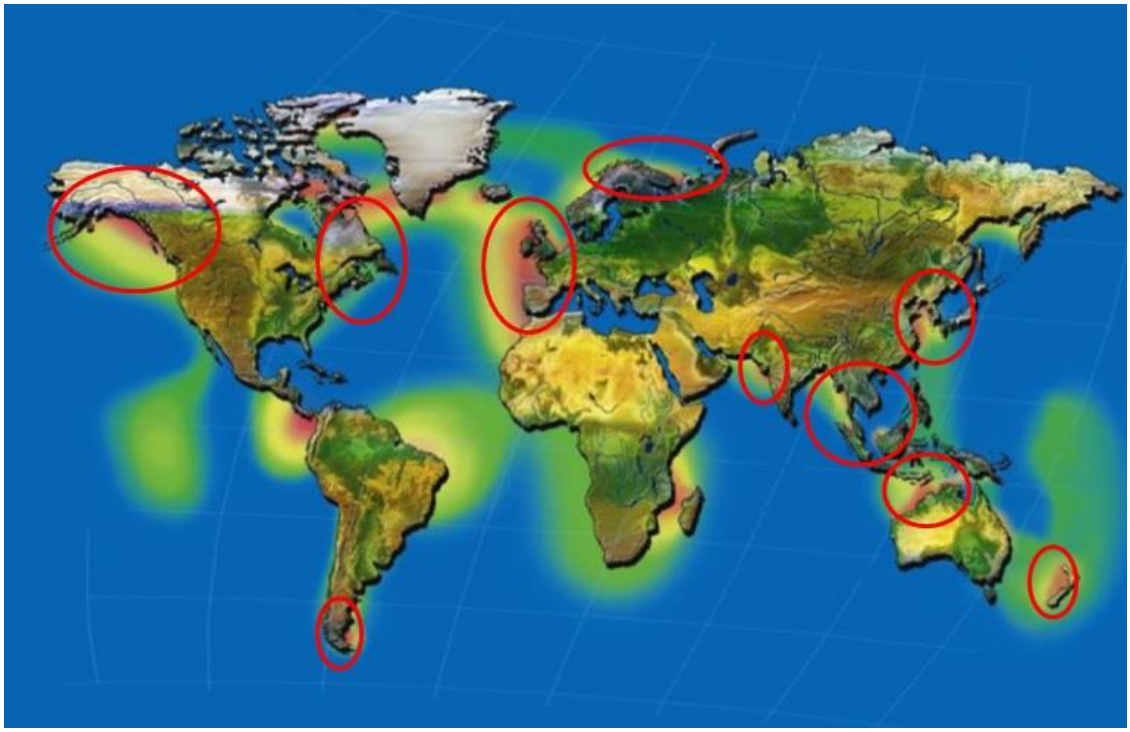

Figure 1.5: World map with areas of higher tidal velocities shown as red. Potential turbine array deployment sites are circled [8].

1.3 Development of Tidal Stream Technologies

There are 6 primary types of tidal stream energy convertors (see Figure 1.6). In all cases, the moving water exerts forces on the convertor as it flows across it causing some part of the convertor (e.g. a rotor) to move, thus converting the kinetic energy of the moving fluid to mechanical energy.

Horizontal axis turbines (HATs) (Figure 1.6 (a)) extract energy from moving water much as wind turbines extract energy from moving air. The tidal stream causes a rotor to turn about its horizontal axis and generate power. Vertical axis turbines (VATs)

(Figure 1.6 (b)) extract energy from the tides in a similar manner, but in their case, the rotor is mounted on a vertical axis. Venturi-effect devices (Figure 1.6 (c)) funnel the water through a duct before it enters the turbine, thus increasing the water velocity. The resultant flow can drive a turbine directly, or the induced pressure differential in the system can drive an air turbine. An oscillating hydrofoil device (Figure 1.6 (d)) involves a hydrofoil attached to an oscillating arm. The tidal current flows either side of the hydrofoil results in lift. This motion then drives fluid in a hydraulic system to be converted into electricity. The Archimedes screw (Figure 1.6 (e)) is a helically shaped device (a helical surface surrounding a central cylindrical shaft) which extracts power from the tidal stream as the water moves up/through the spiral thus turning the screw/turbine. Finally, a tidal kite (Figure 1.6 (f)) is a device much like a normal kite that is tethered to the seabed and carries a turbine below its wing. The kite 'flies' in the tidal stream, swooping in a figure-of-eight shape to increase the speed of the water flowing through the turbine.

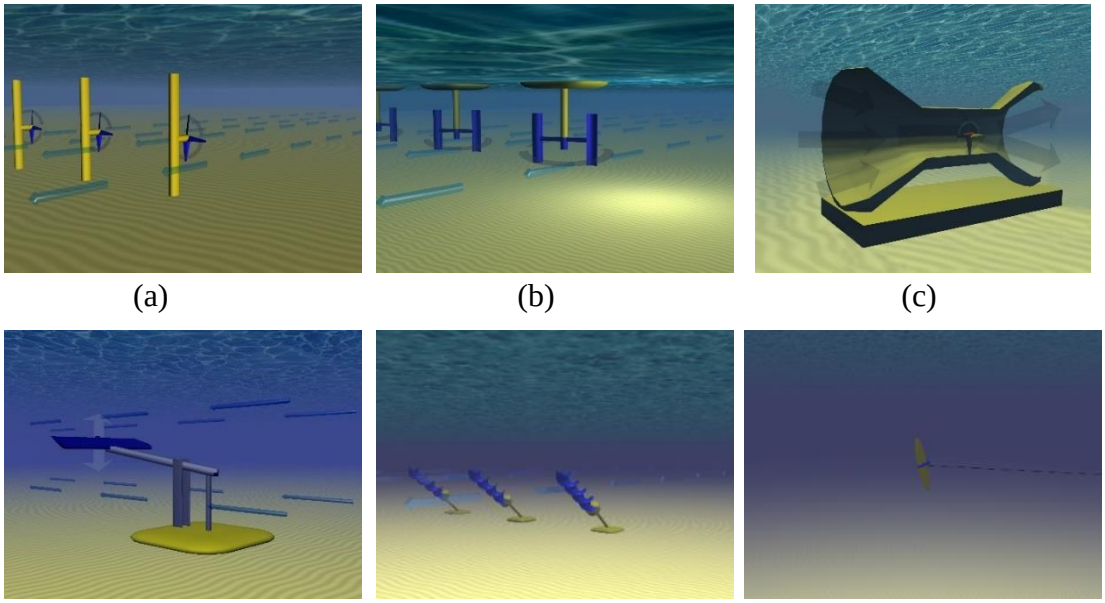

Figure 1.6: Common categories of tidal stream energy convertors: (a) HAT, (b) VAT, (c) Venturi device, (d) Oscillating hydrofoils, (e) Archimedes screw, and (f) tidal kite. [9]

The tidal stream energy industry is still in its early stages. Many tidal stream devices are still under research and development. The path to a mature technology involves many iterations of testing and design developments. A small number of devices, primarily horizontal axis turbine designs, are at an advanced stage of development and have progressed to the deployment of full-scale devices; further details on these devices can be found in the source references of the images in Figure 1.7. An example is the SeaGen device developed by Marine Current Turbine (MCT), a full-scale 1.2 MW, horizontal axis, twin turbine (Figure 1.7 (a)) which was deployed in Strangford Lough, Northern Ireland from 2008 to 2017. The company has since been acquired by Simec Atlantis Energy (formerly Atlantis) and the device has undergone a redesign with the Seagen S series now consisting of two twin, three-bladed, 1 MW rotors of 20 m diameter. Verdant Power's three-bladed horizontal axis turbine (Figure 1.7 (b)) has also been deployed at full-scale. This device consists of a 5 m rotor and has a power capacity of 35 kW. The turbine is deployed on their TriFrame support structure that allows for multiple turbines to be deployed on a single unit.

Other examples of leading technologies are shown in Figure 1.7. These include Simec Atlantis Energy's AR1500 (Figure 1.7 (c)), a Lockheed Martin designed, 1.5 MW turbine consisting of a 3-bladed rotor of 18 m in diameter. The Scotrenewables SR2000 device (Figure 1.7 (d)) is rated at 2 MW at a velocity of 3 m/s. The device comprises two 16 m rotors positioned either side of a long floating support structure. OpenHydro's 2 MW device (Figure 1.7 (e)), is an open centre 16 m diameter turbine. The turbine uses a direct drive permanent magnet generator, which is positioned in a ring outside the rotor. The turbine which weighs approximately 300 tonnes sits unmoored on the seabed floor. Andritz Hammerfest Hydro's HS1500 turbine (Figure 1.7 (f)) is a 3-bladed turbine with a 21 m diameter rotor and a rated power of 1.5 MW. The turbine utilises a gravity-based deployment, weighing approximately 450 tonnes. The Sabella D10 turbine (Figure 1.7 (g)) consists of six blades and has a rated power of 1 MW. The turbine has a 10 m diameter. Finally, Voith's 1 MW HyTide 1000 (Figure 1.7 (h)) has a rotor diameter of 13 m and weighs 200 tonnes. All of these devices are horizontal axis turbine designs.

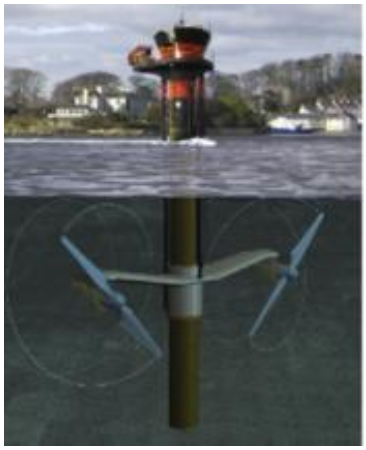

(a) (Source:[10])

(b) (Source:[10])

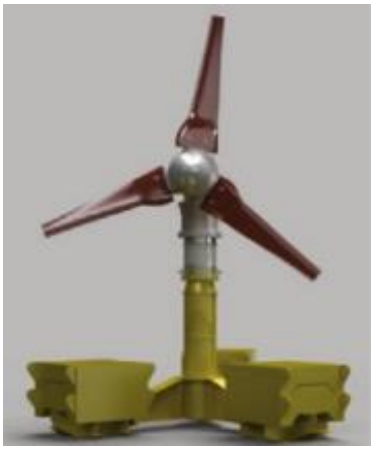

(c) (Source:[10])

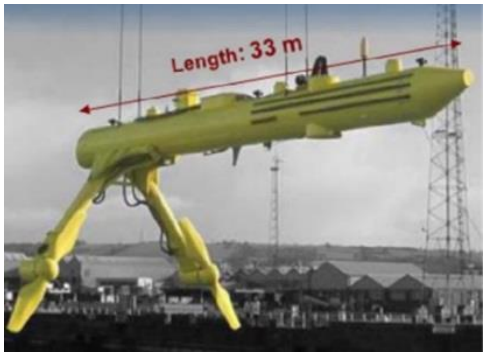

(d) (Source:[11])

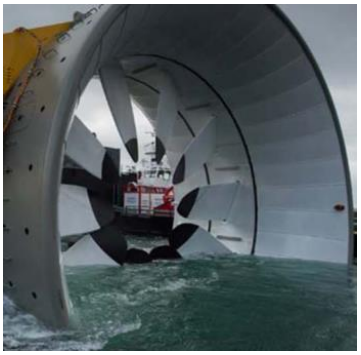

(e) (Source:[12])

(f) (Source:[12])

(g)(Source: [13])

(h) (Source:[11])

Figure 1.7: Tidal energy market leaders, all of which are horizontal axis turbines.

The tidal stream turbine industry faces many challenges. Not least among these is the engineering challenge of designing and building a device that can efficiently generate power, whilst surviving the enormous hydraulic loads generated by flows of up to 5 m/s (Bay of Fundy) and the harsh conditions of the marine environment [14]. Whilst device performance and survivability are probably the two most important design factors; there are also other significant challenges such as environmental impact assessment and mitigation, designing for ease of deployment and maintenance and the need for offshore electrical infrastructure. Overcoming all of these challenges has proven to be extremely expensive; a fact highlighted by the recent liquidation of OpenHydro, who were one of the most promising tidal device developers in recent times.

Manufacturing costs for full-scale devices can be hugely expensive, so developers need to have a fully optimised design which has been evaluated at smaller scales. While financial expenses are lower for performance evaluation of smaller scale devices; they can still be prohibitive. Experimental testing should be carried out in conjunction with the performance evaluation of numerical methods. This involves physical and numerical modelling at various scales and for different prototype designs. Even laboratory testing of turbines can be expensive, and suitable facilities are relatively scarce. Field testing is even more costly and is further hampered by the difficulties of working in a highly dynamic marine environment. Numerical modelling offers a cost-effective alternative for assessment and optimisation of prototypes at any scale. However, numerical models require experimental data for validation purposes to ensure confidence in the model's accuracy.

1.4 Industry Progression

While many of the leading companies mentioned in the previous section have deployed single full-scale devices, commercial feasibility will require deployments of turbine farms similar to wind farms.

In 2007, US turbine developer Verdant Power's Roosevelt Island Tidal Energy (RITE) project saw the deployment of the world's first grid-connected tidal turbine array (off Roosevelt Island, New York) comprising of six 5 m diameter turbines [10]. The Bay

of Fundy between New Brunswick and Nova Scotia is the most promising location in North America for tidal energy and could potentially produce as much as 30,000 MW of energy [15]. Several leading companies, including Simec Atlantis Energy (and formerly OpenHydro), are actively testing their technologies at the Fundy Ocean Research Centre for Energy (FORCE) and investing in demonstration projects there. OpenHydro's turbine was to be used for the 300 MW Cape Sharp tidal project that is being developed with Emera in Nova Scotia. The partners hoped to deploy a fully grid-connected 4 MW tidal array (2 x 2 MW OpenHydro devices) in the Bay of Fundy, one of which had been deployed.

In Scotland, Simec Atlantis Energy is the majority shareholder in the 398 MW Meygen tidal stream project, located at the Inner Sound in the Pentland Firth. As the largest fully consented tidal stream project in Europe, it is widely acknowledged as a flagship project for the industry. Construction began in January 2015, and the delivery of the first 6 MW is complete, comprising of four 1.5 MW turbines – three Andritz Hammerfest Hydro HS1500 turbines and an Atlantis AR1500. The next 6 MW stage is expected to start construction next year (2019) and will comprise of next-generation Seagen U tidal turbines developed by MCT. Completion of the full 398 MW array is expected around 2021. Simec Atlantis Energy have also acquired Scottish Power Renewables' two project portfolio of tidal projects and they plan to install a total of 640 MW tidal capacity (including Meygen) in Scotland by 2022. The Simec Atlantis Energy group has lease agreements for two further Scottish tidal sites, one at the Mull of Galloway in south-west Scotland and the other at Brough Ness in the Pentland Firth [16].

Elsewhere in Europe, work on a planned 100 MW tidal energy plant near Ballycastle, off the north Antrim coast could start by late 2018 or early 2019. The €450 million (using 2018 conversion rate) Fair Head Tidal project is a joint venture between DP Energy and Bluepower NV [16]. Prior to its liquidation, OpenHydro had been testing its Open-Centre Turbine at the European Marine Energy Centre (EMEC) in Orkney intermittently since 2006, and Scotrenewables have also been testing their SR2000 2 MW device at this site since October 2016, which to date has produced more than 3 GWh of renewable electricity in less than 12 months. The Fair Head Tidal project is in close proximity to a second 100 MW project being developed at Torr Head by Tidal

Ventures Limited (TVL), which was a joint venture between OpenHydro and Brookfield Renewable Energy Group [16]. TVL hoped to have the 70 MW phase of the project completed by 2020 but with the liquidation of OpenHydro, the project future is now uncertain. Tidal stream projects were also being developed in France through OpenHydro although with their recent liquidation it remains to be seen how these will progress. Two 16 m OpenHydro tidal turbines were to be installed in Paimpol-Brehat and a further seven for the 14 MW Normandie Hydro project; both projects were being developed in partnership with EDF [16]. OpenHydro were also working with Alderney Renewable Energy to develop a 300 MW tidal array in Alderney waters. They had recently opened a new manufacturing facility in Cherbourg where the devices for these projects were to be manufactured; the plant was estimated to be capable of producing 50 turbines per year.

1.5 The Irish Context

In Ireland, an assessment of the available tidal stream energy resources for the entire island of Ireland was conducted by the Sustainable Energy Authority of Ireland (SEAI) (formerly known as Sustainable Energy Ireland) in 2008 [17]. It was concluded that there is an annual tidal resource availability of 10.46 TWh; this was based on an assessment of sites with peak spring tidal currents in excess of 2 m/s. However, when shipping lanes and military zones were accounted for this value reduced to 2.63 TWh, and 11 potential deployment sites were identified (shown in Figure 1.8). To put this figure in context, a technical report by Eirgrid [18] shows that for the year 2014 the total electricity consumption for the entire island of Ireland was approximately 36 TWh. Tidal stream energy, therefore, has the potential to contribute 7.3 % of this demand.

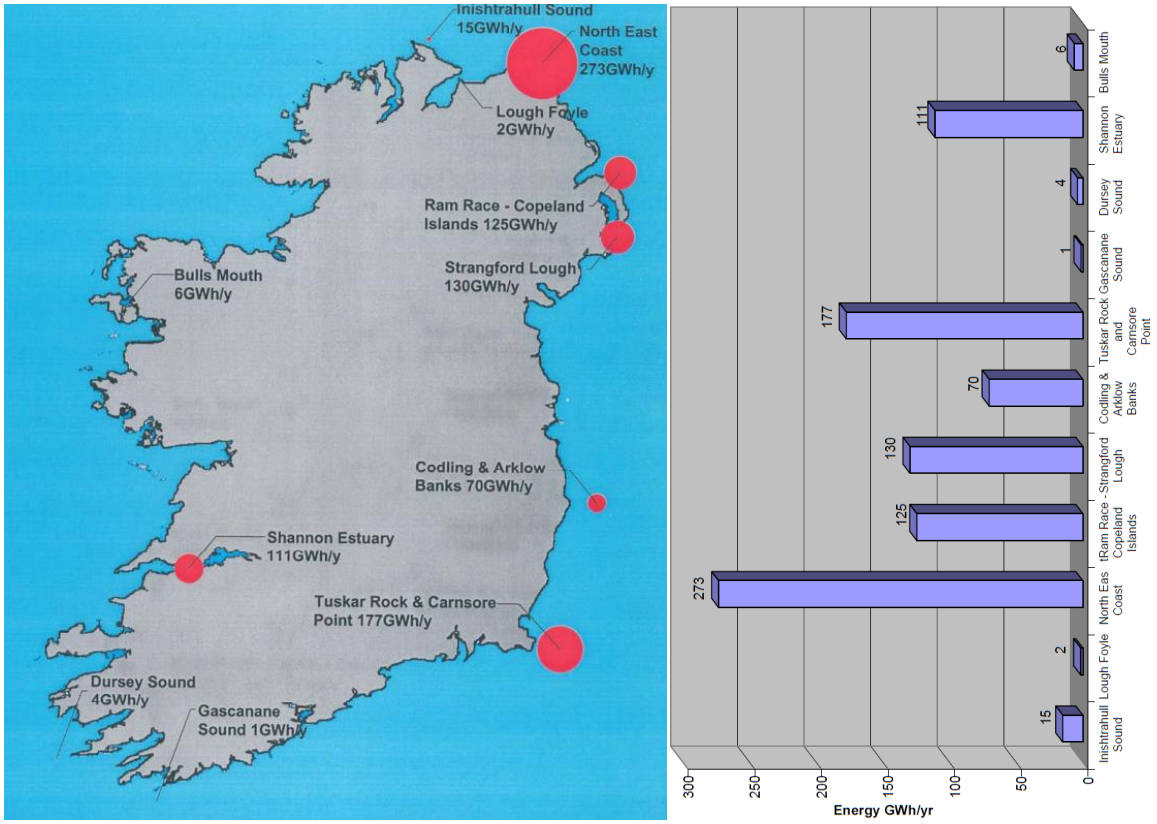

Figure 1.8: Accessible tidal resource assessment for the island of Ireland with locations above 2 m/s identified [17].

Renewable energy device developers in Ireland have access to various organisations, from whom they can seek both financial support and expertise. SEAI is one such organisation which is partially financed by Ireland's EU Structural Funds programme cofounded by the Irish Government and the EU. The role of SEAI is the reduction of the environmental impact of energy production and use, particularly in regards to greenhouse gas emissions, and they have a remit to advance the development and competitiveness of renewable energy devices. Device developers can, therefore, apply to avail of development grants of between 60 to 100 % of the financial cost of development through the SEAI Prototype Development Fund.

Device developers in Ireland can also apply for EU funding such as Horizon 2020, the most prominent EU research and innovation programme with a budget of almost €80 billion over seven years (2014 to 2020). The MaRINET2 project is an EU supported project that provides financial assistance for experimental testing of ocean energy device prototypes including offshore wind, wave and tidal stream. MaRINET2 has a

budget of €10.5 million and can provide access to 39 different testing facilities across 13 European countries.

Science Foundation Ireland (SFI) [19] oversee government research funding in the areas of science, technology, engineering and maths. In 2013, SFI funded the national centre for Marine and Renewable Energy in Ireland (MaREI). MaREI marries the expertise of 6 Irish research institutions with industry partners, with the shared objective of solving the scientific, technical and economic challenges encompassing the marine and renewable energy sectors in Ireland. MaREI has more than 200 researchers collaborating with 45 industry partners. To develop a commercially successful marine and renewable energy sector, both academia and industry need to work in partnership. Through MaREI industry partners have gained access to the testing facilities and research expertise available in member research institutes. The research project presented in this thesis was co-funded by SFI and the Irish tidal turbine development company, GKinetic Energy Ltd., through MaREI. The research was primarily focussed on the development of numerical modelling tools for assessment of the company's novel tidal stream turbine.

1.6 The GKinetic Turbine

The turbine which is the focus of this research is of vertical axis design. Figure 1.9 shows a conceptual image of the device from late 2013 (Figure 1.9 (a)) and a more recent picture of a design iteration of the device at 1:10 scale (Figure 1.9 (b)). The device, which comprises of two vertical axis turbines (VAT) on either side of a central supporting bluff body, has two unique design features. First, the bluff body acts to accelerate the entrance flows to the turbines above free-stream levels, and second, the pitch of the turbine blades is controlled to maximise the turbine torque. The blade pitching mechanism comprises a patented cam track which controls the pitch of the blades.

The turbines consist of six NACA 0018 blades selected for their symmetrical profile. At a specific location in the turbine's rotation cycle, the blades undergo a 70° change in pitch, and the symmetrical profile ensures that both sides of the blade exhibit the same lift and drag characteristics. The turbine rotors are positioned at the point of

maximum flow acceleration around the bluff body, as determined from a scale study of the bluff body [20]. The device is designed to float in the water column such that the turbines are fully submerged, and moored to the seabed. The bluff body also acts as a ballast tank, with water added or removed during deployment and retrieval, and as a pivot about which the device can rotate to align with flood and ebb tides. A device with fixed bluff body positioning is also under design for river deployments.

(a) (b)

Figure 1.9: GKinetic device as: (a) a concept in late 2013, and (b) a viable 1:10 scale device.

The SEAI report on Ireland's tidal stream resource [17] identified 11 suitable locations for the deployment of tidal turbine arrays around Ireland. However, as most tidal turbines require peak current speeds of between 2 to 2.5 m/s [21] for operation the assessment ignored any site that has a flow velocity below 2 m/s. However, as the GKinetic device is capable of accelerating the free-stream flow, there are many more possible deployment sites around Ireland alone.

1.7 Aims and Objectives

The principal motivation for the undertaking of this research was to help further the development of the GKinetic device toward a viable commercial-scale device. This involved experimental testing, numerical modelling and design analysis of the device. While the research into the GKinetic device is novel in and of itself as the device is new and novel; the major academic novelty is in the development and assessment of

appropriate numerical modelling techniques for VATTs for which there are relatively few published modelling studies. The hydrodynamic modelling research focusses on the development and validation of performance assessment models for high solidity vertical axis turbines in general, and the GKinetic device, in particular. The research will present the development and application of several numerical models, primarily Computational Fluid Dynamics (CFD) and Blade Element Momentum Theory (BEMT) models; the latter being a combination of momentum theory and blade element theory. The performance of the models is assessed against experimental data from scale experimental tests.

The objectives of the research are as follows:

- Experimentally characterise the mechanical performance of the GKinetic device at various scales, in controlled and uncontrolled environments. Testing also offered the opportunity to critically analyse device components post-testing and convey design improvements to the industry partner, where required.
- Develop a BEMT modelling approach for low and high solidity VATTs and assess model performance against published experimental test data.
- Develop a structured 2D and 3D CFD modelling methodology for VATTs and assess model performance against measured experimental data. Investigate any potential means of improving the accuracy of notoriously inaccurate 2D CFD models.
- Apply the 2D CFD modelling methodology to the GKinetic device and validate the model against experimental test data.

1.8 Thesis Layout

The layout and content of this thesis are as follows:

Chapter 2 presents a literature review of relevant research including experimental testing and numerical modelling of tidal stream turbines. The experimental approaches used by previous researchers are reviewed. These results are used as a benchmark for performance quantification of the GKinetic device. The review of relevant numerical modelling literature focuses on performance prediction using BEMT models and CFD models. The novel aspects of the current research are then outlined relative to the

findings of the literature review.

Chapter 3 presents the CFD modelling theory. The governing differential equations and their formulations are outlined and discussed. The model solution scheme is described, particularly regarding the Reynolds Averaged Navier-Stokes (RANS) equations. Various turbulence models are presented, and the derivation and implementation of those turbulence models relevant to VAT modelling are discussed and explained in detail.

Chapter 4 presents details of the experimental testing of the GKinetic turbine at 1:40, 1:20 and 1:10 scales. Detailed information is included on development and calibration of the various instrumentation used during testing. Flow characterisation of the bluff body alone (i.e. without the turbine in place) was carried out to assess the levels of flow acceleration. Mechanical power performance of the device was determined over a broad range of flow velocities and tip speed ratios. Device drag loads and subsequently drag coefficients were also determined.

Chapter 5 presents the development of the BEMT model for VATs. The majority of BEMT models in the literature use an iterative approach for determining the axial induction caused by the rotor. However, this research implements an alternative graphical approach recently developed, for highly loaded or high solidity horizontal axis wind turbines, and subsequently adapted for vertical axis wind turbines. The approach has never been used for tidal VATs. The implementation of various corrective approaches used to improve model accuracy is also documented.

Chapter 6 presents the development and validation of a CFD modelling methodology for VATs using the sliding mesh technique. The methodology is assessed by the application (in 2D and 3D) to a 0° fixed pitched, vertical axis tidal turbine (VATT) which was built and tested by University of New Hampshire; however, the methodology can be applied to any VAT. Both 2D and 3D CFD models are compared for accuracy against published measured data and a method for improving 2D model accuracy is proposed.

Chapter 7 details the development of a 2D CFD model of the GKinetic turbine using the modelling methodology of Chapter 6. A nested sliding mesh technique is used to

model the variable pitch blades, and a method was developed to accurately control the pitch of the blades to reflect the experimental setup. The model is validated against experimental test data and is subsequently used to investigate the effects of some design decisions on device performance.

Mechanical and structural analysis and redesign of the GKinetic device also formed part of the project. However, as this was beyond the scope of the research it is presented for completeness in Appendix A.

Finally, Chapter 8 presents a summary of the research, along with the author's final conclusions and recommendations for further progress of the research.

Chapter 2. Literature Review

2.1 Introduction

The GKinetic turbine which is the focus of this research is a VATT. This literature review, therefore, focuses on the operation, testing and modelling of VATs. While the focus of the research was on tidal turbines, due to their longer history, studies of vertical axis wind turbines (VAWT) were also included.

Although many of the leading tidal stream turbine technologies are horizontal axis turbines, there is still significant interest in VATs. This is mainly because of the advantages of VATs over HATs. VATs are omnidirectional, eliminating the necessity of a yawing system. During operation, they produce significantly less noise than HATs [22]. The generator for a VAT can be positioned in a convenient location for installation and maintenance purposes whereas the generator for a HAT is usually housed in the nacelle. In addition, the generator is not limited by weight restrictions, as is the case with HAT designs due to additional shaft bending stresses. The blade manufacturing process is less arduous for VATs as they are usually straight and of constant chord-length [23]. Finally, VATs have three times the power density at one-tenth of the height in contrast to HATs [24]. Power density in this instance is calculated as the turbine rated power divided by the area of the circular swept area. As HATs need to be yawed 360^{o} they occupy significantly more ground area in comparison to VATs.

The main disadvantages of fixed pitched VATs emanate from large variations in the angle of attack of the blade within a single rotor rotation [25]. The consequence of this is that optimal lift and drag performance cannot be maintained over the course of a full rotation, thereby resulting in lower efficiencies in contrast to HATs [26]. Furthermore, as blade loads of a VAT are highly cyclic, fatigue performance is reduced in comparison to HATs and oscillations occur in torque output and by extension mechanical power.

2.2 The Principals of Operation of Vertical Axis Turbines.

Lift based turbines use aerofoils/hydrofoil profiles (Figure 2.1) to enhance the lift forces generated as the fluid flows around them. The aerofoil/hydrofoil shape and the angle of attack, α, of the fluid (the angle between the relative velocity of the fluid, V_{rel}, and the foil chord-line, see Figure 2.1) cause a difference in velocity between the top and bottom surfaces of the aerofoil/hydrofoil [27]. This velocity difference also results in a pressure variation due to conservation of energy. This pressure variation results in a force on the aerofoil which is comprised of component forces perpendicular and parallel to the direction of fluid flow, namely the lift, F_L, and drag, F_D, forces [27]. The forces acting normal and tangential to the foil chord-line can be determined using trigonometry from the lift and drag forces. The tangential force is the main contributor to torque for lift-based devices. The main difference in lift and drag operated devices, as the name suggests, is the component of flow which is predominantly used to generate torque, and subsequently power. In lift-based devices, the aim is to maximise lift, while keeping drag to a minimum. In contrast, drag-based devices operate on the premise of maximising the drag force by obstructing as much of the flow as possible. The Savonius rotor is the most common type of drag turbine.

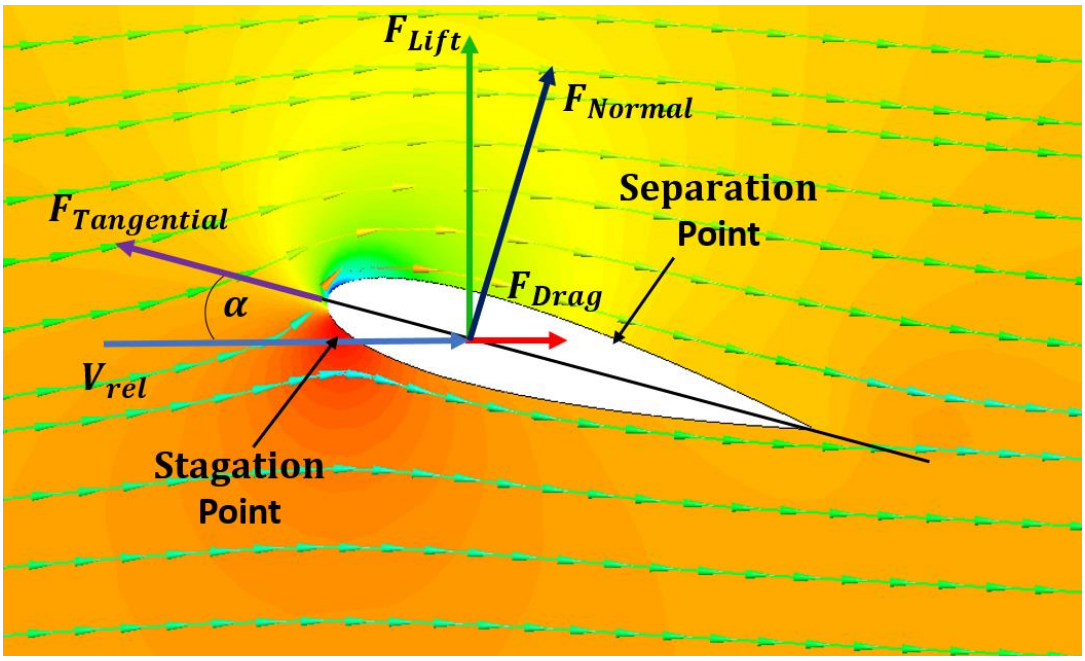

Figure 2.1: Flow around aerofoil with contour map coloured by pressure and streamlines coloured by velocity. Pressure increases from blue through green, yellow and orange to red. Also indicated are key variables and locations.

A stagnation point (shown in Figure 2.1) where local velocity goes to zero is seen to occur near the front of the foil. Stagnation points occur where fluid flows are blocked by the presence of an obstacle, in this instance an aerofoil/hydrofoil. The energy equation [27] shows that static pressure is highest when velocity is zero; therefore, static pressure is at its maximum at stagnation points.

A separation point, also shown in Figure 2.1, is a point on the surface of an aerofoil/hydrofoil where a high-pressure gradient occurs. Once this pressure gradient grows strong enough, the flow is no longer capable of overcoming it and starts separating. The flow subsequently starts to reverse towards the leading edge; at this point, the shear stress on the surface is zero. Flow separation results in loss of lift and blade stall. Stall is discussed in more detail in Section 2.3. There also exists a flow phenomenon similar to separation, known as the laminar separation bubble, that occurs near the leading edge of the foil, but here the flow does not separate. Instead, the flow reattaches and contributes to lift [28].

The lift and drag forces generated on a foil are a function of the lift and drag coefficients, C_{L} and C_{D}, of the foil, which in turn are dependent on foil shape, angle of attack and Reynolds number. Figure 2.2 presents a plot of static C_{L} versus α with the location of stall onset identified. As is clear in the figure, stall results in a significant reduction in the lift generated by an aero/hydrofoil with increasing angle of attack. The value of α where stall starts to occur is known as the critical angle of attack, or the static stall angle, α_{SS}, and is typically about 10^{o} to 15^{o}. Its value is dependent on foil shape and Reynolds number.

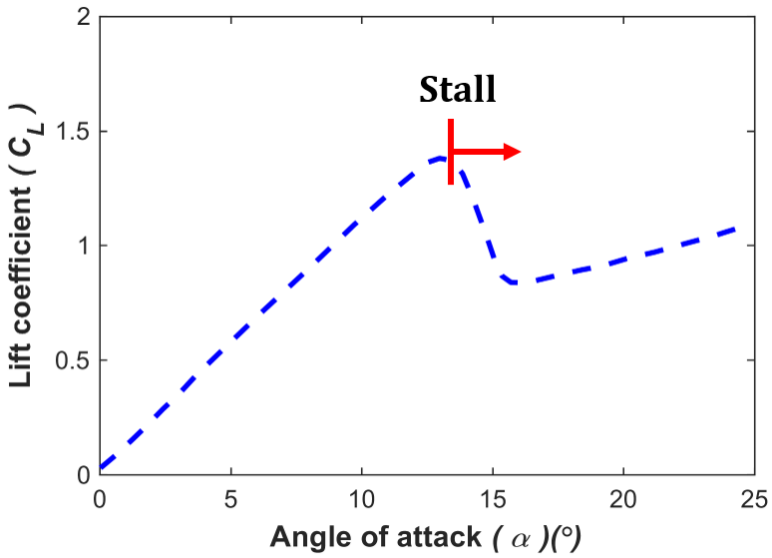

Figure 2.2: Plot of static lift coefficient versus angle of attack, with the location of stall onset identified.

The National Advisory Committee for Aeronautics (NACA) aerofoil profiles and more specifically the NACA 4-digit series are the most commonly used profile for turbines. An example is the NACA 4218 profile. The first digit of the name specifies the maximum camber (asymmetry) as a percentage of chord-length. The second indicates the location of the maximum camber in tenths of chord-length, and the last two numbers provide the maximum thickness of the aerofoil profiles in percentage of chord-length. So for example, the NACA 4218 profile has a maximum thickness of 18 % with a camber of 4 % located 20 % back from the aerofoil leading edge. In symmetrical profiles, the first two digits are zeros and take the form of 00XX.

2.2.1 Turbine Power Performance and Tip-speed Ratio

The mechanical performance (or efficiency) of a wind/tidal stream turbine is measured by the power coefficient (C_P), defined as the ratio of mechanical power generated by a turbine, P_mech, to the power available from the fluid flow, P_avail:

$$C_\mathrm{P} = \frac{P_\mathrm{mech}}{P_\mathrm{avail}} = \frac{Q\Omega}{\frac{1}{2}\rho A {U_\infty}^3} \tag{2.1}$$

where, Q is torque, Ω is the turbine rotational velocity, U_∞ is the free-stream velocity and A, the reference area (full device entrance area).

C_P is highly dependent on the tip speed ratio or TSR (λ) which is the ratio of the tangential velocity of the turbine blade to the ambient/free-stream fluid velocity:

$$\text{TSR } (\lambda) = \frac{\Omega R}{U_\infty} \tag{2.2}$$

where, R is the turbine radius.

The power performance curve for a wind/tidal turbine is obtained by plotting C_P against λ and the curve generally has a bell-shaped distribution. Figure 2.3 shows a sample power curve for a typical lift-operated VAT. The peak of the bell-curve indicates the maximum C_P that can be achieved by the turbine and the optimum λ value at which this occurs. At higher and lower λ values, power performance drops off.

With reference to the sample power curve, at low λ values, significant variations in blade angle of attack occur during each rotation of the turbine, resulting in deep stall for much of the blade's azimuthal rotation. Increased drag levels, in addition to the relative velocity of the blade not far exceeding that of the free-stream velocity, results in low torque output and indeed negative torque in some cases. As λ increases, the range of variations in angle of attack is reduced and performance rapidly increases, as large azimuthal regions of attached flow are achieved. Turbine performance in this region is dominated by dynamic stall (discussed in detail in section 2.3.1) which delays both blade stall and subsequently flow reattachment. At yet higher λ values, the maximum performance is achieved (for straight bladed turbines) when variations in the angle of attack are reduced to the point where blade stall no longer occurs at any azimuthal location. Large lift forces relative to small drag forces result in large blade forces in the direction of rotation, and thus large shaft torque. Increasing λ above the optimum value, results in a continual decrease in the range of variations in blade angle of attack. This results in parasitic effects, as zero lift-drag and spoke drag begin to dominate in this higher λ region, causing significant reductions in turbine performance.

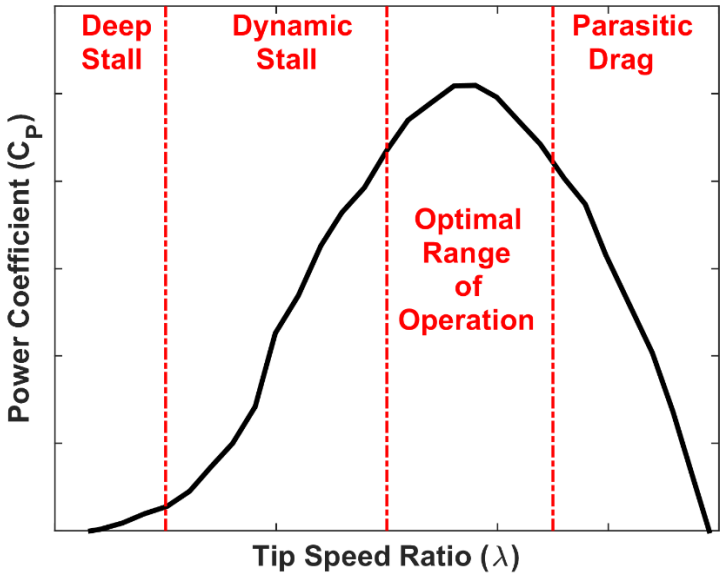

Figure 2.3: Typical VAT power curve (adapted from Paraschivoiu *et al.*[17])

2.3 Normal and Dynamic Stall

Normal stall is the result of flow separation occurring over the low-pressure surface of an aero/hydrofoil. As the angle of attack of the aero/hydrofoil is increased, the stagnation point moves back along the high-pressure surface of the aero/hydrofoil. As a result, the flow must then accelerate around the nose of the aero/hydrofoil, causing the minimum pressure on the opposing surface to drop and move towards the leading edge. In turn, a large adverse pressure gradient forms downstream of the minimum pressure location. At a critical angle of attack, the flow momentum within the boundary layer can no longer overcome the growing adverse pressure gradient, at which point the flow stops and reverses [29]. As a result, the flow separates and places the aero/hydrofoil into the stall regime. At high Reynolds numbers, stall is delayed to greater α values and higher lift force coefficients are obtained. One of the primary reasons for this behaviour is the transition from laminar to turbulent flow. Transitional flow regimes have a significant impact on the onset of stall [30]. In a laminar flow boundary layer, there is less momentum in the flow near the aero/hydrofoil surface, and thus is more prone to separation. Several studies have been performed by the NACA, as well as other international organizations, to quantify this behaviour for numerous aero/hydrofoil shapes and Reynolds numbers [31–34].

2.3.1 Dynamic Stall

Dynamic stall is a non-linear, unsteady aero/hydrodynamic effect that occurs when the pitch angle or angle of attack of an aero/hydrofoil is rapidly changed. This results in highly dynamic flows over the surface of the aero/hydrofoil which exhibit far different behaviour than steady state flow [30]. The resultant unsteady variation in the lift, drag and moment forces acting on the aero/hydrofoil are related to the pitching rate, the maximum pitch angle and the conditions of the oncoming flow, amongst several other things.

2.3.2 Static and Dynamic Stall Behaviour

Aerofoil characteristic data (e.g. lift, drag coefficients and stall angle) are typically collected during steady-state or static loading tests where the following conditions apply:

- The desired angle of attack is reached by slowly adjusting the pitch of the aero/hydrofoil.
- The aero/hydrofoil remains at a fixed angle for the duration of the test.
- Steady-state conditions are allowed to be reached and transient flow conditions diminish.

In contrast, dynamic loading data is obtained by rapidly pitching an aero/hydrofoil and shows large differences with the steady state loading data. From the analysis of the experimental test data, it has been identified that if an aero/hydrofoil undergoes rapid increases in α, overshoots in lift, drag, and pitching moment occur [35,36]. Stall is, therefore, delayed to higher α values than those of static stall. This behaviour is referred to as "dynamic stall". It has been shown that the loss of lift during a deep dynamic stall is much more sudden and lasting then during static stall [37].

The dynamic stall process has been shown to be a function of numerous variables such as aero/hydrofoil shape, the rate of change of angle of attack, Reynolds number and Mach number as well as three-dimensional effects, such as downwash. The 2D dynamic stall process is depicted in Figure 2.4.

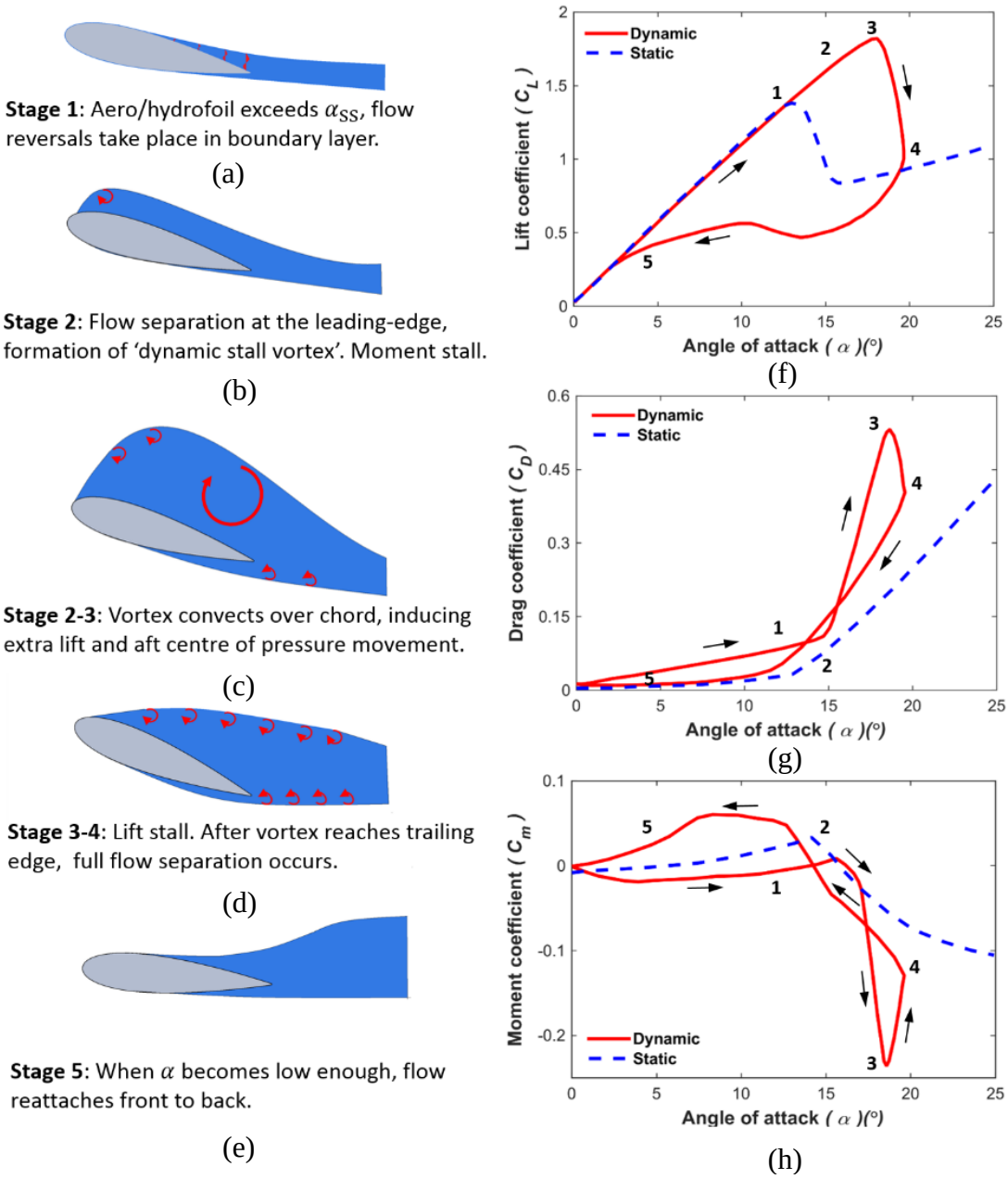

Figure 2.4: An illustration of the 2D dynamic stall process on an aero/hydrofoil undergoing pitching oscillations. Graphical representations of stages 1 to 5 are shown in (a) to (e), while the hysteresis loops for lift, drag and moment coefficients are presented in (f) to (h), respectively. The numbers on the graphs refer to stages 1 to 5.(adapted from Leishman [28])

Stage 1. The aero/hydrofoil pitches upward increasing α past the static stall angle, α_{SS}, resulting in flow reversal within the boundary layer (Figure 2.4 (a)). However, the onset of flow reversal, and boundary layer separation, is delayed to a higher α than the static stall angle by positive virtual camber (flow curvature due to the pitch-up

motion) and vorticity shed from the trailing edge reduces the adverse pressure gradient for the dynamic case.

Stage 2. With further increases in α, the separation point moves towards the leading edge. Boundary-layer separation results in negative wall shear forces acting along the low-pressure surface. The movement of the aero/hydrofoil's centre of pressure (a reduction in the leading edge suction peak due to boundary-layer separation) results in a large, nose-down pitching moment, termed moment stall (observed in Figure 2.4 (h)). Boundary-layer separation is responsible for a sharp rise in the form drag (drag due to aerofoil shape), as illustrated in Figure 2.4 (g). Briefly unaffected by separation on the low-pressure surface of the aero/hydrofoil, lift as shown in Figure 2.4 (f) continues to rise, over-shooting the maximum static values. Streamline curvature around the leading edge creates high local velocities at the point of separation resulting in significant vorticity in the recently formed free-shear layer. This shear layer then begins to wrap-up, forming the dynamic stall vortex, maintaining streamline curvature above the aero/hydrofoil, blade normal pressure gradients, and hence lift as illustrated in Figure 2.4 (b).

Stage 3. Further vorticity builds up from the leading edge causing the growth of the dynamic stall vortex (Figure 2.4 (c)), reducing the rate of the structure's stream-wise convection. Whilst the dynamic stall vortex remains above the aero/hydrofoil, large streamline curvature and correspondingly high values of lift are maintained, Figure 2.4 (f).

Stage 4. Once the dynamic stall vortex convects past the trailing edge of the aero/hydrofoil, streamline curvature can no longer be maintained across the highly separated flow field above the aero/hydrofoil's low-pressure surface. Lift is then shown to drop sharply (Figure 2.4 (f)), termed lift stall, and full aero/hydrofoil separation results, characterised by a pair of quasi-stable free shear layers originating from the aero/hydrofoil's leading and trailing edges (Figure 2.4 (d)). At this stage, aero/hydrofoil forces and moment tend towards static values (see Figure 2.4 (f), Figure 2.4 (g) and Figure 2.4 (h)).

Stage 5. When the foil pitches downwards, similar stall delays observed in stages 1, 2 and 3 occur, concerned with the effects of negative virtual camber and the requirement

to convect the vortices downstream of the aero/hydrofoil prior to the establishment of new flow conditions. In this case, the re-attachment of the upper surface boundary layer (Figure 2.4 (e)) results in an under-shoot in lift below static values (Figure 2.4(f)). With further decreases in α, attached flow is re-established, thus closing the force and moment hysteresis loops.

Many numerical models, of varying levels of complexity, have been developed aspiring to simulate the above dynamic effects. These have been based on either steady 2D aero/hydrofoil data or dynamic aero/hydrofoil coefficients (obtained from wind tunnel tests) and information on aero/hydrofoil dynamics without resorting to costly higher order methods such as CFD. A review of dynamic stall models applied to wind turbines by Larsen *et al.* [38] lists the following frequently used models: the Boeing-Vertol model [39], the ONERA model, the Leishman-Beddoes model [40], with modifications of the Leishman-Beddoes model by Øye [41] forming the Øye model and modifications by Hansen *et al.* [42] forming the Risø model. Increasingly empirical in nature, the more advanced Leishman-Beddoes dynamic stall model, the Risø and Øye derivatives and the ONERA model require fitting coefficients derived from unsteady experimental data. This makes them more complex to implement and they were therefore not considered for this research.

The main requirements of a dynamic stall model within the scope of this thesis is that it covers the broad effects of stall delay and subsequent reattachment on lift and drag (but not pitching moment) for the purpose of cyclic averaged power predictions for turbine operation at various tip-speed-ratios. Dynamic stall models are discussed further in Chapter 5.

2.3.3 Aero/Hydrofoil Characteristic Data

Lift and drag characteristic data are key input data for several numerical models of wind/tidal turbines, such as BEMT models. Sheldahl and Klimas [34] present tabulated lift and drag characteristic data that are often used in turbine modelling studies [25,43,44]. The Sheldahl and Klimas [34] data is a hybrid of experimental results and results from a Panel Method numerical code. Panel methods are a type of discrete potential flow solution involving distribution of singularity elements over the surface of the aerofoil. This inviscid solution is frequently combined with an integral

boundary layer solution, which utilises the inviscid pressure distribution. Where the displacement thickness of the boundary layer can be used to update the geometry of the inviscid solution. Such viscous-inviscid coupling usually involves an iteration of the two solutions.

Sheldahl and Klimas [34] used the Profile (panel method) code of Eppler and Somers [45], often known simply as Eppler's model, in conjunction with experimental data to produce lift and drag characteristic data for NACA 0012, 0015, 0018, 0021 and 0025 series aerofoil profiles over an extensive range of angle of attacks and Reynolds numbers. Pre- and early stall section information was calculated, using the Profile code. Late and post-stall section characteristics were taken from the measured data. The high angle of attack data assumes Reynolds number independence, in that high angle of attack data is the same across all Reynolds numbers. It also assumes independence for the thicker sections (the NACA 0015 data are used for the 0018, 0021 and 0025 sections). These data are frequently used in blade element momentum theory models (this being their intended use) but are sometimes mistakenly referred to as being of purely experimental origin [46].

With regard to the Sheldahl and Klimas data, the precise α value where data switched from calculated to measured characteristic coefficients was determined by trial and error, based on a multiple stream-tube model developed by Sandia [47] called the DARTER code. The DARTER model was used empirically until the modelled C_{P} values agreed with the measured C_{P} values obtained from VAWT experiments. As the use of the DARTER code conflates static and dynamic stall performance, the "static" coefficients published by Sheldahl and Klimas have received criticism in the literature [48]. The panel method data for the NACA 0012 and 0015 sections show somewhat lower maximum lift coefficients than the experimental data of Sheldahl and Klimas for the Reynolds numbers which may be compared, and also show a more gradual pattern of stall. Despite the criticisms of the Sheldahl and Klimas dataset, its comprehensive nature (it covers a large range of aerofoil sections, angles of attack and Reynolds numbers) means it is still the data set most commonly used in BEMT models. It has also been shown to be more accurate than other methods of computed characteristic aerofoil data such as XFoil [49].

2.4 Experimental Testing of Tidal Turbines

Literature was examined in relation to the physical testing of scaled, and full-sized, VATs. Much of the early research relating to vertical axis wind turbines were carried out by the Sandia National Laboratories [50–53]. Most of the literature focused on the determination of the power coefficient for the turbine. Much less attention was devoted to the characterisation of the turbine wake.

2.4.1 Tidal Turbine Testing Standards and Best Practices

The literature review identified two testing protocols and an International Electrotechnical Commission (IEC) standard related to structured testing and development of tidal turbines. These were:

- "Tidal-current energy device development and evaluation protocol" developed by the University of Southampton [54],
- "Best practice for tank testing of small marine energy devices" developed by EquiMar [55].
- "Wave, tidal and other water current converters. Part 200: Electricity producing tidal energy converters — Power performance assessment" developed by the IEC [56]

The University of Southampton protocol recommends a "stage-gate" approach to device development with a total of five stages and gates. A stage represents the development activities, and a gate is the point of evaluation of those activities. Where a decision is taken to proceed to the next level, or perhaps to iterate within the same level until certain criteria specified in the gate are fulfilled. Each stage is subdivided into technology development and evaluation, followed by economic evaluation. The economic evaluation is refined at each stage, to produce a range of estimates of the final cost of energy for a particular sized array of devices. The development stages 1 to 3 detail mandatory scale testing and analytical requirements in conjunction with research and development. Stages 4 to 5 are concerned with full-scale testing in the sea.

The EquiMar protocol sets out methods for tank testing of tidal (and wave) energy

converters. It contains explicit methodologies for experiment design and uncertainty analysis. The protocol recommends that these experimental methodologies should be considered the minimum requirement for tank testing of scale tidal energy devices. The protocol places particular emphasis on experiment repeatability, quantification of uncertainty, and estimation of accuracy.

The IEC standard relates to testing of electricity-producing tidal energy converters. The standard is useful as it provides guidelines on methodologies and recommendations on such aspects as device placement, data collection and data processing etc. The standard gives a good basis for testing methods and data analysis techniques, such that different devices can be directly compared in terms of site characteristics, turbine performance and operation.

There are two main dimensionless parameters relevant for scaling of marine energy converters, Froude number (Fr) and Reynolds number (Re). In undertaking any scaling evaluation, only one parameter can be considered; therefore, devices can only be realistically scaled in terms of the surface effects or blade effects respectively, but not both.

The review of the testing protocols/standards showed that, that in general, the power performance of a turbine should be studied by establishing the C_{P}, over a range of λ values. C_{P} and λ are dimensionless parameters that readily facilitate hydrodynamic performance comparison for turbines of different specifications and under different assumed flow conditions. The free-stream or towing speed should be recorded in a location or manner which is unaffected by the local flow around the device. This is important to ensure accurate calculation of the power available to the device and, by extension, the power coefficient. Variables such as rotor thrust and torque should be measured using a calibrated torque transducer mounted so that it experiences forces prior to any frictional losses. The use of strain gauges or purpose-built load cells incorporating resistors or piezoelectric elements for load measurement is endorsed. Sampling rates in the region of 30 to 500 Hz are deemed adequate for data recording.

If blockage ratio (device area relative to the testing area) is greater than approximately

5 %, the results should be corrected to free-stream conditions, while blockage ratios in excess of 20 % should be avoided if possible. The difficulty associated with blockage correcting of experimental results for vertical axis turbines is discussed in Section 2.4.2.4. It is acknowledged in the IEC standard that there is a potential for power performance results to be influenced by turbulence inherent in the tidal flow. It is recommended that no corrections for the effect of turbulence be performed, due to the unavailability of acceptable methods.

2.4.1.1 Test Facilities

The most common approaches used for testing scale tidal turbines include placement in recirculating flumes or towing tanks, attachment to moving vessels or placement in rivers or the open sea. Controlled laboratory tests are recommended for small and intermediate scale devices, while field tests are more suitable for larger scale devices [55]. Laboratory tests are, in general, performed for a range of flow speeds and varying turbine rotational velocities to allow production of power curves. Examples of laboratory facilities used in Europe include the recirculating flumes of IFREMER in Boulogne-sur-Mer, France, and CNR-INSEAN in Italy. CNR-INSEAN also has a towing tank that is regularly used in the evaluation of tidal devices, as is the Kelvin Hydrodynamics Laboratory (KHL) tow tank in the University of Strathclyde, Edinburgh, Scotland. A summary of the physical conditions of these laboratories is presented in Table 2.1.

Table 2.1: Main characteristics of commonly used testing facilities [57].

Institution	IFREMER	CNR-INSEAN 1	KHL	CNR-INSEAN 2
Facility Type	Flume	Flume	Towing	Towing
Length (m)	18	10	76	220
Cross-section (m)	4 x 2	3.6 x 2.25	4.6 x 2.5	9 x 3.5
Velocity range (m/s)	0.1 to 2.2	0.3 to 5	0.1 to 5	0.1 to 10
Turbulence Intensity (%)	3 to 15	2.5 to 12	N/A	N/A

For near commercial-scale devices, the European Marine Energy Centre (EMEC) is the location most commonly used for sea trials. Simec Atlantis, Scotrenewables and OpenHydro devices have all been tested at EMEC. Figure 2.5 shows an image of

Scotrenewable's SR250 device being testing at EMEC. Scotrenewables are currently testing a larger version of this device (the SR 2000) at EMEC and it is successfully producing electrical power to the grid.

Figure 2.5: Scotrenewable's SR250 device being testing at EMEC [9].

Gaurier *et al.* [57] carried out a comparative round robin testing programme as part of a MaRINET project in order to evaluate the variation in turbine power coefficient for the same turbine tested in different recirculation flumes and towing tanks. A 3-bladed horizontal axis tidal turbine of diameter D = 0.7 m was tested in four different test facilities, towing tanks at CNR-INSEAN and the Kelvin Hydraulics Laboratory (KHL) in Strathclyde University; and two recirculation flumes at CNR-INSEAN and IFREMER. The tests were conducted in the range of 0.6 to 1.2 m/s, with λ controlled in the range of 0 to 7. The average power coefficient shows good agreement (See Figure 2.6 (a)) between results with each test facility predicting a maximum average power coefficient $C_{\mathrm{P}max} \cong 0.43$ at $\lambda = 3.5$. Gaurier *et al.* state that some tests were repeated for every λ and so, in some cases, several curves are available (See Figure 2.6). Therefore, the error-bars plotted in the figure depict the dispersion of the different results obtained for identical configurations.

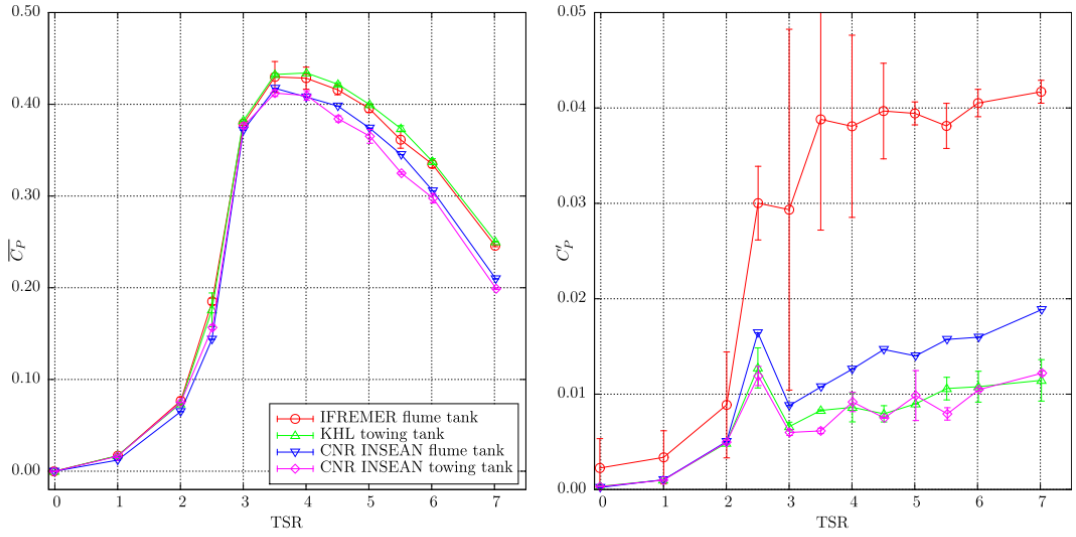

(a) $\overline{C_P}$ (b) C'_P

Figure 2.6: Mean and standard deviation of the power coefficient obtained for each test facility for U_∞ = 1.0 m/s

Mycek *et al.* [58] examined the effect of ambient turbulence intensity upstream of the turbine on the behaviour of horizontal axis tidal turbines. Turbulence intensities of 3 % and 15 % were investigated and it was found that the variation in turbulence intensity had very little effect on the mean power performance of the turbine. It did, however, have an effect on the standard deviation of the power coefficient and thrust coefficient; this is important in relation to fatigue of the turbine. It was also shown that the turbine wake is dispersed much faster with a higher inlet turbulence intensity.

2.4.2 Device Testing and Results

Most tidal energy turbines (both HAT and VAT) are predominantly lift-based, as drag-type turbines such as the Savonius turbine tend to have lower efficiencies [59]. Ever since its commissioning in 2007, MCT's "SeaGen" device has long been the benchmark for comparative purposes for turbine performance. It achieved peak mechanical efficiency of 48 % and water to wire efficiency of 44 % [60]. Verdant Power's three-bladed horizontal axis turbine has also been deployed at full-scale and achieved a mechanical efficiency of 43 % [61]. Table 2.2 presents a summary of the characteristics of large scale tidal turbines, all of which are horizontal axis designs.

Table 2.2: Performance characteristics of large-scale HATTs [11].

Device	DCNS OpenHydro	Atlantis AR1000	MCT SeaGen S	Voith	Sabella D10	GE-Alstom
Rated Power (MW)	2	1	2	1	1.1	1
Rated Velocity (m/s)	4.0	2.65	2.4	2.9	4.0	2.7
Number of Rotors	1	1	2	1	1	1
N_B (one rotor)	10	3	2	3	6	3
Rotor diameter D (m)	16	18	20	16	10	18
Swept area (m^2)	181	254	314	194	78.5	254
Estimated C_{Pmax}	0.34	0.41	0.48	0.41	0.43	0.39

2.4.2.1 VATT Studies

A summary table of several published studies on experimental testing of VATs is shown in Table 2.4. Of the tidal turbine studies, Shiono *et al.* [62] test a straight blade VATT for different flow speeds, and number of blades (N_B). The results presented show that that a single bladed turbine, outperforms it's 2 and 3-bladed counterpart for a constant solidity. They also conclude that, for rotors with four or more blades, there are no azimuthal regions where the torque becomes negative. Therefore, overcoming the start-up issue. Coiro *et al.* [63] test both a wind and tidal turbine, the presented results for the tidal turbine show that an efficiency of 25 % was achieved, representing 160 kW at a flow speed of 3.5 m/s. Birjandi *et al.* [64] test a scale turbine in a water tunnel at various water levels. Their results show that when the water level is reduced, the power coefficient of the turbine improves due to free-surface effects.

One of the most detailed VATT studies in the literature with regard to data collection is the study conducted by Bachant and Wosnik [65]. Bachant and Wosnik built and tested a straight, 3-bladed VATT at the University of New Hampshire (UNH), henceforth referred to as the UNH Reference Vertical Axis Turbine (UNH-RVAT). A simple schematic of the device is shown in Figure 2.7 (a). In line with the aims of the US Department of Energy's reference model programme, the model was designed as a generic test case, which would produce an extensive set of measured data against which various numerical modelling approaches could be calibrated and validated.

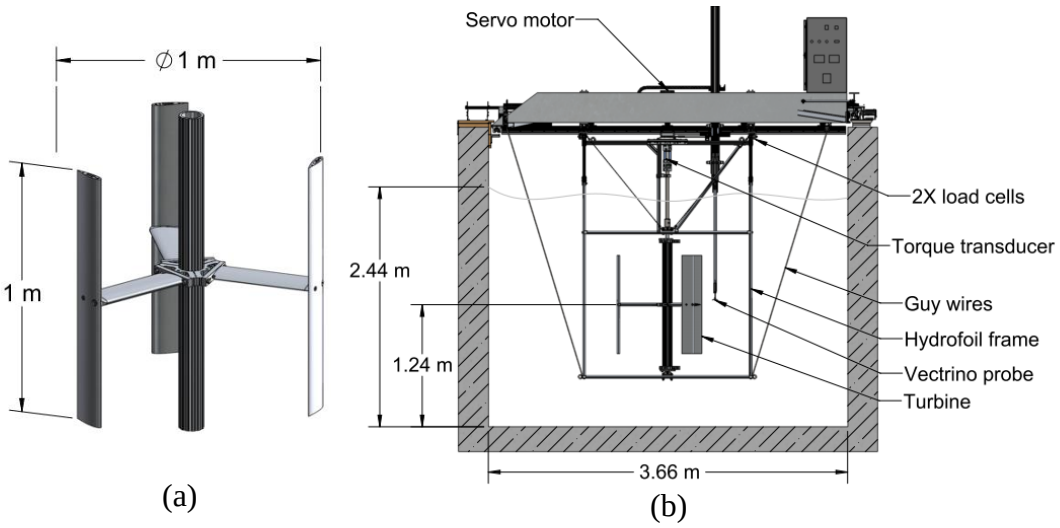

Figure 2.7: (a) Turbine schematic with outlining dimensions. (b) Schematic of experimental setup [65].

During the UNH-RVAT testing programme, approximately 1,500 tows in total were carried out for different Reynolds numbers, with 31 tows required to produce each Reynolds number dependent power curve. Plots of mean power and drag coefficients at λ = 1.9 (corresponding to peak C_P) versus Reynolds number, produced by Bachant and Wosnik [65] are shown in Figure 2.8. While, Figure 2.9 presents the C_P versus λ curves for the various Reynolds numbers investigated. From Figure 2.8, Bachant and Wosnik concluded that the performance of the turbine becomes essentially Re-independent at an approximate Reynolds number based on the turbine diameter of $Re_D \cong 1 \times 10^6$ or based on the blade chord of $Re_c \cong 2 \times 10^5$. This threshold is consistent with the behaviour of the blade boundary layer transitioning from laminar to turbulent conditions, thereby promoting either the suppression or reattachment of the laminar separation bubble [66].

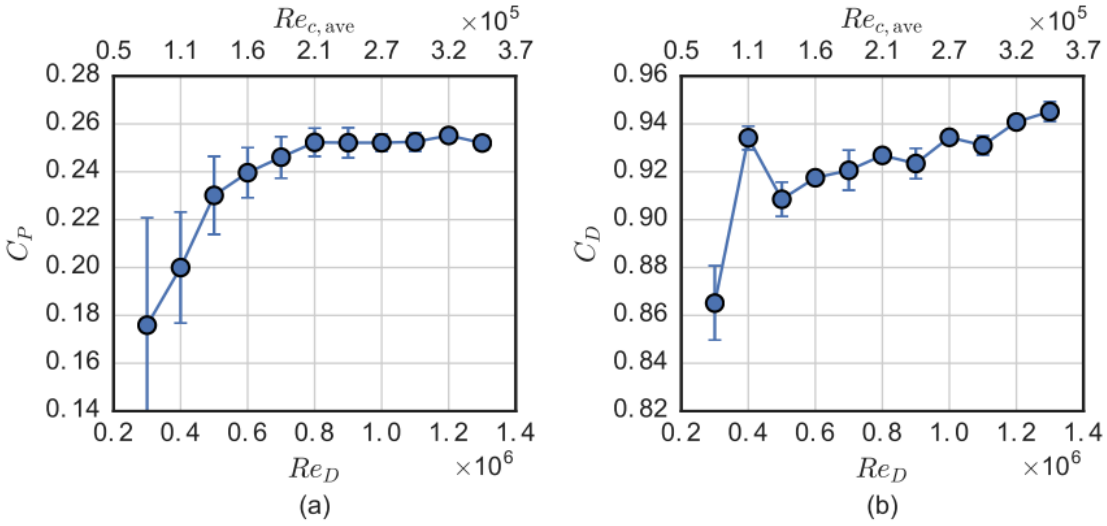

Figure 2.8: UNH-RVAT measured: (a) mean power and (b) drag coefficients at λ = 1.9 plotted versus the Reynolds number [65].

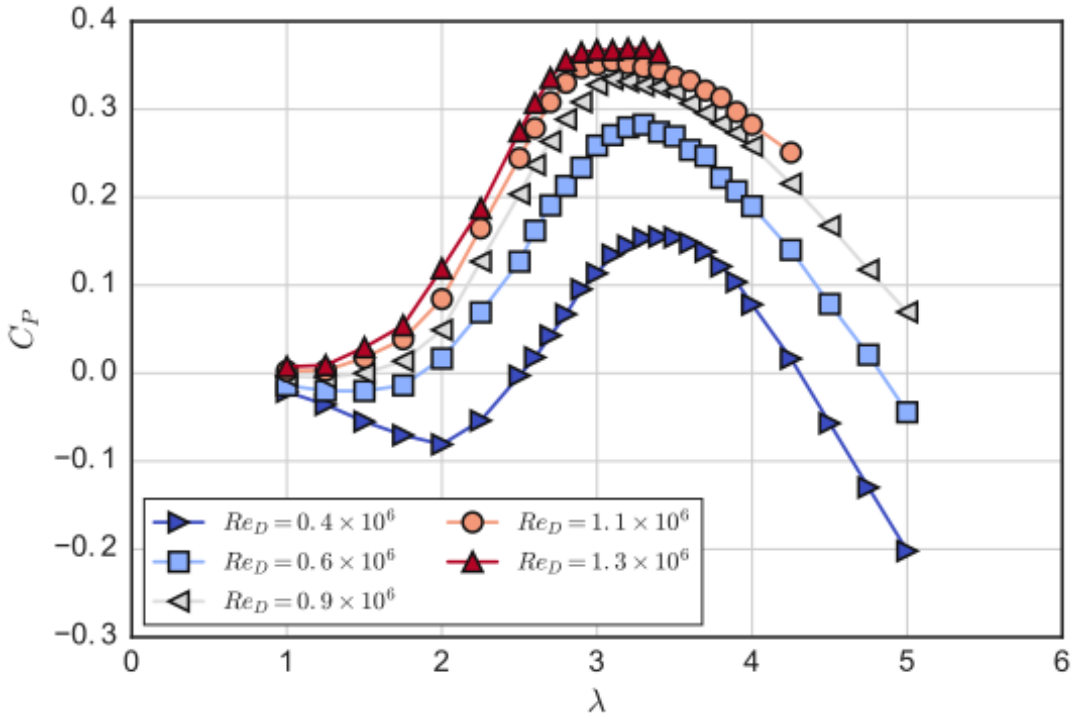

Figure 2.9: Power performance curves for various Reynolds numbers in the study by Bachant and Wosnik [65].

Bachant *et al.* [67] also tow tested a 1:6 scale vertical axis turbine of the US Department of Energy's reference model VAT – the DoE Reference Model 2. The DoE Reference Model programme established reference models of the primary types of tidal and wave energy convertors that could be used to benchmark technology performance and modelling. The rotor was 1.075 m in diameter and the blades were 0.807 m long. The blade chord tapered from 0.067 m at the roots, or half-span, to 0.040 m at the tips, giving a range of chord-to-radius ratios c/R of 0.12 to 0.07. The power performance and drag coefficient were determined for the device under a range of conditions. A maximum power coefficient ($C_{\mathrm{P}max}$) of 0.37 at λ = 3.1 was recorded with a corresponding C_{D} of 0.84. The effects of the support struts were also analysed. A drastic reduction in $C_{\mathrm{P}max}$ was noted when cylinders were used as struts as opposed to NACA 0021 profiles. In fact, the cylindrical struts prevented the turbine from producing any mechanical power at any tip speed ratio. Similar to the UNH-RVAT study, Bachant and Wosnik concluded Reynolds number independence occurred at $Re_D \cong 1 \times 10^6$. However, as shown in Figure 2.10, this was not as evidently clear as in the case of the UNH-RVAT results of Figure 2.8.

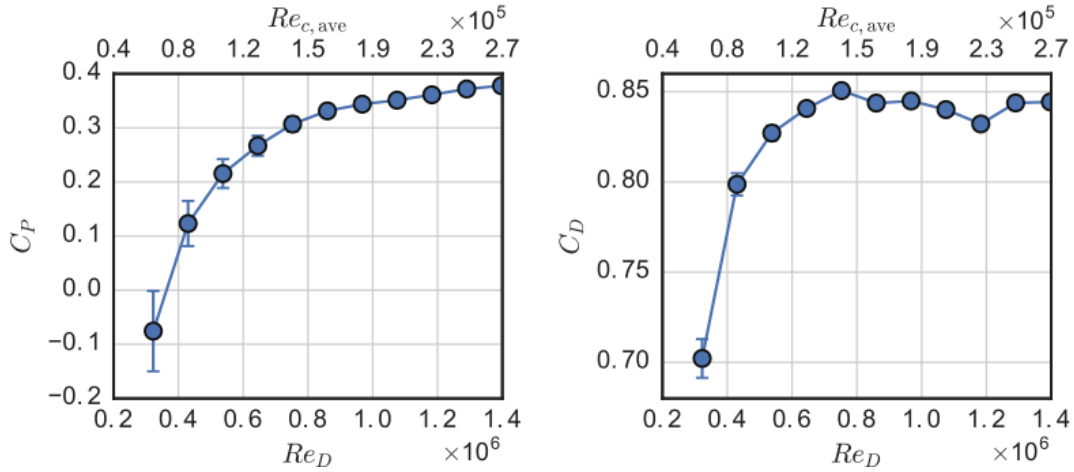

Figure 2.10: Reynolds Number effects on performance. Power and drag coefficient at λ = 3.1 plotted versus turbine diameter and approximate average blade root chord Reynolds number [67].

Although they involve greater manufacturing complexity than straight-bladed VATs, helical turbines have the technical advantage of smoothing out torque variation or "ripple" on the turbine shaft. Furthermore, the overall stream-wise and cross-stream forces on the turbine are less unsteady which results in decreasing vibration and fatigue loading of mounting structures [68]. Due to this, in recent times, helical turbines are being increasingly researched. Bachant and Wosnik [68] carried out power and drag measurements in the UNH towing tank for two further VATTs (shown in Table 2.3): (1) a cylindrical Gorlov Helical Turbine (GHT) and (2) a Lucid Spherical Turbine (LST). The cylindrical GHT outperformed the spherical LST in terms of mechanical power coefficient, this higher performance was accompanied by a higher drag coefficient. The GHT reached a $C_{\mathrm{P}max} = 0.35$ at $\lambda = 2.3$, whereas, the LST reached a $C_{\mathrm{P}max} = 0.24$ at $\lambda = 2.2$. Bachant and Wosnik say that these results were not surprising given that the LST is designed for higher blockage flow conditions.

Table 2.3: Rotor characteristics of the cylindrical GHT and spherical LST

	GHT	**LST**
Diameter (m)	1.00	1.14
Blade Length (m)	1.32	0.97
Frontal area (m^2)	1.32	0.96
Blockage Ratio	0.15	0.11
Number of Blades	3	4
Solidity	0.14	0.22
Blade Profile	NACA 0020	NACA 0020
Blade Overlap	0.5	2.0

Table 2.4: Example studies conducted on the experimental testing of VATs.

Ref	Wind/ Tidal	Test Facility	Turbine Type	Operation Principle	NACA Profile	N_B	$c\ (m)$	$D\ (m)$	$l\ (m)$	TSR/λ	Velocity (m/s)	Results
[54]	Tidal	Flume	VAT	Lift	63-018	1 to 6	0.034 to 0.17	0.3	0.2	0.5 to 2	0.6 to 1.4	C_p vs λ, V_u, V_d
[55]	Wind	Tunnel	VAT VP	Lift	0018	2, 3, 4, 6	0.15	2.1	0.8	N/A	N/A	P_{Mech} vs RPM
[55]	Tidal	Field	VAT VP	Lift	0018	3	0.4	6	5	1.5 to 2.6	N/A	C_p vs λ
[56]	Tidal	Flume	VAT	Lift	0021	2	N/A	0.3	0.3	0.5 to 4	0.5 to 0.7	C_p vs λ
[61]	Wind	Tunnel	VAT	Lift	0015	3	0.4	2.5	3	0.25 to 2	5 to 11	C_p vs λ
[62]	Wind	Tunnel	VAT	Lift	0022	2,3	0.1	0.6	0.4	1.8 to 2.8	5.07	C_p vs λ
[63]	Wind	Tunnel	VAT VP	Lift	0018, 0021	3	0.2	0.8	0.8	0.25 to 1.′	4 to 10	C_p vs λ
[64]	Wind	Tunnel	VAT	Drag	Cup	8	0.25	1.59	2	0 to 0.6	0 to 20	P_{Mech} vs λ, Pressure
[65]	Wind	Tunnel	VAT	Drag	Cup	8,16	N/A	0.3	0.075	N/A	5.5 to 12.5	T vs RPM
[66]	Wind	Tunnel	VAT	Lift	0018	2	0.06	1	1	4.5	9.3	$3D\ V_u, 3D\ V_d$

*Note. Where there is an N/A entry in the table, the specified detail is not presented in the research.

2.4.2.2 Blade Pitch Studies

The GKinetic turbine incorporates controlled variable pitching of the blades. One of the main issues with lift-based VATs is that they have a limited self-starting capacity. A number of authors have studied the effect of blade pitch on VAT performance [68–77]. Small lift forces at low rotational speeds, means there is often insufficient torque to overcome frictional forces at start-up. Additionally, blades of a lift-based rotor are stalled for most azimuthal angles at low λ values. Variable pitching blades can help to alleviate this start-up torque issue by altering the pitch of blades at different azimuthal angles to ensure lift producing α values. In addition, variable pitch controlling of the blades can also be utilised to keep α values of the aero/hydrofoil within the optimum range and therefore maximise power production. The major difficulty with implementing a pitch control regime is that such mechanisms can add considerably more complexity to turbine designs. Many turbine developers feel that this added complexity compromises reliability and, therefore, negates any potential benefit in terms of improved power performance. An example of a pitch control mechanism implemented in a VAWT [75] is presented in Figure 2.11.

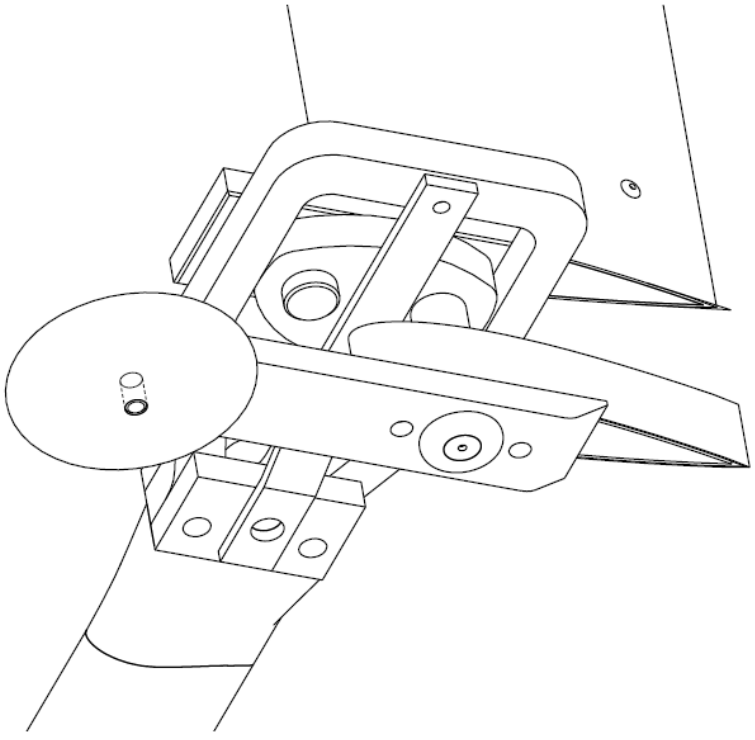

Figure 2.11: Example of a passive variable pitch control mechanism [75].

Jing *et al*. [76] investigated the effects of passive variable blade pitching on power performance when testing a number of vertical axis turbines of varying rotor solidities. The effects of chord-length and the number of blades on power performance were also investigated. The study states that when the passive pitch angle was restricted to between $\pm$ 3° of the tangent track circle of the turbine, the value of $C_{\mathrm{P}max}$ was 8 % higher than that of the blade in unrestricted free motion (note: while the blade was considered to be in free motion, the pitch angle range was in fact limited to $\pm$ 30°). Although the accompanying graph that they present implies that the opposite is true (see Figure 2.12), they repeat the claim in their conclusions and so it is assumed that the legend names in the published graph are mislabelled and the tighter pitch control scheme did indeed give the better results.

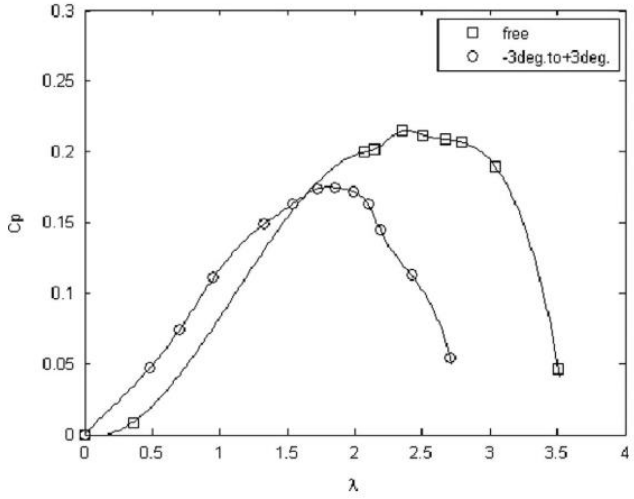

Figure 2.12: Comparison of results for two pitching schemes [76].

Somoano and Huera-Huarte [77] studied the performance of a VAWT with a chord-to-diameter ratio of 0.16 in a wind tunnel for different blade pitches. They studied the performance of the turbine for a range of fixed pitches of the foils from 8° toe-in to 16° toe-out. Results showed that the power performance was highly dependent on pitch angle at all Reynolds numbers investigated (3×10^5 to 5×10^5) and that the highest performance levels were achieved when blade pitch was configured with an angle of 8° toe-out. The best performance of $C_{\mathrm{P}max} > 0.25$ was reached at a λ slightly above 2.

Zhang *et al*. [78] also investigated the hydrodynamic performance of a passive variable pitch VATT. In their study, they investigated the limiting pitch values for three different setups. The turbine had three blades consisting of NACA 0018 hydrofoils with a chord-length of 0.08 m and a turbine diameter of 0.833 m. The study was conducted in a recirculating flume. Figure 2.13 presents the results from their experimental investigation where a negative pitch represents an inward pitch. As is clear in Figure 2.13, results showed that a passive pitch control regime that limits pitching in the range of $-10°$ to $0°$, achieved the highest mechanical performance for the turbine. Similar to other studies on blade pitch, the self-starting capabilities of the turbine were shown to superior to a 0^{o} fixed pitched device.

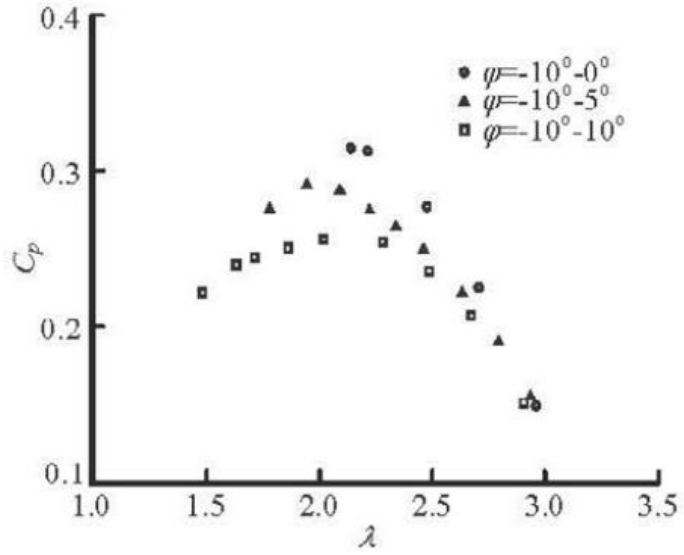

Figure 2.13: Mechanical power performance curve for a passive pitch VATT implementing three different pitch range limits.

Aggarwal *et al.* [79] present a study of a VAWT consisting of three NACA 0018 straight blades with active pitch control implemented using linkages and servomotors. They reported that a positive initial pitch angle broadens the C_{P} versus λ curve, while a negative pitch angle shortens it. The results showed that a positive 3° pitch increased $C_{\mathrm{P}max}$ by 12.5 % (0.35 to 0.4) compared to a non-pitched turbine.

2.4.2.3 Flow Acceleration / Deflection Studies

The GKinetic turbine incorporates a central bluff body with the purpose of accelerating inlet flows to the turbines positioned either side of the bluff body. Introducing obstacles to a flow causes localised accelerations of the flow around the obstacle. This topic has been widely studied in the literature. Graf and Yulistiyanto [80], for example, studied flow around cylinders in a tilting flume and noted localised accelerations of depth-averaged flow speeds of up to 100 %, at the widest point of the cylinder.

The potential applications of flow acceleration around an obstacle in relation to tidal turbines have been studied by Roddier *et al.* [81]. They showed the potential for accelerating current velocities for the purpose of energy extraction by using a large structure (i.e. a bluff body) to cause an acceleration of local current velocities onto an underwater disc (representing a turbine). A flume study was performed to measure the force on the disc, with and without the accelerating structure. It was determined that the force was 50 % higher with the accelerator in place.

Gerrard [82] also studied flow around cylinders but with a focus on the downstream wake. They demonstrated that the inclusion of a splitter plate on the downstream end of the cylinder led to a weakening in downstream vortex strength and frequency. This is significant in regards to the GKinetic device for device stability and also to the downstream proximity of devices deployed in arrays.

Some studies have shown that the introduction of flow deflector plates upstream of VATs can improve power performance. An experimental study was carried out by Golecha *et al.* [83] to find the optimal upstream position of a straight plate deflector for a Savonius tidal turbine. Figure 2.14 shows the eight different positions which were investigated. The deflector plate acts as an obstacle to reduce the negative or reverse torque exerted on the returning blade. From the experiment, it was presented that all configurations (except configuration 5 in Figure 2.14) demonstrated an improvement in $C_{\mathrm{P}max}$. The highest $C_{\mathrm{P}max}$ was 0.14 at λ of 0.7 which corresponds to a 50 % increase compared to that achieved without a deflector.

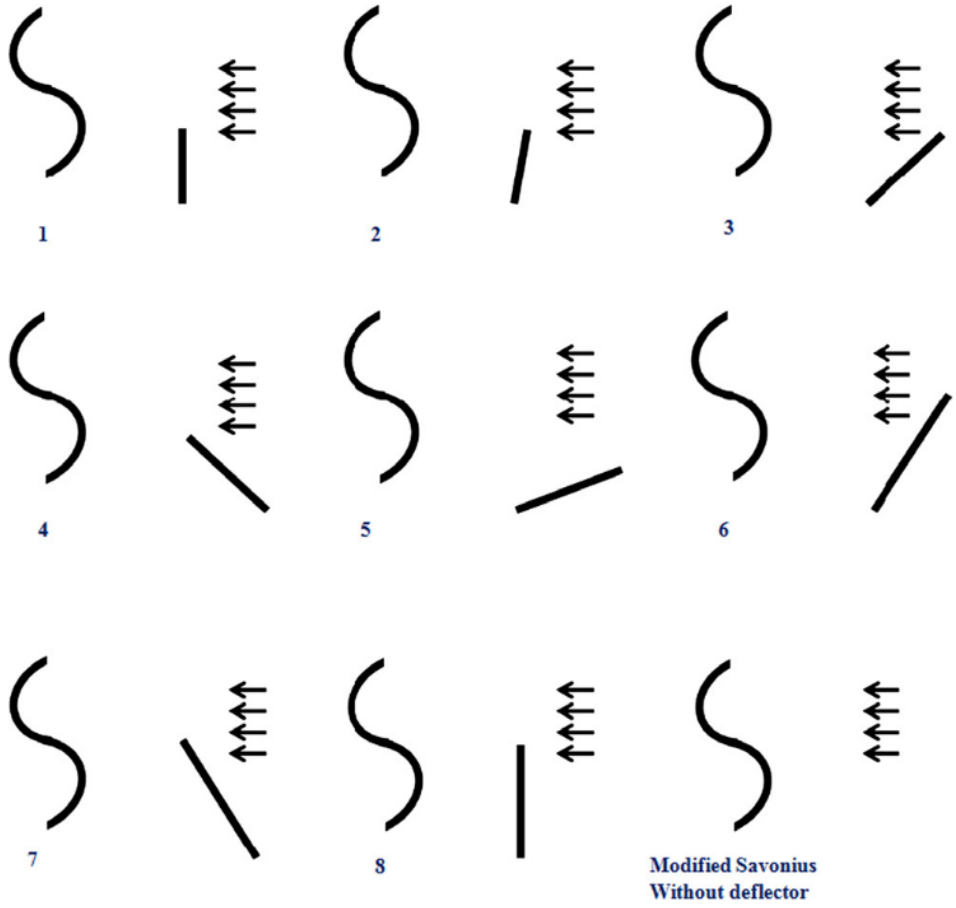

Figure 2.14: Eight different deflector positions investigated for a Savonius tidal turbine by Golecha *et al.* [83].

Shaughnessy and Probert [84] introduced the V-shaped deflector (shown in Figure 2.15) mounted at the upstream of a Savonius wind turbine. Experiments were carried out to obtain the optimum angle of the V-shaped deflector and the distance from the turbine. The study showed that with the V-shaped deflector the turbine was able to self-start and that the maximum C_P was obtained with a deflector angle (θ in Figure 2.15) of 37°. This C_P value was approximately 20 % greater than that achieved without the V-shaped deflector. However, they noted that optimum positioning of the V-shaped deflector is important to ensure maximum power extraction.

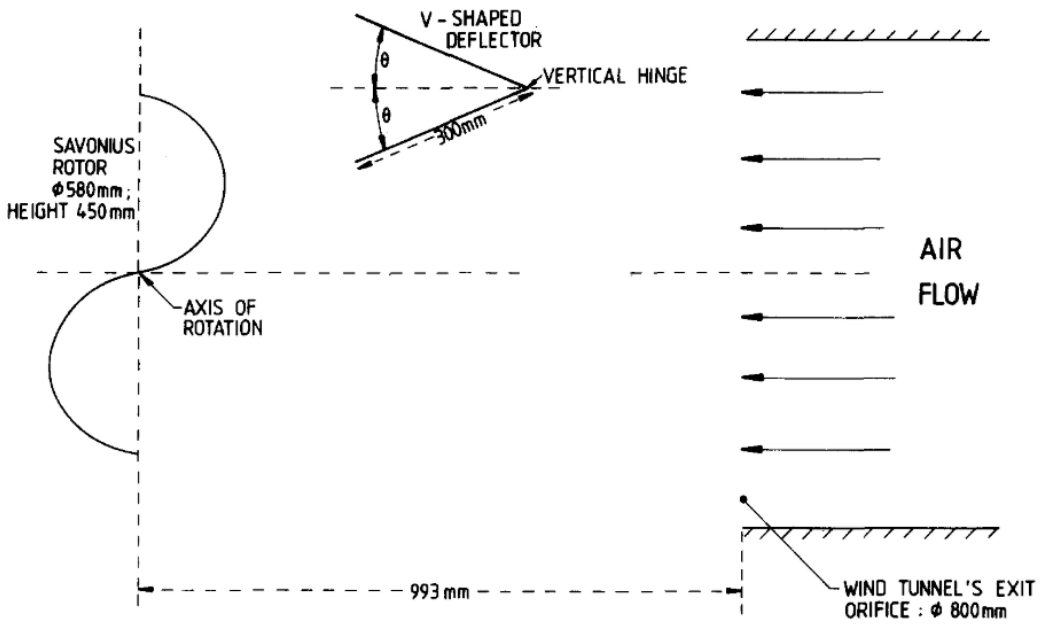

Figure 2.15: Schematic of the V-shaped deflector and turbine used by Shaughnessy and Probert [84].

Research by Kim and Gharib [85] applied the straight plate deflector (shown in Figure 2.16) for a lift-type counter-rotating VAWT to improve the efficiency. A single flat plate deflector was placed upstream of a counter-rotating straight-bladed VAWT. They found that the inclusion of the deflector increased the local wind velocity around the turbine thereby significantly increasing the performance of the VAWT. However, when the deflector was placed too close to the VAWT, the deflector had a negative effect on performance.

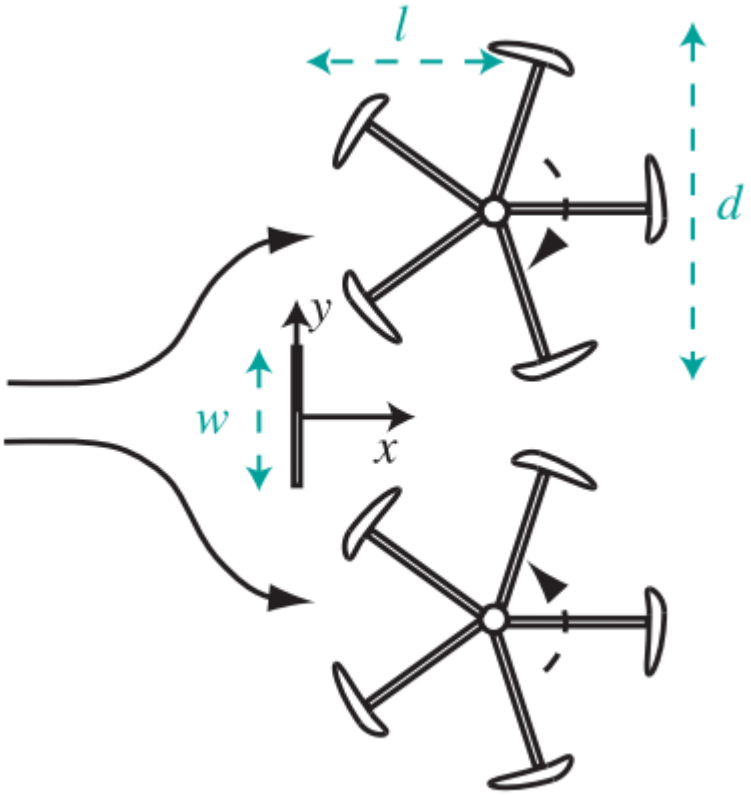

Figure 2.16: Schematic of deflector plate relative to dual turbines in the study by Kim and Gharib [85].

Some turbine technology developers claim that flow acceleration using ducts can be used to overcome the Betz limit. However, this is impossible since Betz theory is based purely on considerations of taking momentum out of a flowing fluid and therefore the limit applies to all devices regardless of how they work. The confusion arises if one calculates the available power using the smaller entrance area of the turbine as the reference area, rather than the larger entrance area to the duct. The larger area should always be used and in such cases, Betz limit cannot be exceeded; using the former can result in Betz limit being exceeded. McAdam *et al.* [86] and Ohya and Karasudani [87] both show the inclusion of a nozzle or duct improved turbine performance, in comparison to conventional turbine design, and in the process exceeded Betz limit, but both studies used the smaller turbine area as the reference area. Jin *et al.* [88] also showed that by placing a deflector plate upstream of dual vertical axis turbines, turbine efficiency could be increased from 33 % to 42 %. Again though, the reference area

was reported as the turbine swept area and did not account for the additional area of the deflector; likewise, with Kim and Gharib [85]. Fraenkel [60] expressed the following concerns about the use of ducts to enhance performance: *"There is a fallacy in these assumptions because speeding up the flow through a venturi has no effect on the energy content; energy is neither added nor removed, so the power flow through any cross-section remains nominally constant (other than friction losses in the duct may cause a small loss of power as the flow moves along the duct)".*

2.4.2.4 Effect of Blockage on Experiments.

In an unconfined environment, i.e. for low blockage ratios, the flow is free to diverge around the blockage presented by the turbine. Placing a turbine in a confined environment such as a towing tank will force flow through the turbine at a higher velocity compared with the unconfined environment. Consequently, higher levels of blockage can lead to increased turbine performance, and a shift in optimal operating parameters, e.g. λ.

Harries *et al.* [89] investigated the performance of a prototype drag-driven VATT in two recirculating flumes. In a flume at Cardiff University, the turbine reached $C_{\mathrm{P}max}$ of 0.132 at the λ value of 0.441. Subsequent testing at IFREMER reduced the blockage factor from 0.17 at Cardiff University to 0.01. Testing in the almost unblocked environment at IFREMER, under similar flow conditions as the Cardiff tests, resulted in a 43 % lower $C_{\mathrm{P}max}$ of 0.067 at a lower λ value of 0.346. Harries *et al.* [89] conclude that the results highlight the importance of accounting for blockage effects during tank testing. Failure to account for the effects of blockage can lead to exaggerated performance results.

Many blockage correction approaches have been developed over the years such as those of Werle [90], Pope & Harper [91] and Bahaj *et al.* [92]. These approaches, however, are largely based on 1D actuator disc theory and were developed for horizontal axis turbines. To date, no accepted blockage correction approach has been developed for VATs. Cavagnaro and Polagye [93] investigated the effectiveness of 1D blockage correction methods for VATs and concluded that no one was universally effective as they do not account for the full physics present in the confined flow

problem. At transitional Reynolds numbers, the effect of blockage is likely to be convolved with the Reynolds number dependence of unsteady lift and drag. The work of Dossena *et al.* [94] agrees with the conclusions of the aforementioned research and recommend that new blockage corrective approaches need to be developed for VATs.

2.5 Numerical Modelling for Performance Prediction of VATs

Due to the limited availability of controlled testing environments and the financial cost associated with testing in general, the majority of early-stage turbine development relies on some kind of performance prediction modelling. The two most common types of numerical model used in the performance prediction of stream turbines are BEMT models and CFD models. BEMT models are attractive as they have much lower computational costs than the much more complex CFD models but they tend to have a lower order of accuracy. Both modelling approaches are discussed in more detail in the following sections.

An alternative modelling method to BEMT is the free-vortex model. It is based on the replacement of the aerofoil blade with a bound vortex filament, called a lifting line, that changes its strength as a function of azimuthal position [95]. The first of these free-vortex models applied to VATs by Strickland *et al*. [96]. Blade forces are calculated within the free-vortex model using the blade element method based on aerofoil data (e.g. Sheldahl and Klimas [34]) and the forces are applied with knowledge of blade local velocity vectors. Li and Calisal [97] used a vortex model to accurately reproduce the vertical axis wind turbine performance test data of Templin [98]. However, when the same model was used to simulate power performance data from tow tests of a VATT conducted by the University of British Columbia, it resulted in a 20 % (approximately) over-prediction of the peak power coefficient. While the computation times of free-vortex models are a fraction of CFD models, their accuracy is lower. One of the causes of inaccuracy is that they use a bound vortex to represent the blade and thus are incapable of modelling near blade effects [99]. Free vortex modelling was not considered for this research.

2.6 Blade Element Momentum Theory Modelling

Blade element momentum theory models are widely used for early-stage device development for both VATs and HATs. They model the power performance of a turbine and are therefore suited to the investigation of the effects of design changes on power performance. They are computationally cheap and can usually achieve a satisfactory level of accuracy for evaluation of design iterations. BEMT theory combines blade element theory and linear momentum (i.e. actuator disc) theory where the rate of change in the momentum of the fluid is equated to the stream-wise aero/hydrodynamic forces on the hydrofoils.

BEMT was first introduced for propellers by Glauert [100] who adopted the lift and drag coefficients of two-dimensional aerofoils obtained from wind tunnel tests. Templin [98] then adapted this approach for VAWTS through the development of a single stream-tube model (Figure 2.17 (a)). Templin's approach was extended by Strickland [101] by dividing the single stream-tube into aerodynamically or hydrodynamically independent multiple stream-tubes to create the single multiple-stream-tube model (Figure 2.17 (b)); the use of multiple stream-tubes allows a variation in the interference factor across the turbine.

The disadvantage of single multiple stream-tube models is that they cannot account for the induction of velocity between the upstream and downstream of a VAT. The model, therefore, assumes a symmetrical relationship between the loads upstream and downstream. A solution to this problem was achieved by placing two actuator discs in tandem in order to analyse the upstream and downstream halves of the rotor separately [102,103] (Figure 2.17 (d)); this allowed the variation of induced velocity between the upstream and downstream to be modelled. Paraschivoiu [104] and Read and Sharpe [103] have developed similar models referred to as double multiple stream-tube (DMST) models. Read and Sharpe [103] added extra complexity to their DMST to enable it to account for the stream-tube expansion that occurs due to the conservation of mass between the upstream and downstream actuator discs.

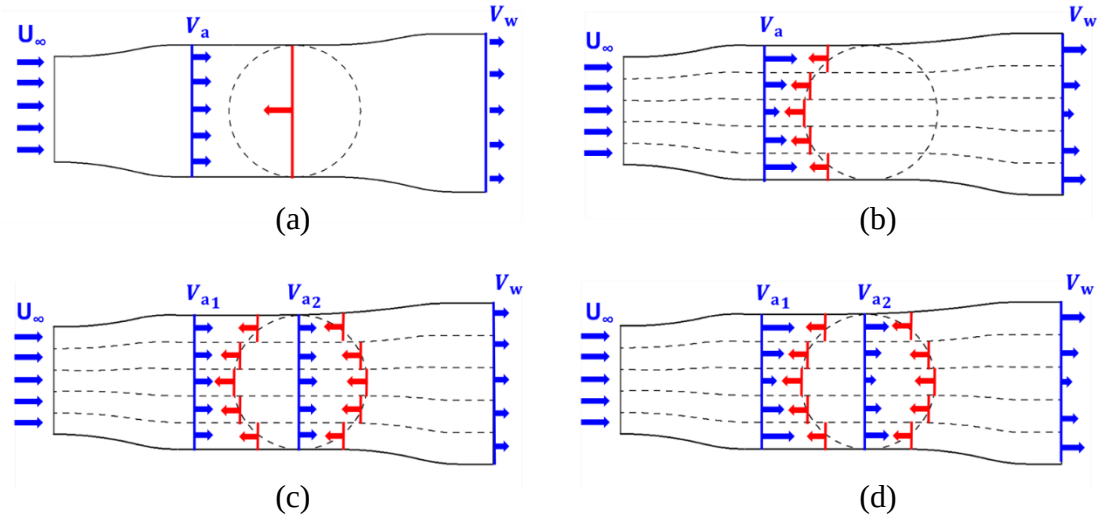

Figure 2.17: Stream-tube model variations: (a) Single steam-tube model, (b) Single multiple stream-tube model, (c) Double multiple stream-tube (DMST) model with constant induction factor, and (d) Double multiple stream-tube (DMST) model with varying induction factor.

A key step in BEMT model codes is the calculation of the local axial induction factor (a) for each stream-tube. The local axial induction factor is the fractional decrease in flow speed caused by the presence of a turbine rotor. Nearly all BEMT models developed to date have relied on Strickland's iterative approach to determine the local axial induction factor for a stream-tube. The approach is discussed in Chapter 5. By way of summary, the iterative approach involves an initial guess for the axial induction factor, which is subsequently used to calculate the blade element forces. The a value is then recalculated. This procedure continues until a specified convergence criteria is reached and the a value is deemed to be converged. For highly loaded discs, this iterative approach can lead to problems such as erratic solutions and convergence failures [101,105–107]. The use of a relaxation factor can improve the model but does not irradicate these issues. This led McIntosh *et al.* [44] to develop an alternative graphical approach for determination of the local induction factor.

In the graphical approach, the force coefficients for the momentum and blade element models are graphed as the value of a is varied and the point of intersection of the two graphed lines, i.e. the crossing point, is then regarded as the appropriate induction factor for that stream-tube. This is then repeated for all stream-tubes. Soraghan *et al.*

[25] successfully adopted this method in relation to VAWTs. McIntosh *et al.* also provided a method for dealing with cases where there are multiple crossing points. They report that multiple crossing points are caused by stall, which results in a sharp drop in the applied stream-wise force coefficient resulting in multiple intersections between the blade-element and momentum models. They also hypothesise that the multiple crossing points are the cause of the convergence issues associated with the iterative approach.

In attempting to improve the accuracy of BEMT models, many researchers have contributed methods for dealing with previous shortcomings in BEMT models. As mentioned, Read and Sharpe [103] pioneered the flow expansion approach for VAWTs. They observed that due to conservation of mass if velocity downstream is reduced due to induction then the cross-sectional area of the stream-tube must expand. This is most significant in the cases of highly loaded rotors. The Read and Sharpe approach is documented in detail in *Wind Energy Conversion Systems* [108]. Paraschivoiu *et al.* [109] consider an alternative approach for flow expansion based on sudden expansion, where the azimuthal angle is used in the calculation as opposed to the definition of a new angle by Read and Sharpe.

As previously explained, dynamic stall is an erratic nonlinear anomaly, primarily caused by the rapid change in the angle of attack on a foil, and can result in a significant loss in lift due to flow separation. The stall angle of a rotating foil is different to that of a static foil [37] and as BEMT models typically utilise static foil data, corrective approaches have been developed to account for their use. Paraschivoiu [110] provides a detailed overview of the stall models which have been adapted for VATs. The Gormont model [39], with modifications by Massé [111] and Berg [112], is widely implemented in BEMT codes for VATs as it can be easily incorporated. Alternatively, there is the Leishman–Beddoes model, developed by Beddoes [113] and modified by Leishman *et al.* [40], which models the attached and separated flow conditions. However, both approaches have been shown to exhibit discrepancies in comparison to experimental data for normal and tangential coefficients [43]. It should be noted though that these discrepancies may be by other processes not being modelled correctly within the BEMT model.

Foil lift and drag characteristic data that are used in BEMT models, e.g. the Sheldahl and Klimas dataset [34], are only available for blades of infinite length. Some researchers have looked at the development of corrective approaches for the use of infinite length blade data for finite length blades. When the angle of attack is less than the static stall angle, Lanchester-Prandtl theory [114] is used to make this correction. When the angle of attack exceeds the stall angle the corrective approach developed by Viterna and Corrigan [115] and modified by Raciti Castelli *et al.* [116] is used.

A key output of DMST models is the distribution of forces on the blade elements at various azimuthal positions. These results can be used to form the basis of structural analysis to investigate candidate blade materials and design. BEMT models are discussed in more detail in Chapter 5.

2.6.1 BEMT Model Accuracy.

Although the majority of published BEMT models are used to inform initial design decisions and therefore generally omit comparisons to experimental performance data, there are numerous studies which do evaluate the accuracy of the models. The following are some examples.

Strickland's BEMT [101] model of the 17 m SANDIA turbine was shown to relatively accurately predict the peak performance and overall shape of the power curve. The model, however, over-predicted the turbine's performance over the full range of the power curve with peak performance being over-estimated by approximately 5 to 10 %. Raciti Castelli *et al.* [116] also assessed the accuracy of their BEMT model against the experimental data from SANDIA's 17 m Darrieus turbine. Their model included dynamic stall, finite aspect ratio correction and a sudden flow expansion correction for the downstream portion of the azimuthal cycle. The model accurately predicted peak performance but significantly over-predicted performance levels above the optimum λ.

Soraghan [117] assessed their BEMT model accuracy for the VAWT 450, a wind turbine of 450 m^2 frontal area. The model over-predicted peak performance by between 12 to 15 % and there was a phase shift in the power curve with optimum peak performance predicted to occur at an approximate λ value of 4 instead of the experimental optimum λ of 3.

2.7 Computational Fluid Dynamics Models

2.7.1 Introduction

The governing equations of flow in CFD models are the Navier-Stokes equations and a number of approaches are used to solve them including Direct Numerical Simulation (DNS), Large Eddy Simulation (LES), Detached Eddy Simulation (DES), and the RANS approach. Currently, it is not possible to use DNS for VAT modelling, and while LES [118] and DES [119] studies are beginning to become more popular, they are still only feasible for research purposes as computation times are still prohibitive. These modelling techniques are discussed in more detail in Chapter 3. The most commonly used approach is the RANS approach, which although incapable of representing all turbulent flows, has proven to be accurate at determining the average forces on a physical body [120]. ANSYS® FLUENT® is an example of a commercial CFD software that has been extensively used in turbine modelling studies [121,122].

CFD modelling of turbines can be done in steady-state or transient modes depending on the objectives of the research and the computational resources available. If computational resources are scarce, relatively simple steady flow models can be used to model the turbine blades in different azimuthal positions and the results aggregated, e.g. Gupta and Biswas [123]. A more common approach is transient modelling of the moving blades through the use of the unsteady Reynolds Averaged Navier-Stokes (URANS) approach [124–129]. Although more complex, URANS is more accurate, particularly where blade interaction occurs. Transient modelling techniques require the simulation to explicitly represent the turbine blade movement through the fluid. This can be accomplished using sliding mesh techniques [130–132] where one part of the mesh moves while the remainder is static.

An important point of consideration when using the RANS approach is the choice of turbulence model. From the literature, the RANS turbulence models used in VAT model studies include the Spalart-Allmaras [133], $k-\varepsilon$ [134], $k-\omega$ [135], $k-\omega$ shear stress transport (SST) [136] and Transitional SST models [137]. The SST models have been shown to be the most accurate and are recommended by the Fluent manual [138]. These are discussed in more detail in Chapter 3.

2.7.2 2D CFD Modelling of VATs

For some time now, 2D CFD models have been used in the design and analysis of VATs. There is an abundance of literature available on the topic and it seems that all possible variations of model parameters and turbulence models have been utilised. Table 2.5 presents a summary of some of the studies reviewed. The one aspect that is consistent between studies is the use of the sliding mesh technique.

The choice of domain width used in sliding mesh turbine models varies between studies. In some cases, it is restricted to the extents of the experimental domain [139] while other studies define domain sizes relative to blade chord-length [127]. Model accuracy has also been shown to be quite sensitive to the ratio of the rotating domain to turbine diameter. Raciti Castelli *et al.* [140,141] conclude that a ratio of rotating domain diameter of approximately two is required for accurate solutions. The following subsections cover some of the main issues affecting the accuracy of 2D VAT models.

The primary results of interest in 2D CFD model studies have been the turbine power coefficient and the power curve, i.e. the variation of power coefficient, C_P, with λ. Balduzzi *et al*. [142] carried out a conclusive 2D analysis on full spatial and temporal discretisation studies which is discussed in the following relevant subsections.

Table 2.5: Summary of 2D CFD VAT Studies

Ref.	Turbine Type	Turbulence model	y^+	No. of Rotations	Time-step	ΔQ Convergence
[141]	VAWT	$k-\varepsilon$	>30	N/A	1º	1 %
[142]	VAWT	$k-\omega$ SST	< 1	20	0.15º	0.1 %
[143]	VATT	$k-\omega$ SST	~1	11	1º	1 %
[130]	VATT	$k-\omega$ SST	~1	14	1.5º	1 %
[144]	VAWT	LES and DES	~1	6	0.25º	1 %
[125]	VAWT	Transition SST	~1	N/A	0.35º	1 %
[126]	VAWT	Transition SST	~1	N/A	0.36º	0.1 %
[145]	VAWT	Transition SST	< 1	N/A	0.07º	2 %

*Note. In the above table, an N/A entry denotes that the specified detail is not specified in the research.

2.7.2.1 Over-prediction due to Blockage.

The blockage ratio in 2D models has been shown to affect model accuracy, particularly in cases where blockage ratio is high. As 2D models do not account for depth (in VAT modelling), they will inherently have a higher blockage ratio than in reality as the turbine will usually not extend the full depth of the tank/testing area. This higher blockage forces more of the flow through the turbine rotor, resulting in higher velocities and by extension performance. Bachant and Wosnik's 2D model [139], for example, over-predicted peak mechanical performance of their VATT by approximately 96 %. Bachant and Wosnik attributed this over-prediction to the elevated blockage of the 2D CFD model relative to the actual blockage of the experimental setup. By comparison, in a study where the blockage was not significant Balduzzi *et al.* [142] achieved agreement within 5 % of peak performance for their 2D model of a scaled vertical axis wind turbine.

2.7.2.2 Spatial and Temporal Resolution

The spatial resolution of the computational mesh near walls is particularly important to correctly capture flow properties in the boundary layer region. The dimensionless wall distance for a wall-bounded flow, y^+, is used to determine the appropriate mesh resolution near solid boundaries.

y^+ values vary between studies and depend on the selected turbulence model. Mohamed *et al.* [146] and Mohamed [147] implemented the $k-\varepsilon$ model on a VAT with a mesh designed to result in a y^+value in excess of 30. Lain and Osorio [130] and Maître *et al*. [143] used the $k-\omega$ SST model in their VAT model and chose to directly resolve the boundary layer using a y^+ of approximately 1. Rolland *et al.* [148] and Velasco *et al.* [149] used a similar y^+ value with the Transitional SST model in their VAT model studies. The targeted y^+ value is dependent on the turbulence model being used. High Reynolds number models which work with wall functions and require y^+ of more than 30 and while wall resolving low Reynolds models require a y^+ of around 1 to directly resolve the viscous sublayer. Logarithmic-based wall functions are not recommended where flow separation is likely, such as for VATs [138]. Instead, either a $k-\omega$ based model or a Spalart-Allmaras based model should be used and the viscous sublayer directly resolved using $y^+ < 1$. y^+ needs to be evaluated at the peak

performance (optimum) λ value, and also at lower λ values where there is a likelihood of flow separation occurring. The optimum mesh resolution is one which gives acceptable accuracy at the lowest computational cost. It is important to ensure that the CFD solution is mesh independent before conducting scenario modelling. The Richardson extrapolation is a method based on error estimating that is commonly used in the literature for determining CFD model spatial convergence [150].

Selection of the computational time-step is a perennial modelling problem. Too large a time-step can lead to solutions that are not entirely time independent, while too small a time-step may yield accurate results but at an excessive computational cost. For turbine modelling, it is common practice to normalise time-step values to correspond with the azimuthal rotation per time-step. Rossetti and Pavesi [151] found that a time-step representative of 2° azimuth per time-step is required by assessing torque, while other researchers such as Maître *et al*. [143] and Trivellatoa and Raciti Castelli [141] suggest smaller time-step values of 1° and less than $0.5°$, respectively, are required. Ferreira *et al*. [152] showed that a time-step reflective of $< 0.5°$ azimuth is required to provide a time-step independent solution. However, Balduzzi *et al*. [142] showed that smaller time-steps are required for lower λ values, where large separation regions occur.

2.7.2.3 Solution Convergence

Solution convergence is deemed to be achieved when particular convergence criteria have been achieved within the simulation. The Fluent manual [138] recommends that residual convergence is achieved when residuals of the order of $1\ x10^{-5}$ are observed. Additionally, model parameters of interest are also used to assess solution convergence. In relation to turbine modelling, this is usually the turbine torque. In the literature, the number of turbine rotations required for a converged solution is, generally, determined based on the variation in the average torque loading of the rotor between subsequent rotations [140,142,143,147,153]. The number of rotations for convergence has been found to vary, likely due to the turbine design, but is generally found to lie between 8 to 15 rotations [143,153]. The general consensus [143,147] is that a solution is converged if the difference between the torque values of successive rotations is less than 1 %. Balduzzi *et al*. [142] showed that this criterion is not stringent enough and should be lowered to $\overline{\Delta Q} < 0.1$ % between one rotational torque

average and the next.

2nd order spatial discretisation schemes are most commonly used in the studies reviewed and have been shown to provide accurate model results. There is no general agreement on the best Fluent solver for VAT modelling. All four available solvers have been implemented: SIMPLE (Semi-Implicit Method for Pressure-Linked Equations) [147], SIMPLEC (Semi-Implicit Method for Pressure-Linked Equations-Consistent) [154], PISO (Pressure-Implicit with Splitting of Operators) [155] and COUPLED (pressure-velocity coupling method) [142].

2.7.3 3D CFD Modelling of VATs

Until very recently, limitations in computational resources meant that 2D CFD models of VATs were much more common than 3D models. With the recent advances in high-performance computing, 3D models are now also being developed on an ongoing basis. Table 2.6 and Table 2.7 present a list of 3D VAT CFD model studies. However, even when running on supercomputers, the computational cost of 3D models can still be prohibitive.

3D models of VATs tend to be quite similar in nature to 2D models, i.e. they tend to use the same discretisation schemes and turbulence models. For example, Orlandi *et al.* [156] carried out a study of a VAT in misaligned flow using 3D URANS with a $k-\omega$ SST turbulence model. Zamani *et al.* [157] implemented 3D URANS in OpenFOAM (an open source CFD code) to evaluate the enhanced mechanical performance of "J-blades" as compared to conventional NACA 0015 blades. Marsh *et al* [158] used 3D URANS with the $k-\omega$ SST turbulence model to investigate the performance of a straight 3-bladed VAT with included strut supports. Similar to 2D model studies, the primary results of interest in 3D model studies have been the turbine power coefficient, C_P. Levels of accuracy vary widely between model studies, but for maximum power coefficient, differences of less than 5 % between measured and modelled values are rare. Zamani *et al.* [159], for example, achieved agreement of approximately 8 % at peak power in their 3D VAT model study.

Table 2.6: Details of model domains for previous 3D CFD studies conducted.

Ref.	Wind/ Tidal	NACA Profile	N_B	c (m)	D (m)	H (m)	λ	Domain Size (W x L x H)
[156]	Wind	0018	2	0.08	0.755	0.5	2.33, 4.6	5 D x 15 D x 4 D (N/A)
[158]	Tidal	63021	3	0.06	0.914	0.686	1.5 to 3.5	10 D x 20 D x 2.5 D (3 D rotating)
[160]	Wind	0015, 0018	3	0.42	2.8	0.82	0.5 to 2	5 D x 17 D (0.75 D rotating)
[161]	Wind	0018	2	0.06	1	1	3 to 5	10 D x 16 D x 8 D (1.5 D rotating)
[162]	Wind	0021	3	0.3	1.98	1.15	0.4 to 1.8	6 D x 16 D x 6 D (1.5D rotating)
[163]	Wind	0015	2	0.61	17	17	2 to 8	60 D x 60 D x 11 D (3 D rotating)
[164]	Tidal	0021	3	0.14	1	1	N/A	N/A x 30 D x N/A (N/A)
[165]	Wind	0018	2	0.08	0.75	0.5	2.9 to 3.5	16 D x 24 D x 12 D (N/A)
[166]	Tidal	0020	3	0.44	3	7.2	1.8 to 3	7.5 D x 11.25 D x 7.5 D (2 D rotating)
[167]	Wind	0015	3	0.45	2.7	3	0.8 to 2.5	8.1 D x 14.8 D x 1.5 D (5.6 D rotating)
[168]	Wind	0012, 0015, 0030	2,3, 4	0.42	2.7	3	1 to 3	8.1 D x 14.8 D x 1.5 D (5.6 D rotating)

Table 2.7: Summary of model details for previous 3D CFD studies on VATs

Ref	Turbulence model	Number elements	y^+	No of Revs.	Time-step ($\circ/\Delta t$)	Results Recorded
[156]	$k-\omega$ SST	2.7×10^6	< 5	7	1	C_P vs λ vs exp. $C_{T,}$ C_N vs θ
[158]	$k-\omega$ SST	16.2×10^6	< 1	N/A	0.9	C_P vs λ
[160]	2.5 D LES	5.2×10^6	N/A	6	0.5	C_P vs λ vs exp. $C_{T,}$ C_N vs θ vs exp
[161]	$k-\omega$ SST, IDDES	3×10^6	2.5	32	0.5	C_P vs λ. V_{wake} vs exp
[162]	$k-\varepsilon$	9.5×10^6	< 10	15	3.6	C_m vs θ. C_P vs λ
[163]	Transition SST, $k-\omega$ SST	9.0×10^6	< 2.5	20	1	C_P vs λ vs exp
[164]	DDES	133×10^6	1	22	0.36	V_{wake}
[165]	$k-\omega$ SST, $k-\varepsilon$	2.9×10^6	N/A	7	N/A	C_P vs λ vs expV_{wake}
[166]	$k-\omega$ SST	1.5×10^6	< 5	N/A	1.2	C_P vs λ
[167]	Transition SST	2.8×10^6	< 1	12	2	C_P vs λ, C_P vs θ
[168]	Transition SST	2.8×10^6	< 3	6	2	C_P vs λ vs exp, C_m vs θ, vorticity

*Note. In the above tables, an N/A entry denotes that the specified detail is not presented in the research.

2.8 Summary of Literature Review

The primary aims of this research are the characterisation of the mechanical performance of the GKinetic vertical axis turbine from scale experimental test data. The subsequent development of a hydrodynamic model (of the device) capable of simulating its power performance, validated using the aforementioned experimental data. The review, therefore, focussed on the current understanding of the principles of operation, experimental testing and numerical modelling of VATs. The main conclusions from the review and the novelty of the present research are outlined below. The review showed while HATs are the leading tidal turbine technology, there is still substantial interest in VAT designs. It is clear from the literature that the principles of operation of VATs are well understood, with much of this understanding coming from the study of wind turbines which have a much longer history of research and development. The key finding in this respect was that dynamic stall has a significant impact on VAT performance and should, therefore, be included in any proposed performance model. The review showed that while studies have reported the potential benefits of using obstacles or deflector plates to accelerate turbine inlet flows and varying blade pitch to enhance power performance, there are relatively few examples of tidal (or wind) VATs that incorporate these ideas and none that incorporate both. The GKinetic turbine is, therefore, in and of itself, extremely novel and by extension, the experimental testing and modelling of the device presented in this thesis are also novel.

The review of experimental testing protocols, standards and published papers on experimental testing of tidal turbines revealed that turbine power performance is best reported as the non-dimensionalised power coefficient C_P as this allows inter-comparison between different turbine designs. For a given free-stream flow speed, C_P is typically measured for a range of turbine rotation speeds and plotted against λ to produce a power curve which indicates the optimum λ value that achieves the maximum C_P. Following this procedure, this research used experimental test data to develop a series of power curves which characterise the performance of the GKinetic turbine; this is the first time that experimental power curves have been produced for this novel device.

A difficulty in testing of VATs can be the measurement of torque. This research

developed a non-intrusive technique for torque measurement using a torque meter comprising of a data logger connected to four strain gauges configured in a full Wheatstone bridge. Pre-calibration of the meter enabled development of a relationship between applied torque and measured strain.

In the case of turbines making use of a flow acceleration structure, literature [21] recommends that the reference area used in C_P calculations should be the total entrance area of the flow accelerating structure and the turbine, rather than just the turbine area. As the GKinetic turbine uses a bluff body to accelerate flows into the turbine, all C_P calculations use the full device area (bluff body plus turbine) as the reference area.

Experimental testing protocols recommend that when channel blockage by a turbine in a test setup is greater than 5 % the test results should be corrected for blockage [54]. To date, however, blockage correction methods have only been developed for HATs and no acceptable correction method has been developed for VATs. Additionally, the correction methods developed to date are based on 1D actuator disc theory and therefore assume that flow is uniform across the turbine swept area. Due to the acceleration of flow by the buff body, this is not the case for the GKinetic turbine. Therefore, it was not possible to correct the scale experimental test results in this research for blockage. The uncorrected performance data are, however, still applicable for validation of CFD performance models since they can replicate the test conditions and, therefore, applying blockage corrections, in this case, may even complicate CFD model validation efforts. Blockage corrections cannot accurately replicate the full flow physics of unconfined flow. The review identified BEMT and CFD as the two most common approaches for performance modelling of VATs. BEMT models have a low computational cost making them suitable for initial design studies but they are less accurate than CFD models due to the assumptions and simplifications made in their representation of the turbine structure and flow behaviour. CFD models are more realistic in their representation of the turbine and flow behaviour and are, therefore, more accurate but their computational cost is orders of magnitude greater than BEMT models. The Sheldahl and Klimas data are used as input data for the developed BEMT model presented in Chapter 5. Some of the assumptions of the BEMT model make it unsuitable for modelling the GKinetic turbine and it was concluded that CFD modelling would be used. However, given the significant savings of BEMT models

over CFD, the research endeavoured to assess the accuracy of both modelling approaches for performance prediction of more standard VATTs. This served two purposes, first, it allowed assessment of the accuracy of the two different modelling techniques. Second, it allowed validation of the proposed CFD modelling methodology for a typical VATT before its application to the more complex GKinetic turbine. The UNH-RVAT [65] was selected as the comparison test case as an extensive set of measured data is provided.

The literature showed that the most suitable type of BEMT model for VATs is the DMST model which can account for the velocity induction between the upstream and downstream faces of a VAT. The review found that the iterative approach for determination of the induction factor that is typically used in BEMT models is not suitable for highly loaded or high solidity turbines. A number of corrections for BEMT models have been developed to account for missing/simplified physics/processes such as dynamic stall, which is particularly important for VATs, and flow expansion. In this research, a DMST BEMT model for VATTs is developed. Instead of the iterative approach for determining induction factors, the model utilises a graphical approach developed by McIntosh *et al.* [44] for wind turbines. The aspect of the research is significant as tidal turbines, particularly VATTs, typically have a higher solidity than wind turbines and thus Strickland's iterative approach is generally not valid. To the author's knowledge, this is the first time the graphical approach has been applied to VATTs. As well as developing a BEMT model, the research also implements and assesses (individually and collectively) the effects on model performance of corrections for dynamic stall, flow expansion and use of infinite length blade data.

A CFD modelling methodology was developed from the review of CFD turbine modelling literature. The use of the URANS approach in conjunction with the sliding mesh technique is most common for modelling VATs. The turbulence models of choice are the SST models. This agrees with the recommendations of the ANSYS Fluent manual. Confirmation of model convergence is crucial for CFD model credibility. Due to the sensitivity of model performance to mesh structure and time-step, it is critical to carry out mesh and time-step independence studies. Mesh refinement is shown to be key for model accuracy with high refinement required near the blades. The use of quadrilateral inflation layers is recommended in this region in

order to accurately model the boundary layer. For transient turbine modelling studies, solution convergence is generally determined by comparing the difference in a key parameter, such as torque, between successive solutions. While spatial and temporal convergence is accessed by investigating the variance in solutions. In addition to accessing this variability, the Richardson extrapolation method can also be used. The Richardson extrapolation is used in this work to assess mesh convergence. Choice of independence criteria will affect model accuracy and Balduzzi *et al.* [142] showed that a criterion of $\overline{\Delta Q} < 0.1$ % is optimal. This criterion was adopted in the author's URANS sliding mesh CFD modelling methodology.

The validity of the CFD modelling methodology was assessed by modelling Bachant and Wosnik's experimental testing of a standard VATT [65]. Both 2D and 3D CFD models were developed and assessed for accuracy by comparison with the measured data. This work is significant for two reasons. First, it has been widely reported that 2D CFD models over-predict the performance of VATTs. Bachant and Wosnik [139] attributed this to the elevated blockage of 2D models relative to the actual blockage of the experimental setup. The present work investigates this hypothesis and presents a corrective 2D modelling approach that reduces the level of over-prediction of 2D models. The use of this approach may allow a 2D model to achieve satisfactory levels of accuracy without the need for much more computationally intensive 3D modelling. Second, turbine models can and should be, validated against both power performance and wake characteristics; however, model developers and, as a consequence, the published literature tend to focus primarily on power performance. Of the 3D CFD studies of VATTs reviewed, only Bachant and Wosnik [139] validated their model against both power performance and wake characteristics, but even then power performance validation was conducted for just a single λ value. The current research provides validation of the power performance curve and downstream near-wake velocities and turbulent kinetic energy. A holistic approach like this is crucial in ensuring model accuracy. It should be noted, however, that the averaging nature of the URANS approach means it is not best suited for modelling far-field wakes; more computationally expensive methods such as LES or DES are better suited for this.

The final modelling component of the research was the development of the 2D CFD model of the GKinetic turbine. This modelling was restricted to 2D as the

computational cost of 3D was prohibitive. The model includes both the bluff body and the variable pitching of the blades. The variable pitching was enabled through the use of a nested sliding mesh technique where the blades sit within their own sliding meshes which are nested within a larger sliding mesh representing the turbine. Model results are compared with measured data for both power coefficients and wake velocities and the model is used to investigate the effect of some design decisions on device performance.

Figure 2.18 presents a summary flow chart of the approach adopted for the development and optimisation of the GKinetic turbine which formed a key component of the research. The plan for experimental testing was informed by the testing protocols [54] [55] and the IEC standard on testing of tidal turbines [56]; as a result, tests were conducted at 1:40 to 1:20 to 1:10 scale. Likewise, the modelling methodology was informed by the review of literature on VAT operation and computational modelling.

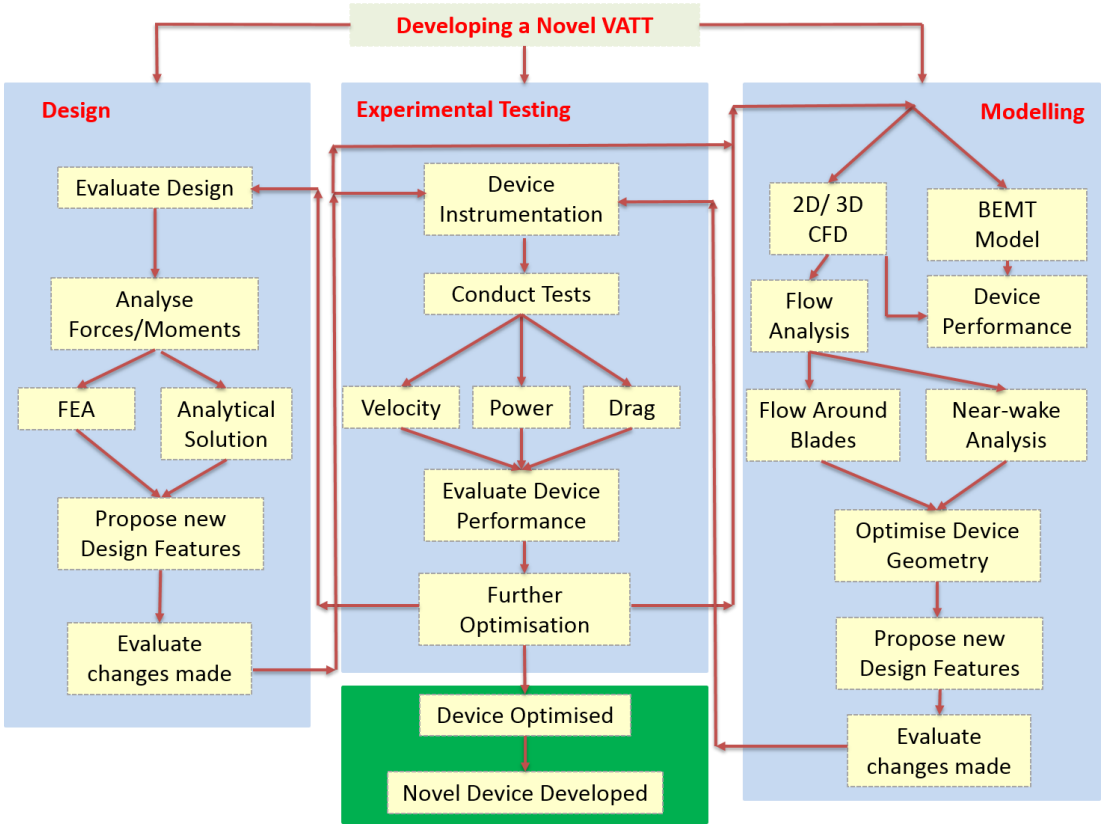

Figure 2.18: Flowchart depicting the design progression plan towards a fully optimised commercial scale GKinetic device.

Chapter 3. CFD Modelling Theory

3.1 Introduction

CFD models solve systems of partial differential equations that represent the physics of fluid behaviour and thus, allow one to simulate fluid movements and interactions with solid objects. The technique is used in a wide range of industrial and research application areas. Some examples include heat transfer in buildings, the aerodynamics of aircraft or vehicles and, more recently, hydrodynamic analysis of tidal turbines.

This chapter details the theory, which the majority of commercial and non-commercial CFD modelling software are based upon. Particular focus is given to the RANS approach as it is used in this research. Model development is also addressed concerning discretisation schemes. CFD packages, although extremely powerful, have inherent errors associated with them, some more significant than others depending on the application; the different types of errors are discussed, as well as methods of minimising them. The aspects of CFD discussed in this chapter are somewhat biased towards turbine modelling.

3.2 Governing Equations

The three conservation laws of mass, momentum and energy govern fluid flow. Applying these laws to a parcel of fluid, one can derive the Navier-Stokes equations – the governing equations of fluid flow. An assumption made throughout this research and agreed upon by tidal and wind energy industries is that the process of energy extraction using a stream turbine is an isothermal process. This assumption allows the energy equation to be omitted from all models, thus keeping computational expense to a minimum. From this point onwards, thermal effects are, therefore, not discussed in regards to energy extraction.

NOTE: Boldface characters are used throughout this chapter to denote vectors.

3.2.1 Conservation of Mass

Conservation of mass, when applied to fluids, results in the continuity equation and requires that the sum of the fluid mass entering and leaving a control volume, in a given time period must equal the change in mass of the fluid within the volume, during the same time period. Consider an infinitesimally small control volume, $d\forall$, (volume is denoted as $\forall$ to avoid confusion with velocity) of dimensions dx, dy, dz. Assuming the flow of mass through each face of the element is one dimensional, the Reynolds transport theorem establishes a relationship between the system rates of change to the control volume surface (CS) and volume (CV) integrals. For a fixed control volume, we can therefore write:

$$\int_{\mathrm{CV}} \frac{\partial \rho}{\partial \mathrm{t}}\, d\forall + \int_{\mathrm{CS}} \rho(\mathbf{U} \cdot \boldsymbol{n})\, dA = 0 \tag{3.1}$$

where

$$\mathbf{U} = \begin{bmatrix} u \\ v \\ w \end{bmatrix} = u\mathbf{i} + v\mathbf{j} + w\mathbf{k} \tag{3.2}$$

and

$$\begin{aligned} u &= u(x, y, z, t) \\ v &= v(x, y, z, t) \\ w &= w(x, y, z, t) \end{aligned} \tag{3.3}$$

Mass flow terms materialise along all six faces with three inlets and three outlets. Considering that all properties of the fluid are uniformly varying in time and position, then if the mass flux at the inlet is ρu, the value at the outlet is $\rho u + \frac{\partial}{dx}(\rho u)dx$. Figure 3.1 shows the mass fluxes across each of the 6 element faces, described mathematically in Table 3.1.

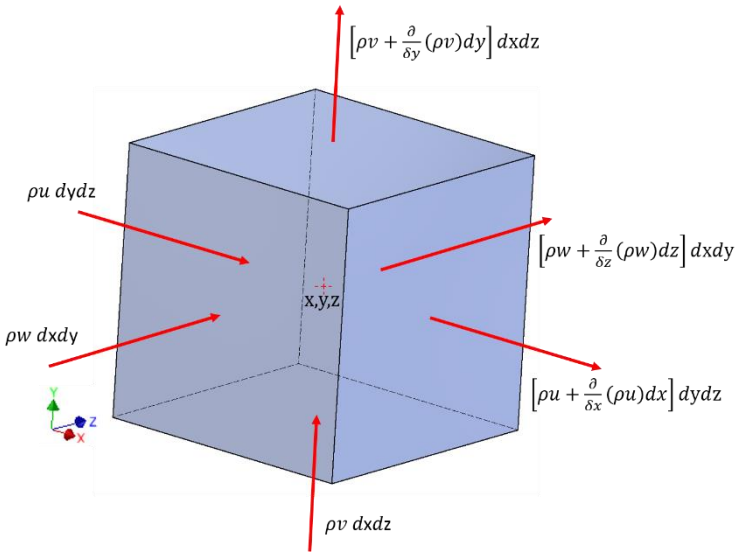

Figure 3.1: Elemental Cartesian fixed control volume, showing inlet and outlet mass fluxes on the X, Y and Z faces.

Table 3.1: Mass fluxes of the inlets and outlets on the X, Y and Z faces.

Face	Inlet mass flux	Outlet mass flux
x	$\rho u\ dy\ dz$	$\left[\rho u + \frac{\partial}{dx}(\rho u)dx\right]dy\ dz$
y	$\rho v\ dx\ dz$	$\left[\rho v + \frac{\partial}{dy}(\rho v)dy\right]\ dx\ dz$
z	$\rho w\ dx\ dy$	$\left[\rho w + \frac{\partial}{dz}(\rho w)dz\right]dx\ dy$

Writing the control volume integral in a differential form (which we can do because the element being considered is infinitesimal) and replacing the control surface integral with a summation of inlet and outlet fluxes from Table 3.1, we obtain the equation for conservation of mass of an infinitesimal control volume, or the continuity equation:

$$\frac{\partial \rho}{\partial \mathrm{t}} + \frac{\partial}{\partial \mathrm{x}}(\rho u) + \frac{\partial}{\partial \mathrm{y}}(\rho v) + \frac{\partial}{\partial \mathrm{z}}(\rho w) = 0 \qquad (3.4)$$

The compact form of the continuity equation is:

$$\frac{\partial \rho}{\partial \mathrm{t}} + \boldsymbol{\nabla} \cdot (\rho \mathbf{U}) = 0 \tag{3.5}$$

and if the flow is incompressible this equation reduces to:

$$\boldsymbol{\nabla} \cdot \mathbf{U} = 0 \tag{3.6}$$

3.2.2 Conservation of Momentum

For conservation of momentum in a system, Newton's second law is applied which states that the rate of change of momentum in a system is equal to the sum of the forces acting on the system, as defined in Equation (3.7). Applying the Reynolds transport theorem, we can develop the expression for a control volume in Equation (3.8).

$$\boldsymbol{F} = m\boldsymbol{a} = m\frac{\mathrm{d}\mathbf{U}}{\mathrm{dt}} = \frac{\mathrm{d}}{\mathrm{dt}}\,(m\mathbf{U}) \tag{3.7}$$

$$\sum \boldsymbol{F} = \frac{\mathrm{d}}{\mathrm{dt}}\left(\int_{\mathrm{CV}} \mathbf{U}\rho\, d\forall\right) + \int_{\mathrm{CS}} \mathbf{U}\rho(\boldsymbol{U} \cdot \boldsymbol{n})\, dA \tag{3.8}$$

where $\Sigma\, F$ is the vector sum of all forces acting on the system, body forces and surface forces. Similar to the mass fluxes of Figure 3.1, momentum fluxes occur across all six faces of the control volume with three inlets and three outlets. Table 3.2 presents the six momentum fluxes.

Table 3.2: Momentum fluxes of the inlets and outlets on the X, Y and Z faces.

Face	Inlet momentum flux	Outlet momentum flux
x	$\rho u\, \mathbf{U}\, dy\, dz$	$\left[\rho u\mathbf{U} + \frac{\partial}{dx}(\rho u\mathbf{U})dx\right] dy\, dz$
y	$\rho v\, \mathbf{U}\, dx\, dz$	$\left[\rho v\mathbf{U} + \frac{\partial}{dy}(\rho v\mathbf{U})dy\right] dx\, dz$
z	$\rho w\, \mathbf{U}\, dx\, dy$	$\left[\rho w\mathbf{U} + \frac{\partial}{dz}(\rho w\mathbf{U})dz\right] dx\, dy$

The surface forces in Equation (3.8) are due to the stresses on the surfaces of the control volume. These stresses are the sum of the hydrostatic pressure and viscous stresses (τ_{ij}) that arise from motion with velocity gradients.

$$\sigma_{ij} = \begin{vmatrix} -P + \tau_{xx} & \tau_{yx} & \tau_{zx} \\ \tau_{xy} & -P + \tau_{yy} & \tau_{zy} \\ \tau_{xz} & \tau_{yz} & -P + \tau_{zz} \end{vmatrix} \tag{3.9}$$

The subscript notation for these stresses is explained in Figure 3.2. Stresses σ_{ij} and τ_{ij} and strain rates ε_{ij} are dissimilar to the velocity vector **U**, in that they are nine component tensors and require two subscripts to define each component. It is not these stresses, but their gradients, that cause a net force on the differential control surface. This can be seen more clearly by examining Figure 3.3, which shows the x direction stresses.

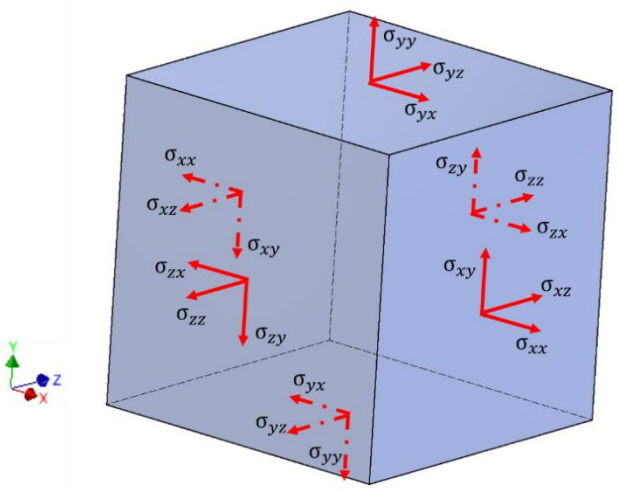

Figure 3.2: Notation for stresses on each of the 6 elemental faces.

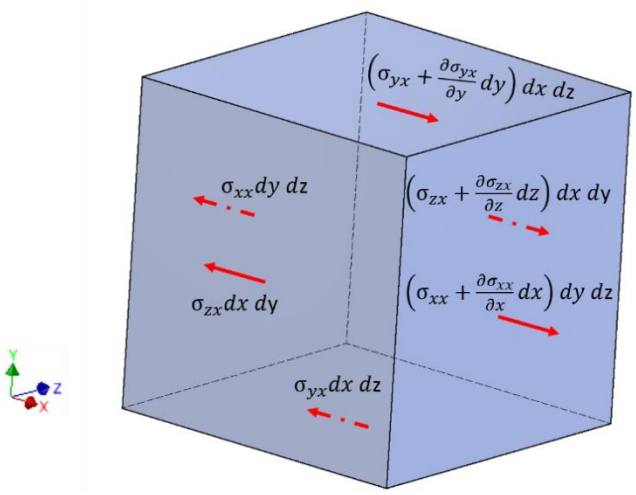

Figure 3.3: Elemental Cartesian fixed control volume showing the surface forces in the X, Y and Z directions.

The basic differential momentum equation for an infinitesimal element can be expressed as:

$$\rho \boldsymbol{g} - \boldsymbol{\nabla} \mathrm{P} + \boldsymbol{\nabla} \cdot \boldsymbol{\tau}_{ij} = \rho \frac{d\mathbf{U}}{dt} \tag{3.10}$$

where

$$\frac{d\mathbf{U}}{dt} = \frac{\partial \mathbf{U}}{\partial t} + u \frac{\partial \mathbf{U}}{\partial x} + v \frac{\partial \mathbf{U}}{\partial y} + w \frac{\partial \mathbf{U}}{\partial z} \tag{3.11}$$

Expressing Equation (3.10) in words

$$\begin{aligned} &Gravity\ force\ per\ unit\ volume + pressure\ force\ per\ unit\ volume \\ &\quad + viscous\ force\ per\ unit\ volume \\ &\quad = density\ x\ acceleration \end{aligned} \tag{3.12}$$

Rewriting Equation (3.10) in full gives:

$$\begin{aligned} \rho g_x - \frac{\partial P}{\partial x} + \frac{\partial \tau_{xx}}{\partial x} + \frac{\partial \tau_{yx}}{\partial y} + \frac{\partial \tau_{zx}}{\partial z} &= \rho \left(\frac{\partial u}{\partial t} + u \frac{\partial u}{\partial x} + v \frac{\partial u}{\partial y} + w \frac{\partial u}{\partial z} \right) \\ \rho g_y - \frac{\partial P}{\partial y} + \frac{\partial \tau_{xy}}{\partial x} + \frac{\partial \tau_{yy}}{\partial y} + \frac{\partial \tau_{zy}}{\partial z} &= \rho \left(\frac{\partial v}{\partial t} + u \frac{\partial v}{\partial x} + v \frac{\partial v}{\partial y} + w \frac{\partial v}{\partial z} \right) \end{aligned} \tag{3.13}$$

$$\rho g_z - \frac{\partial P}{\partial z} + \frac{\partial \tau_{xz}}{\partial x} + \frac{\partial \tau_{yz}}{\partial y} + \frac{\partial \tau_{zz}}{\partial z} = \rho\left(\frac{\partial w}{\partial t} + u\frac{\partial w}{\partial x} + v\frac{\partial w}{\partial y} + w\frac{\partial w}{\partial z}\right)$$

This is the full form of the differential momentum equation and it is valid for any fluid, in any general motion, and particular fluids being characterised by specific viscous stress terms.

Equation (3.13) is unusable until the viscous stresses are written in terms of velocity components. The simplest assumption is frictionless flow, i.e. $\boldsymbol{\tau}_{ij} = 0$, This is Euler's equation for inviscid flow.

$$\rho \boldsymbol{g} - \boldsymbol{\nabla} \mathrm{P} = \rho \frac{d\mathbf{U}}{dt} \tag{3.14}$$

3.2.3 Navier-Stokes Equations

Figure 3.4 shows 1D fluid flow along a wall. The fluid has velocity $u(y)$ where y is perpendicular distance from the wall. For Newtonian fluids, it can be shown that the viscous shear stress is proportional to the velocity gradient accordingly, as expressed in Equation (3.15). The constant of proportionality is the dynamic viscosity coefficient, μ.

$$\tau = \mu \frac{du}{dy} \tag{3.15}$$

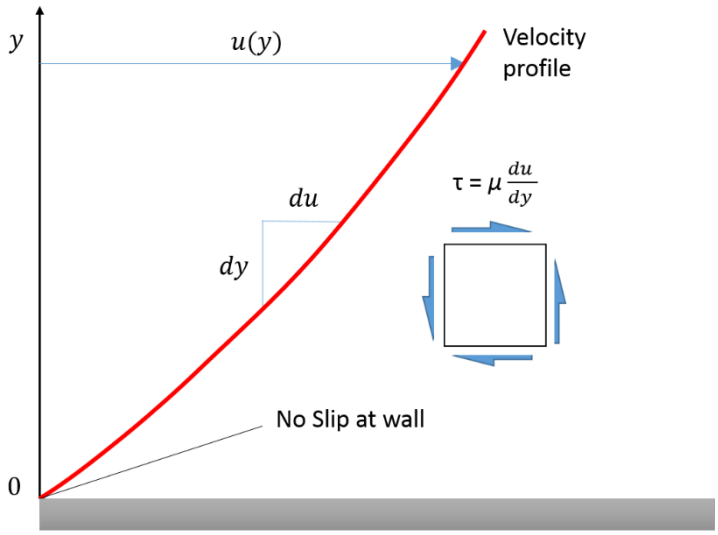

Figure 3.4: Shear distribution within a shear layer of a Newtonian fluid. The shear stress is proportional to the slope of the velocity profile. The no-slip at the wall is also identified.

Expanding this relationship to three-dimensional viscous flow and substituting into Equation (3.13) gives the differential momentum equation for a Newtonian fluid with constant density and viscosity.

$$\begin{aligned}
\rho g_x - \frac{\partial P}{\partial x} + \mu\left(\frac{\partial^2 u}{\partial x^2} + \frac{\partial^2 u}{\partial y^2} + \frac{\partial^2 u}{\partial z^2}\right) &= \rho\frac{du}{dt} \\
\rho g_y - \frac{\partial P}{\partial y} + \mu\left(\frac{\partial^2 v}{\partial x^2} + \frac{\partial^2 v}{\partial y^2} + \frac{\partial^2 v}{\partial z^2}\right) &= \rho\frac{dv}{dt} \\
\rho g_z - \frac{\partial P}{\partial z} + \mu\left(\frac{\partial^2 w}{\partial x^2} + \frac{\partial^2 w}{\partial y^2} + \frac{\partial^2 w}{\partial z^2}\right) &= \rho\frac{dw}{dt}
\end{aligned} \tag{3.16}$$

These are the Navier-Stokes equations for incompressible flow. They are second-order, nonlinear partial differential equations.

Consolidating Equation (3.16) into vector form gives:

$$\rho\left(\frac{d\mathbf{U}}{dt}\right) = \rho\boldsymbol{g} - \nabla P + \mu\nabla^2\mathbf{U} \tag{3.17}$$

When a flow is both frictionless and irrotational, things simplify. First, the Navier-Stokes equations (Equation (3.16)) reduce to Euler's equation and, second, there is a significant simplification in the acceleration term.

$$\frac{d\mathbf{U}}{dt} = \frac{\partial\mathbf{U}}{\partial t} + (\mathbf{U}\,.\nabla)\mathbf{U} \tag{3.18}$$

A vector identity exists for the second term on the right

$$(\mathbf{U}\,.\nabla)\mathbf{U} \equiv \nabla\left(\frac{1}{2}U^2\right) + \boldsymbol{\zeta}\times\mathbf{U} \tag{3.19}$$

where $\boldsymbol{\zeta}$ is the curl of **U** (vorticity).

If we combine Equations (3.16) and (3.19), divide by ρ, and rearrange the left-hand side, we can then take the dot product of the entire equation into an arbitrary vector

displacement $d\boldsymbol{r}$:

$$\left[\frac{\partial \mathbf{U}}{\partial t} + \nabla\left(\frac{1}{2}V^2\right) + \boldsymbol{\zeta} \times \mathbf{U} + \frac{1}{\rho}\nabla \mathrm{P} - \mathbf{g}\right] \cdot d\mathbf{r} = 0 \tag{3.20}$$

Integrating along a streamline in frictionless compressible flow and taking, $\mathbf{g} = -\mathrm{g}k$, Equation (3.20) reduces to:

$$\frac{\partial \mathbf{U}}{\partial t} \cdot d\mathbf{r} + \mathrm{d}\left(\frac{1}{2}\mathrm{U}^2\right) + \frac{dP}{\rho} + \mathrm{g}\,\mathrm{dz} = 0 \tag{3.21}$$

Integrating between any two points, 1 and 2 along the streamline gives Bernoulli's equation for frictionless unsteady flow along a streamline:

$$\int_1^2 \frac{\partial \mathbf{U}}{\partial t}\, ds + \int_1^2 \frac{dP}{\rho} + \frac{1}{2}(\mathrm{U}^2{}_2 - \mathrm{U}^2{}_1) + \mathrm{g}\,(z_2 - z_1) = 0 \tag{3.22}$$

where, ds, is the arc length along the streamline. For incompressible steady flow, this reduces to

$$P + \frac{1}{2}\rho \mathrm{U}^2 + \rho \mathrm{g}\, z = contant\ along\ stramline \tag{3.23}$$

3.3 Turbulence Modelling

Most real-world flows are turbulent. In turbulent flows, the flow paths of fluid particles are quite chaotic (see Figure 3.5) with sudden changes in speed and direction. Modelling turbulence is, therefore, difficult and much research has been devoted to this. Three different averaging concepts have been introduced for turbulence modelling research: (1) time averaging, (2) spatial averaging and (3) ensemble averaging. For time averaging, an instantaneous flow variable is expressed as $f(x_\mathrm{i}, t)$. For spatial averaging, the average is taken over all spatial coordinates by calculating a volume integral. Ensemble averaging is the most general type of averaging. As an example, using Reynolds decomposition, the velocity can be divided up into the time-averaged velocity, $U_{\text{.}}$ and a fluctuation about this value, u', i.e. the turbulence component (Figure 3.5).

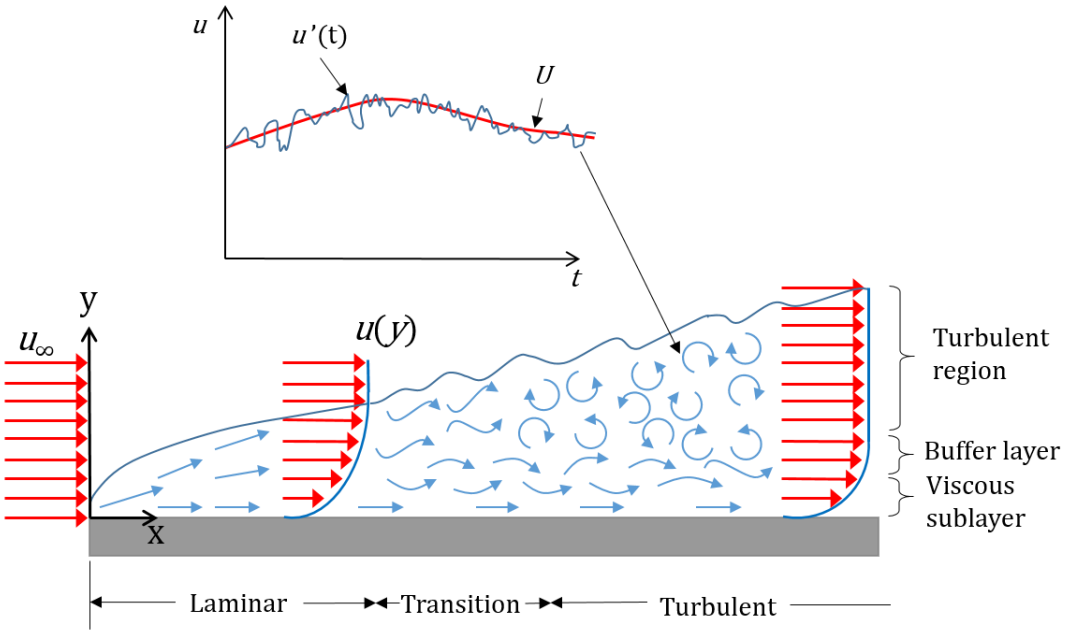

Figure 3.5: Velocity boundary layer development on a flat plate, with the chaotic nature of turbulent flow shown. The velocity fluctuations ($u'(t)$) due to the turbulence is also shown (adapted from White [27]).

A generalised form of Reynold's decomposition of any variable, ϕ, is given as:

$$\phi(t) = \Phi + \phi'(t) \tag{3.24}$$

The kinetic energy of the turbulence is the mean kinetic energy per unit mass associated with eddies in turbulent flow and is defined as:

$$k = \frac{1}{2}\left(\overline{u'^2} + \overline{v'^2} + \overline{w'^2}\right) \tag{3.25}$$

The turbulence intensity is linked to the kinetic energy and mean flow as:

$$T_I = \frac{\left(\frac{2}{3}k\right)^{1/2}}{U} \tag{3.26}$$

Or simply:

$$T_I = \frac{u'}{U} \tag{3.27}$$

3.3.1 DNS, LES and DES.

DNS involves the complete three dimensional and time-dependent solutions of the Navier-Stokes and continuity equations. This requires the whole series of spatial and temporal scales of turbulence to be resolved. All the spatial scales of the turbulence must be solved in the computational mesh, from the smallest dissipative scales (Kolmogorov scales), up to the integral scale, related to the motions containing most of the kinetic energy. Such simulations are, in principle, numerically-accurate solutions of exact equations of motion and, in principle, the proper solution to the turbulence problem. However, due to the huge computational expense associated with DNS modelling, it is currently restricted to very simple geometries and is therefore not a viable option for turbine modelling.

The premise of LES is that the largest turbulent eddies are directly influenced by the boundary conditions, and carry most of the Reynolds stress, and must be computed. The small-scale turbulence is diluted and contributes less to the Reynolds stresses; it is therefore not considered as vital and is ignored. It is nearly isotropic and has near universal characteristics; which makes it more amenable to modelling. Because LES involves ignoring the smallest eddies, the elements can be larger than the Kolmogorov length, and larger time-steps can be used than are possible in DNS. Hence, it is possible to obtain a solution at a given Reynolds number more cheaply, computationally, in LES than DNS.

The DES method was developed as a computational cost reducing method that treats the large eddies using conventional LES while treating boundary layers and thin shear layers with the conventional RANS approach. In practice, cell spacing in a DES model is of the same order of magnitude as the boundary-layer thickness.

DES is as an extension of a RANS approach using a more standard turbulence model into more complex flows. This is made possible by computing the geometry-dependent, three-dimensional eddies whose details are lost in Reynolds-averaging, with the hope that the DES converges toward an LES as the grid is refined.

As with DNS and LES, accurate numerical methods are vital, especially for the LES

aspect. The RANS component of the computation requires selection of a suitable turbulence model. The difference with the DES model is that it relies only on the RANS resolution in the boundary layers. The application of DES, however, may still require significant CPU resources and it is recommended that the conventional turbulence models employing the RANS approach be used for most practical calculations [138].

3.3.2 RANS

Reynolds introduced the concept of expressing a continually changing variable as the sum of its mean and fluctuating parts. The approach is used to develop the time-averaged forms of the Navier-Stokes equations, which are commonly called the Reynolds-averaged Navier-stokes equations. The non-linearity of the Navier-Stokes equations lead to momentum fluxes that act as stresses throughout the flow. Equations are derived to resolve these stress terms, which results in additional unknown quantities. This leads to the closure issue of the RANS equations, i.e. the need to establish an adequate number of equations to solve all unknowns.

Recall the incompressible Navier-Stokes equations, where the velocity vector, **U,** has components u, v and w, in the x, y and z directions respectively:

$$\begin{aligned} \boldsymbol{\nabla} \cdot \mathbf{U} &= 0 \\ \frac{\partial u}{\partial t} + \boldsymbol{\nabla} \cdot (\mathrm{u}\mathbf{U}) &= -\frac{1}{\rho}\frac{\partial u}{\partial t} + \mu\nabla^2 u \\ \frac{\partial v}{\partial t} + \boldsymbol{\nabla} \cdot (\mathrm{v}\mathbf{U}) &= -\frac{1}{\rho}\frac{\partial v}{\partial t} + \mu\nabla^2 v \\ \frac{\partial w}{\partial t} + \boldsymbol{\nabla} \cdot (\mathrm{w}\mathbf{U}) &= -\frac{1}{\rho}\frac{\partial w}{\partial t} + \mu\nabla^2 w \end{aligned} \tag{3.28}$$

To investigate turbulence fluctuation effects, the flow variables in Equation (3.28), **U,** u, v, w and p, are replaced by the sum of a mean and fluctuating component. Therefore,

$$\mathbf{u} = \mathbf{U} + \mathbf{u}';\ u = U + u';\ v = V + v';\ w = W + w';\ p = P + p' \tag{3.29}$$

The time-average is then taken and gives the continuity equation for the mean velocity:

$$\boldsymbol{\nabla} \cdot \mathbf{U} = 0 \tag{3.30}$$

A similar process is carried out on the x-momentum equation, where the time-average of the individual components are:

$$\begin{gathered}\overline{\frac{\partial u}{\partial t}} = \frac{\partial U}{\partial t}; \qquad \overline{\boldsymbol{\nabla} \cdot (\mathrm{u}\mathbf{u})} = \boldsymbol{\nabla} \cdot (U\mathbf{U}) + \boldsymbol{\nabla} \cdot (\overline{\mathrm{u}'\mathbf{u}'}) \\ \overline{-\frac{1}{\rho}\frac{\partial p}{\partial x}} = -\frac{1}{\rho}\frac{\partial P}{\partial x}; \qquad \overline{\mu\nabla^2 u} = \mu\nabla^2 U\end{gathered} \tag{3.31}$$

Substituting these into Equation (3.28) gives the time-averaged x-momentum equation:

$$\underset{(I)}{\frac{\partial U}{\partial t}} + \underset{(II)}{\boldsymbol{\nabla} \cdot (U\mathbf{U})} + \underset{(III)}{\boldsymbol{\nabla} \cdot \left(\overline{\mathrm{u}'\boldsymbol{u}'}\right)} = \underset{(IV)}{-\frac{1}{\rho}\frac{\partial P}{\partial x}} + \underset{(V)}{\mu\nabla^2 U} \tag{3.32}$$

Repeating the same procedure for the y and z directions gives:

$$\begin{gathered}\underset{(I)}{\frac{\partial V}{\partial t}} + \underset{(II)}{\boldsymbol{\nabla} \cdot (V\mathbf{U})} + \underset{(III)}{\boldsymbol{\nabla} \cdot (\overline{\mathrm{v}'\mathbf{u}'})} = \underset{(IV)}{-\frac{1}{\rho}\frac{\partial P}{\partial y}} + \underset{(V)}{\mu\nabla^2 V} \\ \underset{(I)}{\frac{\partial W}{\partial t}} + \underset{(II)}{\boldsymbol{\nabla} \cdot (W\mathbf{U})} + \underset{(III)}{\boldsymbol{\nabla} \cdot (\overline{\mathrm{w}'\mathbf{u}'})} = \underset{(IV)}{-\frac{1}{\rho}\frac{\partial P}{\partial z}} + \underset{(V)}{\mu\nabla^2 W}\end{gathered} \tag{3.33}$$

It is important to recognise that the terms (I), (II), (IV) and (V) also appear in the instantaneous momentum equations, but it is the process of averaging that introduces term (III) which involves the fluctuating velocities.

The viscous normal and shear stress tensor is:

$$\tau_{ij} = \mu\left(\frac{\partial \bar{u}_i}{\partial x_j} + \frac{\partial \bar{u}_j}{\partial x_i}\right) \tag{3.34}$$

The turbulent shear stresses tensor is then defined as:

$$\tau_{ij} = -\rho\overline{\mathrm{u}_i{}'u_j{}'} \tag{3.35}$$

Turbulent shear stresses are usually more substantial than viscous stresses in turbulent flows. The RANS equations are not closed due to the six unknown terms in the form of the Reynolds stresses. Closure (turbulence) models have been developed to resolve this problem. Eddy viscosity models, for example, relate the Reynolds stresses to the mean flow gradients, with the addition of conservation equations for additional variables. The closure problem thus becomes a problem of finding the turbulent viscosity solution. These are the models focused upon in this research. Alternative approaches, which will not be discussed, are second-order closure models, also known as Reynolds stress models.

3.3.3 Governing Equation for the Turbulent Kinetic Energy

The turbulent kinetic energy, k, defined in Equation (3.23), is a common choice of variable for development of a conservation equation, to help resolve the closure issue. The conservation equation can be developed by taking the scalar product of the velocity fluctuation vector within the Navier-Stokes equations and then subtracting the scalar product of the velocity fluctuation vector within the RANS equations. After substantial rearrangement, this reduces to:

$$\underset{(I)}{\frac{\partial(\rho k)}{\partial t}} + \underset{(II)}{\boldsymbol{\nabla}\cdot(\rho k\mathbf{U})} = \underset{(III)}{\boldsymbol{\nabla}\cdot(-\overline{p'\mathbf{v}'}} + \underset{(IV)}{\mu\overline{\mathbf{v}'s'_{ij}}} - \underset{(V)}{\frac{1}{2}\rho\overline{u'_i\cdot u'_iu'_j}}) - \underset{(VI)}{2\mu\overline{s'_{ij}\cdot s'_{ij}}} - \underset{(VII)}{\rho\overline{u'_iu'_j}\cdot s'_{ij}} \tag{3.36}$$

Or, in words:

Rate of change of k	+	Transport of k by convection	=	Transport of k by pressure	+	Transport of k by viscous stress	+	Transport of k by Reynolds stress	+	Rate of dissipation of k	+	Rate of production of k

Terms (III - V) represent the transport/diffusion processes. Term (VI), represents the viscous dissipation of turbulent kinetic energy and is typically defined as the product of density and the rate of dissipation of turbulent kinetic energy per unit mass, ε, such that:

$$\varepsilon = 2\nu\overline{s'_{ij} \cdot s'_{ij}} \tag{3.37}$$

The usual approach for determining the dissipation rate, ε, is to develop a conservation equation. Alternatively, it may be modelled using the turbulent kinetic energy and the mixing length; this is the approach used in one-equation models based on the turbulent kinetic energy. These mixing length models will not be discussed as part of this research as they are unsuitable in situations where flow separation occurs.

The relationship for the specific dissipation rate, ω, is then:

$$\omega \sim \frac{\varepsilon}{k} \tag{3.38}$$

3.3.4 Turbulence Models

The following subsections describe the most commonly used turbulence models in VAT studies.

3.3.4.1 $k - \varepsilon$ model

The standard $k - \varepsilon$ model, attributed to Launder and Spalding [134], is a two-equation turbulence transport model. The eddy viscosity is determined from a single turbulence length scale so the calculated turbulent diffusion only occurs at the specified scale, whereas, in reality, all scales of motion will contribute to the turbulent diffusion. The $k - \varepsilon$ model uses gradient diffusion to relate the Reynolds stresses to the mean velocity gradients and the turbulent viscosity. The turbulence kinetic energy, k, and its dissipation rate, ε, are calculated from transport equations and solved simultaneously. The model is robust and computationally inexpensive. It is most effective in fully turbulent flows, but it performs quite poorly for complex flows involving high-pressure gradients and separated flows.

The transport equations for k and ε used in the model are:

$$\frac{\partial(\rho k)}{\partial t} + \frac{\partial\left(\rho u_j k\right)}{\partial x_j} = P - \rho\varepsilon + \frac{\partial}{\partial x_j}\left[\left(\mu + \frac{\mu_t}{\sigma_k}\right)\frac{\partial k}{\partial x_j}\right] \tag{3.39}$$

$$\frac{\partial(\rho\varepsilon)}{\partial t}+\frac{\partial\left(\rho u_j\varepsilon\right)}{\partial x_j}=C_{\varepsilon1}\frac{\varepsilon}{k}P-C_{\varepsilon2}\frac{\rho\varepsilon^2}{k}+\frac{\partial}{\partial x_j}\left[\left(\mu+\frac{\mu_t}{\sigma_\varepsilon}\right)\frac{\partial\varepsilon}{\partial x_j}\right] \tag{3.40}$$

Turbulent viscosity is modelled as:

$$\mu_t=\rho C_\mu\frac{k^2}{\varepsilon} \tag{3.41}$$

Further explanation of the variables in these equations is presented in Appendix A.1 of this thesis and in the Fluent manual [138].

3.3.4.2 $k-\omega$ model

The $k-\omega$ is another two-equation model solving for the turbulence kinetic energy, k, and the specific turbulent dissipation rate, ω. The primary advantage of the $k-\omega$ model over the $k-\varepsilon$ model is that it can be applied accurately in the boundary layer region without the use of wall functions.

Further revisions of his original $k-\omega$ model [135] were presented by Wilcox in 1998 and 2006. The standard $k-\omega$ model included in Fluent is the 1998 revision. The primary aims of the 1998 revision were to include additional closure coefficients, reduce the model's sensitivity to initial free-stream boundary conditions and incorporate modifications for low Reynolds number effects, compressibility, and shear flow spreading. While the formulation used in Fluent has reduced the dependency on free-stream boundary conditions, they can still have a significant effect on the solution. The 1998 revised model [169] uses the following transport equations for k and it's specific dissipation rate, ω :

$$\frac{\partial(\rho k)}{\partial t}+\frac{\partial\left(\rho u_j k\right)}{\partial x_j}=P-Y_k+\frac{\partial}{\partial x_j}\left[\left(\mu+\frac{\mu_t}{\sigma_k}\right)\frac{\partial\omega}{\partial x_j}\right] \tag{3.42}$$

$$\frac{\partial(\rho\omega)}{\partial t}+\frac{\partial\left(\rho u_j\omega\right)}{\partial x_j}=\frac{\alpha\omega}{k}P-Y_\omega+\frac{\rho\sigma_d}{\omega}\frac{\partial k}{\partial x_j}\frac{\partial\omega}{\partial x_j}+\frac{\partial}{\partial x_j}\left[\left(\mu+\frac{\mu_t}{\sigma_\omega}\right)\frac{\partial\omega}{\partial x_j}\right] \tag{3.43}$$

The eddy viscosity is then determined using:

$$\mu_t = \alpha^* \frac{\rho k}{\omega} \tag{3.44}$$

The α^* coefficient damps the turbulent viscosity causing a low-Reynolds number correction.

Further explanation of the variables in these equations is presented in Appendix A.2 of this thesis and in the Fluent manual [138].

3.3.4.3 $k-\omega$ SST model

The $k-\omega$ SST model was initially developed by Menter [136] as an attempt to overcome the shortcomings of the $k-\omega$ and $k-\varepsilon$ models, but also to take advantage of their various strengths. The $k-\omega$ SST model combines the original Wilcox $k-\omega$ model for use near walls, with a $k-\varepsilon$ behaviour in the free-stream. It has undergone minor revisions by Menter *et al.* [170]. The model used in Flunet, is the later 2003 model. Menter added a blending function, F_1 into the original definitions of the transport equations for k, and ω, and also multiplied the definitions of k and ε by $(1-F_1)$ to give the following transport equations:

$$\frac{\partial(\rho k)}{\partial t} + \frac{\partial\left(\rho u_j k\right)}{\partial x_j} = P_k - D_k + \frac{\partial}{\partial x_j}\left[(\mu + \sigma_k \mu_t)\frac{\partial k}{\partial x_j}\right] \tag{3.45}$$

$$\frac{\partial(\rho\omega)}{\partial t} + \frac{\partial\left(\rho u_j \omega\right)}{\partial x_j} = \alpha\rho S^2 - \beta\rho\omega^2 + \frac{\partial}{\partial x_j}\left[(\mu + \sigma_\omega \mu_t)\frac{\partial \omega}{\partial x_j}\right] + 2(1 - F_1)\frac{\rho\sigma_{\omega 2}}{\omega}\frac{\partial k}{\partial x_j}\frac{\partial \omega}{\partial x_j} \tag{3.46}$$

The turbulent eddy viscosity is defined as follows:

$$\mu_t = \frac{\rho a_1 k}{\max(a_1 \omega, SF_2)} \tag{3.47}$$

Further explanation of the variables in these equations is presented in Appendix A.3 of this thesis and in the Fluent manual [138].

3.3.4.4 Transitional SST model.

The Transitional SST model sometimes called the $\gamma - Re\theta t$ SST turbulence model or the Langtry-Menter model after the authors/developers [137,171], is a four-equation model, that is built on the previous SST model work of Menter. Inspection of the state of CFD modelling at the time led Langtry and Menter to realise that the effects of laminar-to-turbulent transition were omitted from the majority of CFD codes. The model accounts for free-stream turbulence intensity, pressure gradients and flow separation. The Transitional SST model incorporates two further equations compared to the $k - \omega$ SST model for intermittency (γ) and the transitional momentum thickness Reynolds number ($\overline{Re}_{\theta t}$). γ is used to determine whether the Transitional SST model should be active. When γ = 0, the production of turbulent kinetic energy, k is suppressed and the flow is effectively laminar. When γ = 1, the Transitional SST model is fully active and the flow is assumed to be fully turbulent. $\overline{Re}_{\theta t}$ controls the transition criterion between laminar and turbulent flow. The critical Reynolds number, $Re_{\theta c}$, occurs where intermittency begins to increase in the boundary layer. It occurs upstream of the Reynolds number of transition onset, $Re_{\theta t}$, as turbulence must first build up to appreciable levels in the boundary layer before any change in the laminar profile can occur. As a result, $Re_{\theta c}$ is the location where turbulence starts to grow and $Re_{\theta t}$ is the location where the velocity profile starts to deviate from a purely laminar profile. The four transport equations of the model are presented below for k, ω, γ and $\overline{Re}_{\theta t}$ respectively:

$$\frac{\partial(\rho k)}{\partial t} + \frac{\partial(\rho u_j k)}{\partial x_j} = \tilde{P}_k - \widetilde{D}_k + \frac{\partial}{\partial x_j}\left[(\mu + \sigma_k \mu_t)\frac{\partial k}{\partial x_j}\right] \tag{3.48}$$

$$\frac{\partial(\rho\omega)}{\partial t}+\frac{\partial\left(\rho u_j\omega\right)}{\partial x_j} = \frac{\gamma}{\rho\mu_t}P_k-\beta\rho\omega^2+\frac{\partial}{\partial x_j}\left[(\mu+\sigma_\omega\mu_T)\frac{\partial\omega}{\partial x_j}\right]+2(1-F_1)\frac{\rho\sigma_{\omega2}}{\omega}\frac{\partial k}{\partial x_j}\frac{\partial\omega}{\partial x_j} \quad (3.49)$$

$$\frac{\partial(\rho\gamma)}{\partial t}+\frac{\partial(\rho U u_j\gamma)}{\partial x_j}=P_\gamma-E_\gamma+\frac{\partial}{\partial x_j}\left[\left(\mu+\frac{\mu_t}{\sigma_\gamma}\right)\frac{\partial\gamma}{\partial x_j}\right] \quad (3.50)$$

$$\frac{\partial(\rho\overline{Re}_{\theta t})}{\partial t}+\frac{\partial(\rho u_j\overline{Re}_{\theta t})}{\partial x_j}=P_{\theta t}+\frac{\partial}{\partial x_j}\left[\sigma_{\theta t}(\mu+\mu_t)\frac{\partial\overline{Re}_{\theta t}}{\partial x_j}\right] \quad (3.51)$$

The turbulent eddy viscosity is defined as follows:

$$\mu_t=\min\left[\frac{\rho k}{\omega};\frac{a_1\rho k}{SF_2}\right] \quad (3.52)$$

Further explanation of the variables in these equations is presented in Appendix A.4 of this thesis and in the Fluent manual [138].

3.3.5 Modelling Flow near the Wall

The presence of walls can significantly affect turbulent flows. The velocity field is modified through the no-slip condition that has to be satisfied near the wall. However, turbulence is also changed in other ways. Towards the outer part of the near-wall region, turbulence rapidly develops via the production of turbulent kinetic energy due to large gradients in the mean velocity.

Near-wall modelling significantly impacts the accuracy of CFD solutions since walls are the primary source of mean vorticity and turbulence. The near wall variables have large gradients, where momentum and other scalar transports occur most actively. Accurate portrayal of the flow in the adjacent wall region is paramount for successful modelling of turbulent flows.

The near wall region can be divided into three zones (Figure 3.6). First, closest to the wall is the viscous sublayer where the flow is relatively laminar and the molecular viscosity is vital in relation to momentum and mass transfer. Second, furthest from the wall is the fully turbulent layer where turbulence is dominant. Third, in between the viscous sublayer and the fully turbulent layer, is the buffer region, or blending region, where the effects of molecular viscosity and turbulence are of equal importance.

y^+ is a non-dimensional wall distance for a wall-bounded flow that is used to determine the appropriate grid resolution near a wall for a particular turbulence model. It is defined as:

$$y^+ \equiv \frac{\rho y u_\tau}{\mu} \tag{3.53}$$

where, u_τ is the friction velocity, defined as:

$$u_\tau = \frac{\tau_w}{\rho} \tag{3.54}$$

τ_w is the wall shear stress and is defined as:

$$\tau_w = \mu \left(\frac{\partial u}{\partial y}\right)_{y=0} = \frac{1}{2} \rho C_f {U_\infty}^2 \tag{3.55}$$

where C_f is the skin friction coefficient and can be approximated for a flat plate [172] using:

$$C_f = [2 \log_{10}(Re) - 0.65]^{-2.3} \tag{3.56}$$

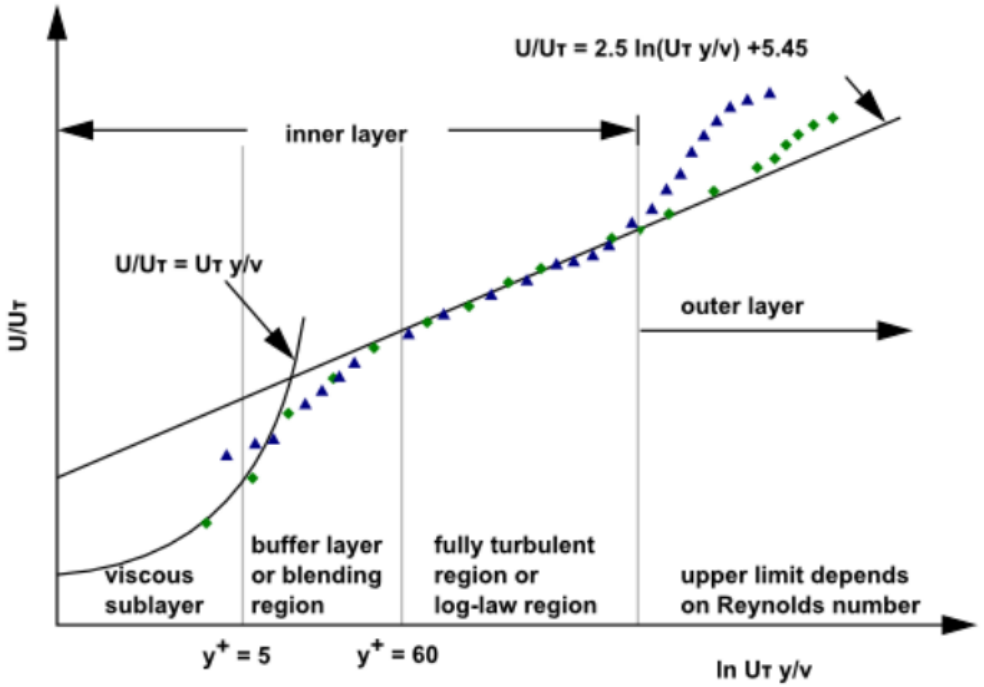

Figure 3.6: Illustration of the Viscous sublayer, fully turbulent region and the buffer layer. Fluent manual [138]

There are two approaches to modelling the near-wall region. In the first, the viscosities of the inner regions (viscous sublayer and buffer layer) are not resolved. Instead, semi-empirical formulations, "wall functions", are used to link the viscosity-affected zone at the wall and the fully turbulent region. The use of wall functions eliminates the necessity to modify the turbulence models to account for the presence of the wall. This is known as the high Reynolds number approach and requires a $y^+ > 30$.

In the second approach, the turbulence models are modified to enable the viscosity affected region to be resolved with a mesh all the way to the wall, including the viscous sublayer. This is known as the low Reynolds number approach and requires a $y^+ \approx 1$.

The primary deficiency of wall functions (except the scalable wall function) is that the numerical results degrade under refinement of the mesh in the wall normal direction; y+ values below 15 will result in unbounded errors in wall shear stress. Although scalable wall functions can overcome this drawback, they still rely on empirical wall functions to model the boundary layer. The Fluent manual recommends the use of the low Reynolds number approach combined with adequate mesh refinement in the near

wall region because the empirical basis utilised in developing the wall functions is not for separated flows. The use of an SST model with automatic near wall treatment to model the effects in the viscous sublayer is also recommended.

Accurate CFD results for the wall boundary layer will only be obtained if mesh refinement of the boundary layer is sufficient. For unstructured meshes, the theory manual recommends that 20 or more prism layers at the wall, are required for accurate modelling of the boundary layer. The thickness of the prism layers should be designed to ensure that 15 or more nodes are actually covering the boundary layer. After obtaining a solution, it can be verified that a sufficient number of prism layers are used by looking at the location of the maximum turbulent viscosity since this occurs in the middle of the boundary layer. Therefore, twice this distance (the location of maximum turbulent viscosity to the wall) gives an approximation for the edge of the boundary layer [138]. It is imperative that the prism layer is larger than the boundary layer as otherwise there is a danger that the prism layer will confine the growth of the boundary layer.

3.4 Solution Methods

The finite volume method is a method of representing and solving the governing partial differential equations in algebraic form. It is the most common numerical method used across CFD packages and is used in ANSYS Fluent. There are three critical stages/steps in the finite volume method.

Step 1: Grid Generation

This involves subdividing the domain into discrete control volumes. The boundaries (or faces) of control volumes are positioned mid-way between adjacent nodes; each node is surrounded by a control volume or cell. Figure 3.7 shows a general nodal point, P, and its neighbouring nodes in a two-dimensional geometry; N, S, E and W identify the nodes to the north, south, east and west respectively. The west side face of the control volume is referred to by *w* and the east side control volume face by *e*, similarly for the north and south faces. The distances between the nodes *W* and *P*, and between nodes *P* and *E*, are identified by ΔxWP and ΔxPE. Similarly, distances between face w and point P and between P and face e are denoted by ΔxwP and ΔxPe, respectively.

The same convention is used for denoting distances between north and south faces / nodes.

Step 2: Discretisation

The second key step of the finite volume method is the integration of the governing equation (or equations) over a control volume to yield a discretised equation at its nodal point P. In order to derive useful forms of the discretised equations, the interface diffusion and variable gradients are required. Following well-established practice, the values of any model variable, ϕ, and the diffusion coefficient are defined and evaluated at nodal points. To calculate variable gradients (and hence fluxes) at the control volume faces, an approximate distribution of properties between nodal points is used. Linear approximations are most commonly used and are the simplest way of calculating interface values and the gradients.

Step 3: Solution of Equations

Discretised equations must be set up at each of the nodal points in order to solve the problem. For control volumes that are adjacent to the domain boundaries, the general discretised equation is modified to incorporate boundary conditions. The resulting system of linear algebraic equations is then solved to acquire the distribution of the property ϕ at nodal points.

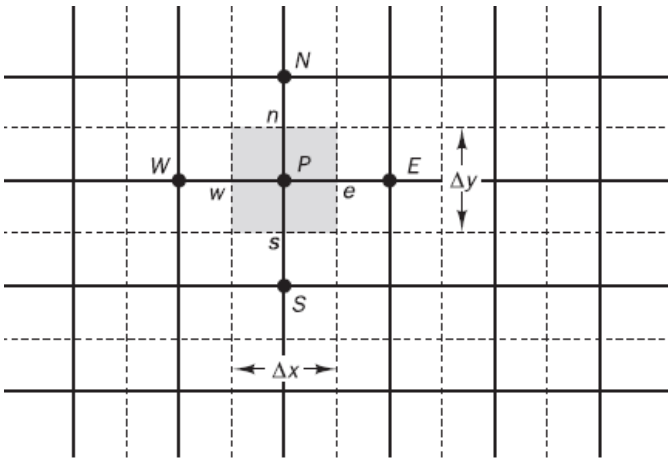

Figure 3.7: A sample 2D grid used for discretisation, with node P in the middle of neighbouring nodes, N, S, E and W.

3.4.1 Evaluation of Variable Gradients and Derivatives

Variable gradients are needed not only for constructing values of a scalar at the cell faces, but also for determining secondary diffusion terms and velocity derivatives. The gradient, $\Delta\phi$, of a given variable, ϕ, is used to discretise the convection and diffusion terms in the flow conservation equations. The gradients are computed in Fluent using one of the following three methods:

- Green-Gauss Cell-Based
- Green-Gauss Node-Based
- Least Squares Cell-Based

3.4.2 Pressure-Velocity Coupling

The pressure based solver in Fluent allows solving using either a segregated or coupled approach. Fluent enables implementation of one of the following pressure-velocity coupling schemes: SIMPLE, SIMPLEC, PISO, and Coupled. SIMPLE, SIMPLEC and PISO use the pressure-based segregated algorithm, while Coupled uses the pressure-based coupled solver.

3.4.2.1 SIMPLE

The Semi-Implicit Method for Pressure-Linked Equations (SIMPLE) scheme uses a correlation between velocity and pressure corrections to implement mass conservation and to resolve the pressure field. The momentum equation is solved with a guessed pressure field and resulting face flux is then determined.

3.4.2.2 SIMPLEC

The SIMPLE-Consistent (SIMPLEC) scheme is very similar to the SIMPLE scheme. The only difference is in the definition of the face flux correction which allows additional under-relaxation to be applied in cases that suffer convergence issues due to the pressure-velocity coupling. In some cases, this additional under-relaxation can lead to instability and it is recommended (by the Fluent manual) that a different scheme is then used.

3.4.2.3 PISO

The Pressure-Implicit with Splitting of Operators (PISO) scheme is based on the higher degree of approximation between the corrections for pressure and velocity. A limitation of the SIMPLE algorithm, and by extension SIMPLEC, is that new velocities and corresponding fluxes do not appease the momentum balance after solving the pressure-correction. This requires the calculation to be repeated until the balance is satisfied. To improve the efficiency of the computation, the PISO algorithm performs two additional corrections – the neighbour correction and the skewness correction.

3.4.2.4 Coupled

The Coupled method has some advantages over the segregated techniques; the coupled scheme obtains a robust and efficient single-phase implementation for steady-state with superior performance compared to the segregated solution schemes. For transient flows, using the coupled algorithm is recommended to overcome poor quality meshes or if large time steps are implemented. The coupled scheme solves the momentum and pressure-based continuity equations together. Fully implicit coupling is achieved through an implicit discretisation of pressure gradient terms in the momentum equations, and an implicit discretisation of the face mass flux [138].

3.4.3 Under-relaxation Factors

As mentioned, under-relaxation factors are used to help with convergence issues. After each iteration, at each cell, a new value for a variable, ϕ, in cell, i, is then updated using the following equation

$$\phi_i^{new,used} = \phi_i^{old} + \alpha\left(\phi_i^{new,predicted} - \phi_i^{old}\right) \tag{3.57}$$

where, α in this instance is the relaxation factor. $\alpha < 1$ corresponds to under-relaxation, this may slow down convergence speed, but increases the stability of the calculation by decreasing the possibility of divergence or oscillations in the solutions. $\alpha = 1$ corresponds to no relaxation and $\alpha > 1$ is over-relaxation, which can sometimes be used to accelerate convergence, but decreases the stability of the calculation.

3.5 Boundary Conditions

Fluent offers an extensive range of possible boundary conditions that can be implemented for various scenarios. The boundary conditions presented in the following subsections are the ones used throughout this research.

3.5.1 Inlet

The inlet boundary condition involves specification of the values of the velocity components and turbulence quantities. The inlet boundary condition implemented throughout this research was a velocity inlet as incompressible fluids were used. The boundary turbulence quantities of interest were turbulence intensity T_{I} and the eddy viscosity ratio ($\mu t/\mu$), known in Fluent as the turbulent viscosity ratio (TVR).

3.5.2 Outlet

For the outlet boundary, static pressure was specified. Pressure outlet boundary conditions require the specification of a static (gauge) pressure at the outlet boundary. All other flow quantities are extrapolated from the interior.

3.5.3 Interface

An interface boundary is defined between two zones. It is implemented for problems which include moving reference frames or sliding meshes. This type of boundary condition ensures that the fluxes flow from one side of the interface to the other.

3.5.4 Wall

The wall boundary condition is used to bound fluid and solid regions. For viscous flow, a no-slip condition is enforced at the wall, i.e. the tangential fluid velocity is equal to the wall velocity, and the normal velocity component is set to zero. Alternatively, shear stress can be specified at the wall. Roughness on the wall surface can also be included for turbulent flow.

3.6 Lift and Drag Forces and Moments

Aerodynamic/hydrodynamic forces and moments acting on an aerofoil/hydrofoil are due to pressure variation around the body and shear stress distribution along the aerofoil/hydrofoil surface. The pressure acts perpendicular to the surface while the shear stress acts parallel to the surface. The net effect of the pressure and shear stresses integrated around the aerofoil/hydrofoil is a resultant force and moment acting on that aerofoil/hydrofoil.

3.6.1 Pressure Distribution around Aerofoil/Hydrofoil.

As fluid flows around an aerofoil/hydrofoil, its shape and angle of inclination cause the velocity of the fluid to be different on the top surface compared to the bottom. Due to the conservation of energy (Bernoulli's equation), this results in a pressure difference between the two surfaces and therefore a force imbalance. Integrating the pressure around the aerofoil/hydrofoil multiplied by the foil area gives the resultant aerodynamic/hydrodynamic forces acting on the aerofoil/hydrofoil. This force can be resolved into two components, the lift force (F_L) which acts perpendicular to the fluid flow, and the drag force (F_D) which acts parallel to the fluid flow (See Figure 3.8).

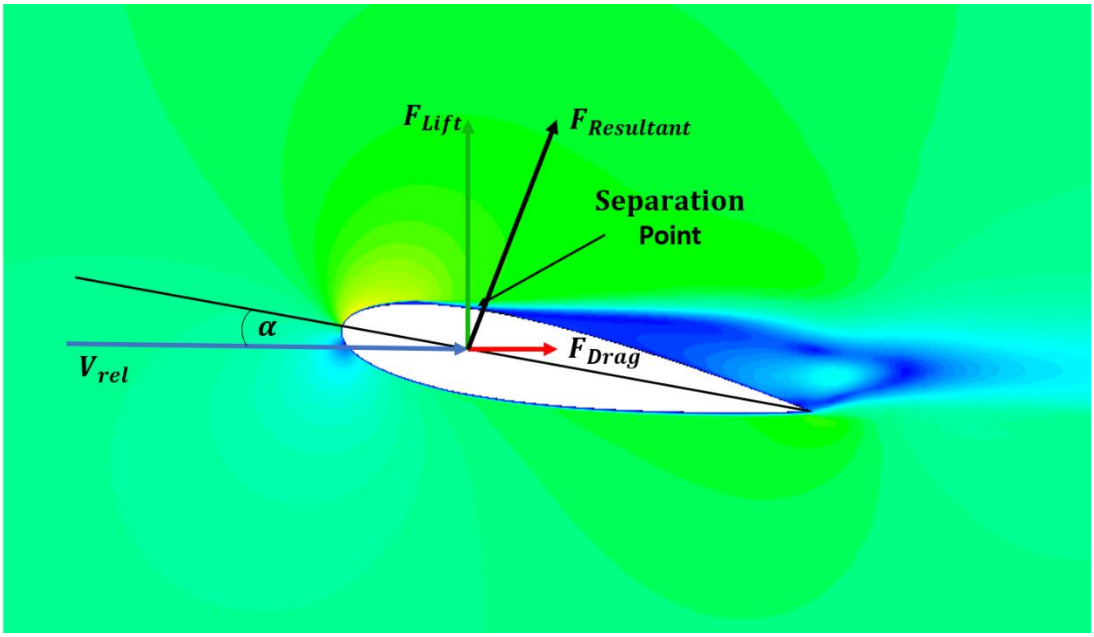

Figure 3.8: Flow around aerofoil/hydrofoil with key components identified.

With the presence of boundary layer effects, it is not straightforward to calculate the pressure distribution for a known velocity distribution. The average location of the pressure variation is known as the centre of pressure, and the force acts through the centre of pressure; however if the angle of attack, varies the pressure variation and subsequently the centre of pressure also differ. If the aerodynamic force is applied at a location $\frac{1}{4}$ chord back from the leading edge, the magnitude of the aerodynamic/hydrodynamic moment remains almost constant with varying angle of attack, this location is known as the aerodynamic centre. For symmetrical foils, the moment about the aerodynamic centre is zero for all angles of attack. For cambered foils, the moment is non-zero but usually constant.

3.6.2 Shear Stress Distribution along an Aerofoil/Hydrofoil Surface.

As fluid flows over a surface, there is a frictional force between the two. This frictional force is equal and opposite on both the solid and the fluid. The surface experiences a drag force in the direction of the fluid flow, parallel to the surface. The fluid experiences a deceleration force which decreases the local flow velocity. The shear stress experienced is directly proportional to the viscosity of the fluid since the viscosity of a fluid is defined as its resistance to deformation by shearing stresses. As was established earlier, the shear force at the wall is:

$$\tau_w = \mu \frac{\partial u}{\partial y} \tag{3.58}$$

The total drag force experienced by a body is the summation of the pressure drag, also known as the form drag, and the drag from the shearing stresses (skin friction drag). The skin friction coefficient as previously defined is:

$$C_f = \frac{\tau_w}{\frac{1}{2}\rho U^2} \tag{3.59}$$

3.6.3 Forces on an Aerofoil/Hydrofoil.

Aerofoils and hydrofoils are designed so that a significant lift force is generated during operation while drag force is minimised. Applications of aerofoils and hydrofoils

include aircraft, wind/tidal turbines, fans, propellers, compressors, etc. Examining a single foil (See Figure 3.8), the flow separates near the leading edge (exact location of separation is dependent on α) and passes along the upper and lower surfaces of the blade. The higher velocities on the upper surface of the foil result in a lower pressure than ambient, while the lower velocities on lower surface result in higher pressure. This difference in pressure contributes to the lift force and part of the drag force experienced by the aerofoil. By integrating the distributions of normal pressure forces and tangential shear stresses normal and parallel to the direction of upstream flow, the lift and drag forces can be calculated as follow:

$$F_L = \int dF_y = \int -(P\ sin\ \theta)dA + \int (\tau_w \sin\theta)dA \tag{3.60}$$

$$F_D = \int dF_x = \int (P\ cos\ \theta)dA + \int (\tau_w \sin\theta)dA \tag{3.61}$$

where A is the projected surface area and θ is, in this instance, the angle of the lift/drag forces relative to the resultant force.

The lift and drag forces and the resulting moment on a foil can be non-dimensionalised into the lift, drag and moment coefficients, C_{L}, C_{D} and C_{M}, respectively, as follows:

$$C_L = \frac{F_L}{\frac{1}{2}\rho {V_{rel}}^2 A} \tag{3.62}$$

$$C_D = \frac{F_D}{\frac{1}{2}\rho {V_{rel}}^2 A} \tag{3.63}$$

$$C_M = \frac{M}{\frac{1}{2}\rho {V_{rel}}^2 cA} \tag{3.64}$$

3.7 CFD Accuracy – Verification and Validation

Credibility in CFD results can be achieved by assessing levels of uncertainty and error in the final results. These levels of error and uncertainty are evaluated through a process of verification and validation of the results. The AIAA guide to CFD error is

an excellent source of information [173].

For the purpose of distinction between the two, 'uncertainty' is defined as: "*A potential deficiency in any phase or activity of the modelling process that is due to the lack of knowledge*." while 'error' is defined as: "*A recognisable deficiency in any phase or activity of modelling and simulation that is not due to lack of knowledge*" [173].

3.7.1 Acknowledged Error

Physical approximation error: This error is defined as the difference between the actual flow and the solution to the conservation equations. This is often related to turbulence model assumptions, e.g. the use of the $k-\varepsilon$ turbulence model for simulations with high flow separation would lead to significant errors due to the model's inability to accurately simulate flow separation.

Computer round-off error: These errors are associated with the representation of floating point numbers by the computer and the precision at which these numbers are stored. The use of double precision numbers can ensure that these errors are minimised.

Discretisation errors: are errors that occur from the representation of the governing flow equations as algebraic expressions in a discrete domain of space (finite-volume) and time. The discrete spatial domain is known as the mesh. The temporal discreteness is manifested through the time-step value taken. These types of errors can be minimised by using refined spatial resolutions and appropriately low time-steps; however, this comes at the expense of increased computational cost.

3.7.2 Unacknowledged Error

Computer programming error: These errors arise due to errors or bugs within the model code being implemented.

User error: These errors are a result of mistakes made by the user when setting up, running and/or analysing the simulation.

3.7.3 Verification.

Verification is defined as *"the process of determining that a model implementation accurately represents the developer's conceptual description of the model and the solution of the model."* [173]). Verification of a CFD simulation involves verification of (1) the code being used and (2) the convergence of the model solution.

3.7.3.1 Programme Code

One of the most basic tasks of verification assessment is the review of the model programme or code to check for, and identify, computer programming errors or "bugs". This is done by visually inspecting the code and by running subprograms using a test code. This is aided by complete and clear documentation, both internal and external. This step is to detect computer programming errors directly.

3.7.3.2 Iterative Convergence

Generally, CFD methods involve some iterative scheme to arrive at the simulation results. Here, it is assumed that the iteration is with respect to time or a pseudo-temporal quantity and some type of time-step is taken at each iteration. A steady-state flow simulation involves starting with a uniform or fabricated flow field and iterating in time until the steady-state flow field is obtained. This is termed iterative convergence but requires some criteria for determining convergence.

Residuals are the error magnitudes for equations as iterations progress. These are usually scaled or normalized. It is common for the residuals to reduce to a certain level and then level-off as an indication of iterative convergence. For a time-marching solution, this involves examining whether the residual has been reduced to a certain number (usually 5 or 6 orders of magnitude). Residuals measure imbalance (or error) in conservation equations i.e. the Navier-Stokes equations, plus turbulence model equations.

The absolute residual imbalance at a point, P, is defined as:

$$R_P = \left| a_P \phi_P - \sum_{nb} a_{nb} \phi_{nb} - S_u \right| \tag{3.65}$$

while the scaled residual at P is:

$$R_{P,scaled} = \frac{|a_P \phi_P - \sum_{nb} a_{nb} \phi_{nb} - S_u|}{|a_P \phi_P|} \tag{3.66}$$

The absolute residual for all cells in the domain is defined as:

$$R_\phi = \sum_{all\ cells} \left| a_P \phi_P - \sum_{nb} a_{nb} \phi_{nb} - S_u \right| \tag{3.67}$$

while the scaled residuals for all cells in the domain is defined as:

$$R_{\phi,scaled} = \frac{\sum_{all\ cells} |a_P \phi_P - \sum_{nb} a_{nb} \phi_{nb} - S_u|}{\sum_{all\ cells} |a_P \phi_P|} \tag{3.68}$$

where, a_P is the center coefficient, a_{nb} are the influence coefficients for the neighbouring cells, and S_u is the contribution of the constant part of the source term.

3.7.3.3 Spatial and Temporal Convergence

The most critical activity in verification testing is systematically refining the grid size and time-step. As the grid and time-step are refined (i.e. grid cell size is reduced and the number of cells in the domain therefore increases, and time-step size is reduced), the spatial and temporal discretization errors, respectively, should asymptotically approach zero, excluding computer round-off error. When the asymptotic behaviour has been demonstrated, a convergence study is undertaken to check for convergence. If convergence is achieved, then the numerical scheme is said to be both grid and time-step independent.

When the asymptotic behaviour has been demonstrated, Richardson extrapolation is used to calculate the exact solution of a model variable based on the convergence and refinement ratio determined using a series of increasingly refined meshes [150]. Before applying the Richardson extrapolation, it is necessary to determine the apparent convergence condition based on the R^*, defined as:

$$R^* = \frac{\phi_{\text{grid 2}} - \phi_{\text{grid1}}}{\phi_{\text{grid 3}} - \phi_{\text{grid 2}}} \tag{3.69}$$

where ϕ is the model variable for which convergence is being investigated. R^* values are classified as follows:

$R^*>1$	Monotonic divergence
$1 > R^* > 0$	Monotonic convergence
$0 > R^* > -1$	Oscillatory Convergence
$R^* < -1$	Oscillatory divergence

Richardson extrapolation may only be used when the apparent convergence condition is monotonic. A constant mesh refinement ratio, *r*, is defined as:

$$r = \left(\frac{N_{\text{fine}}}{N_{\text{coarse}}}\right)^{\frac{1}{2}} \tag{3.70}$$

where, N_{fine} is the number of elements in the fine mesh and N_{coarse} is the number of elements in the coarse mesh. The order of convergence, *p*, is defined as:

$$p = \frac{\ln\left(\frac{\phi_{\text{grid 2}} - \phi_{\text{grid 1}}}{\phi_{\text{grid 3}} - \phi_{\text{grid 2}}}\right)}{\ln(r)} \tag{3.71}$$

Richardson's extrapolation value is calculated as follows:

$$\phi = \phi_{\text{grid 1}} + \frac{\phi_{\text{grid 1}} - \phi_{\text{grid 2}}}{r^p - 1} + HOT \tag{3.72}$$

where HOT is for any higher order terms.

3.7.4 Validation.

Validation is defined as “the process of determining the degree to which a model is an accurate representation of the real world from the perspective of the intended uses of the model.” [173]). Experimental data is the observation of the "real world" in some controlled manner. By comparing CFD results to experimental data, one can ascertain whether the model is able to represent the "real world" to a satisfactory degree of accuracy. However, it should be borne in mind that the experimental data usually contains some level of error. This is usually related to the complexity of the experiment. Validation assessment calls for a "building block" approach of experiments which sets a hierarchy of experiment complexity.

3.8 Bibliographic Note

The most general theory discussed in this chapter is not specifically referenced and comes from a number of sources. The basic fluid dynamics theory section is informed by White [27] and also, Versteeg and Malalasekera [174]. For the fundamental theory of turbulence, Versteeg and Malalasekera [174] and Wilcox [169] were referenced. The derivations of both SST turbulence models were taken from the model developers own research as cited in the relevant sub-sections, while derivations of the $k-\varepsilon$ and $k-\omega$ models were taken from the Fluent manual. The sections on CFD discretisation, solution theory and boundary conditions also drew from Versteeg and Malalasekera [174] and Wilcox [169]. The section on CFD error was informed by the guide for verification and validation guide [173]. All theory for the Fluent solver comes from the ANSYS Fluent 17.1 theory guide [138].

Chapter 4. Experimental Testing of the GKinetic Turbine

The 1:40 and 1:20 scale laboratory testing and associated numerical modelling presented in this chapter has been published in the peer-reviewed journal "Proceedings of the Institution of Mechanical Engineers, Part A: Journal of Power and Energy" as:

Mannion, B., McCormack, V., Kennedy, C., Leen, S. B., and Nash, S., 2018, "An Experimental Study of a Flow-Accelerating Hydrokinetic Device," Proceedings of the Institution of Mechanical Engineers, Part A: Journal of Power and Energy; doi: 10.1177/0957650918772626

4.1 Introduction

This chapter presents details of the experimental testing of the GKinetic turbine at various scales. 1:40 and 1:20 scale devices (Figure 4.1 (a and b)) were first tested under controlled conditions in a recirculating flume. A 1:10 scale device (Figure 4.1 (c)) was subsequently tow-tested under somewhat controlled conditions in the field. Some initial CFD modelling was also conducted to verify the flow acceleration around the bluff body of the device. The primary objective of the tests was the characterisation of device performance, particularly in relation to determining mechanical power efficiencies and optimum tip speed ratios. The latter of these is important as the operation of the GKinetic turbine involves control of the turbine rotation speed to match the optimum λ value for the ambient free-stream flow speeds. An additional objective was to determine drag loads on the device.

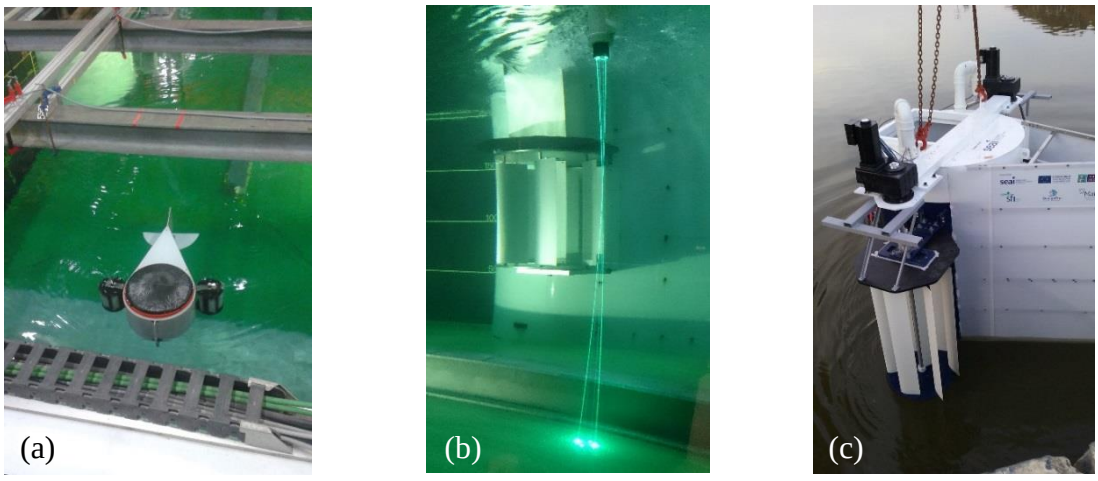

Figure 4.1: Scale devices tested: (a) 1:40 in IFREMER (b) 1:20 in IFREMER (c) 1:10 in Limerick Dock.

Section 4.2 below describes the methodology and instrumentation used for the scale tests. An indirect method of mechanical power measurement was developed and implemented; this is also described. Section 4.3 describes the CFD modelling methodology. Results from the experimental tests are presented in Section 4.4 and numerical model results are presented in Section 4.5. Section 4.6 discusses the results of the testing and modelling.

While the author and by extension, NUI Galway informed device design and experimental methodologies, final decisions on these rested with the turbine developer, GKinetic. These decisions were often driven by budget constraints, for example, the availability of off the shelf 0.2 m chord-length NACA 0018 profile blades largely dictated the dimensions of the rest of the design.

4.2 Experimental Testing Methodology

During the period of this research project, testing of the GKinetic device progressed from a 1:40 scale device, (bluff body diameter of 0.4 m and turbine diameter 0.15 m) to a 1:20 scale device (bluff body diameter of 1.64 m and turbine diameter 0.6 m) and lastly to a 1:10 scale device with the same turbine and bluff body diameters, but had turbine blades twice the length of its predecessor. The scaling is based on the device entrance area.

The 1:40 and 1:20 scale devices were tested at the IFREMER wave-current recirculating flume in Boulogne-Sur-Mer, France. The flume is 18 m long, 4 m wide and 2 m deep (see Figure 4.2) and is capable of producing flow speeds in the range of 0.1 to 2.2 m/s. The 1:10 scale device was tow-tested in Limerick Dock, Co. Limerick, Ireland. Flow acceleration by the bluff body was studied using the 1:20 scale device. (The concept of the flow accelerating bluff body was initially investigated at 1:40 scale in the NUI Galway tidal basin [20]). Device performance was determined for both the 1:20 scale tank tests and the 1:10 scale tow tests. Table 4.1 summarises the tests that were conducted during the research, giving the free-stream velocity ranges tested and the measured performance parameters. CFD modelling of the 1:20 scale bluff body was conducted to investigate discrepancies between the flow acceleration

measurements from the 1:20 scale tests and the 1:40 scale tidal basin tests [20].

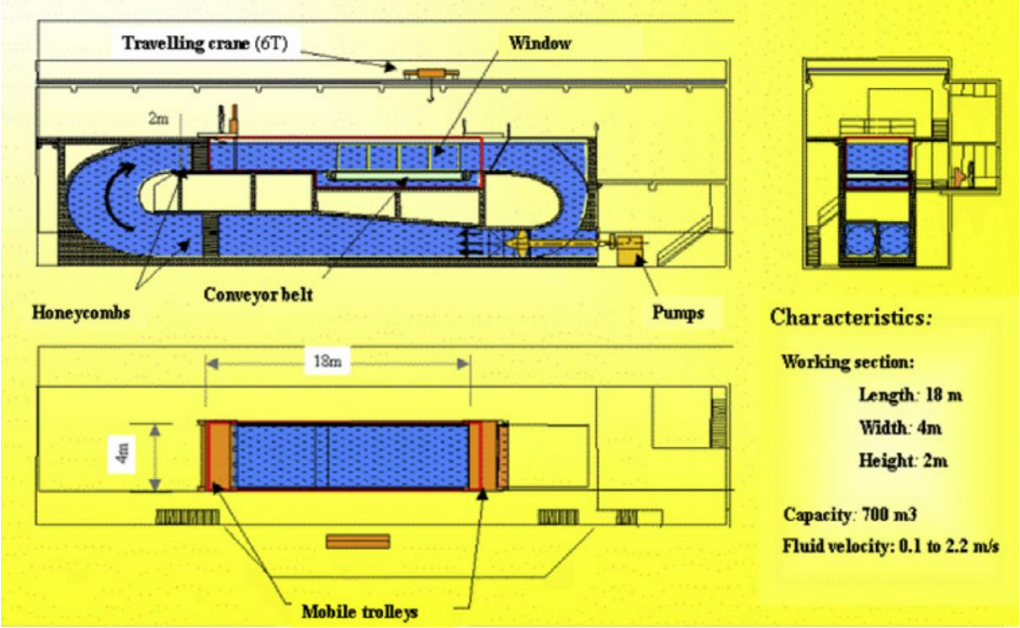

Figure 4.2: IFREMER Wave-Current Basin (source: [175])

Table 4.1: Variables measured for each scale device.

Measured Variables	**Free-stream Flow Speeds (m/s)**		
	1:40 scale	1:20 scale	1:10 scale
Flows around bluff body	0.3	0.8 and 1	-
Flows around device	0.8	0.8	0.5 to 2
Mechanical power	-	0.4 to 1.2	0.5 to 2
Drag loads	0.8 and 1	0.4 to 1.2	0.5 to 2

Table 4.2 compares the Reynolds number values for the 1:10, 1:20 and 1:40 scale tests at a free-stream flow speed of 0.8 m/s. The length scale used is the diameter of the bluff body. The Reynolds numbers determined are in the critical lower transition phase of the flow regime, allowing direct comparison of the results. This comparison of Reynolds number values is based on previous work on flow around cylinders [176]. Since the bluff body is essentially a cylinder with a splitter attached, this comparison is deemed acceptable.

Table 4.2: Reynolds numbers of 1:10, 1:20 and 1:40 scale devices.

Scale	Re
1:10, 1:20	1.3×10^6
1:40	0.398×10^6

4.2.1 Testing at 1:40 Scale at IFREMER

A 1:40 scale device (Figure 4.3) of the full GKinetic device (i.e. including the bluff body and both turbines) was tested in the IFREMER recirculating flume. Although the turbines were able to rotate, the scale of the device meant that the pitch control scheme could not be implemented; the blades were instead able to rotate freely about their pivot supports at the ends. The scaled device was moored using retention points on the floor of the flume and ballast was added to the hollow bluff body until the device was brought to mid-depth. Additional ballast was added at the higher flow speeds to improve stability.

The aims of these experiments were to observe the stability of the device when fully submerged, determine the drag force on the device and assess the flow around the device. A single channel load cell was attached to the device for measurement of the drag load. An LDV (Laser Doppler Velocimeter) was used to characterise the flow field around the device at a free-stream flow speed of 0.8 m/s. LDVs use lasers to track the movement of micro-particles mixed in the water (50 μm glass balls coated in silver were used). Mechanical power performance results were not determined, as the blade pitching control system was not implemented.

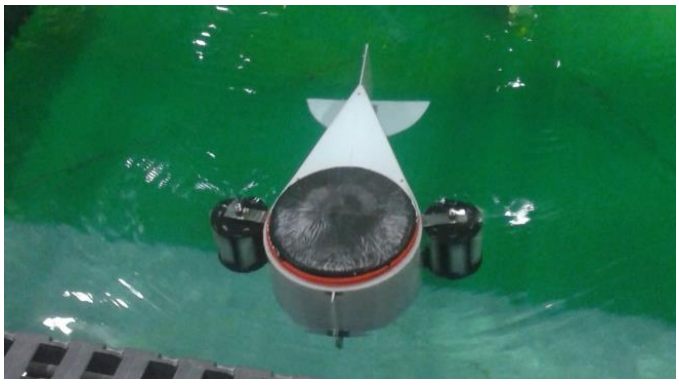

Figure 4.3: 1:40 scale device tested at IFREMER.

4.2.2 Testing at 1:20 Scale at IFREMER

Due to dimensional constraints of the IFREMER flume tank, it was only possible to test half of the complete device at 1:20 scale. This comprised of a half-bluff body and a single turbine. Given that the device is symmetrical, this was deemed an acceptable approach. A dimensioned plan view of the 1:20 scale device tested is shown in Figure 4.4 (a), while an end elevation is presented in Figure 4.4 (b). The benefits of using a flow deflector flap (shown in Figure 4.4 (a)) to direct the inlet flow onto the turbine blades was also examined.

The 1:20 scale device included the blade pitching mechanism designed to enhance performance; this involves a cam track system that orients blade pitch throughout the revolution cycle. Figure 4.5 presents a graphical illustration of the pitching of each of the six blades at an instance in time. In this orientation, the turbine rotates anticlockwise. It can be seen that the blade pitch changes as the blades turn along the upstream (front) end of the turbine; this is due to the gradients in velocity magnitude and direction as one moves outwards from the bluff body. There is also a noticeable difference in the pitch of the blades on the downstream side of the turbine compared to their upstream pitch positions. Between position 3 and position 4, the blade undergoes a pitch transition of about 70^{o} where the angle of attack changes from positive to negative. This location was chosen for this large transition (or flip) to minimise the turbulence generated in doing so. The reason for the flip is because the blades were found to contribute more power from drag rather than lift when turning through the downstream portion of the cycle.

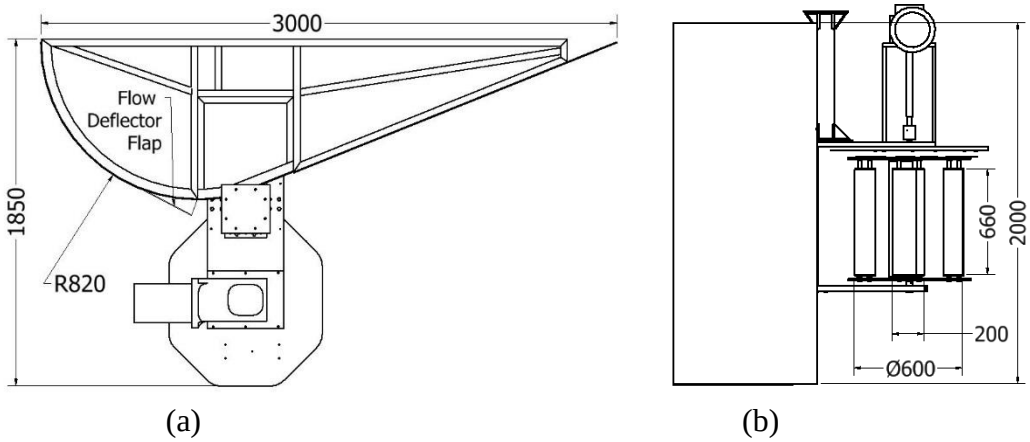

Figure 4.4: 1:20 scale device with outlining dimensions (mm); (a) plan view (b) end elevation.

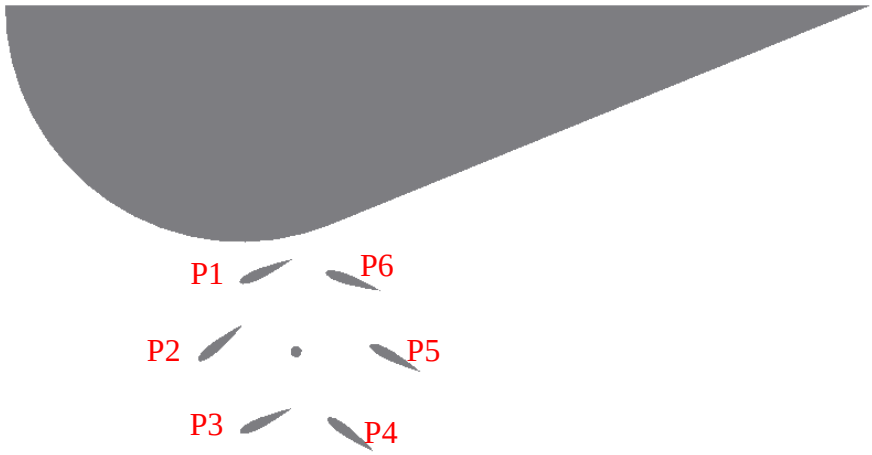

Figure 4.5: Schematic of turbine blade pitching relative to the bluff body.

Flow-fields were measured at a free-stream velocity of 0.8 m/s using the LDV, first around the bluff body alone, and subsequently with the turbine in position (Figure 4.6). The data for the bluff body alone was collected in order to determine the levels of flow acceleration achieved, and make comparisons with the previous tidal tank measurements.

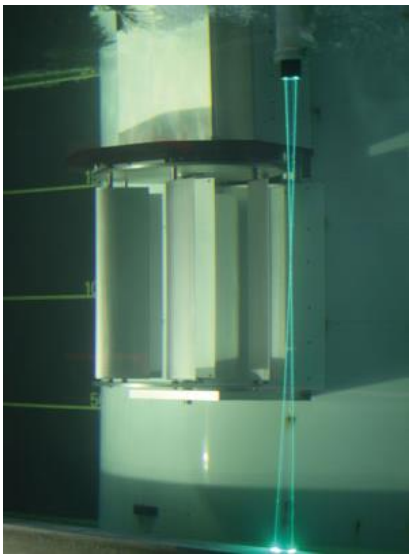

Figure 4.6: LDV characterising the bluff body flow for the tests at IFREMER.

To determine the mechanical power being produced, a torque meter was developed consisting of four strain gauges configured in a full Wheatstone bridge (Figure 4.7 (a)) and attached to the primary shaft of the turbine (Figure 4.7 (b)). The torque meter was

connected to a Versalog BR model logger which recorded data at a frequency of 50 Hz. To convert strain to torque, the torque meter was calibrated. This involved restraining movement of the shaft in all directions at one end while applying a known torque via an incrementally increasing lever at the opposite end. Strain and torque data were graphed and a linear regression line was used to determine the relationship of strain to torque. Figure 4.8 shows the plotted data points, which exhibited a perfectly linear relationship and gave a strain-to-torque conversion factor of 0.596 Nm, in this instance.

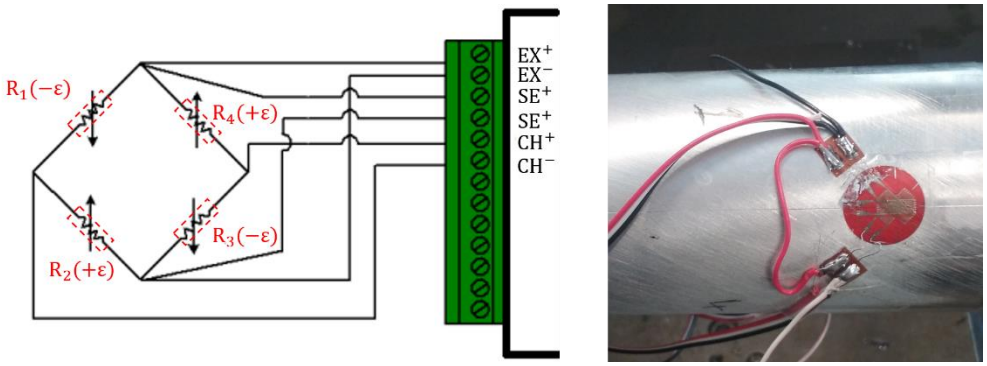

Figure 4.7: (a) Schematic showing full Wheatstone bridge wiring and (b) image of strain gauges affixed to the shaft.

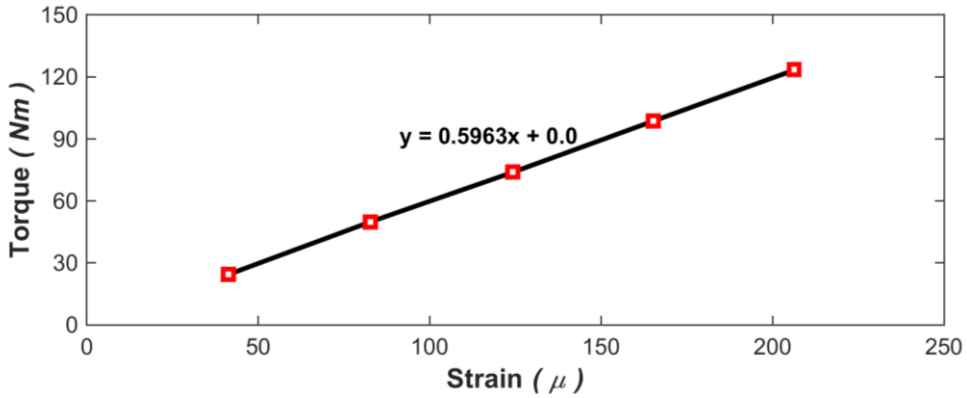

Figure 4.8: Torque meter calibration for strain to torque conversion.

As a check on the strain-torque relationship, torque was calculated from the strain gauge data using classical theory where the relationship of torque and strain is expressed as:

$$Q = \frac{\varepsilon\, E\, J}{(1+\nu)d} \tag{4.1}$$

where ε is the strain in this instance, E is the Young's modulus, ν is Poisson's ratio and J is the second polar moment of area, which is defined for a cylindrical shaft as:

$$J = \frac{\pi d^4}{32} \tag{4.2}$$

where d is the shaft diameter. Table 4.3 shows the torque values calculated (Q_{calc}) from classical theory using the recorded strain are very similar to the torques applied (Q_{act}) to induce the strain (Figure 4.8), thus confirming that the developed method for measuring torque was valid.

Table 4.3: Material properties for aluminium turbine shaft and comparison of torque calculated from recorded strains with corresponding torque applied to the shaft.

$\boldsymbol{\varepsilon}$ $(\boldsymbol{\mu})$	$\boldsymbol{E}$	$\boldsymbol{\nu}$	$\boldsymbol{d}$ $(\boldsymbol{m})$	$\boldsymbol{J}$ $(\boldsymbol{m^4})$	$\boldsymbol{Q_{act}}$ $(\boldsymbol{Nm})$	$\boldsymbol{Q_{calc}}$ $(\boldsymbol{Nm})$
$40.15\,x10^{-6}$	$69\,x10^{9}$	0.33	0.05	$6.14\,x10^{-7}$	25	25.57
$81.68\,x10^{-6}$	$69\,x10^{9}$	0.33	0.05	$6.14\,x10^{-7}$	50	51.4
$119.26\,x10^{-6}$	$69\,x10^{9}$	0.33	0.05	$6.14\,x10^{-7}$	75	75.8
$158.37\,x10^{-6}$	$69\,x10^{9}$	0.33	0.05	$6.14\,x10^{-7}$	100	100.9
$202.53\,x10^{-6}$	$69\,x10^{9}$	0.33	0.05	$6.14\,x10^{-7}$	125	128.6

During the 1:20 scale testing of the turbine, an Invertek variable speed drive was used to control the rotational speed of the turbine. This drive also logged the RPM value which was validated by a tachometer. A speed-increasing gearbox of ratio 73:1 was used. Induction motors have an inherent slippage flaw in their design, the magnitude of which is a function of the air gap between the windings and the stator. This slippage causes a discrepancy between the full load speed and synchronous speed. However, the Invertek variable speed drive has a function known as "slip compensation" that allows the user to input the slippage value of the specific motor and the drive compensates for this slippage. This allowed the pre-set speed of the motor/generator to be more accurately controlled.

To determine the forces acting on the turbine, a load cell with six channels (three for (x, y, z) forces and three for moments) was used. The evaluation of these loads was important, as they can be used to inform the design of the connections between the turbines and the bluff body. The load cell was fixed between an arm on the turbine and a hexapod used to support it from overhead (Figure 4.9) allowing drag loadings on the turbine to be determined. The load-cell was set up for a sampling rate of 100 Hz.

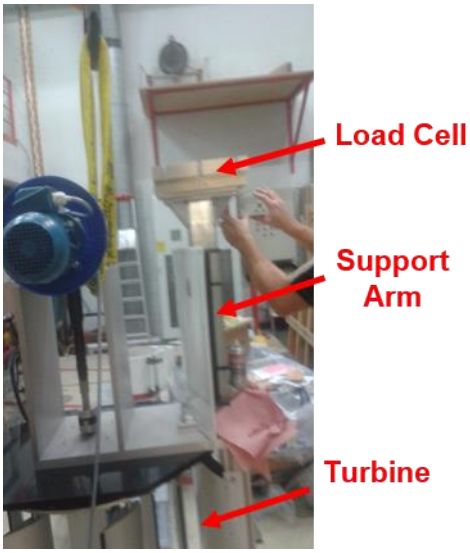

Figure 4.9: Image showing the location of load cell relative to the turbine and support arm.

4.2.3 Testing at 1:10 Scale at Limerick Dock

The 1:10 scale device tow tested in Limerick Dock was a complete device with a full bluff body and a turbine on either side. It retained most of the design features of the 1:20 scale device including a similar turbine and bluff body diameters to allow comparison with the 1:20 scale results. As the devices were scaled by the entrance area, the turbine blades of the 1:10 scale device were approximately twice the length of those on the 1:20 scale device. The device also included the flow deflection flaps assessed during the 1:20 scale tank tests. During testing, the device was ballasted so that the top plates of the turbines were below the water line. Figure 4.10 presents the primary dimensions of the 1:10 device. The device had an onboard PLC control system that could control both turbines remotely and independently of each other. The tests involved towing the device through Limerick Dock which is owned by the Shannon-Foynes Port Company. The device was towed using a bespoke winch designed and manufactured by WindWorks, Dublin, Ireland. The winch was located on the south-

west corner of the dock, and the towpath was approximately 400 m in length. A plan view of the dock is shown in Figure 4.11, showing the location of the winch and the towpath. It should be noted that data collected during start-up and slow-down portions of the tow (outside marker 1 in Figure 4.11) were omitted from the analysis, meaning only data from the steady-state portion of the tow were used in the performance analysis of the turbine. Photos of the winch and the device undertow are shown in Figure 4.12. The dock is connected to the Shannon estuary by dock gates. When the gates are closed, the dock is, therefore, a quiescent waterbody similar to a tow tank. The water depth in the dock varied between 4 to 7.5 m across the testing period, however, the average water depth during tests was between 5 to 6 m. The winch was capable of towing the turbine at a range of speeds up to 2.5 m/s. For each test, the device was towed at a constant speed and the speed of the winch recorded, via its PLC system.

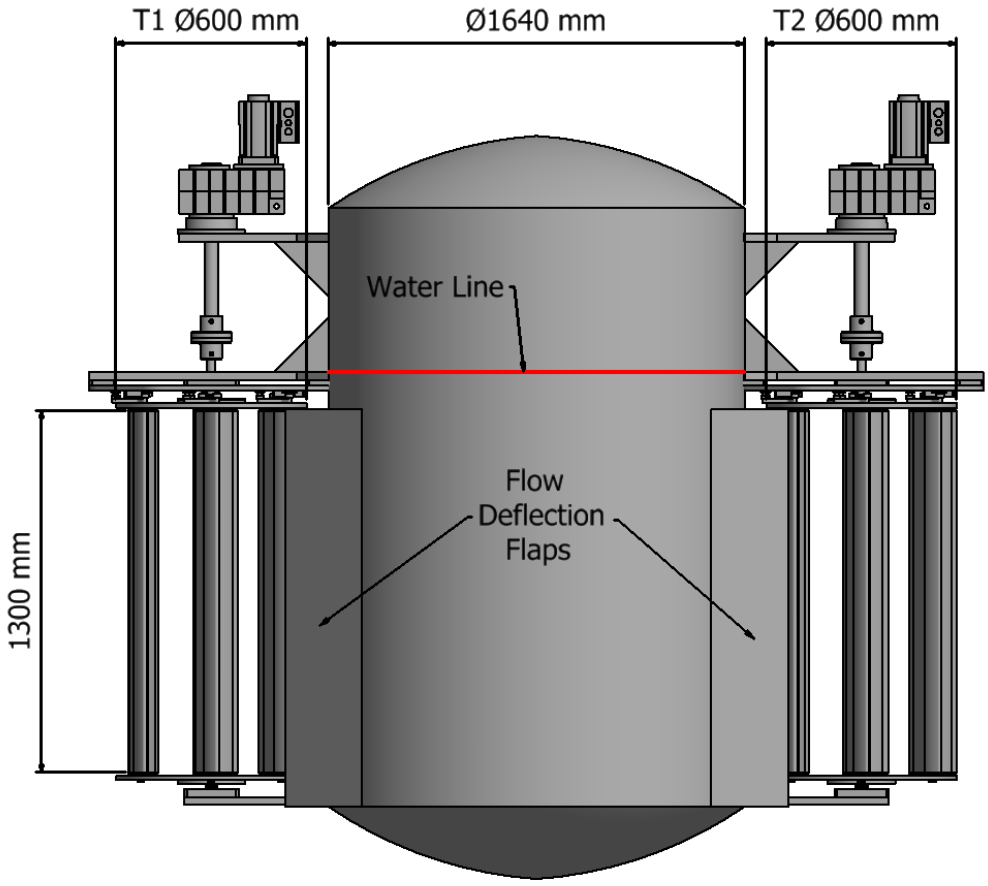

Figure 4.10: Dimensioned schematic 1:10 scale device tow tested in Limerick.

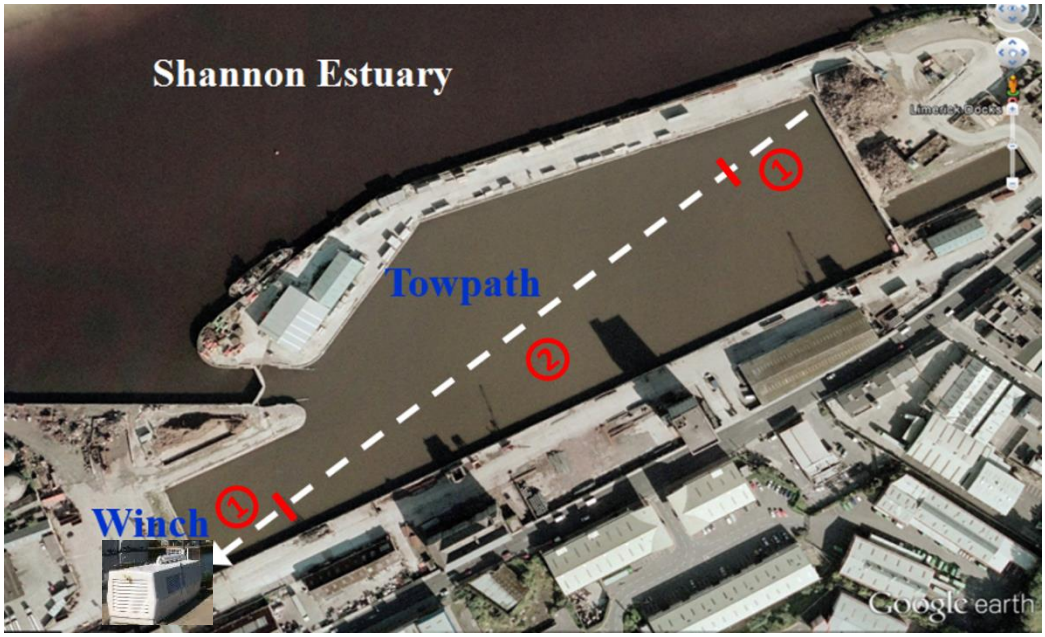

Figure 4.11: Plan view of Limerick Dock showing towpath.

(a) (b)

Figure 4.12: (a) Windworks winch and (b) 1:10 scale device undertow in Limerick Dock.

Two acoustic Doppler current profilers (ADCPs) were mounted on the device (see Figure 4.13 (a)), one at the front of the bluff body looking forward and thus capturing the device inflow, and the other looking through the flow deflection flap at the entrance to one of the turbines, capturing the turbine inflow. Aquadopp Profilers were the type of ADCP used. Initially, the forward-facing ADCP was installed at mid-depth but was reinstalled near the bottom of the bluff body to avoid surface penetration of the acoustic beams. The turbine ADCP was installed at the mid-depth of the turbine to avoid capturing surface and bottom effects of the turbine on the flow.

As shown in Figure 4.13 (b), ADCPs measure current speeds using three narrow acoustic beams (note the instrument in Figure 4.13 (b) is an upward-looking unit whereas the instruments used for the GKinetic tests Figure 4.13 (a) were sideward-looking units). Each acoustic beam measures velocities, parallel to the beam, away from or towards the instrument head (Figure 4.13 (b)). A transformation matrix can be used to compute the corresponding x, y, z velocities. The ADCPs measure current velocities within set spatial intervals (or bins) along each beam, as shown in Figure 4.13 (b), to give measurements at various distances from the head of the instrument.

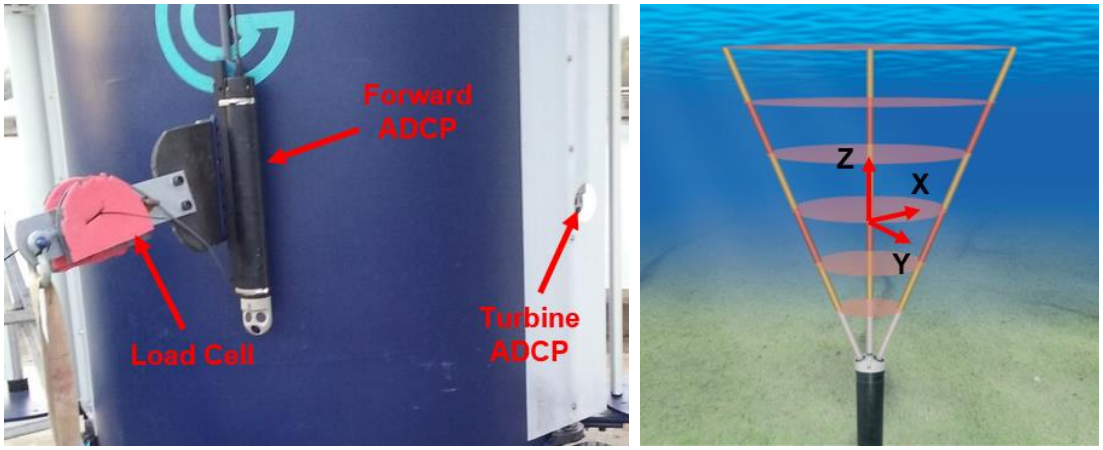

(a) (b)

Figure 4.13: (a) Photo showing front of the device with locations of ADCPs and load cell and (b) graphic showing acoustic beams and cells of upward-facing ADCP (adapted from Nortek user manual [177]).

In addition to current velocity data, the ADCPs have an internal compass that measures the heading (or bearing) and tilt of the instrument. As the ADCPs were secured to the GKinetic device, these data also describe the bearing and tilt of the device itself. ADCP velocity measurements vary in quality depending on the signal strength, with stronger signals resulting in better quality data. Each beam cell reading has an associated quality value, known as the count. Any measurement with a count of less than 25 should be removed from any subsequent analyses.

ADCP velocity measurements will also contain a certain level of noise (fluctuations) resulting from instrument error. Random Doppler-shift measurement errors, which collectively form Doppler noise, are errors in a single part of a profile in a single beam.

These errors are analogous to the uncertainties associated with any scientific measurement, but the magnitude of this uncertainty can be large compared to the velocity being measured. Statistical filters are typically used to remove noise from raw ADCP data but it is essential that the filters also preserve natural fluctuations in the current velocity, arising from turbulence for example. Quality assessment and coordinate transformation of the ADCP data was conducted by Dr Marcel Cure of Numeric Warehouse.

One of the primary objectives of the 1:10 scale testing was to calculate accurately the power the device was generating at a range of flow speeds. This was achieved using two methods:

1) By recording readings from the onboard power take-off system and

2) By instrumenting the turbine shaft in the same way as the 1:20 scale testing.

Method 1 involved using the reported values of percentage torque and RPM from the Lenze drive control system via the onboard Beckhoff PLC. These values were then converted to actual torque on the central shaft and subsequently power. Method 2, the strain gauge method, was used as a backup method as the Lenze power take-off system had not been calibrated nor validated prior to testing and Lenze had no experience of their technology being used for marine renewable energy applications.

A 50 kN, single channel, compression load cell was used to measure the drag force on the device. The load cell was attached between the bluff body and the tow line to ensure that the load cell was experiencing the entire load that the device was subject to. A pre- and post-testing calibration was carried out on the load cell to check for accuracy.

4.3 Numerical Modelling

A CFD model of the bluff body was developed in an effort to reproduce the flow accelerations measured in the 1:20 scale flume tests and the previous 1:40 scale tidal basin experiments. Ansys Workbench version 17.1 and Fluent were used to develop

the model. An unstructured tri-element mesh was employed, with quad-element inflation layers used at the walls to accurately resolve the boundary layer. Model development studies showed that the Transitional SST was the RANS turbulence model gave the most accurate results of flow around an aerofoil. A first layer element height corresponding to a max y^+ value of 1 was used in conjunction with the Transitional SST turbulence model. A total of 35 quad element layers was used, with a growth rate of 1.1. An image of the mesh, which resulted in a mesh independent solution after a convergence study, is shown in Figure 4.14. The entire mesh consisted of 398,000 elements in total with the highest concentration of elements around the bluff body. The mesh had a maximum skewness of 0.81.

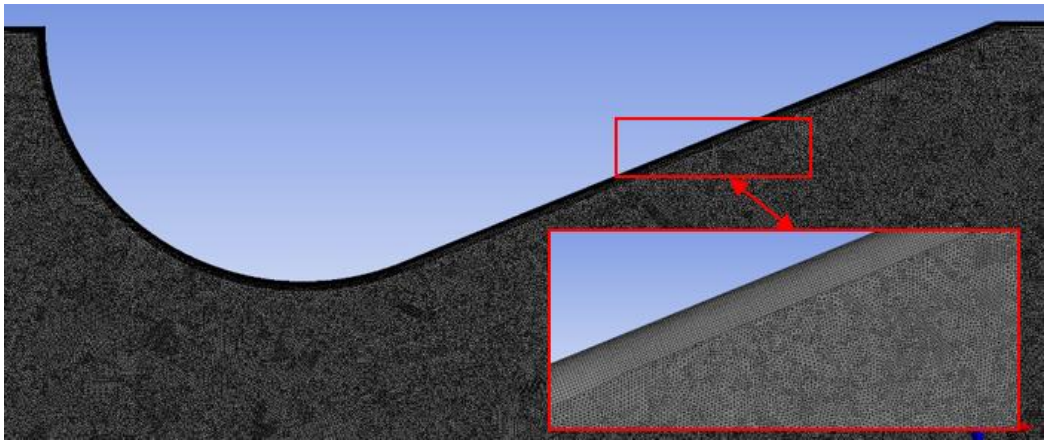

Figure 4.14: Mesh around bluff body with inset images showing the mesh close to the bluff body

To reproduce the 1:20 scale flume results, *no-slip* conditions were applied to the tank walls and to the bluff body surface. The tank walls required appropriate wall roughness conditions. In the absence of measured roughness values for the concrete walls of the IFREMER flume, a trial and error approach was used within a realistic value range for concrete (0.5 mm to 3 mm). The final value used in the model was 1.5 mm. The results from this model were compared to the flow speed measurements from the 1:20 scale tests of the bluff body.

To compare modelled bluff body accelerations to the previous 1:40 scale tidal basin tests of a full bluff body, the wall boundary conditions were modified to remove the wall friction, and symmetry boundary conditions were applied to the walls

representing the tank. The results from both models were used to investigate discrepancies between the two sets of measured accelerations.

4.4 Experimental Results

The following section presents results from testing at three different scales of the GKinetic device.

4.4.1 Experimental Results for 1:40 Scale Device at IFREMER

LDV results for the flow characterisation around the 1:40 scale device are presented in Figure 4.15 for a free-stream flow speed of 0.8 m/s. The turbines in this model did not include blade pitch control but they were able to pitch freely. This means that while the measured flows are not fully representative of the likely flows around a device incorporating pitch control, they should not be too dissimilar and can, therefore, allow a qualitative assessment of the likely flow regime. The flow can be seen to pass through the turbines and the reduced velocities in the turbine wakes are evidence that the turbines are extracting energy from the flow. As the flow at the entrance of the turbine is approximately at or above the free-stream flow speed, it can be deduced that the entrance velocity into the turbines is being accelerated, when axial induction is accounted for. However, the lack of a blade control regime seems to increase the rotor solidity, causing the peak velocities to be de diverted around the turbine rather than through it.

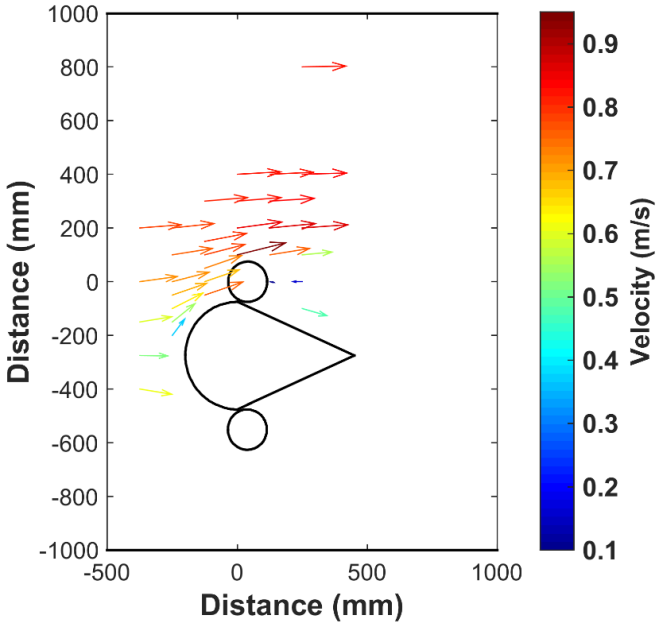

Figure 4.15: Vector plot of LDV data of 1:40 scale tests at IFREMER.

The load cell on the 1:40 scale device measured the hydrodynamic force exerted on the full device (i.e. the full bluff body and two turbines). The axial force component was taken as the drag force. Drag forces were averaged at ten-second intervals and are plotted in Figure 4.16 for free-stream velocities of 0.8 and 1 m/s. Table 4.4 presents the average drag force calculated for each set of data from Figure 4.16. The drag force was averaged over the length of the time period and the drag coefficient was calculated using the previously defined drag coefficient equation in Chapter 3. The averaged device drag coefficient was determined to be 0.68.

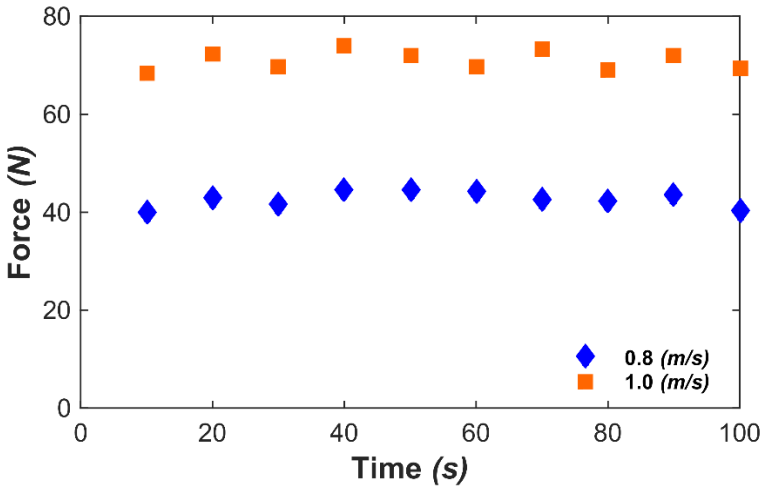

Figure 4.16: Effect of flume velocity on measured drag force time histories for 1:40 scale device from IFREMER tests.

Table 4.4: Drag loads and drag coefficients of the 1:40 scale device.

Flow Speed (m/s)	Drag Force, F_D, (N)	C_D
0.8	42.94	0.66
1	70.95	0.70

4.4.2 Experimental Results for 1:20 Scale Device at IFREMER

Flow measurements for the 1:20 scale device were obtained for the bluff body on its own in order to investigate the induced flow accelerations. The results for a free-stream velocity of 0.8 m/s are presented in Figure 4.17 in the form of a vector plot. It is clear from the figure that flow is indeed accelerated above free-stream levels by the

presence of the bluff body. In the plot, the base of the arrows are the location points of measurement. The highest increases can be seen to occur at the widest point of the bluff body; this agreed with the finding of the 1:40 scale tidal basin tests.

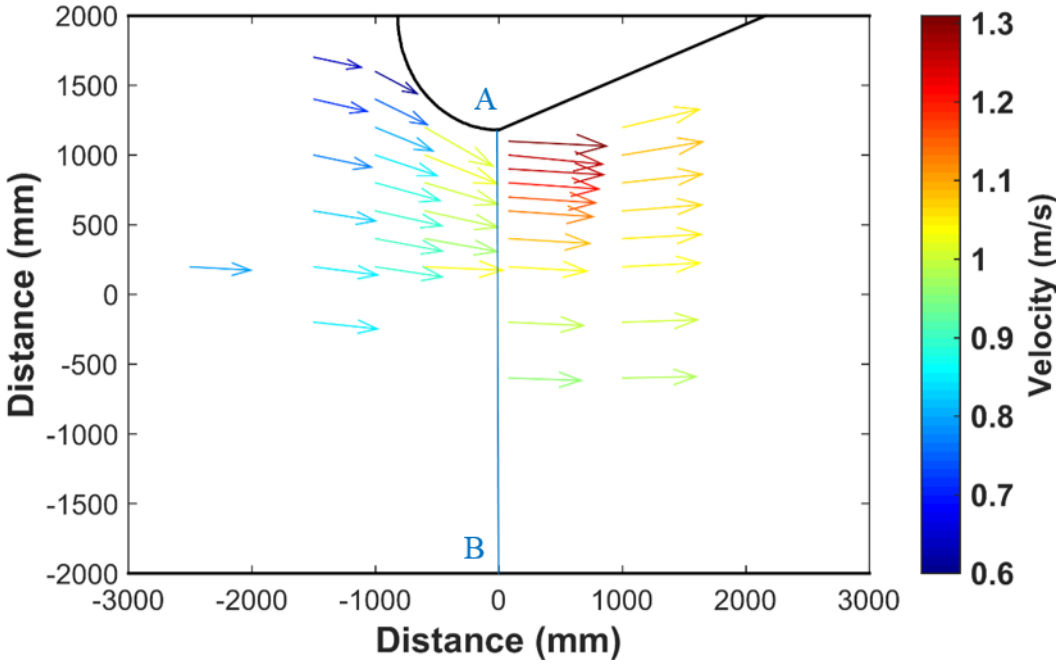

Figure 4.17: Vector plot from LDV data without turbine for 1:20 scale IFREMER test showing flow acceleration due to the bluff body.

Figure 4.18 shows a comparison of measured velocities (normalised against the free-stream velocity) from the IFREMER flume experiments for the 1:20 scale device with those of the 1:40 scale tidal basin tests. The normalised velocities indicate levels of acceleration (> 1) or deceleration (< 1) of the flow. The results are plotted for the line AB shown in Figure 4.17 with distance, x, from the side of the bluff body normalised with respect to bluff body diameter, D_b. Clearly, the 1:40 scale device shows significantly higher levels of acceleration closer to the bluff body. The maximum normalised velocity of 2 represents a flow acceleration of 100 % in the tidal basin tests compared with a maximum normalised velocity of 1.6, and thus a maximum acceleration of just 60 %, in the 1:20 scale experiments. The lower levels of acceleration in the flume tank are considered to be due to the presence of the frictional boundary layer along the wall of the tank upstream of the bluff body. This hypothesis was investigated using the CFD model of the bluff body.

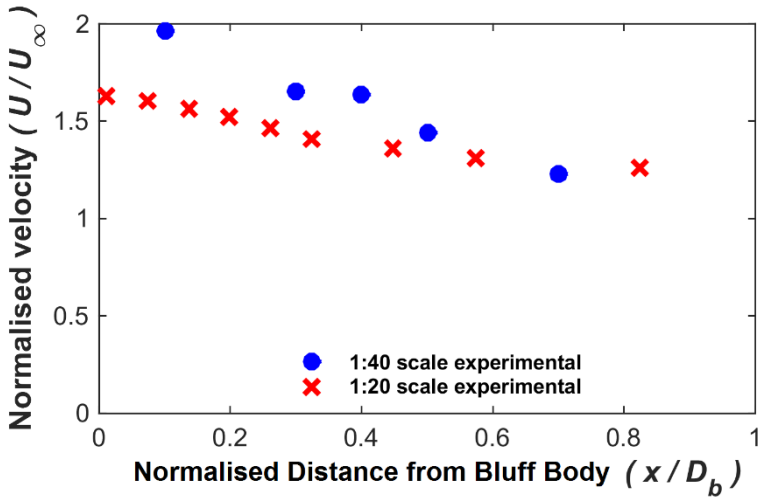

Figure 4.18: Comparison of measure flow acceleration versus distance from the bluff body for 1:20 IFREMER test and 1:40 tidal basin results [20].

To position and support the turbine a hexapod was used, which was attached to an overhead gantry crane. Movement of the LDV required an additional gantry crane; this restricted flow measurement with the turbine in place to two transects downstream of the turbine. The resulting LDV data is shown in Figure 4.19 for a free-stream velocity of 0.8 m/s. This clearly shows the presence of a wake downstream of the device with significantly reduced velocities and flow reversal due to the formation of turbulent eddies. These flow data were later used for the validation of the CFD model in Chapter 7.

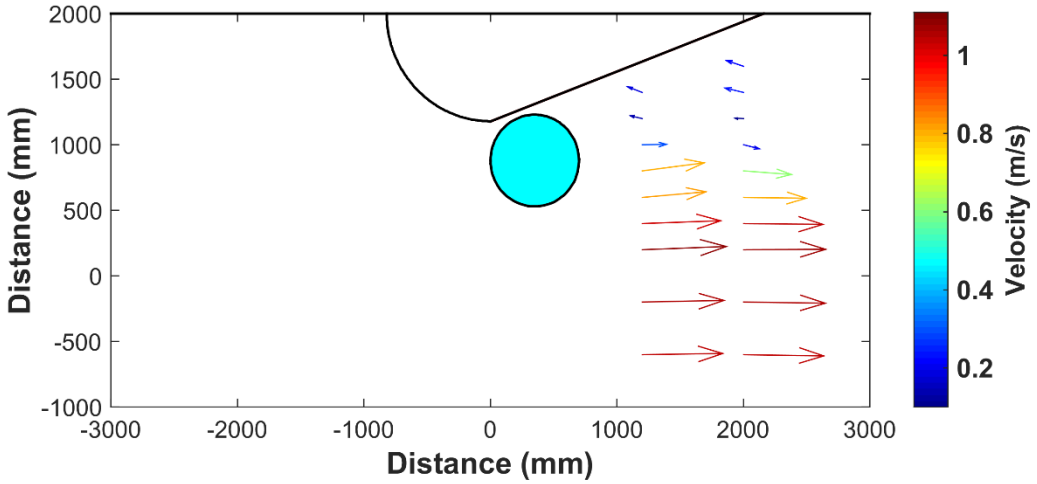

Figure 4.19: Vector plot of LDV data from 1:20 scale IFREMER flume tank tests with the turbine in position.

Following best practice from tidal device testing protocols/standards (as discussed in Chapter 2) the mechanical power is presented as C_P. A key aim of the 1:20 scale tank tests was to determine optimal turbine rotation speed for different free-stream flows. For each free-stream flow condition, a series of tests was conducted at different turbine rotational speeds; 144 tests in total were conducted. Each test was run for sufficient time (approximately 5 minutes) to ensure steady state conditions. Figure 4.20 shows the C_P power curves for the tests. A peak C_P >30 % was achieved for all free-stream flow speeds above 0.6 m/s. Reynolds independence can also be observed for flow speeds above 0.6 m/s. As there are no Reynolds effects, the non-dimensionalised optimum λ value can be applied in the designing of larger scale devices. The power curves for each test without the flow deflection flap (see Figure 4.21) are presented in Table 4.5.

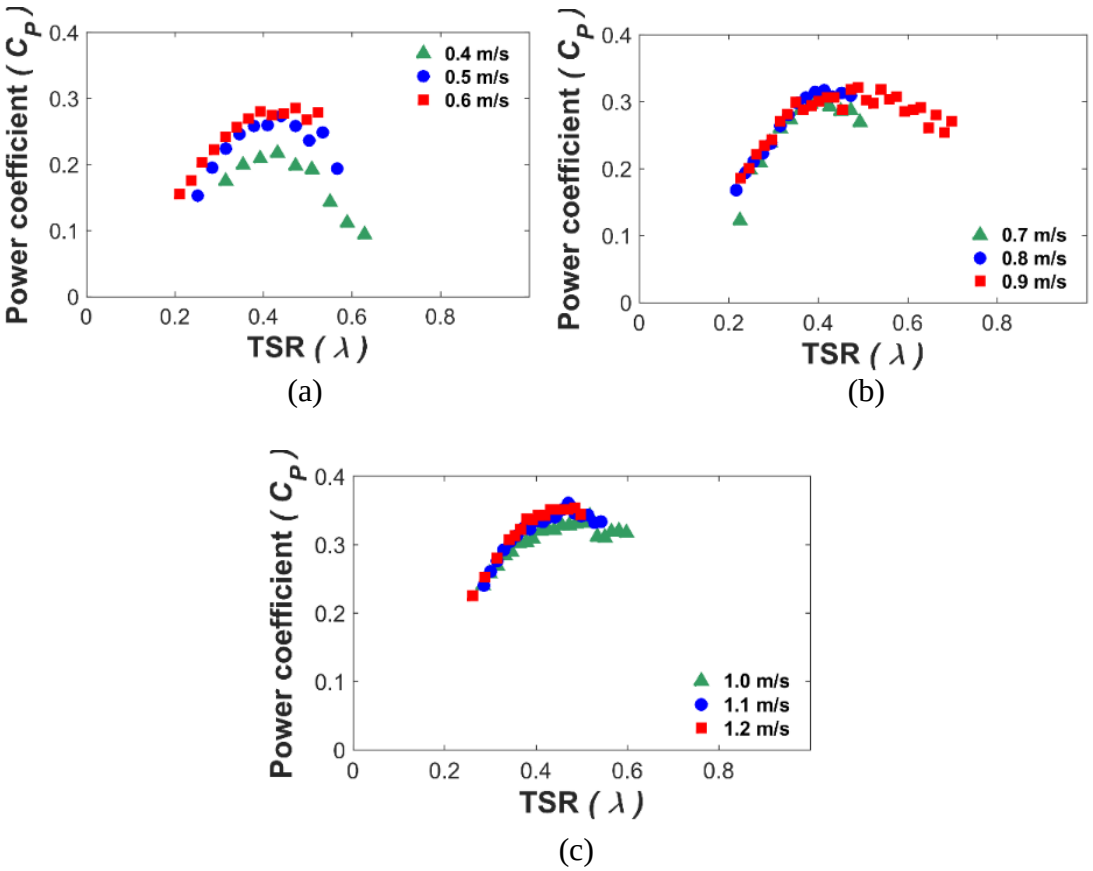

Figure 4.20: Full range of power curves for 1:20 scale IFREMER tests conducted with free-stream velocities ranging from 0.4 m/s to 1.2 m/s (a) 0.4 m/s to 0.6 m/s (b) 0.7 m/s to 0.9 m/s (c) 1 m/s to 1.2 m/s.

Table 4.5: Summary table of results for 1:20 scale experiments without the deflector.

U_∞ (m/s)	0.4	0.5	0.6	0.7	0.8	0.9	1.0	1.1	1.2
C_{Pmax}	0.22	0.27	0.28	0.3	0.32	0.32	0.33	0.35	0.35
RPM	5	6.5	8.5	10	11.5	14.5	16	16	17.5
λ	0.4	0.4	0.45	0.4	0.45	0.5	0.5	0.45	0.45

Based on observations by GKinetic during some earlier stage field tests, a flow deflection flap was attached to the side of the bluff body immediately upstream of the turbine for some additional testing (see Figure 4.21). The flap has the effect of directing the accelerated flow onto the turbine blade as it begins to turn outward from the bluff body beginning its transition across the front end of the turbine. Figure 4.22 shows a comparison of the power curves obtained at a flow speed of 1.1 m/s with and without the deflector. The effect of the flow deflector was to increase C_{Pmax} from 0.35 to 0.4 and the corresponding λ value from 0.5 to 0.55.

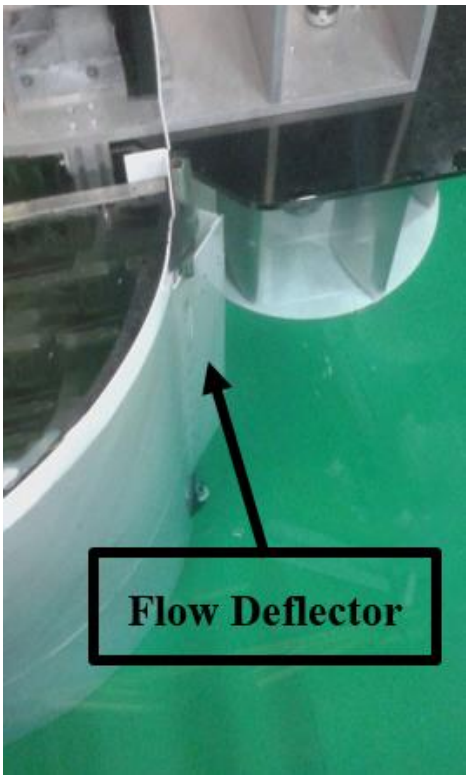

Figure 4.21: Image of flow deflector attached to 1:20 scale bluff body in IFREMER.

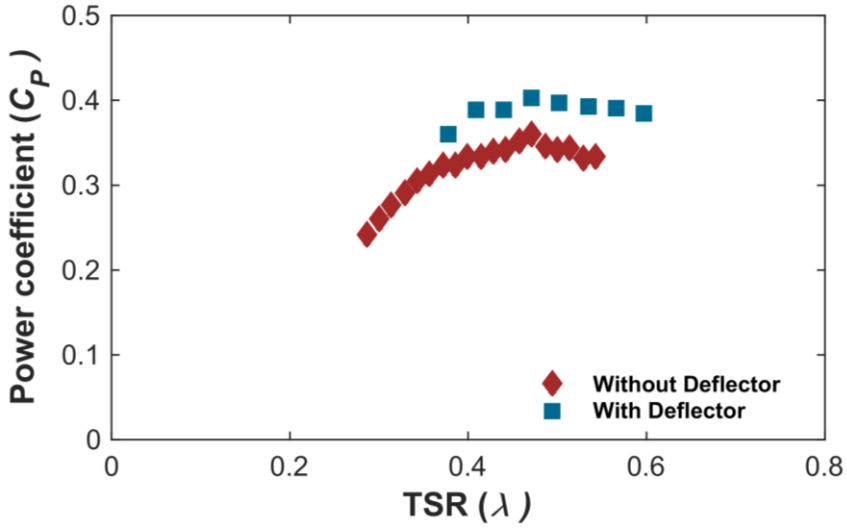

Figure 4.22: The measured effect of flow deflector on the power curve for 1:20 scale IFREMER tests at 1.1 m/s flow speed. C_P versus λ with/without the additional deflector.

Channel blockage, as previously discussed is an essential parameter in the experimental testing of turbines. For the 1:20 scale tests, channel blockage was evaluated to be 25 %. Elevated blockage values can result in overestimation of C_P and the testing protocols recommend experimental results should be corrected for blockage if above 5 %. The literature review found the accepted methods for blockage correction of test data have thus far only been developed for HATs and that these methods have been developed on the basis of 1D theory which is not applicable to the GKinetic VATT. In the absence of a suitable method, performance results in this chapter are left uncorrected. Since the CFD models developed later (Chapter 7) have the capability of replicating confined flow conditions, the uncorrected experimental results could still be used for CFD model validation.

Forces and moments on the turbine were sampled at a frequency of 100 Hz and averaged at one-minute intervals for each of the free-stream velocities tested. The axial force was again taken as the drag force. The data for just three flow velocities (for clarity) are presented in Figure 4.23: The turbine drag force with time histories for 1:20 scale IFREMER tests. An averaged C_D value of 0.75 was determined for the turbine.

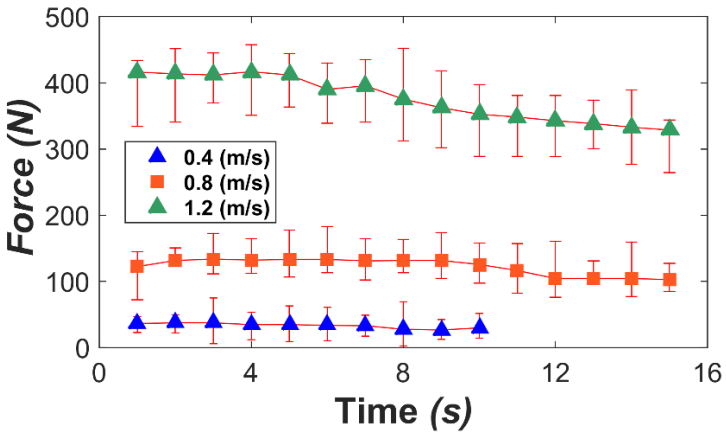

Figure 4.23: The turbine drag force with time histories for 1:20 scale IFREMER tests.

The drag coefficient on a structure in a fluid is dependent on the frontal profile of the structure and can vary from 0.4 for a curved profile to 1.4 for a flat plate [27], these values are, however, Reynolds number dependent. A turbine could be considered to lie somewhere between these two profiles so the C_D value of 0.75 determined seems reasonable, particularly since this device has a high solidity. This C_D value was then applied to omitted data (1 m/s) as a check to see how well it captured the drag loads in comparison to actual experimental data from the load cell. Figure 4.24 shows this comparison with a point for each free-stream velocity tested; the theoretical values determined using the C_D value compare favourably with the experimental values.

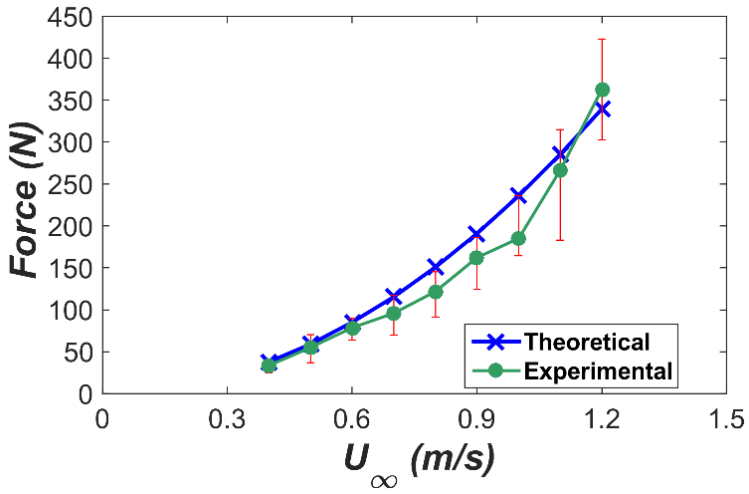

Figure 4.24: Theoretical versus experimental drag force (1:20 scale IFREMER tests) on the turbine from 0.4 m/s to 1.2 m/s.

4.4.3 Experimental Results for 1:10 Scale Device at Limerick Dock

The conducted tow tests involved towing the device through the dock at a constant tow speed with the turbines set at constant rotational speed. However, variations occurred in both parameters over the course of a tow, so for each tow test conducted a time-averaged C_P was calculated. An example of the calculation process is now presented for a sample tow. This is followed by the presentation of the time-averaged C_P results for all tows.

The calculation of available power for the tow tests depended on knowledge of the free-stream velocity. Since the device was being towed, this is actually the velocity of the fluid relative to the device and was measured by the front-mounted ADCP.

Figure 4.25 presents the along stream velocity recorded for the most distant bin (10.4 m) of the forward facing ADCP which represents the free-stream flow speed during the tow. The plot shows that the free-stream fluid speed varied between 0.81 to 0.9 m/s over the duration of the tow. The time-averaged velocity for the tow was 0.85 m/s with variations of ± 0.04 m/s (or ± 5 %) during the tow.

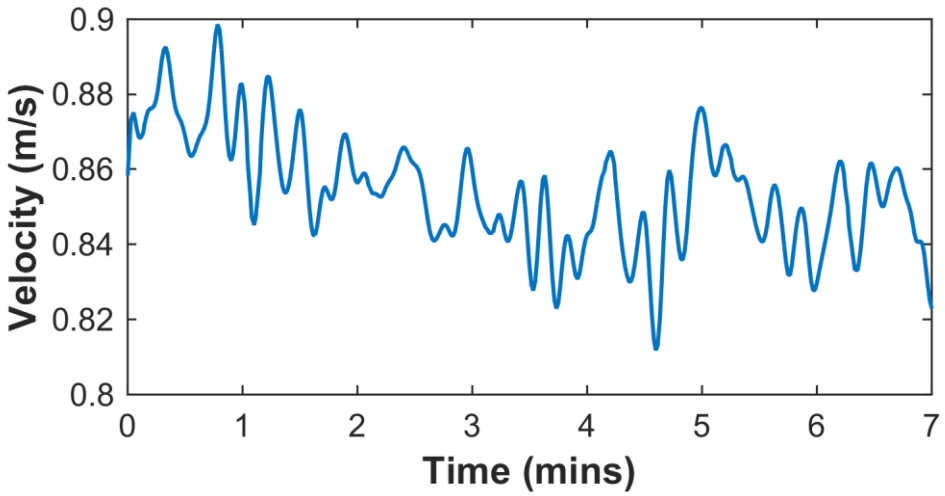

Figure 4.25: Along stream velocity against time for 1:10 scale Limerick Dock tests taken from last bin of forward facing ADCP

The velocity data presented in Figure 4.25 can be used to calculate the power available to the device for extraction. It is assumed that half of the power is available to each

turbine. Figure 4.26 presents a graph of the power available to one of the turbines during the course of the tow. The time-averaged power available to the turbine during this tow was 635 W.

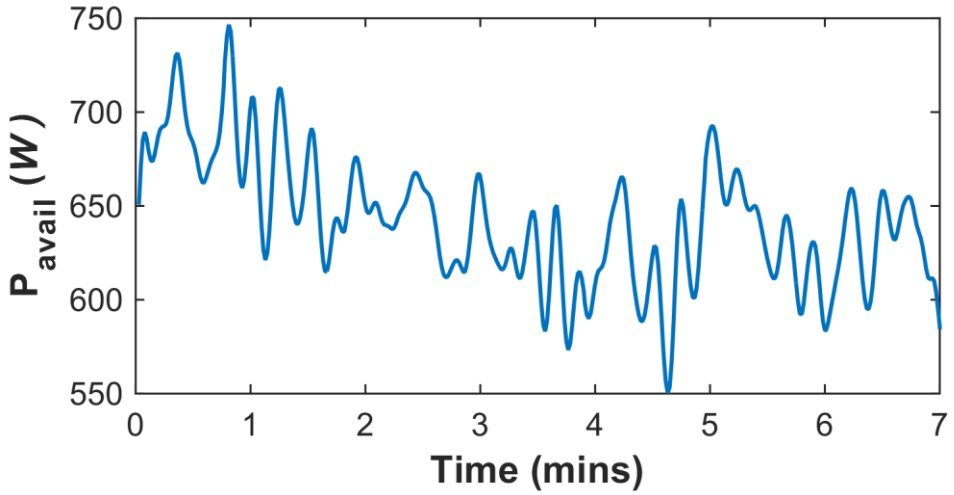

Figure 4.26: Available power against tow time for 1:10 scale Limerick Dock tests

During the tests, power data were calculated for each turbine rotor. In the following results, T1 and T2 correspond to the port side and starboard turbines, respectively (as shown in Figure 4.10). Figure 4.27 presents a comparison of turbine rotor RPMs for T1 and T2 over the duration of the tow. Figure 4.27 (b) is a close-up view of the data presented in Figure 4.27 (a). As seen in Figure 4.27 (a), the turbines' rotational speeds were relatively constant during the tow with time-averages of approximately 13.6 RPM; small variations did occur. From Figure 4.27 (b), it is seen that the variations in RPM were of the order of ± 0.3 rpm (or ± 2%) about the mean. There appears to be a relationship between the variations in RPM (Figure 4.27 (b)) of the two turbines with higher RPMs of T1 generally coinciding with lower RPMs of T2 and vice versa. This may be the result of periodic yawing of the device whilst under tow. This was observed during the tests and is evidenced by the ADCP data in Figure 4.28 which presents the variations in yaw, pitch, and roll of the device during the tow. Yawing motions are most significant with a maximum range in yaw angle of the order of 10^{o}. By comparison, the maximum range in pitch angle was less than 2^{o} and the maximum range in roll angle was approximately 6^{o}.

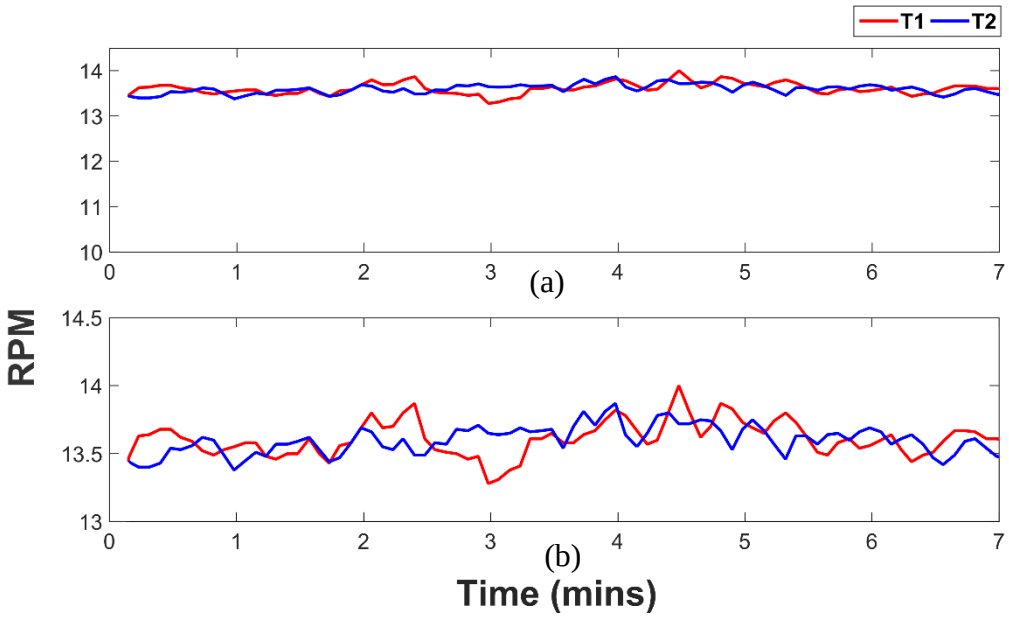

Figure 4.27: Comparison of the variation of turbine rotor RPM for T1 and T2 over the duration of the tow for 1:10 scale Limerick Dock tests. (b) is a magnified view of (a).

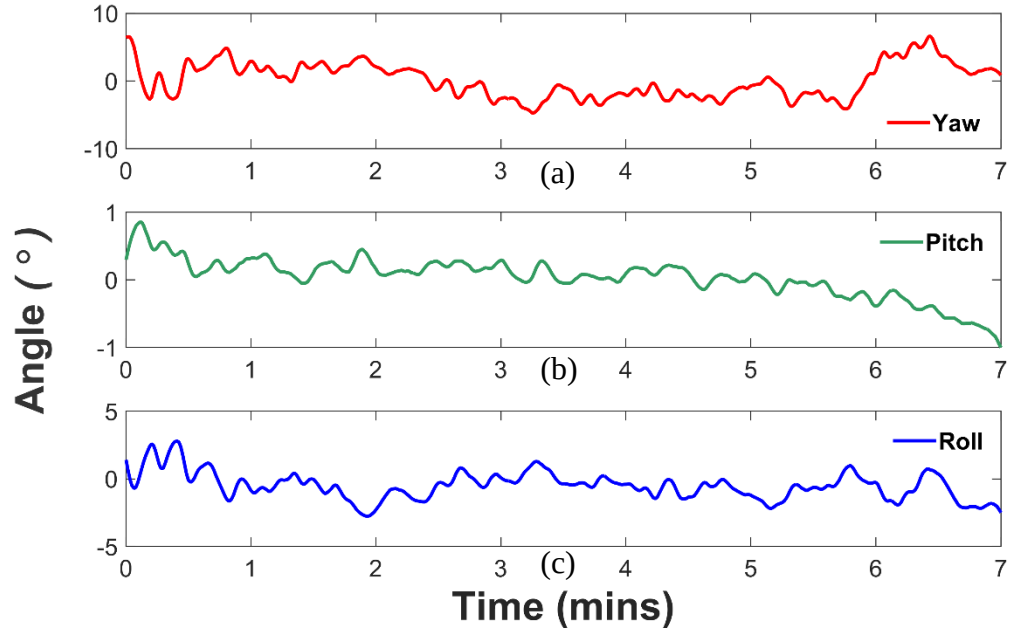

Figure 4.28: Variation of device positioning during 1:10 scale Limerick Dock tow test for (a) yaw, (a) pitch, and (c) roll.

Figure 4.29 presents the C_P values calculated for both rotors using the on-board Lenze system (identified as 'PLC' in the graph) and the strain gauge data recorded by the Versalog data logger (identified as 'Versalog' in the graph). Figure 4.29 (a) presents data for T1 and while Figure 4.29 (b) shows data for T2. Clearly, the C_P values

determined by the Versalog data are significantly higher than those determined using the PLC data. The time-averaged C_P for T1 was 0.14 for the Versalog data compared to 0.06 for the Lenze data. Given its proven performance in previous stages of testing (see Figure 4.20), the Versalog C_P values were assumed to be the more accurate of the two data sets. Interestingly, the Versalog C_P values are less variable with time even though the data used for their calculation were collected at a much higher sampling frequency (50 Hz versus 1 Hz).

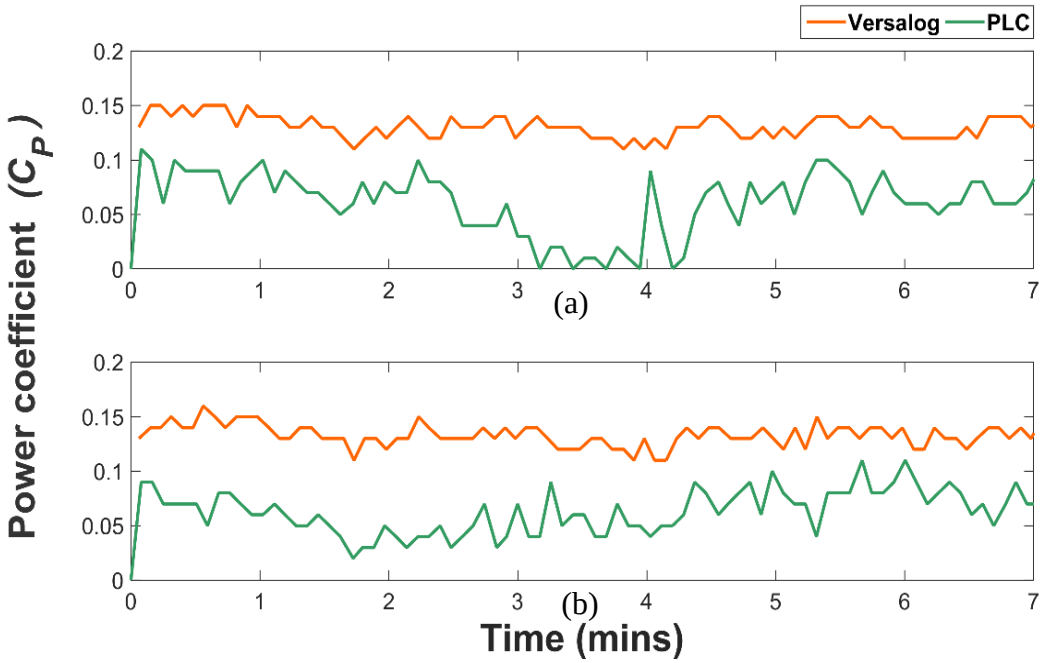

Figure 4.29: Comparison of C_P values for 1:10 scale Limerick Dock tow test determined using both methods for (a) T1 and (b) T2.

Given the variability in data during a tow, time-averaging was performed for each minute of a tow. This resulted in the generation of tables of time-averaged efficiencies for each turbine. These tables are presented in Appendix B.

To provide a general overview of the power analyses for all tow tests, Figure 4.30 plots time-averaged C_P values against time-averaged λ values for both turbines, for all of the analysed tow tests. Each data point represents a minute-averaged C_P value. The C_{Pmax} achieved by the turbines were 0.22 for T1 and 0.27 for T2 while the average C_P was 0.135 in both cases.

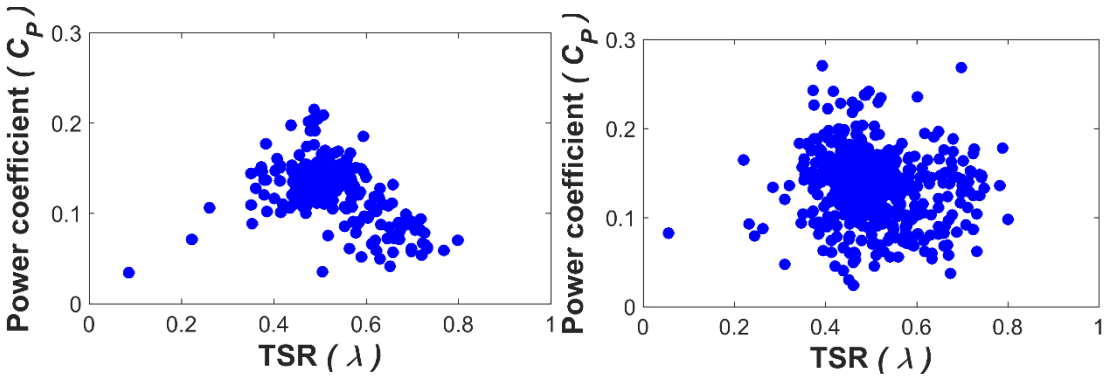

(a) (b)

Figure 4.30: Amalgamated plots showing calculated minute-averaged Versalog C_P values from all tows graphed against the respective λ values for: (a) T1 and (b) T2.

As discussed, a power performance curve is typically bell-shaped as demonstrated by the 1:20 scale power curves in Figure 4.20. C_{Pmax} is achieved at an optimum λ and efficiency decreases for λ values above and below the optimum λ. For a number of reasons, it proved impossible to produce clear power curves in this manner for the tow test data. Figure 4.31 (a and b) show attempts at power curves produced for tow speeds of 0.6 m/s and 0.81 m/s, respectively. Figure 4.31 (a) shows a very broad spread of C_P values for different λ values which makes it impossible to deduce any kind of power curve. Unfortunately, this was the case for the majority of the tow speeds. A possible reason for the large spread in C_P values for particular λ values is the variability in both the tow speed and turbine rotational speed (and therefore free-stream flow speed and λ) during tows which may have meant that steady-state power generation conditions may not have been achieved during a tow. Other contributing factors could be the unstable movement (pitch, roll and yaw) of the device whilst under tow and turbulence.

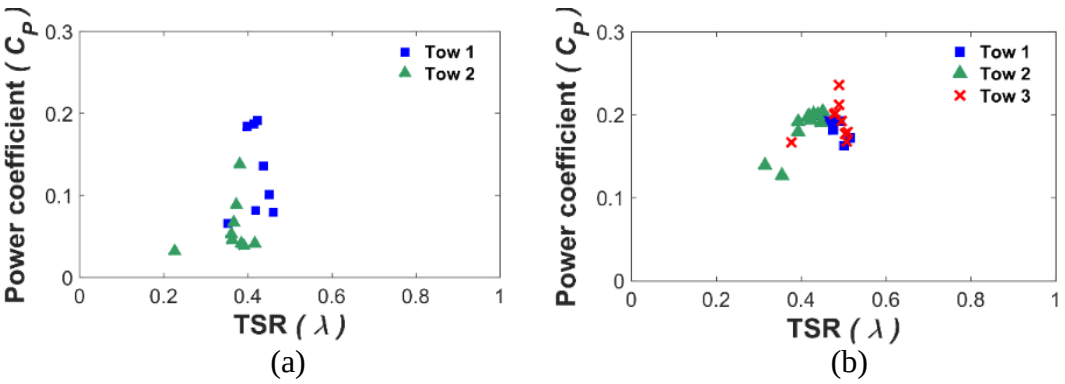

Figure 4.31: Amalgamated Versalog C_P values for: (a) two tows at 0.81 m/s, and (b) three tows at 0.6 m/s

The 0.6 m/s tow data in Figure 4.31 (b) does actually resemble a power curve – with the exception of two outlying data points from Tow 3 at λ = 0.47. Comparison with the power curve obtained from the 1:20 scale testing for the same free-stream velocity of 0.6 m/s (Figure 4.20 (a)) yields some interesting observations. The 1:20 scale test data suggests the optimum λ value for a free-stream flow speed of 0.6 m/s is approximately 0.4. The curve in Figure 4.31 suggests a similar optimum λ in the range of 0.4 to 0.45. Regarding the magnitudes of C_P values, the 1:20 tank test C_P curve shows a C_{Pmax} = 0.28. Ignoring the outliers in Figure 4.31 (b), C_{Pmax} of the power curve, is somewhat lower at 0.2. However, the 1:20 scale test data were of course obtained under highly controlled steady state conditions. It is also possible that Reynolds effects are occurring and, therefore, Reynolds dependence. The confined flow at 1:20 scale potentially lead to higher turbine inlet velocities and, therefore, higher Reynolds numbers. This would mean that Reynolds independence in unconfined conditions would occur at higher free-stream speeds than determined during the IFREMER 1:20 scale tests.

Returning to the disagreement between the PLC and Versalog power data, Figure 4.32 shows the level of agreement of the C_P values calculated using the Lenze data with those calculated using the torque meter data. For each set of measurements, an agreement index was calculated using Equation (4.3).

$$Agreement\ index = \left(1 - \frac{\text{Versalog } C_P - \text{Lenze } C_P}{\text{Versalog } C_P}\right) \qquad (4.3)$$

An agreement index of 1 indicates exact agreement while indices greater than and less than 1 indicate Lenze values being higher or lower, respectively, compared to corresponding Versalog values. An agreement index of 0.75 means the Lenze value was 75 % of the Versalog value. The Lenze C_P values were consistently lower than the Versalog C_P values, highlighting flaws in the control system measurements.

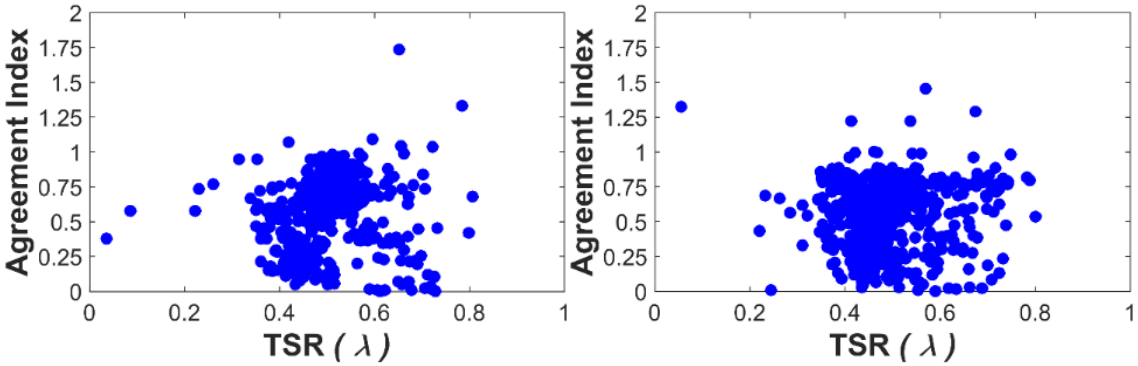

(a) (b)

Figure 4.32: Amalgamated plots for 1:10 scale Limerick Dock tow test showing calculated agreement indices for minute-averaged Lenze C_P values versus Versalog C_P values from all tows graphed against corresponding λ for: (a) T1 and (b) T2.

Finally, the single channel load-cell data was used to determine the drag load on the device during each tow. Figure 4.33 shows the drag force recorded for a 1.2 m/s tow. It is seen that there is significant variation in the drag force on the device throughout the duration of the tow. The variations are most likely due to a non-uniform force being applied by the winch via the tow line and the changes in device yaw, pitch and roll. The changes in heading mean that the frontal area and drag coefficient of the device are constantly changing, thus affecting the drag force on the device.

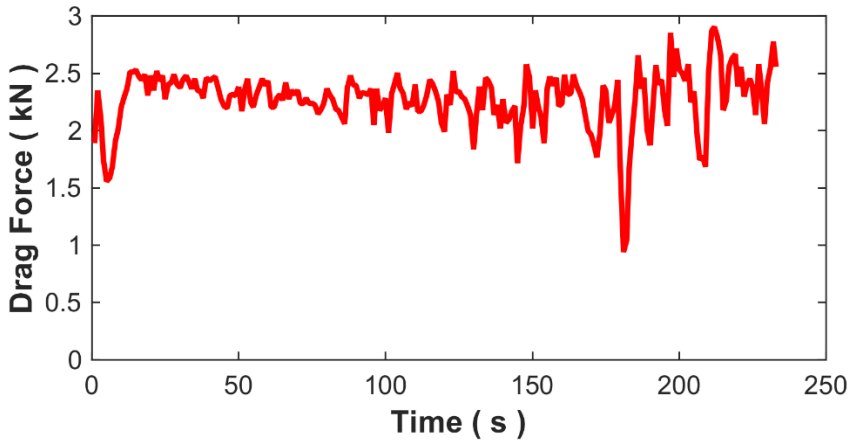

Figure 4.33: Drag force variation of the duration of a 1.2 m/s 1:10 scale Limerick Dock tow test.

Figure 4.34 plots time-averaged drag coefficients (calculated from the drag force determined by the load cell and the full frontal device area) against tow speed (i.e. free-stream velocities) for 25 tow tests from which data were available. The variations observed in the drag coefficients may be due to the variation in device yaw, pitch and roll positioning and therefore frontal area when under tow. Some of this variation is no doubt also a result of the variations in power output of the turbines. It shows that the majority of drag coefficients fall in the range of 0.6 to 0.9 and if one ignores the outlying data point of 1.33, the average of the remaining drag coefficients is 0.83. This is 22 % higher than the full device drag coefficient of 0.68 calculated for the 1:40 scale testing in Section 4.4.1.

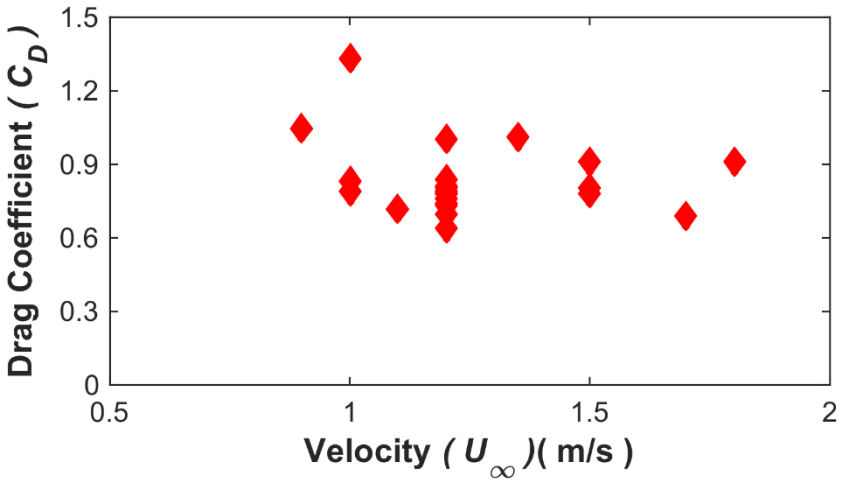

Figure 4.34: Drag coefficients versus velocity for a sample of 25 tows from 1:10 scale Limerick Dock tow tests.

4.5 CFD Model Results

CFD modelling was used to investigate the effect of the tank wall on the flow acceleration around the 1:20 scale bluff body. Two models were created: (1) a flume model which included wall friction to induce realistic wall boundary layers as experienced in the IFREMER flume, and (2) a tidal basin model with friction excluded and using symmetry boundaries instead of wall boundaries, to reflect conditions in the NUIG tidal basin.

Model data were output along three transects corresponding to the measurement locations of the experimental LDV data. A schematic for the location of these transects is presented in Figure 4.35. Comparison of the flume model data versus LDV measured data for the three transects is presented in Figure 4.36. It is clear that there is general agreement (root mean squared error (RMSE) values are presented in Table 4.6) between the model and the LDV data. Presented in Figure 4.37 is a combined vector and contour plot for the flume model velocity. The area of highest acceleration can be observed at the widest point of the bluff body as already discussed. The friction effect of the flume wall on the flow upstream of the bluff body can clearly be seen by the velocities in the boundary layer which have been reduced below the free-stream of 0.8 m/s.

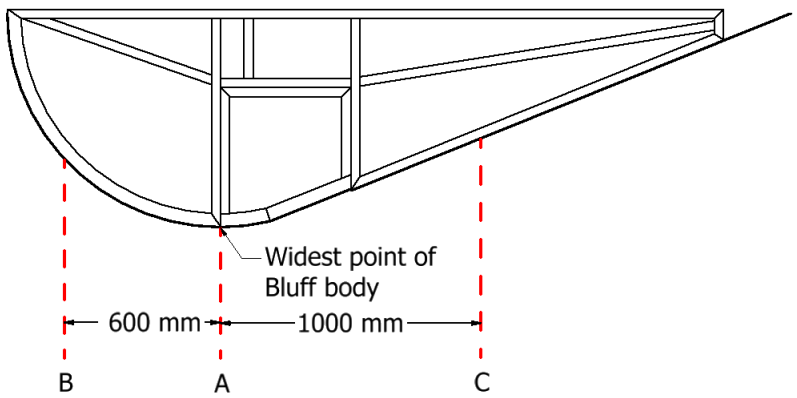

Figure 4.35: Schematic for the location of the three data transects, A, B and C, located at the widest part of the bluff body, 600 mm in front and 1 m behind respectively.

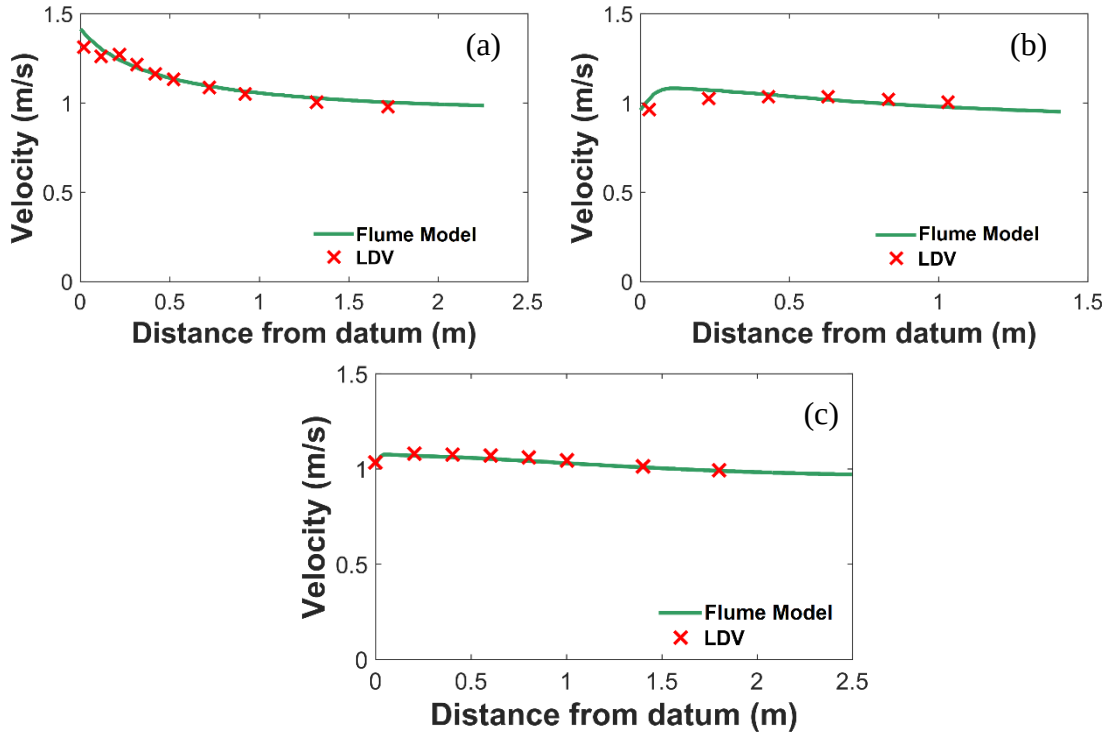

Figure 4.36: Comparison of CFD data versus LDV measured data for 1:20 scale IFREMER tests for the three transects. (a), (b) and (c) with corresponding transects A, B and C.

Table 4.6: RMSE for three data transects presented in Figure 4.36.

Transect	A	B	C
RMSE (m/s)	0.0349	0.0366	0.0186

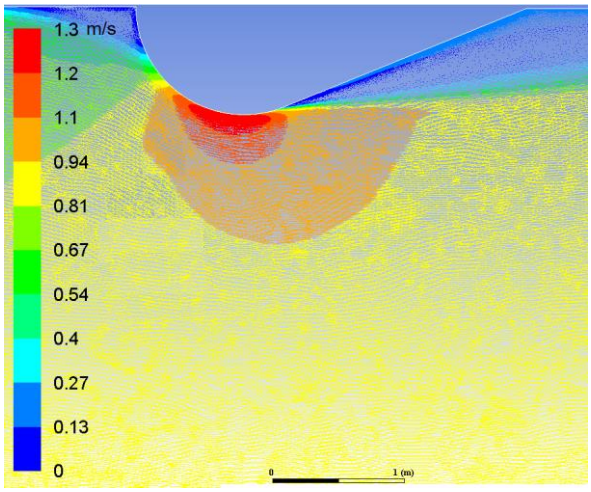

Figure 4.37: CFD Vector plot with included boundary layer effect at the walls.

A combined velocity vector and contour plot from the tidal basin model is presented in Figure 4.38. Again the highest acceleration above the free-stream of 0.8 m/s occurs at the widest part of the bluff body; however, the highest velocity, in this case, was 1.6 m/s, corresponding to a factor of 2 increase in flow speed which matched the level of acceleration measured in the tidal basin tests. It should be noted that the meshes used to model the scenarios presented in Figure 4.37 and Figure 4.38 are identical, only boundary conditions were changed to reflect the various setups.

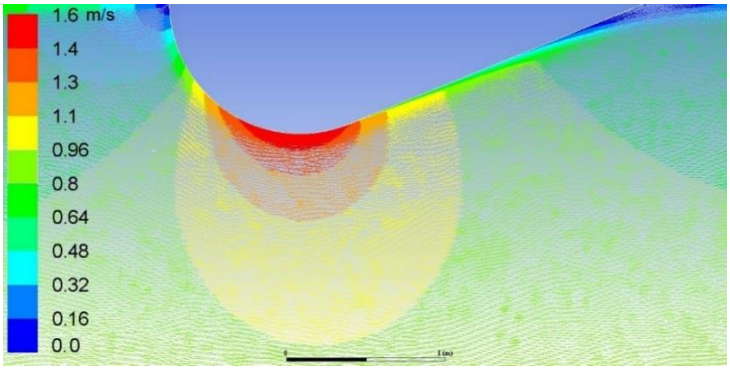

Figure 4.38: CFD vector plot without boundary layer effect at the walls.

Figure 4.39 compares the localised accelerations from the tidal basin model to the measured tidal basin accelerations, along Transect A. There is significantly better agreement with the tidal basin data than was the case for the measured flume data in Figure 4.18. This confirms that the reduced accelerations measured in the 1:20 scale tests can indeed be attributed to the wall friction-induced boundary layer.

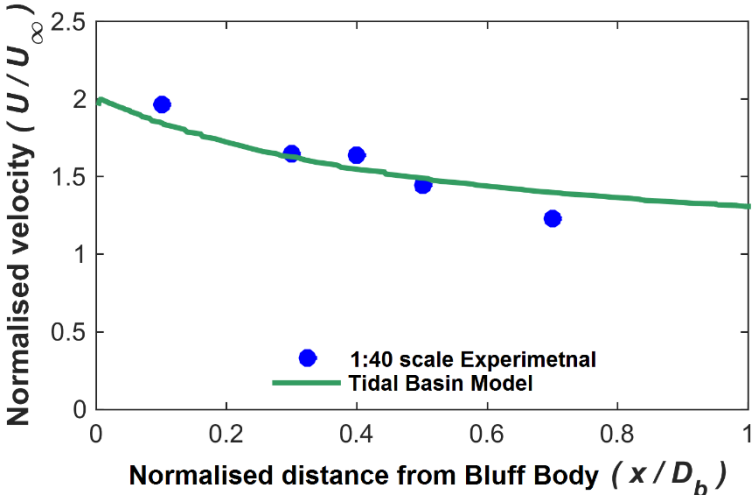

Figure 4.39: Comparison of 1:20 scale CFD model data versus 1:40 scale tidal basin measured results.

4.6 Discussion of Results

The LDV flow measurements for the 1:20 scale experiments of the bluff body confirmed its flow-accelerating potential. Although the levels of localised acceleration (approximately 60 %) were not as high as those measured during previous 1:40 scale tests (approximately 100 %). CFD analysis provided the connection between the two sets of experimental flow data; proving that the lower accelerations in the 1:20 scale tests were the result of the boundary layer formed upstream of the bluff body, due to the friction effect of the tank wall. The CFD results with wall friction included gave good agreement with the measured data and when the wall friction was removed to better reflect conditions in the tidal basin the modelled accelerations increased to levels similar to those recorded in the 1:40 tidal basin tests. The maximum accelerations of the free-stream flow are of the order of 100 % reproduced by the tidal basin CFD model. These are comparable to the levels of localised flow acceleration observed in previous studies of flow around cylinders, e.g. Graf and Yulistiyanto [80]. Who recorded accelerations of 100 % in depth-averaged flow speeds around a submerged cylinder.

The drag loads recorded on the 1:40 scale device made it possible to determine a drag coefficient of 0.68 for the full device (bluff body and two turbines). Knowledge of the drag coefficient will prove beneficial for upscaling of the device and determination of mooring loads for field tests. This compared with 0.83 for the 1:10 scale experiments. A drag coefficient of 0.75 was determined for the turbine alone, during the 1:20 scale experiments.

The method developed for measuring mechanical power, where a torque meter was constructed using strain gauges and a data logger, is much less invasive than the more commonly used torque transducer which involves splitting the turbine shaft and requires additional couplings. The approach worked very well here and yielded accurate results. It may prove useful in other turbine experimental studies where a non-invasive technique is desirable. The torque meter was calibrated in air and applied in water, therefore strain drift is a potential problem. Although it was not thought to have been significant here, it does merit future investigation so that it can either be accounted for or ruled out.

The performance results from the 1:20 scale testing show that the device reached a peak efficiency of 35 % at a free-stream flow speed of 1.1 m/s. By attaching the flow deflector to the bluff body immediately upstream of the turbine entrance, the peak efficiency was improved to 40 % for the same flow speed. These figures should be considered with caution though. The blockage ratio for the tests was at the higher end of the recommended allowable blockage ratios for scale experiments and the results should, therefore, be corrected for blockage. However, due to the absence of any accepted blockage correction method for VATs, this was not possible. Reynolds independence was observed for flow speeds above 0.6 m/s.

By way of comparison to other VATTs, New Energy Corporation [178] achieved an efficiency of 32 % for their fixed-pitch vertical axis turbine, and Jing *et al.* [76] achieved 25 % for their variable-pitch design. The better performance of the device presented here is ascribed to the flow acceleration and the variable pitch blades (although the high blockage is also likely contributing). Without physical test results of a similar device with fixed pitch blades, it is difficult to determine which of the two design features most dramatically influences performance. However, the 2D CFD model of the device presented in Chapter 7 is used to investigate this.

The tow testing undertaken at 1:10 scale proved to be a valuable experience in the device development. It was discovered that the inclusion of a non-specialised, non-calibrated PLC, PTO control system was a mistake. Leaving aside the differences in the calculated power performance, the control system caused the device to become unstable undertow and affected the majority of the data acquired. This instability likely contributed to the much lower efficiencies compared to those recorded during the 1:20 scale flume tests; the maximum and average $C_{\mathrm{P}max}$ across all 1:10 scale tows were 0.27 and 0.135, respectively, compared with the $C_{\mathrm{P}max}$ of 0.4 from the 1:20 scale tests. In addition to the control system, a number of other factors may have contributed to the inferior performance levels of the 1:10 scale device. Changes in yaw, pitch, and roll of the device while undertow will have resulted in variations in the along-stream flow velocities and thus, the power available to the turbine. Additionally, the blade pitching mechanism on the turbine is optimised for steady flow conditions, so unsteady flow conditions and vary-directional inflow, in particular, will likely have resulted in less lift being developed on the blades. In the 1:20 tests, the bluff body

extended the full depth of the water column; thus all entrance flow was forced to flow around its sides and contribute to flow acceleration. In the 1:10 tests, the bluff body only extended about 1.5 m down through the water column which had an average depth of 5 to 6 m during tests. It is possible that this change in setup will have resulted in some entrance flow being diverted under the device rather than around its sides thereby leading to lower levels of acceleration of the turbine inflow. It is also acknowledged that some of the variation between the 1:20 and 1:10 scale power performance results can be attributed to the high channel blockage of the 1:20 scale tests. It is also possible that Reynolds effects are occurring for the 1:10 scale tests in Limerick Dock and, therefore, Reynolds dependence. The confined flow at 1:20 scale potentially might lead to higher turbine inlet velocities and, therefore, higher Reynolds numbers. This would mean that Reynolds independence in unconfined conditions would occur at higher free-stream speeds than determined during the 1:20 scale tests in IFREMER. Further tow tests at higher tow speeds for the 1:10 scale device are required to investigate for Reynolds independency.

Although the lower than expected power performance of the 1:10 scale tests were disappointing, the tests did demonstrate a successful approach for tow testing of large scale turbines in a relatively benign controlled environment compared to the alternative of testing in a much more dynamic open tidal environment. In addition, a post-testing mechanical survey of the 1:10 scale device identified several structural design issues that were thought to have adversely affected the performance of the device. These issues are investigated further in Appendix A of this thesis.

4.7 Chapter Summary

The GKinetic turbine with flow acceleration and variable pitch blades has been tested at 1:40, 1:20 and 1:10 scales. The following are the main conclusions from this work:

- The peak mechanical efficiency of 40 % recorded in the 1:20 scale tests is higher than many other VATs for which performance data are available. It is acknowledged, that the measured efficiencies may contain some over-performance due to the high channel blockage. Unfortunately, there is currently no accepted method for blockage correction of VAT test results.

However, this is balanced by the fact that these were achieved with lower levels of acceleration (factor of 1.6 instead of 2).

- Use of the bluff body acts to accelerate the inlet flows to the turbines. Without the turbines present, the bluff body has been shown to be capable of accelerating the free-stream flow by a factor of 2. The bluff body also increases the capture area of the device without the necessity of significantly larger and more expensive turbines.

- There are a limited number of tidal locations worldwide with the peak flow speeds in excess of 2 m/s, which is generally quoted as the requirement for tidal turbines to operate economically. By accelerating the free-stream flows, the GKinetic device can operate in less energetic tidal, or indeed river currents.

- The LDV was used to measure flow-fields around the device with the turbine in-situ, from which, the effects of the turbine are easily apparent in the turbine wake. These measured datasets proved very valuable, as they were subsequently used for validation of the CFD model (presented in Chapter 7).

Chapter 5. Development and Assessment of a BEMT Model for VATS.

This chapter has been submitted for publication in the peer-reviewed Journal of Ocean Engineering as:

Mannion, B., Leen, S. B., and Nash, S., 2019, "Development and Assessment of a Blade Element Momentum Theory model for High Solidity Vertical Axis Tidal Turbines." Journal of Ocean Engineering.

The basic BEMT model (without corrections) presented in this chapter has been published in a peer-reviewed conference paper presented at Civil Engineering Research in Ireland 2018 (CERI2018). The full reference is:

Mannion, B., Leen, S. B., and Nash, S., 2018, "Double multiple stream-tube model for high solidity vertical axis tidal turbines" Civil Engineering Research in Ireland CERI2018, August 29th - 30th 2018, Dublin, Ireland.

5.1 Introduction

This chapter presents the development of a model and design tool for prediction of the hydrodynamic performance of high solidity and highly loaded vertical axis tidal turbines. The model is based on BEMT and utilises the graphical approach for determining induction factors developed by McIntosh *et al.* [44], rather than the more common iterative approach. The accuracy of this approach is assessed for vertical axis turbines. The research is significant as tidal turbines, and particularly vertical axis tidal turbines, typically have a higher solidity than wind turbines, thus Strickland's iterative approach, which is more suited to low solidity rotors will generally not be valid. The model is developed in the MATLAB programming language.

The chapter begins with brief overviews of the BEMT model (Section 5.2). Section 5.3 documents the actuator disc theory and its equations. While Section 5.4 documents model assumptions. Section 5.5 presents the blade element aspect of the model. In Section 5.6 the graphical approach for determining induction factors is discussed. Section 5.7 presents model modifications for improved accuracy such as dynamic stall, flow expansion, finite aspect ratio correction and a velocity profile. Section 5.8

documents the developed BEMT model structure and solution procedure. Section 5.8.1 describes the representation of the turbine geometry, including how the swept area of the rotor is distributed between stream-tubes and provides a brief description of the aerofoil data used. Section 5.10 discusses the outputs that can be extracted from the BEMT model. This chapter finishes with a model validation comparison to experimentally measured power performance in Section 5.11.

5.2 Overview of BEMT Modelling Approach

BEMT combines blade element theory with momentum (i.e. actuator disc) theory. Accredited to Betz [179], the actuator disc model (Section 5.3) is the simplest of aerodynamic/hydrodynamic models for turbines. It is based on 1D linear momentum theory and simulates the turbine rotor as a porous disc that extracts energy from the fluid, resulting in a momentum change in the fluid. In its simplest form, conservation of momentum is applied along a single stream-tube enclosing the turbine rotor (e.g. Figure 5.1 (a)). Although successful development and application of single stream-tube BEMT models have been used, they are not really suitable for the study of VATTs. The single stream-tube is usually divided into multiple stream-tubes (Figure 5.1 (b)) to accommodate the effects of variations in axial induction with respect to azimuthal position. A second actuator disc can be included (Figure 5.1 (c/d)) so that variations between upstream and downstream interactions of the blades with the fluid can be modelled. The resulting model is generally known as a double multiple stream-tube model (DMST) and is the type of model developed in this research. It should be noted, the figure does not accurately represent stream-tube expansion through the rotor, this has been omitted to avoid over cluttering the figure.

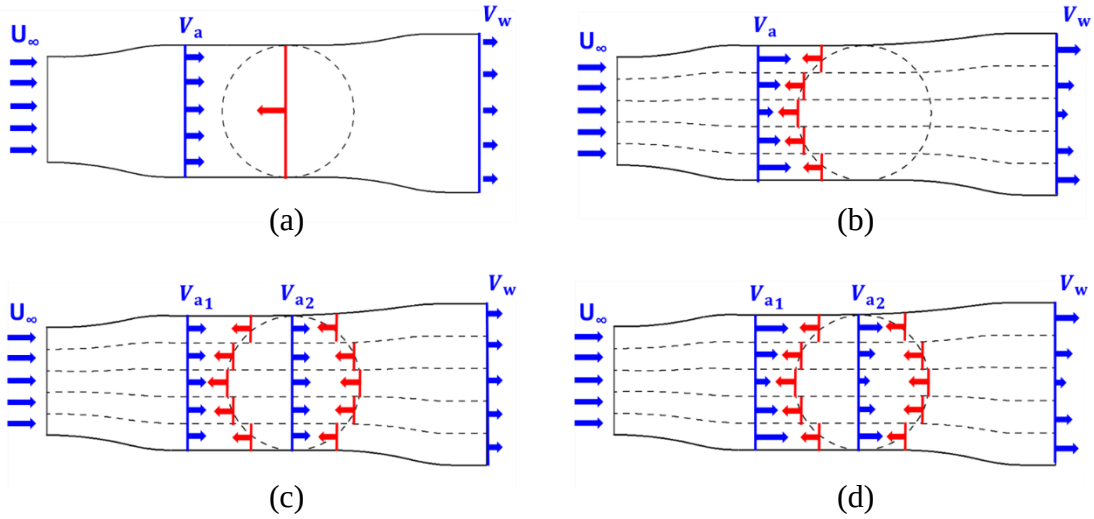

Figure 5.1: Stream-tube model variations: (a) Single steam-tube model, (b) Single multiple stream-tube model, (c) Double multiple stream-tube (DMST) model with constant induction factor, and (d) Double multiple stream-tube (DMST) model with varying induction factor.

5.3 Actuator Disc (Momentum) Model

In modelling of VATs, the turbine is represented as two actuator discs in tandem, as shown in Figure 5.2, which are located at the upstream and downstream faces of the turbine. This results in two consecutive stream-tubes, with all flow entering at the inlet and exiting at the outlet of each stream-tube. The presence of the actuator disc causes a pressure discontinuity within the stream-tube on the fluid passing through it. Actuator disc model theory is based on the following key assumptions:

- The flow is steady-state, homogenous, and incompressible.
- There is no frictional drag exerted by the disc/turbine.
- The thrust over the disc or rotor area acts uniformly within that disc or tube.
- The turbine wake is non-rotating.
- The static pressure far upstream and far downstream of the rotor is equal to the undisturbed pressure.

As shown in Figure 5.2, flow through the actuator disc can be represented by a single stream-tube, or by multiple stream-tubes. In the DMST, conservation of linear momentum is applied to each stream-tube in order to determine the axial thrust exerted by the fluid on the portion of the actuator disc bounded by that stream-tube. The axial

thrust is then used to calculate the extracted power and subsequently power coefficient. Since the same governing equations apply to each disc in Figure 5.2, they are only presented here for one disc; thus the *up* and *down* subscripts included in Figure 5.2 are omitted, but the numbered subscripts identifying specific regions within the stream-tube are included. From conservation of linear momentum, the axial thrust, T, exerted by the disc on the fluid can be calculated as:

$$T = V_1(\rho AV)_1 - V_4(\rho AV)_4 \tag{5.1}$$

where A is the cross-sectional area of the disc, and V is the fluid velocity. From continuity, the mass flow rate ($\dot{m} = \rho AV$) through the stream-tube is constant giving:

$$T = \dot{m}(V_1 - V_4) \tag{5.2}$$

The thrust exerted by the fluid on the disc (which is equal in magnitude but opposite in direction to (2) can be obtained by applying force equilibrium across the disc to give:

$$T = A_2\,(p_2 - p_3) \tag{5.3}$$

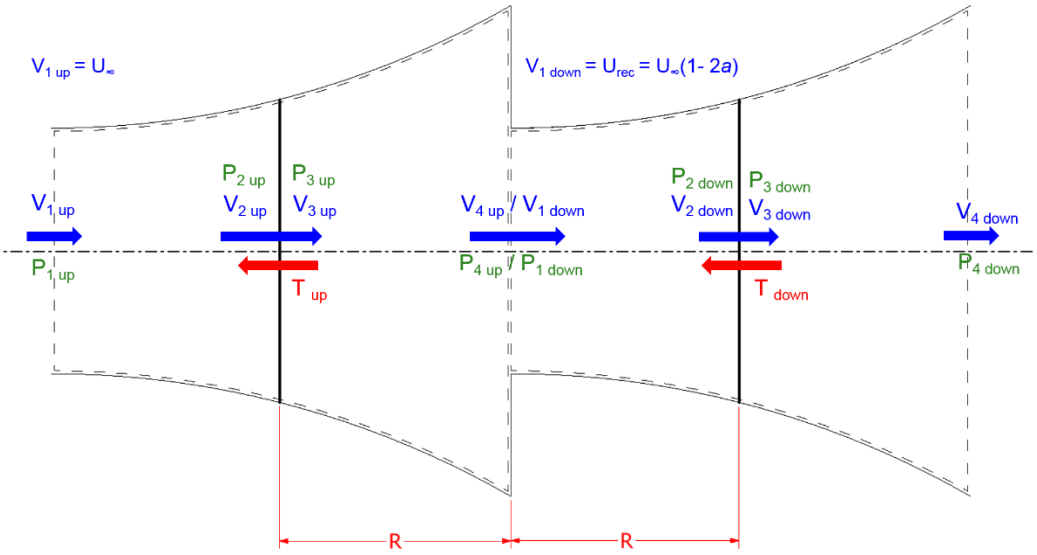

Figure 5.2: Schematic of a single stream-tube, double actuator disc model used for VATs showing two discs/control volumes in series, representing the upstream and downstream sections of the VAT.

Energy is conserved between the upstream stations (1 and 2) and between the downstream stations (3 and 4). Applying energy conservation between the upstream and downstream stations of a disc yields:

$$p_1 + \frac{1}{2}\rho {V_1}^2 = p_2 + \frac{1}{2}\rho {V_2}^2 \tag{5.4}$$

$$p_3 + \frac{1}{2}\rho {V_3}^2 = p_4 + \frac{1}{2}\rho {V_4}^2 \tag{5.5}$$

It is assumed that stations 1 and 4 are sufficiently far upstream and downstream of the disc, respectively, that the pressures are equal ($p_1 = p_4$) and also that stations 2 and 3 are located immediately upstream and downstream of the disc such that $V_2 = V_3$. Solving for $(p_2 - p_3)$ using Equations (5.3) and (5.4) and substituting into Equation (5.5) gives:

$$T = \frac{1}{2}\rho A_2 \left({V_1}^2 - {V_4}^2\right) \tag{5.6}$$

Equating the thrusts from Equations (5.2) and (5.6) and recognising $\dot{m} = A_2 V_2$ gives:

$$V_2 = \frac{V_1 + V_4}{2} \tag{5.7}$$

The fluid velocity through the disc is, therefore, the average of the upstream and downstream velocities. The axial induction factor, a, quantifies by how much a turbine rotor reduces the upstream flow velocity; it is the fractional reduction in velocity between the free-stream and the disc, and is described mathematically as:

$$a = \frac{V_1 - V_2}{V_1} \tag{5.8}$$

The local velocity at the disc, V_2, (also known as the induced velocity, V_a) and the downstream velocity, V_4, can now be expressed as a function of the free-stream velocity and the induction factor as:

$$V_2 = V_1 (1 - a) \tag{5.9}$$

$$V_4 = V_1 (1 - 2a) \tag{5.10}$$

Substituting Equation (5.10) into Equation (5.6), the axial thrust can be defined in terms of the axial induction factor as:

$$T = 2\rho A_2 {V_1}^2 a(1 - a) \tag{5.11}$$

The stream-wise force coefficient, $C_{x,MOM}$ (MOM indicates it is calculated from momentum (actuator disc) theory), is defined as the ratio of the thrust to the dynamic pressure

$$C_{x,MOM} = \frac{2\rho A_2 {V_1}^2 a(1 - a)}{0.5\rho A_2 {V_1}^2} \tag{5.12}$$

and can, therefore, be written as:

$$C_{x,MOM} = 4a(1 - a) \tag{5.13}$$

The power performance coefficient, C_{P}, is then:

$$C_{\mathrm{P}} = \frac{TV_2}{0.5\rho A_2 {V_1}^3} \tag{5.14}$$

Therefore,

$$C_{\mathrm{P}} = 4a(1 - a)^2 \tag{5.15}$$

It can be shown that the theoretical maximum C_{P} of a turbine, known as the Betz limit, is achieved when a =1/3 and is 0.59.

5.4 Important Model Assumptions

Some important fundamental assumptions of BEMT model are now presented to provide context for the model theory presented in subsequent sections:

1. Pressure recovery between tandem actuator discs. DMST models assume that there is sufficient slowing of the flow for pressure to recover to the ambient value between

the actuator discs within the turbine rotor. This is necessary in order to calculate a recovered flow velocity, which can be used for the downstream calculation. However, in the peripheral regions of the turbine, there is limited space between the disc and this assumption leads to overprediction of the recovered flow speeds in these regions.

2. Flow expansion only occurs in the horizontal (x-y) plane. Although flow is likely to expand in both the horizontal and vertical directions in response to the slowing of the fluid speed, flow expansion is limited to the horizontal plane. The consequence of omitting flow expansion in the vertical plane is a small overestimation in the hydrodynamic performance of a VAT [180].

3. Induction only occurs in the stream-wise direction (i.e. tangential induction is neglected). Blade element theory (BET) methods for HATs allow calculation of a tangential induction factor that quantifies wake rotation [181]. This induced flow perpendicular to stream-wise induction conserves angular momentum as a reaction to the flow rotating the blades. VATs also experience similar conditions, although the wake is deflected rather than rotated. Ferreira's BEMT model [180] shows that neglecting tangential induction results in an underestimation of the tangential force coefficient downstream and an overestimation of the tangential force coefficient for small regions of the upstream. As the tangential forces for the majority of the upstream are unaffected, this research adopts the common practice amongst researchers of resolving induction in the stream-wise direction only.

4. Straight stream-tubes: Where stream-tube expansion is accounted for, it is assumed that the stream-tubes are straight (see Figure 5.9) as per Sharpe's method, rather than sudden expansion at the mid-plane.

5.5 Blade Element Theory

The fluid dynamics of VATs are significantly more complicated than their horizontal axis counterparts. The variation in azimuthal position (θ) of the foil as it rotates through 360° results in variations in relative velocity, angle of attack, lift force and drag force, all of which are shown in Figure 5.3.

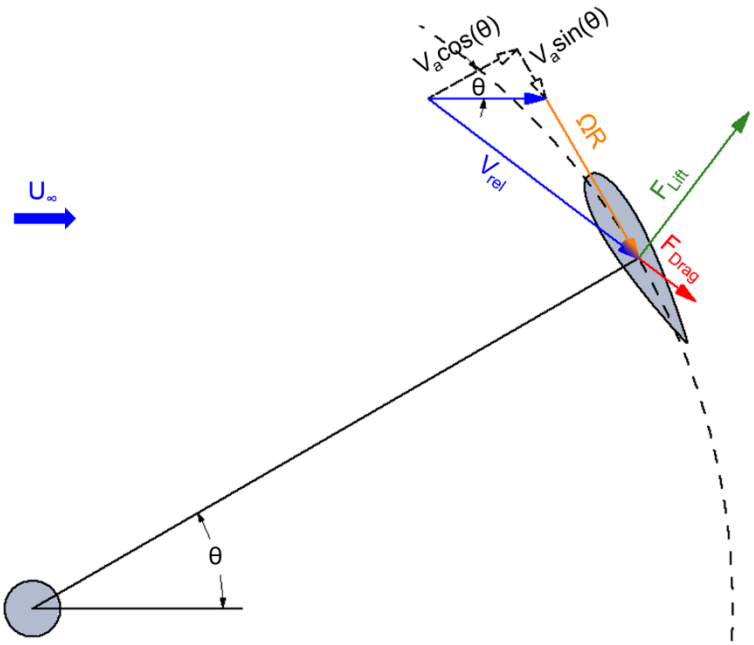

Figure 5.3: Schematic showing angles, forces and velocities on the blade element.

The relative velocity and the angle of attack, are determined using:

$$V_{rel} = \sqrt{V_a\, cos(\theta))^2 + (V_a\, sin(\theta) + \Omega R)^2} \tag{5.16}$$

$$\alpha = tan^{-1}\left(\frac{V_a\, cos(\theta)}{V_a\, sin(\theta) + \Omega R}\right) \tag{5.17}$$

where V_a is the induced actuator velocity, i.e. the reduced velocity at the rotor (as defined in Equation (5.9)), R is the turbine radius.

The lift and drag forces generated by the fluid on a blade element can also be expressed as forces tangential and normal to the blade chord. Non-dimensionalised tangential and normal force coefficients are determined using the tangential and normal components of the lift and drag coefficients as shown in Figure 5.4 and defined in Equation (5.18).

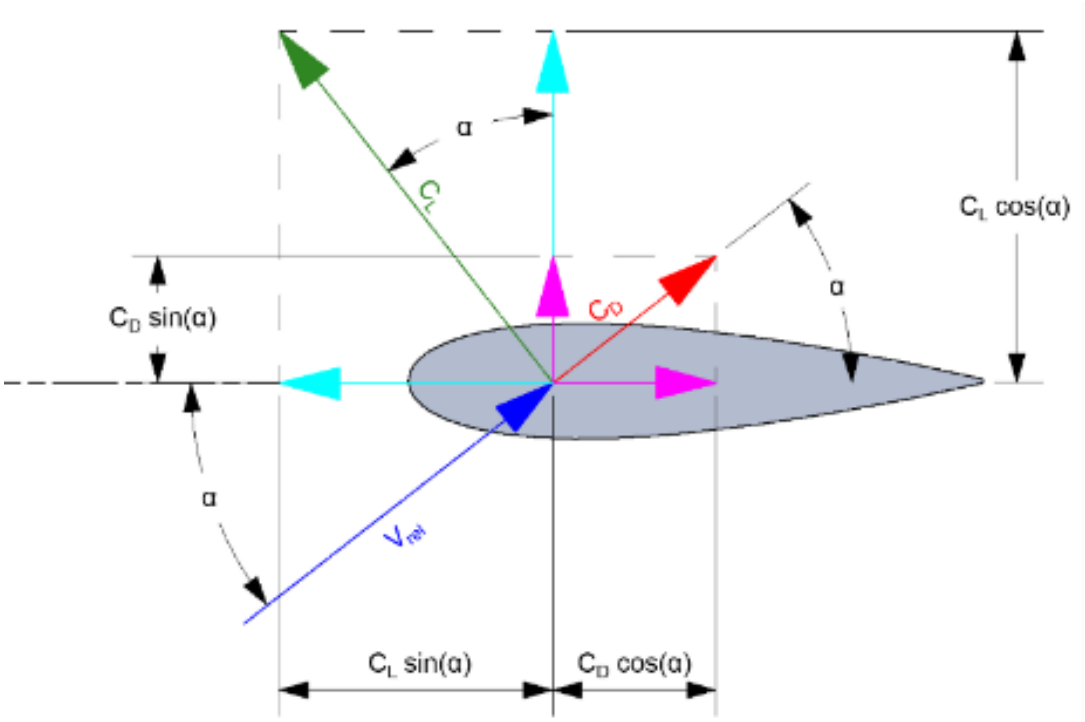

Figure 5.4: Schematic showing how lift and drag are related to the chord tangential and normal coefficients.

$$C_{\mathrm{T}} = C_{\mathrm{L}} \sin(\alpha) - C_{\mathrm{D}} \cos(\alpha)$$
$$C_{\mathrm{N}} = C_{\mathrm{L}} \cos(\alpha) + C_{\mathrm{D}} \sin(\alpha) \tag{5.18}$$

The tangential and normal forces are then determined from the tangential and normal coefficients as:

$$F_{\mathrm{T}} = \frac{1}{2} C_{\mathrm{T}} \rho A_c {V_{rel}}^2$$
$$F_{\mathrm{N}} = \frac{1}{2} C_{\mathrm{N}} \rho A_c {V_{rel}}^2 \tag{5.19}$$

A schematic of one of the multiple stream-tubes of the DMST model is shown in Figure 5.5, where $\Delta\theta$ is the angular portion of the azimuthal position spanned by the stream-tube. As already discussed, it is assumed that pressure recovers to free-stream levels between the upstream and downstream discs, and the incoming, or recovered, flow for the downstream is denoted V_{rec}. The stream-tube cross-sectional area is defined as:

$$A_s = \Delta L_B R \Delta\theta \cos\theta \tag{5.20}$$

where ΔL_B, is the vertical height of the stream-tube section.

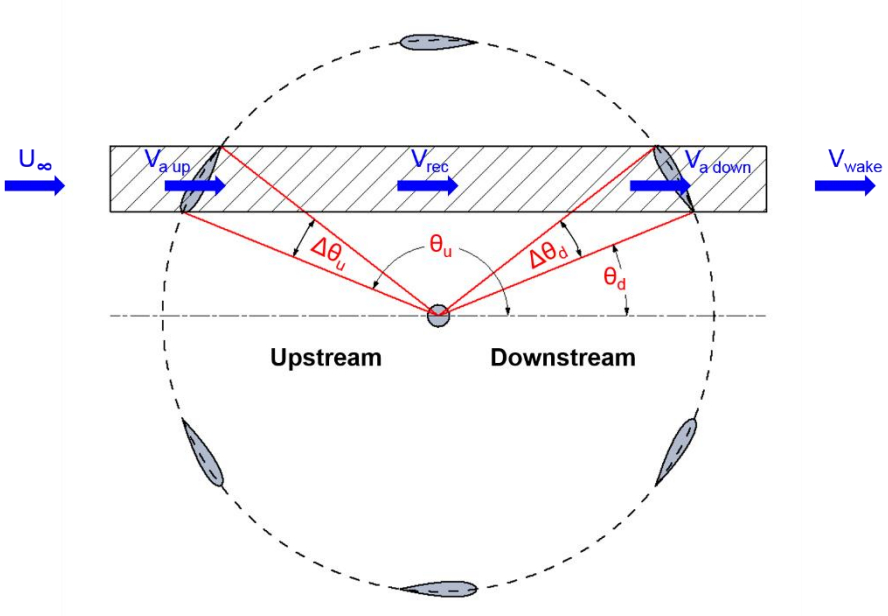

Figure 5.5: Definition of stream tube geometry for a vertical axis turbine (Note. Tube width is not proportional to chord-length, coincidence in the figure).

Each of the N_B blade elements spends $\frac{\Delta\theta}{2\pi}$ of the time in the stream-tube, as shown in Figure 5.5. The axial thrust for a particular stream-tube can be related to the stream-wise force F_x exerted on an individual blade element as it passes through the stream-tube as follows:

$$T = N_B F_x \frac{\Delta\theta}{2\pi} \tag{5.21}$$

Substituting for T from Equation (5.11) and combining with Equation (5.20) yields:

$$\frac{N_B F_x}{8\pi\rho R \Delta L_B cos(\theta) {U_\infty}^2} = a(1-a) \tag{5.22}$$

The tangential and normal forces, F_T and F_N, respectively and their stream-wise

resultant, F_x, are shown in Figure 5.6, and it can be seen that the resultant F_x is given by:

$$F_x = (F_\mathrm{N}\cos(\theta) - F_\mathrm{T}\sin(\theta)) \tag{5.23}$$

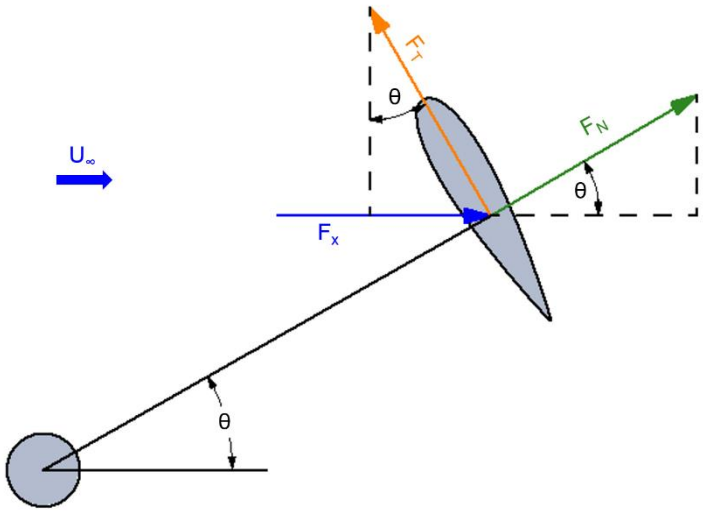

Figure 5.6: Schematic of normal, tangential and stream-wise forces acting on a blade element.

Combining Equations (5.18), (5.19), (5.22), and (5.23), the force coefficient for the BET model becomes:

$$C_{x,BET} = \frac{N_\mathrm{B}c}{8\pi R}\left(\frac{V_{rel}}{U_\infty}\right)^2 \sec(\theta)(C_\mathrm{N}\cos(\theta) - C_\mathrm{T}\sin(\theta)) \tag{5.24}$$

5.6 Graphical Method for Determining Induction Factors

To determine the axial induction factor and, by extension, the induced velocities and forces, either one of two approaches can be used. The first and most commonly used method involves an iteration of the force coefficient and induction factor until convergence is achieved. However, as was discussed in Chapter 2, this method suffers convergence issues for highly loaded rotors or high solidity rotors. The expression for the iteration is shown in Equation (5.25).

$$a = C_{x,BET} + a^2 \tag{5.25}$$

The second method was first introduced by McIntosh *et al*. [44]. The method involves generating two functions for the force coefficient, C_x, one using the force in the stream-wise direction calculated from the momentum model to give $C_{x,MOM}$ and the other using the force in the stream-wise direction calculated from the blade element model to give $C_{x,BET}$. The graphical method by McIntosh *et al*. is the method included in the present model. If the two functions are graphed for different values of a, then the point of intersection of the graphs is selected as the appropriate induction factor for that specific stream-tube. If one only uses Equation (5.13) (i.e. the momentum model) for the force coefficient, a reversed wake occurs for $a > 0.5$; this is erroneous and is due to the fact that for these values of a the majority of the fluid passes around the rotor, rather than through it, meaning the assumption that all of the flow passes through the enclosing stream-tube no longer holds true. The following empirical correction for the momentum model for high induction factors ($a > 0.4$) was developed empirically by Glauert [100]:

$$C_x(a > 0.4) = 0.86 + 1.56(a - 0.143)^2 \tag{5.26}$$

To determine $C_{x,MOM}$ Equation (5.13) is used for $a \leq 0.4$ and Equation (5.26) is used for $a > 0.4$. Equation (5.24) is used to determine $C_{x,BET}$.

With both expressions for force coefficient ($C_{x,BET}$ and $C_{x,MOM}$) fully defined, the graphical approach for determining the axial induction factor is now described. $C_{x,MOM}$ is calculated at the outset of the BEMT computation (twice in total upstream and downstream) while $C_{x,BET}$ is calculated for each individual stream-tube. The a value is seeded in the range of -1 to +1 (as recommended by McIntosh *et al*. [44]) in increments of 0.001. For each seeded value of a, the sign of $(C_{x,BET} - C_{x,MOM})$ is calculated and compared to that for the previous value of a so as to determine any crossing of the two force coefficient functions. If a crossing has occurred, then the current value of a is saved as a possible candidate value and the model then proceeds to the next seeded a value until all possible candidate values have been identified. In

most cases, there will be only one crossing and the corresponding candidate value of a is selected as the induction factor; this is shown in Figure 5.7 where there is a unique solution at $a = 0.275$.

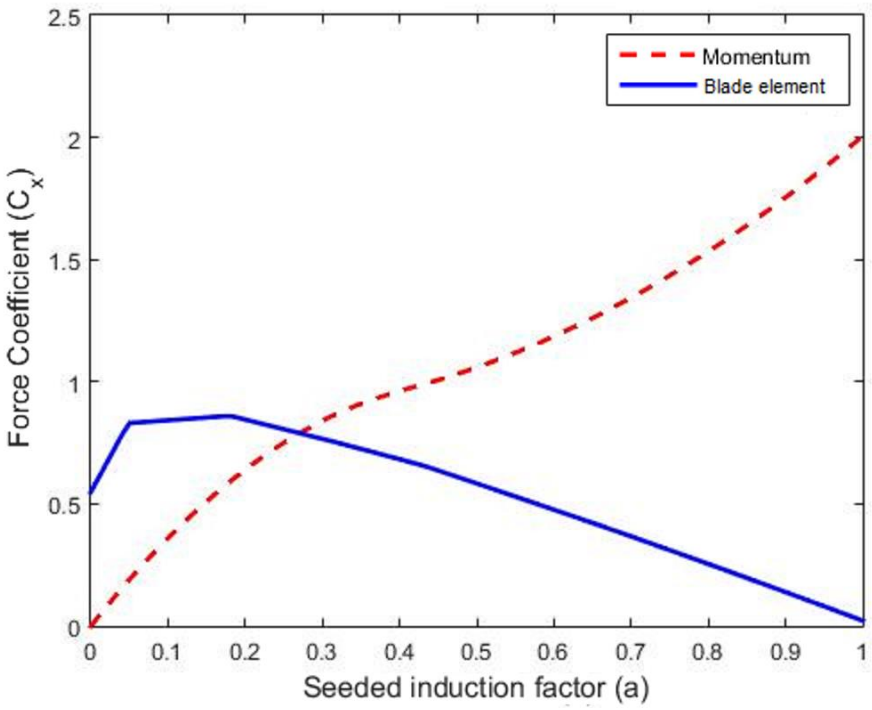

Figure 5.7: Momentum and blade element force coefficient with a single crossing point.

There are conditions, however, that results in multiple crossing points. This usually happens for highly loaded rotors and/or high solidity devices. The onset of blade stall results in a sharp drop in force coefficient resulting in multiple crossing points. McIntosh *et al.* [44] explain in detail the advantage of the graphical scheme over the iterative approach in this regard as it identifies all crossing points and allows the correct value of, a, to be selected. This is based on the current flow state, whereas, the iterative approach fails to determine any solution. Multiple crossing points are a consequence of stall on the blades and can occur during the onset of stall or flow reattachment; it is this issue that leads to convergence problems in the iterative scheme particularly for highly loaded rotors [44]. An example is shown in Figure 5.8. Each of the three crossing points defines a different flow state: (1) attached, (2) partial stall and (3) deep stall; however, partial stall is unstable and should never emerge as a solution [44]. Knowledge of the previous stream-tube solution is used to identify the most suitable of the attached or deep stall solutions.

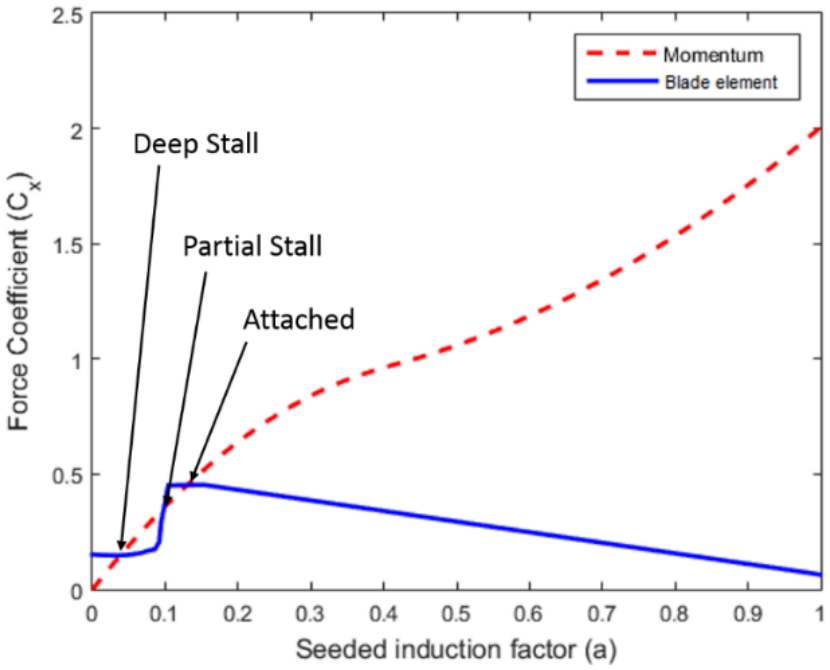

Figure 5.8: Momentum and blade element force coefficients with triple crossing point.

For each stream-tube, once the appropriate values of a are known the induced velocities (both upstream and downstream) are recalculated, as are the relative velocities and angles of attack. The Reynolds numbers are recalculated to determine the appropriate lift and drag coefficients from a prescribed database [34]. Subsequently, forces and overall coefficients are calculated

5.7 Corrections to Basic BEMT Model

Various corrections for the basic BEMT model have been developed by other researchers in an effort to correct or improve model accuracy. Corrections to account for flow expansion, finite aspect ratio blades and dynamic stall and variation of fluid velocity through the turbine height can all be incorporated into the developed model and their effects on model performance assessed. The corrections are implemented via function files in MATLAB which allows the corrections to be included or excluded from a model simulation.

5.7.1 Flow Expansion

The difficulty in accounting for flow expansion in a BEMT model is the delineation of the boundaries of the individual stream-tubes since the azimuthal positions of the

boundaries depend on the amount of flow expansion and, therefore, also on the induction factors. The method proposed by Sharpe [108] overcomes this difficulty by using a straight stream-tube approximation and calculating each stream-tube induction factor in a specific order. Induction factors for the central stream-tube are determined first. This allows calculation of the velocities, which in turn, allows determination of the degree of expansion of the first stream-tube. The alternate numbering convention shown in Figure 5.9 means the locations of the boundaries for stream-tubes 2 and 3 become known. The induction factors and velocities for stream-tubes 2 and 3 are calculated allowing determination of the boundaries for stream-tubes 4 and 5. This process continues until all induction factors and velocities have been determined.

The objective of a BEMT model is to balance blade element forces with the thrust in the direction of the stream-tube. A consequence of flow expansion is that the direction of the incoming flow, U_∞, deforms in a manner that tends to point away from the central stream-tube. The angle, θ, is defined relative to the free-stream direction of V_a. For induction factor calculations, a new angle is introduced in regard to the straight stream-tube. Momentum balance is instead defined using the angle, β, between the azimuthal positon at a stream-tube boundary and the straight stream-tube, as shown in Figure 5.10.

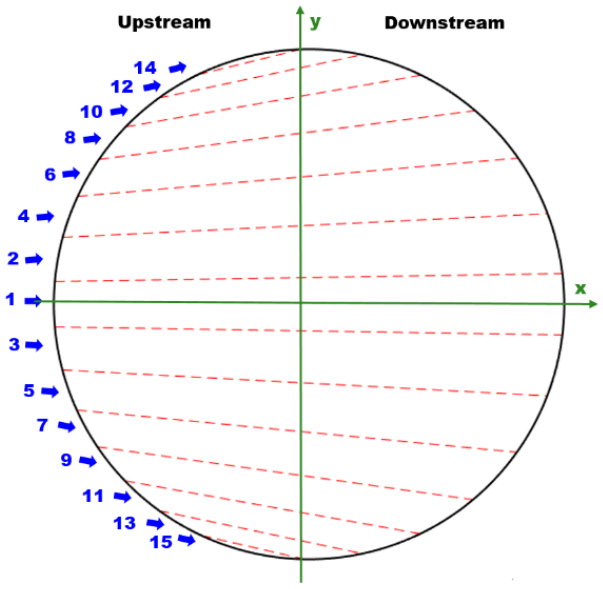

Figure 5.9: Alternating numbering convention used for determining stream-tube expansion.

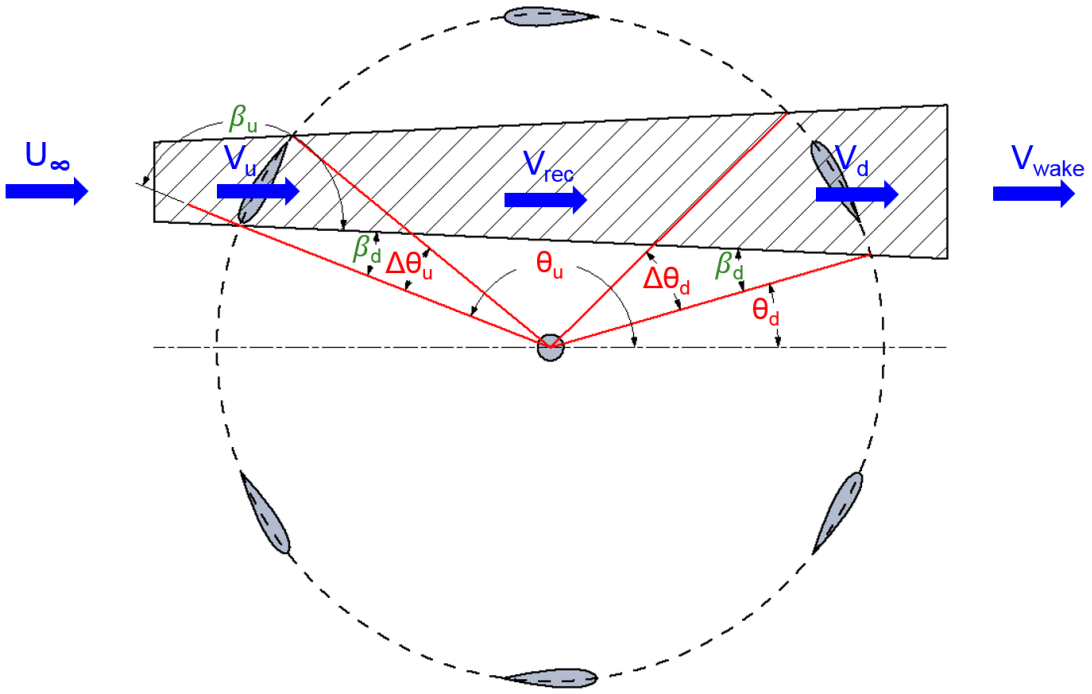

Figure 5.10: Flow and angles upstream and downstream of an expanding stream-tube (note. not an accurate representation of expansion, in reality, tube would be rotated in an anti-clockwise direction as per Figure 5.9.)

The normal and tangential aerodynamic forces can be transformed into the stream-tube direction using β. $\beta = 0^{o}$ for the central stream-tube, and β is then used to calculate the upstream and downstream induction factors and the degree of stream-tube expansion for that stream-tube. To demonstrate how to calculate the upstream and downstream actuator surface areas we use the stream-tube shown in Figure 5.11 with local flow velocities and actuator surface areas labelled. The upstream induction factor, a_u, must be determined before calculating the downstream induction factor, a_d. These are calculated using the method discussed in Section 5.6. Once both induction factors have been calculated for a stream-tube, the flow speeds V_u and V_d can be easily determined. The tube areas, A_u, and, A_d, are now introduced and shown in Figure 5.11.

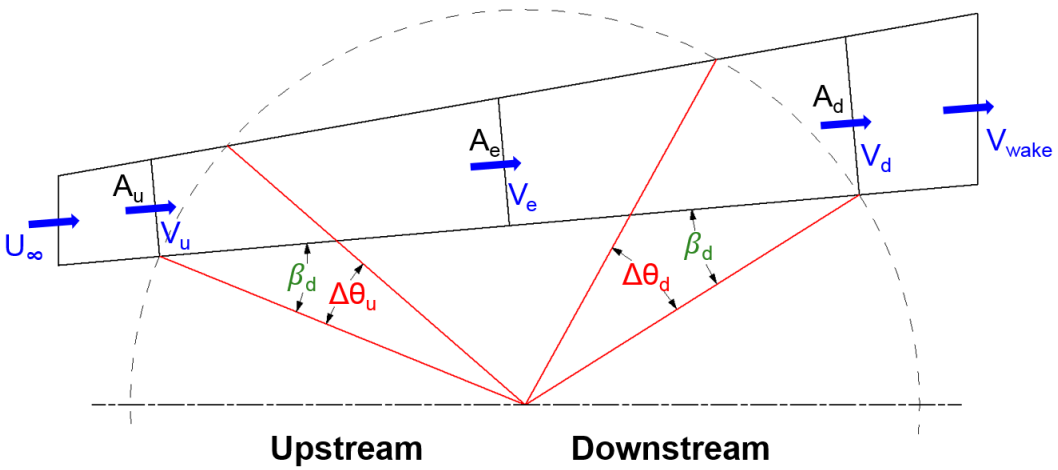

Figure 5.11: Graphical representation of the relationship between velocities and cross-sectional area due to mass conservation within the stream-tube.

Based on the straight stream-tube assumption, when expansion occurs there is one location between the upstream and downstream actuator surfaces that maintains the original area of the stream-tube prior to expansion. This location is referred to as the equilibrium point and the stream-tube area and flow speed at this point are known as the equilibrium stream-tube area, A_e, and the equilibrium flow speed, V_e (see Figure 5.11). A_e is the average of the up- and downstream areas:

$$2A_e = A_u + A_d \tag{5.27}$$

As the stream-tubes are assumed to be enclosed and the fluid density does not vary, conservation of mass gives:

$$V_u A_u = V_e A_e = V_d A_d \tag{5.28}$$

Combining Equations (5.27) and (5.28) gives:

$$2A_e = \frac{A_e V_e}{V_u} + \frac{A_e V_e}{V_d} \tag{5.29}$$

and simplifying this gives,

$$V_e = \frac{2V_u V_d}{V_u + V_d} \tag{5.30}$$

V_e should not be confused with V_{rec} which is the flow speed between the tandem actuator surfaces where pressure has recovered. A_e is independent of the induction factors because the straight streamlines pivot about this point for different induction factors. A_e is expressed as:

$$A_e = R|cos(\beta_d)|\,\Delta\theta\,\Delta L_{\mathrm{B}} \tag{5.31}$$

where $\Delta\theta = \frac{2\pi}{N_{tubes}}$. Splitting up the blade length into incremental ΔL_{B} values is required when blades are not straight, such as in the case of a Darrieus VAT, and also when a velocity profile is added to the model. Conservation of mass allows the up and downstream stream-tube areas, A_u and A_d, respectively to be determined. As mentioned already, flow expansion of the central stream-tube is determined first before considering the adjacent outer stream-tubes. Therefore, the series of arcs subtended by actuator surfaces is built up cumulatively as the procedure progresses from the centre stream-tube towards the edge of the swept area. From Figure 5.11, it is clear the boundaries of the adjacent stream-tubes can be determined if the upstream and downstream expansion angles, $\Delta\theta_u$ and $\Delta\theta_d$ are known.

Since A_u can be defined in two ways as:

$$A_u = R|cos(\beta_d)|\,\Delta\theta_u\,\Delta L_{\mathrm{B}} = \frac{2V_d}{V_u + V_d} R|cos(\beta_d)|\,\Delta L_{\mathrm{B}} \tag{5.32}$$

we can cancel the common terms to give the upstream expansion angle:

$$\Delta\theta_u = \frac{2V_d}{V_u + V_d} \tag{5.33}$$

Similarly, we can calculate the downstream expansion angle as:

$$\Delta\theta_d = \frac{2V_u}{V_u + V_d} \tag{5.34}$$

5.7.2 Finite Aspect Ratio

For an aero/hydrofoil, the aspect ratio (AR) is the ratio of the foil length to the chord-length:

$$AR = \frac{L_B}{c} \tag{5.35}$$

Foil databases, such as those from Sheldal and Klimas [34], are only available for infinite aspect ratios. Since rotor blades have a finite aspect ratio, the use of an infinite aspect ratio databases in a BEMT model can lead to inaccuracies. Corrected C_L and C_D values can be calculated for foils of finite aspect ratios. Different correction methods are used depending on the angle of attack and the static stall angle. Infinite aspect ratio C_L values will be larger at all angles of attack, while infinite aspect ratio C_D values will be smaller for $\alpha < \alpha_{ss}$ (Figure 5.12) and larger for $\alpha > \alpha_{ss}$.

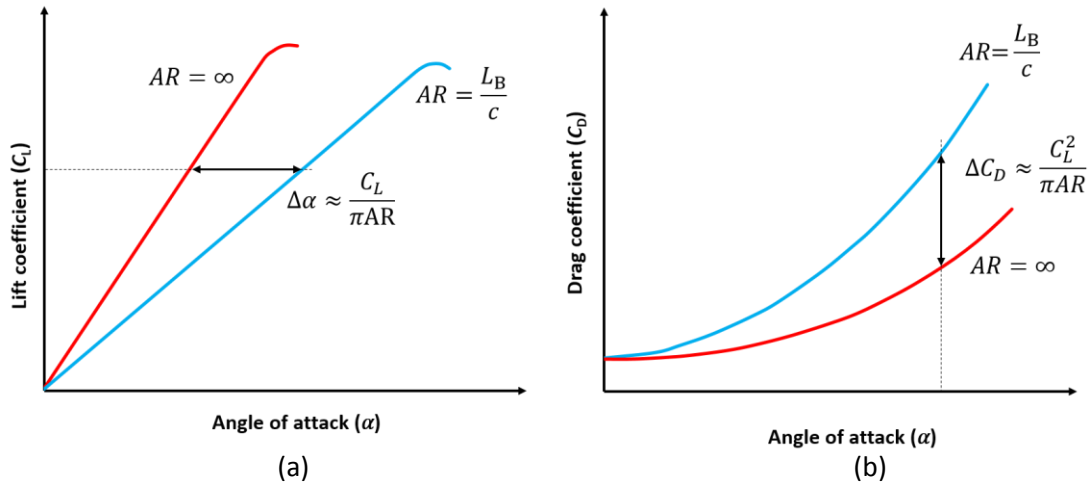

Figure 5.12: Effect of finite aspect ratio on (a) lift and (b) drag of an aerofoil showing effective angle of attack increase and induced drag increase. (Adapted from White [27])

Below α_{ss}, the Lanchester-Prandtl theory can be used to accurately estimate the finite aspect ratio aerofoil lift and drag characteristics from infinite aspect ratio data [114]. Finite aspect ratio blades experience blade tip vortices which cause a downwash and alter the effective angle of attack and aerofoil characteristics. The linear part of the lift curve is calculated using:

$$C_{\mathrm{L}} \approx \frac{2\pi\left(\alpha + 2\frac{h}{c}\right)}{1 + \frac{2}{AR}} \tag{5.36}$$

where h/c is the maximum camber expressed as a fraction of the chord-length. For aerofoils that are not cambered, h/c is equal to zero.

The effective angle of attack increases and the amount by which it changes can be related to the lift coefficient using the expression:

$$\Delta\alpha \approx \frac{C_{\mathrm{L}}}{\pi AR} \tag{5.37}$$

The drag coefficient also increases and this increase can be calculated using:

$$\Delta C_{\mathrm{D}} \approx \frac{C_{\mathrm{L}}^2}{\pi AR} \tag{5.38}$$

For angles of attack greater than the static stall angle and up to 90^{o}, Viterna and Corrigan [115] developed the following set of correction equations:

$$C_{\mathrm{L}_{VC}} = A_1\, sin(2\alpha) + \ A_2 \frac{\cos^2(\alpha)}{\sin(\alpha)} \tag{5.39}$$

$$C_{\mathrm{D}_{VC}} = B_1 \sin^2(\alpha) + \ B_2 \cos(\alpha) \tag{5.40}$$

where $C_{\mathrm{L}_{VC}}$ and $C_{\mathrm{D}_{VC}}$ are the Viterna and Corrigan corrected lift and drag coefficients, respectively.

For $AR \leq 50$, the coefficients A1 and B1 can be calculated as follows:

$$A_1 = \frac{C_{\mathrm{D}_{max}}}{2} \tag{5.41}$$

$$B_1 = C_{\mathrm{D}_{max}} \tag{5.42}$$

where $C_{\mathrm{D}_{max}}$, the maximum drag coefficient for a finite aspect ratio foil, is calculated from the AR value as:

$$\mathrm{C_{D_{max}}} = 1.11 + 0.18\,\mathrm{AR} \tag{5.43}$$

The variables of A_2 and B_2 for the Viterna and Corrigan model are solved at the static stall angle condition for continuity with the 'below stall' data determined using the Lanchester-Prandtl theory.

$$A_2 = \left(C_{\mathrm{L}_{SS}} - C_{\mathrm{D}_{max}}\, sin(\alpha_{SS})\, cos(\alpha_{SS})\right) \frac{\sin(\alpha_{SS})}{\cos^2(\alpha_{SS})} \tag{5.44}$$

$$B_2 = C_{\mathrm{D}_{SS}} - \frac{C_{\mathrm{D}_{max}} \sin^2(\alpha_{SS})}{cos(\alpha_{SS})} \tag{5.45}$$

Castelli *et al.* [116] reported that the data correction method of Viterna and Corrigan resulted in an overestimation of the lift coefficient after the stall angle. Together with a decrease of the drag coefficient, this can result in an overestimation of rotor performance. To avoid this over-prediction, Castelli *et al.* [116] recommended computing modified finite aspect ratio aerofoil characteristics based on a linear interpolation between the two-dimensional values of aerofoil lift and drag coefficients and the finite aspect ratio coefficients obtained by the Viterna and Corrigan model, giving:

$$C_{\mathrm{L}} = \frac{\left(C_{\mathrm{L}_{AR=\infty}} + C_{\mathrm{L}_{VC}}\right)}{2} \tag{5.46}$$

$$C_{\mathrm{D}} = \frac{\left(C_{\mathrm{D}_{AR=\infty}} + C_{\mathrm{D}_{VC}}\right)}{2} \tag{5.47}$$

This is the approach that has been adopted in the present BEMT model.

5.7.3 Velocity profile

The author's BEMT model has the capability to account for the vertical variation in velocity distribution through a fluid. The model allows for incremental calculations along the vertical length of the blade, therefore allowing the incoming velocity to be varied along the vertical span of the turbine rotor. The velocity profile is described using a power law where the velocity at height, z, above the seabed (U_z) is defined as:

$$U_z = \left(\frac{z}{\zeta\, h_w}\right)^{\frac{1}{n}} \overline{U} \tag{5.48}$$

where ζ is the roughness coefficient, h_w is the total water depth and $\overline{U}$ is the depth averaged velocity. Values of n = 7 and ζ = 0.4 are used as recommended by literature [182]. It was shown that on average the power law accurately represented the velocity profile for numerous sites for over one month's worth of ADCP data. Figure 5.13 shows how the velocity profile varies with height using the power law. The model can be run using either a depth-averaged velocity or the more realistic velocity profile described.

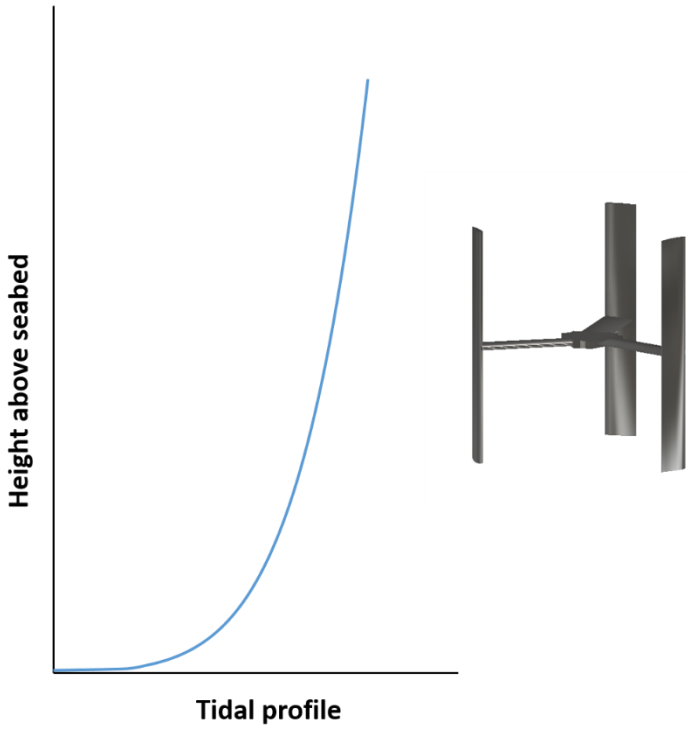

Figure 5.13: Velocity profile determined using power law with turbine showing the vertical variation of inlet velocity (drawing not to scale).

Although developed for tidal turbines, the BEMT model is also applicable to wind turbines and one of the performance assessment applications in the results section is a 500 kW wind turbine. For large turbines like this, it is important to account for the variation of wind velocity with height. The following formula from McIntosh [183] is used to estimate the wind shear velocity profile:

$$U_z = U_{ref} \frac{\left(ln\frac{z}{z_0}\right)}{\left(ln\frac{z_{ref}}{z_0}\right)} \tag{5.49}$$

U_{ref} is the velocity at a reference height, z_{ref}, while z_0 is the terrain roughness height. Table 5.1 presents a comprehensive guide for what z_0 value should be incorporated into the calculation, depending on terrain.

Table 5.1: Terrain roughness heights for various categories [183].

$\boldsymbol{z_0}$ (m)	Classification	Landscape description
0.0002	Sea	Water surface: open sea or lake
0.005	Smooth	Featherless land: beaches, marsh and fallow land
0.03	Open	Level open country: Heather, moor and tundra.
0.1	Roughly open	Open agricultural: Cultivated or natural area, low crops
0.25	Rough	Built agricultural: High crops and buildings.
0.5	Very rough	Suburban: Landscape with many large obstacles
1	Skimming	Towns: Densely built-up area.
≥ 2	Chaotic	High-rise: Mixture of low and high-rise buildings.

5.8 Model Structure and Solution Procedure

The model was created by encoding the relevant actuator disc and blade element model equations and the graphical approach for determination of induction factor within MATLAB. This basic BEMT model was then augmented by encoding corrections to the governing equations for the effects of flow expansion, finite aspect ratio blades, dynamic stall and a depth-varying velocity profile. Code to read in required input data and generate required model output was also written. The final BEMT model is structured in three separate parts represented graphically in Figure 5.14 and summarised as follows:

Stage 1 - *Model Initialisation*: The model is initiated by reading in the required input data including turbine geometry, free-stream flow conditions, lift and drag coefficients for the particular aerofoil, and the specification of the stream-tube geometry.

Stage 2 – *Local Solution*: First, fluid velocities are calculated using seeded induction factor values. These velocities are subsequently used to calculate more accurate induction factor values using the graphical approach and the velocities are then recalculated (Section 5.6). This procedure is repeated for every actuator point (2 per stream-tube, i.e. upstream and downstream) around the turbine swept area. At the end of the stage, all local flow velocities, angles and dynamic forces for each stream-tube are stored for a particular λ value. Corrective methods can be switched on and off in the model in an attempt to improve the model accuracy. The methods incorporated into the developed BEMT model include: Flow expansion (Section 5.7.1), Finite aspect ratio correction (Section 5.7.2), and Dynamic stall (Section 5.8.1).

Stage 3 – *Global Solution*: the contributions from each stream-tube are calculated and combined to determine the performance of the rotor as a whole in terms of torque, thrust and power. The relevant model variables are output for interrogation/analysis.

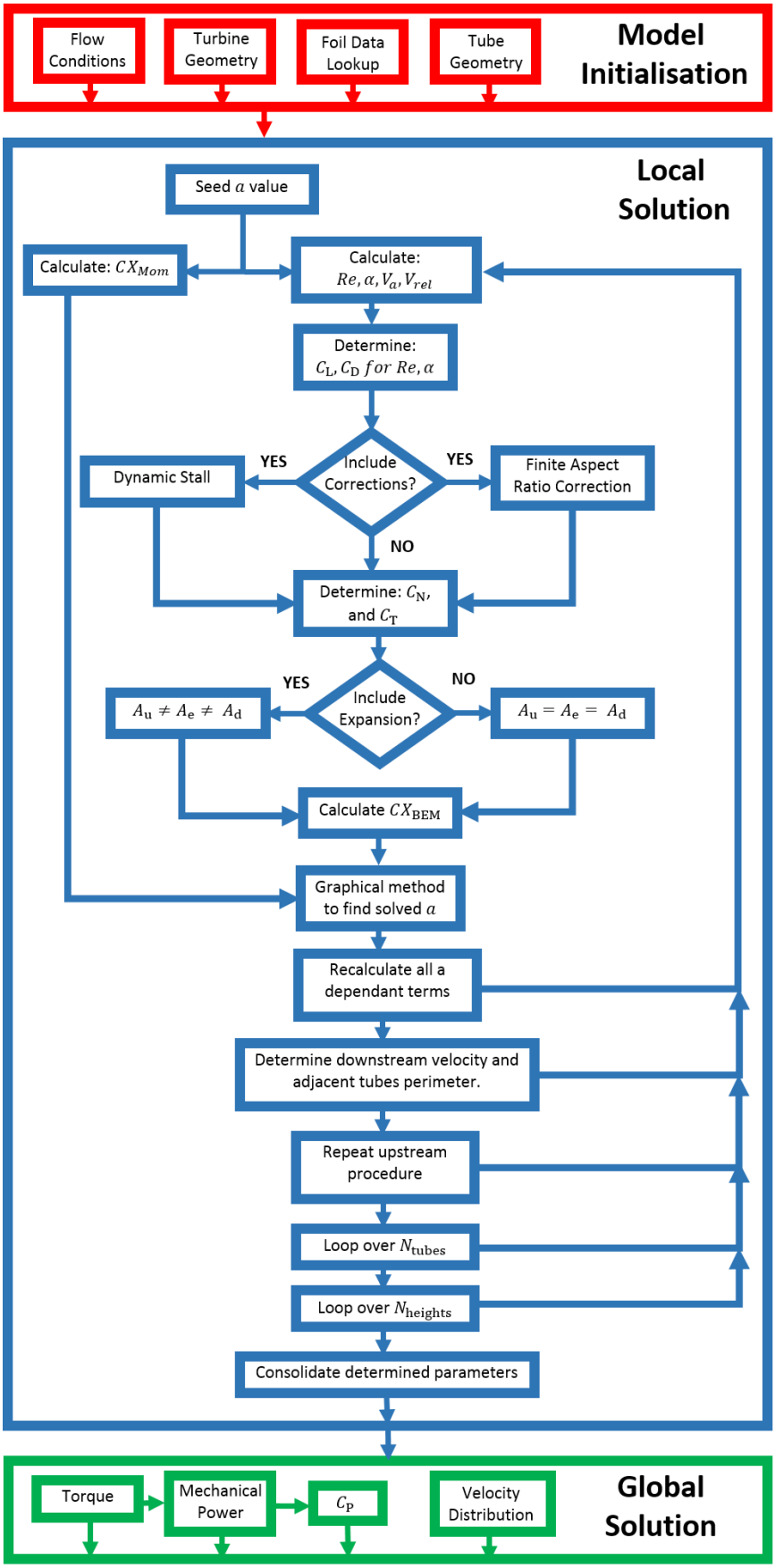

Figure 5.14: Process flowchart showing BEMT code structure

5.8.1 Dynamic Stall

A dynamic stall model was implemented in the BEMT model in order to correct for the use of static foil lift and drag coefficients. Dynamic stall is most significant at lower λ values where the local angle of attack is above the static stall angle. As the blade rotates, the angle of attack changes and a vortex is shed from the leading edge of the foil. Dynamic stall is dependent on a wide range of parameters including foil shape, Mach number, Reynolds number and the rate of change of angle of attack. The dynamic stall model implemented here is based on Gormont's model [39], with modifications by Massé [111] and Berg [112] included. As the Gormont model was initially used to predict the performance of helicopter rotors, Massé [111] and Berg [112] made modifications to enable this model to be applied to VATs. In order to apply the Gormont model, the time derivative of α ($\dot{\alpha}$) is required.

The Gormont model empirically mimics the hysteresis behaviour of an aerofoil by defining a reference angle of attack at which the static two-dimensional coefficient data is considered. This reference angle of attack, α_{ref}, is expressed as:

$$\alpha_{ref} = \alpha - K_1 \Delta\alpha \tag{5.50}$$

where,

$$K_1 = \begin{cases} 1 & \text{when } \dot{\alpha} \geq 0 \\ -0.5 & \text{when } \dot{\alpha} < 0 \end{cases} \tag{5.51}$$

and,

$$\Delta\alpha = \begin{cases} \gamma_1 S & \text{when } S \leq S_c \\ \gamma_1 S_c + \gamma_2 (S - S_c) & \text{when } S > S_c \end{cases} \tag{5.52}$$

The variables in Equation (5.52) have the following expressions:

$$\gamma_1 = \begin{cases} \frac{\gamma_2}{2} & \text{for lift} \\ 0 & \text{for drag} \end{cases} \tag{5.53}$$

$$\gamma_2 = \gamma_{max} max\left\{0, \min\left[\frac{1, M_a - M_2}{M_2 - M_1}\right]\right\} \tag{5.54}$$

$$S_c = 0.06 + 1.5(0.06 - t_c) \tag{5.55}$$

where t_c is the profile thickness

$$S = \sqrt{\frac{c\dot{\alpha}}{2V_{rel}}} \tag{5.56}$$

In Equation (5.54), M_a is the Mach number and is given by:

$$M_a = \left|\frac{V_{rel}}{c_{speed}}\right| \tag{5.57}$$

Expressions for the other variables in Equation (5.54) are given in Table 5.2.

Table 5.2: Specific forms of M_1, M_2, and γ_{max} for lift and drag.

	Lift	Drag
M_1	$0.4 + 5(0.06 - t_c)$	0.2
M_2	$0.9 + 2.5(0.06 - t_c)$	$0.7 + 2.5(0.06 - t_c)$
γ_{max}	$1.4 - 6(0.06 - t_c)$	$1.0 - 2.5(0.06 - t_c)$

The dynamic stall lift and drag coefficients are then calculated as:

$$C_{\mathrm{L}}^{dyn} = C_{\mathrm{L}}(\alpha_0) + m(\alpha - \alpha_0) \tag{5.58}$$

$$C_{\mathrm{D}}^{dyn} = C_{\mathrm{D}}(\alpha_{ref}) \tag{5.59}$$

where α_0 is any convenient angle of attack but is typically taken as the zero-lift angle

of attack and m is calculated as:

$$m = \left[\frac{C_{\mathrm{L}}(\alpha_{ref}) - C_{\mathrm{L}}(\alpha_0)}{\alpha_{ref} - \alpha_0}, \frac{C_{\mathrm{L}}(\alpha_{SS}) - C_{\mathrm{L}}(\alpha_0)}{\alpha_{SS} - \alpha_0}\right] \tag{5.60}$$

In Gormont's model for helicopter blades, the maximum angle of attack reached is much lower than in the case of a VAT blade. As observed by Massé [111] and reported by Mason *et al.* [184] this means that the Gormont model overpredicts the effects of the dynamic stall on VAWT performances. In order to avoid this, Massé [111] proposed to calculate modified dynamic coefficients based on a linear interpolation between the dynamic coefficients predicted by the Gormont model and the static coefficients as follows:

$$C_{\mathrm{L}}^{mod} = \begin{cases} C_{\mathrm{L}} + \left[\dfrac{A_{\mathrm{M}}\,\alpha_{SS} - \alpha}{A_{\mathrm{M}}\,\alpha_{SS} - \alpha_{SS}}\right]\left(C_{\mathrm{L}}^{dyn} - C_{\mathrm{L}}\right) & \alpha \le A_{\mathrm{M}}\,\alpha_{SS} \\ C_{\mathrm{L}} & \alpha > A_{\mathrm{M}}\,\alpha_{SS} \end{cases} \tag{5.61}$$

$$C_{\mathrm{D}}^{mod} = \begin{cases} C_{\mathrm{D}} + \left[\dfrac{A_{\mathrm{M}}\,\alpha_{SS} - \alpha}{A_{\mathrm{M}}\,\alpha_{SS} - \alpha_{SS}}\right]\left(C_{\mathrm{D}}^{dyn} - C_{\mathrm{D}}\right) & \alpha \le A_{\mathrm{M}}\,\alpha_{SS} \\ C_{\mathrm{D}} & \alpha > A_{\mathrm{M}}\,\alpha_{SS} \end{cases} \tag{5.62}$$

where $A_M = 6$ is a revised value for A_M proposed by Berg [112], over the initial value of $A_M = 1.8$ proposed by Massé, as Berg found the revised value gave better agreement with experimental data for a SANDIA wind turbine. Berg [112] also recommended that α_{ss} be taken as the angle where C_{L} is no longer increasing linearly as opposed to previous work which took α_{ss} as the angle of maximum C_{L}. These dynamic stall corrections were incorporated into the model.

5.9 Model Geometry and Foil Characteristic Data

This section outlines how the turbine rotor perimeter is subdivided into a collection of actuator surfaces and discusses the characteristic aerofoil data for lift and drag that are incorporated into the model.

5.9.1 Rotor Mesh and Stream-tube Expansion

The perimeter of the turbine rotor is subdivided into a number of sections which make up the actuator discs. As DMST models use two actuator discs in tandem, the 15 tubes shown in Figure 5.15 have a total of 30 actuator surfaces (15 upstream and 15 downstream). The angle convention used in the author's model (explained in Section 5.7.1) follows that used by Sharpe [108] in the development of his BEMT model which includes stream-tube expansion using the assumption of straight stream-tubes.

The inclusion of flow expansion adds more complexity to the model. Sharpe's method of calculating from the central stream-tube outwards allows identification of adjacent stream-tube boundaries. As was documented earlier in this thesis, mass conservation within a stream-tube means that if the downstream velocity decreases due to axial induction, the area occupied by the flow must expand. A BEMT model which captures flow expansion must, therefore, have upstream tube areas that are smaller than the downstream tube areas, as is shown in Figure 5.15 (b). The increasing cross-sectional area of each stream-tube in the stream-wise direction means that the rotor spends more time in the downstream section of each stream-tube compared to the upstream section. The symmetrical nature of the stream-tube expansion shown in Figure 5.15 (b) is a consequence of neglecting tangential induction. Flow expansion correction was discussed in Section 5.7.1.

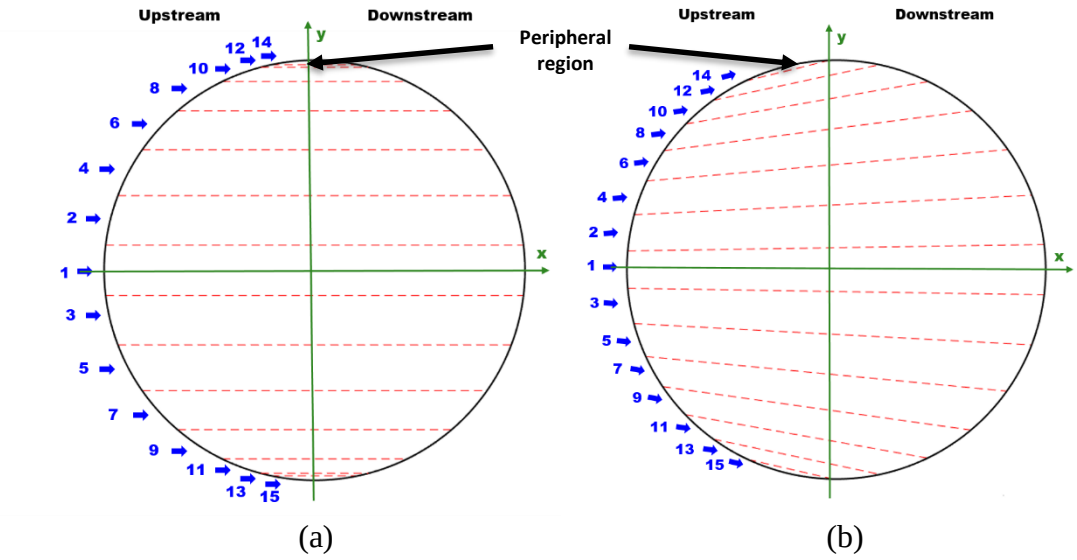

Figure 5.15: Stream-tubes showing a typical rotor division (a) without flow expansion and (b) with flow expansion.

5.9.2 Aerofoil Lift and Drag Data

The performance of any turbine rotor is greatly influenced by the choice of aero/hydrofoils and foil lift and drag data is, therefore, a required input to all BEMT models to enable calculation of blade element forces. These data are usually stored in lookup tables that contain the coefficients of lift and drag for a range of angles of attack and Reynolds numbers (chord-length). All of the model simulations in this research use symmetric NACA aerofoils and the appropriate aerofoil database sourced from Sheldahl and Klimas [34].

Reynolds number has a significant impact on the aerodynamic/hydrodynamic characteristics of the aerofoil/hydrofoil and the Reynolds number varies as the blade rotates. It is therefore imperative that a VAT performance estimation model incorporates the correct Reynolds number for every azimuthal position. The developed BEMT model recalculates the Reynolds number at each azimuthal location around the path of rotation and for every value of a, since there is a direct relationship between a, Reynolds number and relative velocity. Figure 5.16 and Figure 5.17 shows how C_{L} and C_{D}, vary for a range of α values and for different Reynolds numbers. The data presented in the figures is for a NACA 0018 aerofoil section from the Sheldahl and Klimas database.

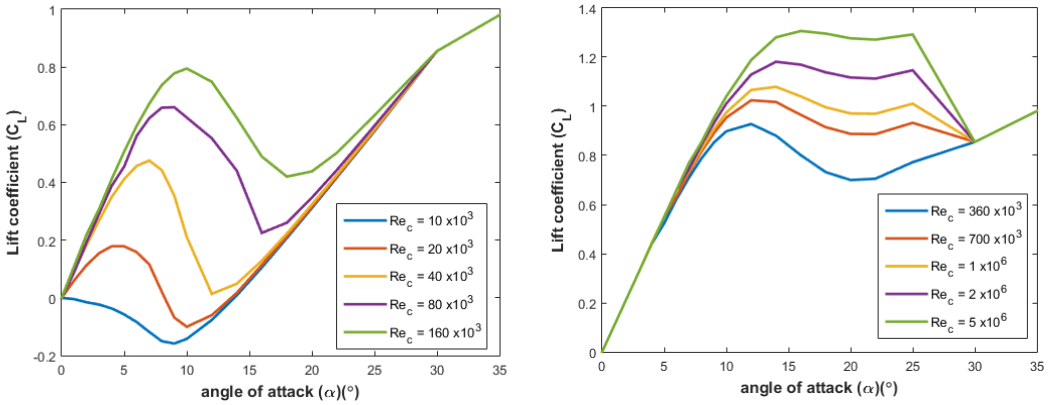

(a) (b)

Figure 5.16: Variation of lift coefficient with Reynolds number over a range of angle of attack

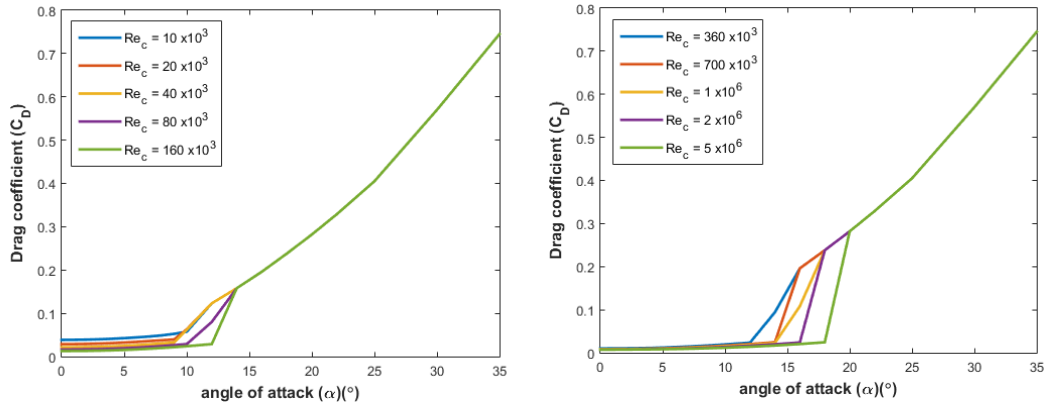

(a) (b)

Figure 5.17: Variation of drag coefficient with Reynolds number over a range of angle of attack.

5.10 Model Outputs

The overall turbine torque can be determined by taking moments about the axis of rotation of the forces acting on a unit length of blade as shown in Figure 5.18. This torque may then be expressed as:

$$Q = \frac{1}{2} {V_{rel}}^2 \rho c \left(C_T R \pm C_N \frac{c}{4} \right) \tag{5.63}$$

The thrust, T, is an instantaneous force (in that it occurs only as a blade crosses a stream-tube) but a time-averaged force is required. To obtain this, the chord-length, c,

in Equation (5.63) is replaced by:

$$\tilde{c} = \frac{Nc\Delta\theta}{2\pi} \tag{5.64}$$

where, $\frac{\Delta\theta}{2\pi}$ is the probability of a given blade being in any particular position during a time interval. From Equation (5.32), for a unit length of blade, $A = R|cos(\beta_d)|\,\Delta\theta$. Rearranging in terms of $\Delta\theta$ and substituting into Equation (5.64), therefore, gives:

$$\tilde{c} = \frac{N_\mathrm{B} c \mathrm{A}}{|cos(\beta_d)|2\pi R} = \frac{N_\mathrm{B} c}{2\pi R} A|sec(\beta_d)| \tag{5.65}$$

Replacing c in Equation (5.63) with $\tilde{c}$ gives the following expressions for the upstream (Q_u) and downstream (Q_d) torque:

$$Q_\mathrm{u} = \frac{1}{2}\rho {V_{\mathrm{rel}_\mathrm{u}}}^2 \frac{N_\mathrm{B} c}{2\pi R}|sec(\beta_d)|A_u \left(C_{\mathrm{T}_\mathrm{u}} R + C_{\mathrm{N}_\mathrm{u}} \frac{c}{4}\right) \tag{5.66}$$

and,

$$Q_\mathrm{d} = \frac{1}{2}\rho {V_{\mathrm{rel}_\mathrm{d}}}^2 \frac{N_\mathrm{B} c}{2\pi R}|sec(\beta_d)|A_d \left(C_{T_d} R - C_{N_d} \frac{c}{4}\right) \tag{5.67}$$

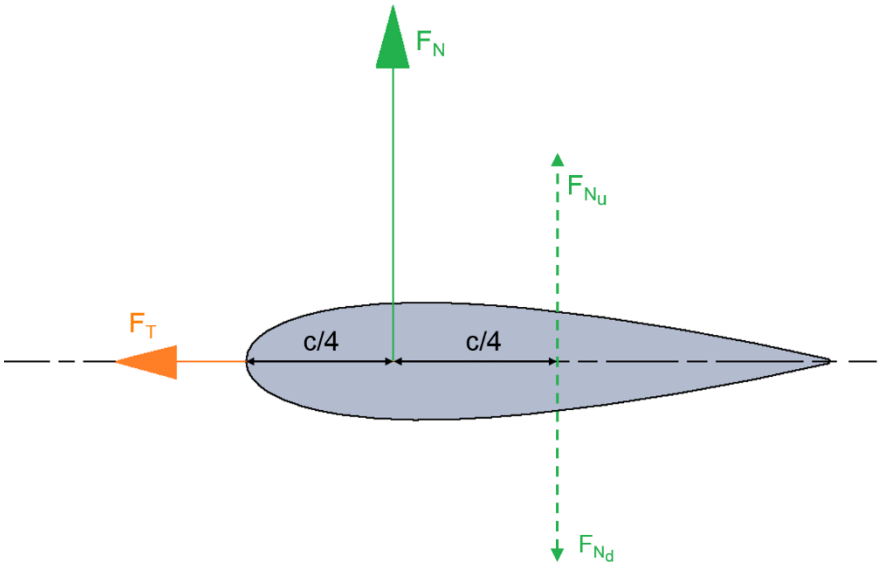

Figure 5.18: Blade element forces, showing the normal changing direction between up and downstream at the centre of rotation.

The average torque on a whole turbine, with blades of length L_B can then be determined by integrating along the span of the blade as well as around the circumference of the rotor and is given by:

$$Q_{avg} = \frac{N_B c}{2\pi R}\rho R \int_0^{L_B} \int_{-\frac{\pi}{2}}^{\frac{\pi}{2}} \left[{V_{rel_u}}^2 V_d \left(C_{T_u} R + C_{N_u} \frac{c}{4} \right) + {V_{rel_d}}^2 V_u \left(C_{T_d} R - C_{N_d} \frac{c}{4} \right) \right] \frac{1}{(V_u + V_d)} d\beta dL_B \tag{5.68}$$

The thrust force on the turbine can be determined by integrating the stream-wise forces:

$$T_{avg} = \frac{N_B c}{2\pi}\rho \int_0^{L_B} \int_{-\frac{\pi}{2}}^{\frac{\pi}{2}} \left[{V_{rel_u}}^2 V_d \left(C_{N_u} \cos(\beta_d) - C_{T_u} \sin(\beta_d) \right) + {V_{rel_d}}^2 V_u \left(C_{N_d} \cos(\beta_d) - C_{T_d} \sin(\beta_d) \right) \right] \frac{1}{(V_u + V_d)} d\beta dL_B \tag{5.69}$$

As mentioned by Sharpe [108], calculation of thrust in this way is not completely accurate, particularly for high λ values, because the expanding streamlines are not parallel and so stream-wise forces cannot be added algebraically. However, it is the most common method used in conjunction with the Sharpe method for flow expansion. The overall turbine power coefficient, C_P, has been defined in previous chapters.

Similarly, the overall turbine torque coefficient is defined as:

$$C_Q = \frac{Q_{avg}}{0.5\rho A {U_\infty}^2 R} \tag{5.70}$$

and the overall thrust coefficient is defined as:

$$C_T = \frac{T_{avg}}{0.5\rho A {U_\infty}^2} \tag{5.71}$$

5.11 Model Results

The performance of the BEMT model was assessed first, for a low solidity VAWT rotor and second, for a high solidity VATT rotor (Solidity is defined as Equation (5.72)). In both cases, modelled power performance data were compared with measured data obtained from published literature. The low solidity device was a full-scale 2-bladed 500 kW VAWT, the VAWT-850, tested by Mays *et al.* [185] while the high solidity turbine was a 3-bladed scale model VATT tested by Bachant and Wosnik [65]. The main physical characteristics of the turbines are summarised in Table 5.3. Five different models of each turbine were run to assess the effect of the various corrections on model performance both individually and cumulatively. The models are listed in Table 5.4 along with their respective acronyms. A wind velocity profile was incorporated into the BEMT for the VAWT 850 using Equation (5.48) and Table 5.1. As the turbine was constructed at a relatively open terrain, a terrain value of 0.03 m was used to develop the velocity profile. As the high solidity turbine was tow tested, As the high solidity turbine was tow tested, the inlet velocity was taken as the tow speed., rather than apply the velocity distribution profile as described previously. The power performance results from the various models are presented in, C_{P}, versus λ curves.

$$\sigma = \frac{\text{total blade area}}{\text{rotor swept area}} = \frac{N_{\mathrm{B}} c L_{\mathrm{B}}}{\pi D L_{\mathrm{B}}} = \frac{N_{\mathrm{B}} c}{\pi D} \tag{5.72}$$

Table 5.3: Details of the low and high solidity VATs used to assess model accuracy.

Blades $\boldsymbol{N_{\mathrm{B}}}$	Turbine Type	Diameter $\boldsymbol{D}$ (m)	Chord-length $\boldsymbol{c}$ (m)	Blade Length $\boldsymbol{L_{\mathrm{B}}}$ (m)	NACA Profile	Solidity $\boldsymbol{\sigma}$
2	Wind	35	1.5 to 1.75	24.3	0018	0.03
3	Tidal	1	0.14	1	0021	0.28

Table 5.4: Description of model acronyms presented in figures.

Description	Model Acronym
Basic BEMT model without any corrections.	Basic-BEMT
Basic BEMT plus flow expansion correction only.	BEMT-FE
Basic BEMT plus finite aspect ratio correction only.	BEMT-FAR
Basic BEMT plus dynamic stall model only.	BEMT-DS
Basic BEMT plus all corrections.	BEMT-ALL

Figure 5.19 compares BEMT model results with measured data for the low solidity wind turbine. The basic BEMT model predicts the appropriate performance trend with the peak performance ($C_{\mathrm{P}max}$) occurring at the same λ value of 3.5 as the measured data but it overpredicts C_{P} for all λ values. Looking first at the individual effects of the model correction, when flow expansion is included there is no obvious change in model results for $\lambda < 3$ but model accuracy is improved for higher λ values (i.e. $\lambda > 3.5$); this is most likely because the stream-tubes experience greater expansion at higher λ values. The finite aspect ratio correction has a negligible effect overall although it does slightly improve model accuracy at lower λ values ($\lambda < 2$). Including dynamic stall leads to a reduction of C_{P} values for lower λ values ($\lambda < 4$) and thus better agreement with measured data for this portion of the power curve. Of all three corrections, this one results in the most accurate prediction of $C_{\mathrm{P}max}$ compared to the basic BEMT model with a difference of just 6.4 % compared to the measured value. As λ increases above 4, the effect of the dynamic stall model diminishes and above $\lambda = 5$ it has no discernible effect. This is likely because as λ increases the ranges of α values experienced by the VAT blades reduces until the turbine operates completely out of stall and dynamic stall is no longer significant.

Figure 5.20 compares the C_{P} predicted by the BEMT model when all three corrections are applied together with the measured data of Mays *et al.* [185] and the basic BEMT model predictions. It can be seen that model performance is significantly improved when the corrections are included. Although the BEMT-All still over-predicts C_{P}, the level of over-prediction is much reduced from the Basic BEMT model. The error in $C_{\mathrm{P}max}$ was reduced from 17.5 % to 6.4 % at $C_{\mathrm{P}max}$ and the average RMSE for all measured data points was reduced from 0.079 to 0.034.

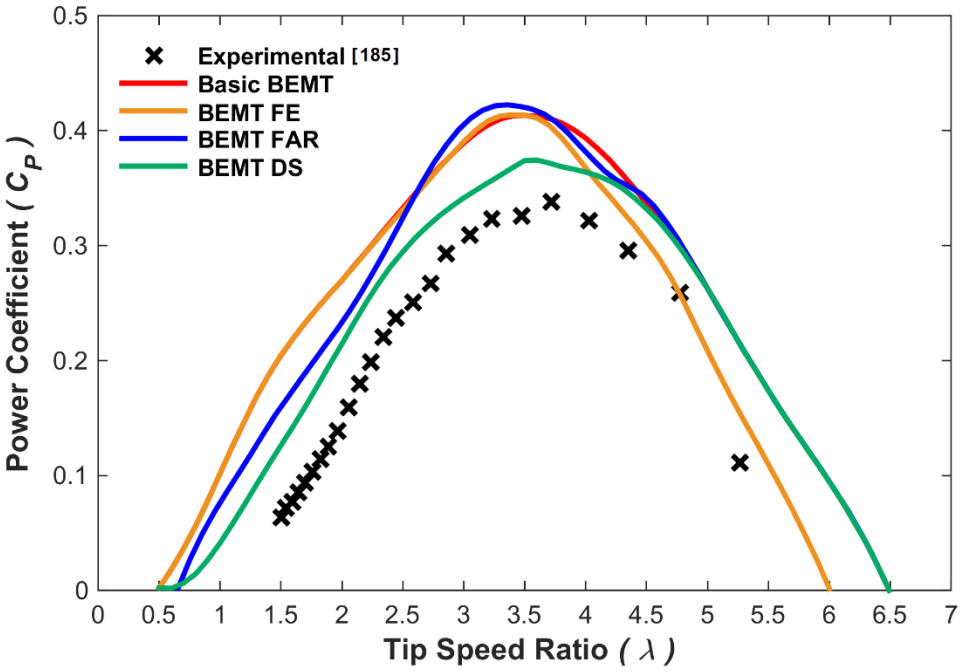

Figure 5.19: Comparison of BEMT model turbine performance with measured data [185] for a low solidity wind turbine.

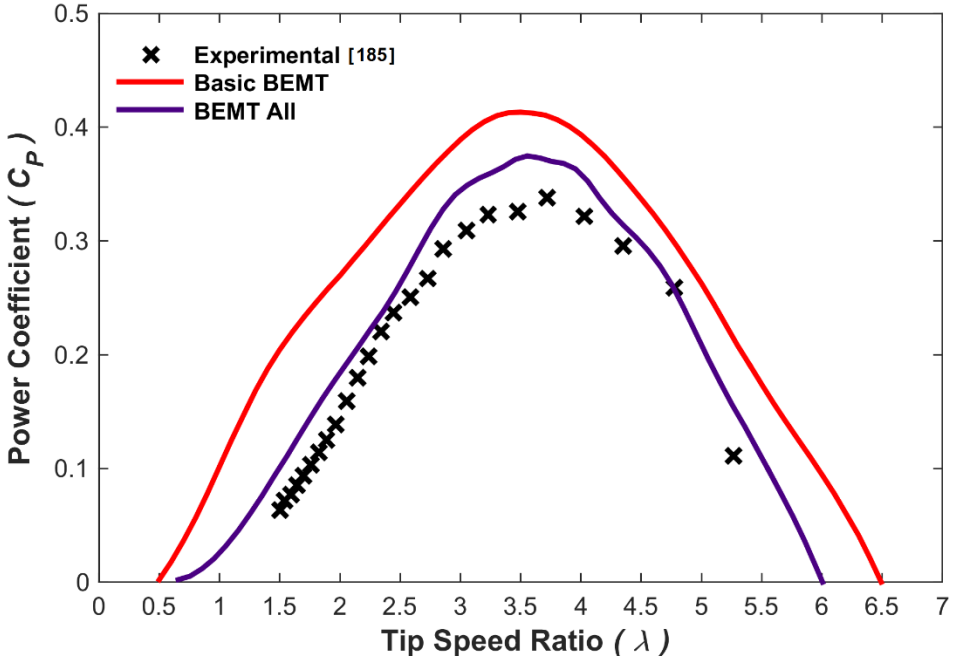

Figure 5.20: BEMT model predicted performance with all corrections applied; compared to measured performance for low solidity VAT [185].

Figure 5.21 presents the comparison of C_{P} results predicted for the high solidity turbine rotor to the measured data of Bachant and Wosnik [65]. The Basic BEMT model over-predicts $C_{\mathrm{P}max}$ by 46.9 % and determines the optimum λ value to be 2.4 compared to the measured value of 1.9. Looking at the effects of the corrections individually, flow expansion results in lower C_{P} values and thus improved accuracy for $\lambda > 2.2$ but has a negligible effect for λ values lower than this, this is similar to the observations for the low solidity rotor. Inclusion of the finite aspect ratio correction has the effect of reducing C_{P} in the regions where stall dominates ($\lambda < 1.5$), while marginally increasing C_{P} in the peak performance region. Looking lastly at the effect of the dynamic stall correction, initially, deep stall conditions exist and the effect of dynamic stall is to permit larger C_{L} which results in higher C_{P} values than the Basic BEMT. As λ increases towards the optimum value, dynamic stall has the effect of reducing C_{P}. For tip speed ratios higher than the optimum value, the dynamic stall correction has a negligible effect on the model performance. Figure 5.22 compares the BEMT model C_{P} values when all three corrections are included together with the measured values and the basic BEMT model. While the corrections have little effect on the phase shift in the power curve, they do result in improved model accuracy, with lower C_{P} values in general and a reduction in the error in $C_{\mathrm{P}max}$ from 46.9 % to 27 %. As a result, the average RMSE is reduced from 0.155 for the Basic BEMT to 0.121 for BEMT-ALL. RMSE values for each of the model corrections are shown in Table 5.5.

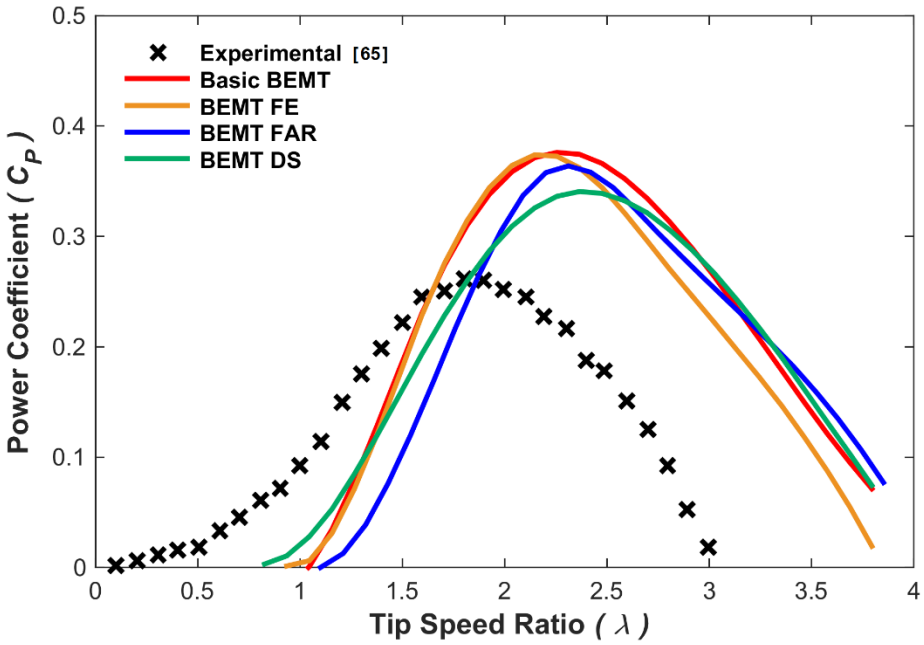

Figure 5.21: Comparison of BEMT predicted turbine performance to measured data [65]. Effect of each model correction compared to data without corrections.

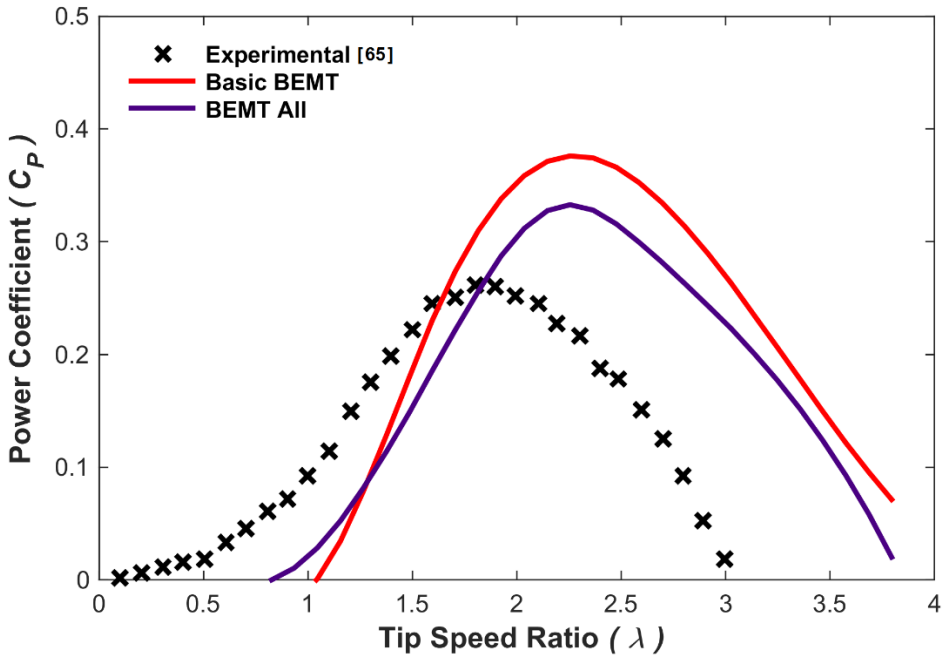

Figure 5.22: BEMT model predicted performance with all corrections applied; compared to measured performance for high solidity VAT [65].

Table 5.5: RMSE values for performance prediction of BEMT model for high and low solidity rotors.

	C_P RMSE	
	Low Solidity	High Solidity
Basic BEMT	0.079	0.155
BEMT-FE	0.068	0.140
BEMT-FAR	0.083	0.148
BEMT-DS	0.054	0.137
BEMT-ALL	0.034	0.121

5.12 Chapter Summary

This chapter presented the development and assessment of a bespoke BEMT model to predict the performance of both low and high solidity rotors which is applicable to both wind and tidal turbines. BEMT models are extremely attractive to early-stage developers due to their suitability for rapid evaluation of design iterations. They are much more cost-effective than experimental testing and significantly less computationally expensive than other numerical modelling performance prediction techniques, such as CFD and vortex models.

The chapter outlines the model development with a particular focus on the novel contributions contained within the model. The model uses a graphical approach for determining induction factors which makes it suitable for application to high solidity rotors and, to the author's knowledge, this is the first time this approach has been applied to vertical axis tidal turbines. Fir a VAT, Reynolds number can vary significantly for a VAT around the azimuthal rotation, and the developed BEMT model captures this by recalculating Reynolds numbers for each location and for every potential induction factor. Correction factors for flow expansion, finite aspect ratio correction, and dynamic stall are implemented in the model and can be switched on and off as desired.

BEMT model performance was evaluated for both low solidity and high solidity turbine rotors by comparison with published experimental data. For both low and high

solidity rotors, the inclusion of the dynamic stall model had the most significant effect on improving model accuracy. In relation to the low solidity rotor results, the model was shown to be quite accurate in predicting power performance with an average RMSE of just 0.034 when all corrections were applied simultaneously and a difference in $C_{\mathrm{P}max}$ of just 6.4%. For the high solidity case, model performance was not as good. Most significantly, a phase shift was present in the predicted BEMT power curves compared to the measured curve. It is thought that this may be the result of 3D flow effects of the confined tank. that are not accounted for in the BEMT model, such as The difference in measured and modelled $C_{\mathrm{P}max}$ for the best performing model (when all corrections were included simultaneously) was 27 %. However, as BEMT models are usually used as early stage design evaluation tools, this level of accuracy may still be acceptable.

Applications of BEMT models to high solidity rotors, in particular, tidal turbines, are rare in the literature. This is due to the fact that for high solidity applications, the iterative approach for the calculation of induction factors experiences convergence issues [186] which causes model failure. For this reason, BEMT models are largely overlooked as a means of modelling high solidity rotors. It is therefore not possible to conclusively say whether the presented level of accuracy is acceptable for early assessment of a high solidity VATT. However, as a comparison, Li and Calisal [97] overpredicted peak performance of a VATT by 20 % using the more computationally-intensive vortex model approach. Therefore, the presented model shows promise in predicting the performance of high solidity turbines and merits further investigation.

Chapter 6. Development and Assessment of 2D/3D CFD Models for VATTs.

This chapter has been published in the peer-reviewed Journal of Renewable and Sustainable Energy as:

Mannion, B., Leen, S. B., and Nash, S., "A Two and Three-Dimensional CFD Investigation into Performance Prediction and Wake Characterisation of a Vertical Axis Turbine," Journal of Renewable and Sustainable Energy 10, 034503 (2018); doi: 10.1063/1.5017827

6.1 Introduction

This chapter presents the development of 2D (Section 6.3) and 3D (Section 6.4) CFD models of a 3-bladed VATT and assesses their levels of accuracy in the prediction of power performance and near-wake properties. The turbine models are developed using the sliding mesh technique and model performance is assessed using the results of experimental tow tank testing of a VATT, conducted by Bachant and Wosnik [65] (Section 6.2). The primary aim of the research was to determine the suitability of the sliding mesh technique for CFD modelling of vertical axis turbines before applying the technique to the GKinetic turbine. A secondary aim of the research was to test the hypothesis that over-prediction of power performance by 2D CFD models is a result of their higher blockage ratio. This was achieved by testing a blockage correction approach for 2D models. In addition to common spatial and temporal convergence studies, 2D sensitivity studies are presented with respect to modelling decisions such as the diameter of the rotating domain, and specification of inlet parameters for turbulence intensity (T_I) and turbulence viscosity ratio (TVR) (Section 6.6).

The key contribution of the work presented in this chapter is the author's detailed modelling approach which is shown to achieve very high levels of accuracy. The approach is intended to provide a template for the development of highly accurate 3D models of vertical axis turbines. Particular focus is placed on mesh spacing, particularly in the boundary layer region, the size of the rotating mesh and the turbulence model. Turbine models can be validated against both power performance and near-wake characteristics; however, model developers tend to focus on one or the

other, usually the former. Of the 3D dimensional CFD studies of VATTs reviewed, only Bachant and Wosnik [139] validate their model against both parameters and, even then, power performance validation was conducted for just a single λ value. The current research provides validation of the full power performance curve as well as downstream near-wake velocities and turbulent kinetic energy (see Sections 6.5 and 6.7). A holistic validation approach like this is crucial, particularly with a view to subsequent turbine array modelling where both hydrodynamic impacts and power capture are intrinsically linked. An additional novelty of the research in this chapter is the use of the Transitional SST turbulence model which, based on a review of the literature, is a first in 3D modelling of vertical axis tidal turbines.

6.2 Details of the Experimental Testing

The turbine modelled here is a straight-bladed VATT built and tested by researchers at the University of New Hampshire, referred to as the UNH-RVAT. A simple schematic of the device is shown in Figure 6.1. The model was designed as a generic test case which would produce an extensive set of measured data against which various numerical modelling approaches could be calibrated and validated.

The UNH-RVAT turbine is 1 m in diameter and consists of three 1 m long NACA 0020 aluminium hydrofoils with a chord-length of 0.14 m. These are connected to a 95 mm diameter aluminium central shaft via mid-span support struts. The struts are also NACA 0020 aluminium hydrofoils used to reduce restrictive drag. Table 6.1 presents a summary of device dimensions.

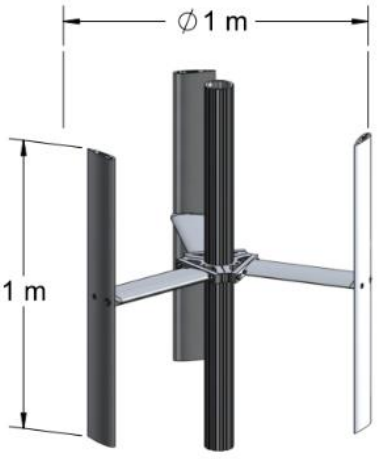

Figure 6.1: A schematic of the UNH-RVAT with primary dimensions (source: [65]).

Table 6.1: UNH-RVAT device details, experimentally tow tested in UNH.

Turbine Parameter	Value
Rotor diameter (RD)	1 m
Blade profile type	NACA 0020
Blade chord (c)	0.14 m
Blade length (L_B)	1 m
Number of blades (N_B)	3
Mid-span struts profile type	NACA 0020
Shaft diameter	0.095 m

Details of the experimental testing are given by Bachant and Wosnik [65] and are summarised as follows. The turbine was tow-tested in UNH's tow tank which measures 2.44 m deep, 3.66 m wide and 36 m long. The blockage ratio, defined as the ratio of turbine frontal area to tank cross-sectional area, was 11.2 %; this is within the range of <20 % recommended for experimental testing of scale tidal turbines [54]. The turbine was positioned on a specially designed towing rig constructed of NACA 0020 hydrofoils and was suitably instrumented. The turbine's rotational velocity was controlled through a permanent magnet servomotor which incorporated a 20:1 speed increasing gearbox. An additional permanent magnet servomotor and timing belt controlled carriage motion. Both servomotors were encoded into the central motion controller, allowing for high accuracy control of λ. The torque produced by the turbine was measured via a 200 Nm rotary torque transducer. Wake velocities were measured using a *Nortek Vectrino+* ADV which had an approximately 6 mm diameter sampling volume and sampled at 200 Hz. The ADV and data acquisition system sampling times were synchronized by triggering the start of data acquisition via a pulse sent from the motion controller. Approximately 1,500 tows were carried out in total for different Reynolds numbers, with 31 tows required for each Reynolds number dependent power curve.

6.3 2D Model Development

2D model meshing was implemented using ANSYS Workbench Meshing. The mesh is primarily an unstructured tri-element mesh with quad-element inflation layers around the walls. The model contains two mesh domains, an inner rotating domain representing the turbine which sits within an outer static domain. An interface boundary condition is applied to the edges where the domains meet. The static domain of the mesh extended 10 RDs upstream of the turbine centre and 35 RDs downstream.The rotating domain had a diameter of 2 m. Presented in Figure 6.2 are images of the 2D mesh that led to a mesh independent solution.

(a) (b)

Figure 6.2: Section of 2D mesh showing (a) sliding mesh within the static domain and (b) the mesh around one of the hydrofoils with 45 inflation layers.

In order to avoid any potential divergence issues that may have arisen from using 2nd order schemes and sliding meshes immediately upon simulation start-up, a progressive solution procedure is employed. Initially, the turbine is modelled as a moving reference frame (MRF) problem with 1st order discretisation schemes included. The model is run for 10,000 iterations in this setup before switching to *mesh motion.* The model is run using 1st order schemes until the torque has reached a quasi-periodic state, before finally switching to 2nd order schemes for the remainder of the simulation. The pressure-based solver was used throughout this process in conjunction with the coupled pressure-velocity scheme. The most prevalent turbulence models used in CFD performance prediction of VAT's (wind or tidal) are the $k-\omega$ SST and Transitional SST models. Both turbulence models were implemented here for comparative assessment.

6.3.1 Solution Convergence and Independence

The parameter used to assess convergence and independence was the average moment coefficient for a turbine rotation C_{m}. The criterion was $\Delta C_{\mathrm{m}} < 0.1$ % between successive rotations / simulations [142]. The convergence and independence studies were carried out at the optimum λ value of 1.9, and a λ value of 1.4 where flow separation was likely. Figure 6.3 shows that 12 rotations were required for convergence of the model solution.

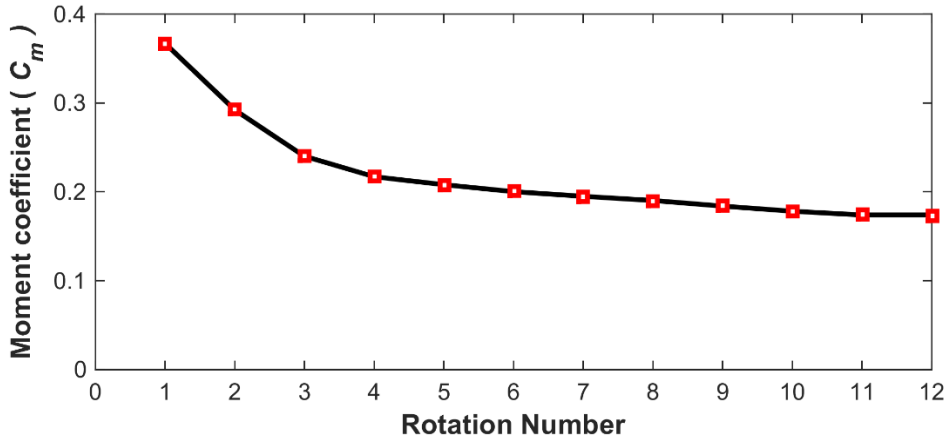

Figure 6.3: Graph of C_{m} versus rotation cycle number showing solution convergence.

Mesh independence was determined by developing a series of models of varying densities (see Table 6.2). Higher mesh densities were achieved by primarily increasing the number of nodes around the edges of the hydrofoils. The number quoted in Table 6.2 is the total number of nodes over a single hydrofoil; this was split evenly between the upper and lower surfaces of the foil. The edges on both sides of the domain interface were selected to ensure a corresponding number of elements on either side of the interface.

Figure 6.4 (a) shows the effect of the mesh on C_m (calculated over the final rotation) for three different λ. Mesh *M3* was chosen for subsequent model set-ups. Its geometric characteristics are presented in Table 6.3. All of the values presented are within the recommended limits for the FLUENT solvers.

A time dependence study was carried out using a number of different time-steps and

comparing the final C_m as seen in Figure 6.4 (b) compares C_m values computed using the different time steps for $\lambda = 1.4$. A time-step value representing 0.2 azimuthal degrees rotation per time-step ($0.2^{\circ}/\Delta t$) was identified as the optimum time-step value, with smaller time-steps resulting in a negligible difference in C_m.

Table 6.2: Mesh Parameters for Mesh Independence Study.

	No. of Nodes over hydrofoils	No. of Quad rows	Interface No. of divisions	1st layer element height (m)	Total number of elements
M1	500	25	600	1 x 10^{-5}	430 x 10^3
M2	750	35	700	1 x 10^{-5}	670 x 10^3
M3	1000	45	900	1 x 10^{-5}	980 x 10^3
M4	1200	55	1000	1 x 10^{-5}	1130 x 10^3

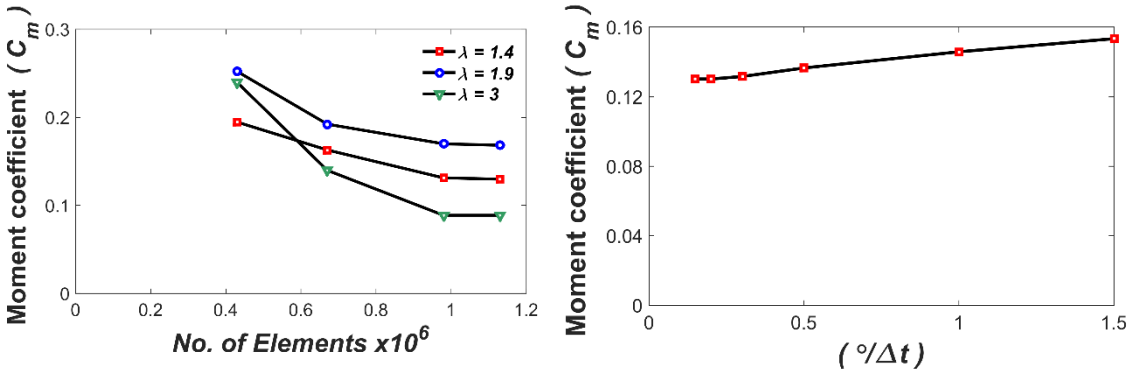

(a) (b)

Figure 6.4: (a) Effect of mesh density on C_m for different tip speed ratios and (b) effect of time-step (expressed as degrees of rotation per time-step) on C_m for $\lambda = 1.4$.

Table 6.3: Details of M3 mesh used in the 2D model.

Description	Value
Average skewness	0.0059
Max skewness	0.76
Average quality	0.82
Max y^+	1
Number of elements	980 x 10^3

6.3.2 2D Models Used for Sensitivity Analyses

In a 1:1 2D model of the experiment, the blockage ratio is 27.3 %, compared to 11.2 % in the experiment. It is, therefore, logical to hypothesise that this considerably higher blockage might result in turbine performance over-prediction. To test this hypothesis, a blockage correction approach was assessed where a *Low Blockage* 2D model was developed with the lateral walls of the tank extended (see Figure 6.5) to give the same blockage ratio as the experiment set-up. The results of this model were compared with those from the *High Blockage* model.

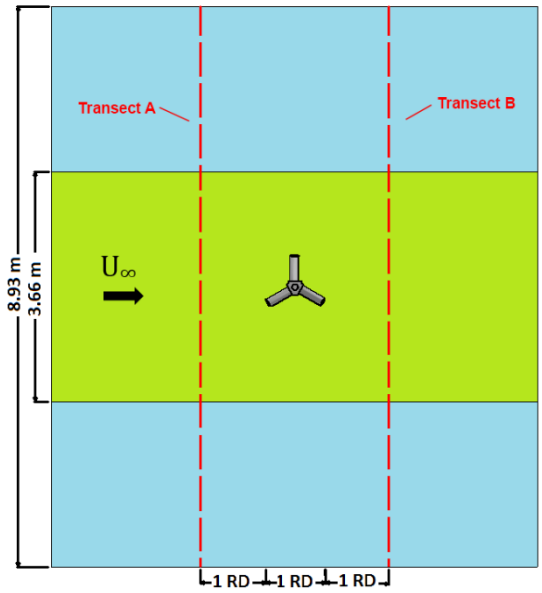

Figure 6.5: Schematic comparing static domain sizing, *High Blockage* model domain with 3.66 m width and *Low Blockage* model with 8.93 m lateral width.

2D model sensitivity to the size of the rotating domain was carried out using three models with different diameters of rotating domain. Measured relative to the turbine rotor diameter, the domain diameters were $2\,RD$, $1.4\,RD$ and $1.1\,RD$. The domain extents are presented in Figure 6.6. The prescription of turbulence properties (e.g. turbulence intensity (T_I) and turbulence viscosity ratio (TVR)) at the inlet and outlet boundaries may have an effect on the model results. The effect of their specification was investigated for varying inlet and outlet values of T_I and TVR. The Fluent user manual [138] specifies ranges for these parameters for interior and exterior flows. Models were run for T_I values of 1 %, 5 %, 10 % and 15 % and TVR values of 0.2, 1, 2 and 5. Table 6.4 lists the different models used in the sensitivity analyses and the

associated model acronym.

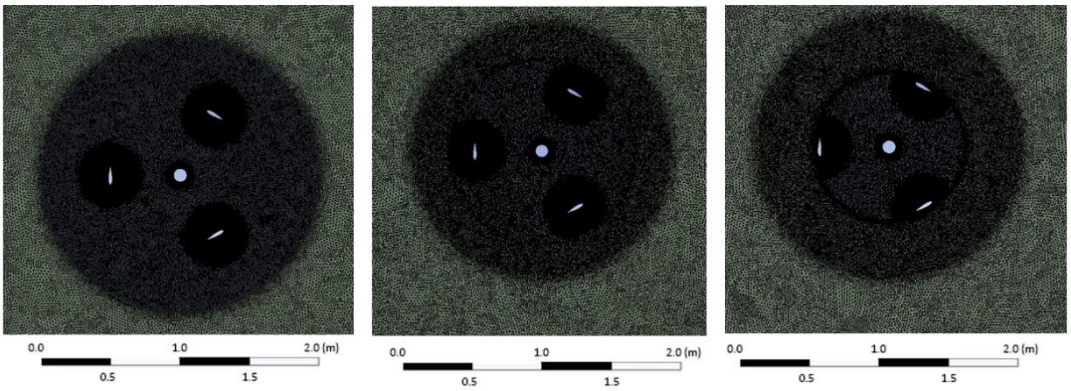

(a) (b) (c)

Figure 6.6: Central sections of model domains showing the different diameter sliding meshes for (a) $2RD$ model, (b) $1.4RD$ model and (c) $1.1RD$ model.

Table 6.4: Summary details of the developed 2D models.

Model Description	Acronym
Lateral tank walls at 3.66 m with blockage of 27.3 %	High Blockage
Lateral tank walls at 8.93 m with blockage of 11.3 %	Low Blockage
Low blockage model with rotating domain diameter of 2RD	$2RD$
Low blockage model with rotating domain diameter of 1.4RD	$1.4RD$
Low blockage model with rotating domain diameter of 1.1RD	$1.1RD$

6.4 3D Model Development

3D model development followed a similar approach to 2D. The static domain was modelled based on the tow tank dimensions. The full turbine was modelled, including the mid-span support struts, the turbine shaft and full-length blades. The rotating domain extended the full depth of the tank and had a diameter of $1.8\,RD$. Figure 6.7 and Figure 6.8 show different views of the 'independent' mesh. Similar to the 2D model, the static domain of the mesh extended $10\,RD$ upstream and $35\,RD$ downstream. *Mapped Faced* Meshing ensures a uniform mesh; this was applied to the blades, struts, shaft, domain interface and the strut-shaft hubs. The rotor was divided into a number of separate sections to enable Mapped Faced Meshing to be used.

Convergence and independence studies were used to determine the optimal number of turbine rotations, mesh density and time-step. The final 3D model details are summarised in Table 6.5.

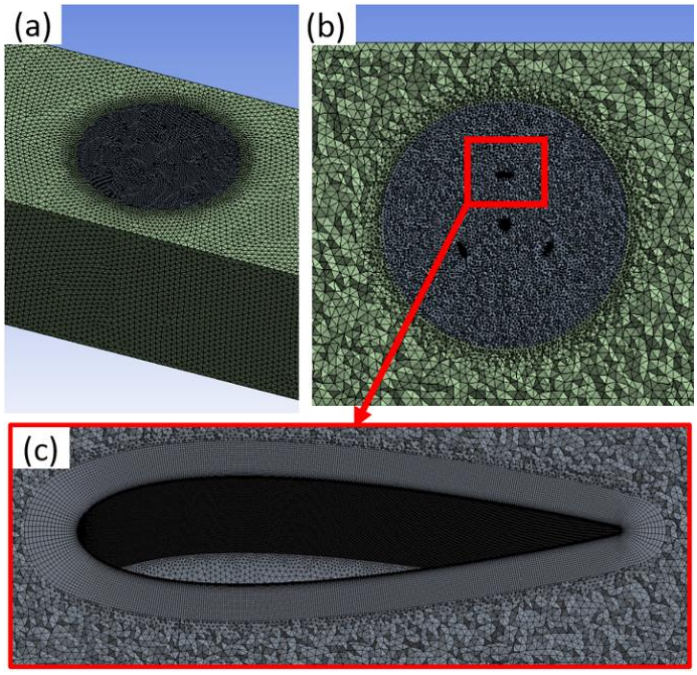

Figure 6.7: (a) 3D view of the mesh showing sliding mesh embedded in the static mesh (b) horizontal section through the model mesh showing the 3 blades and centre shaft and (c) section view of the mesh around each blade showing the 35 inflation layers.

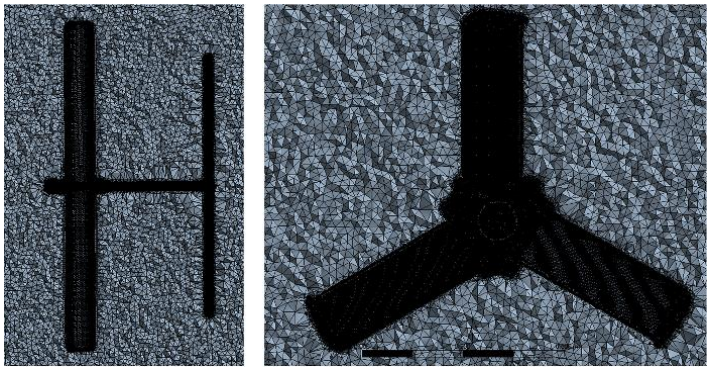

(a) (b)

Figure 6.8: (a) Vertical section through the centre shaft and a single blade and support strut, and (b) horizontal section through the support struts.

Table 6.5: Details of the final 3D mesh and model parameters.

Definition	Value
No. of quad inflation layers	35
1st layer element height	1 x 10^{-5} m
No. of elements span-wise on the blades	600
No. of elements span-wise on the struts	150
No. of nodes around hydrofoil edge	500
Total number of elements	21.84 x 10^{6}
Max skewness	0.899
Average skewness	0.49
Converged time-step ($°/\Delta t$)	0.35
No of Rotations to convergence	9

The accuracy of the 2D and 3D models was assessed by comparing modelled mechanical power coefficients with the experimental data. This was done for a free-stream velocity of 1 m/s, giving a rotor diameter dependant Reynolds number of 1x10^6. Bachant and Wosnik [65] showed the turbine power performance was Reynolds number independent for this number. Modelled near-wake velocities and turbulent kinetic energy were also compared to the test data to assess the accuracy of the near-wake dynamics prediction.

6.5 2D Model Results

Figure 6.9 shows the comparison of 2D power curves for the *High* and *Low Blockage* models with the experimental test data, using two different SST turbulence models. It is clear from Figure 6.9 (a) that the *High Blockage* model vastly over-predicted power (by more than 100 %). This was consistent with the findings of a similar 2D modelling approach by Bachant and Wosnik [139]. The peak predicted power also occurred at a much higher λ value. By comparison, the *Low* Blockage model (Figure 6.9 (b)) showed much better agreement with the experimental data. It still over-predicted $C_{\mathrm{P}max}$ but the over-prediction was reduced to 20 %. As shown in Table 6.6 the RMSE for Low Blockage model were significantly lower at approximately 0.06 compared to 0.26 for the High Blockage model. The *Low Blockage* model correctly predicted the optimum λ value of 1.9; however, it under-predicted C_{P} at lower λ values and over-predicted at higher λ values. There was relatively little difference in performance for

the turbulence models but the Transitional SST gave a little more accuracy, particularly at lower λ values as a transitional phase is more likely to occur with lower Reynolds numbers.

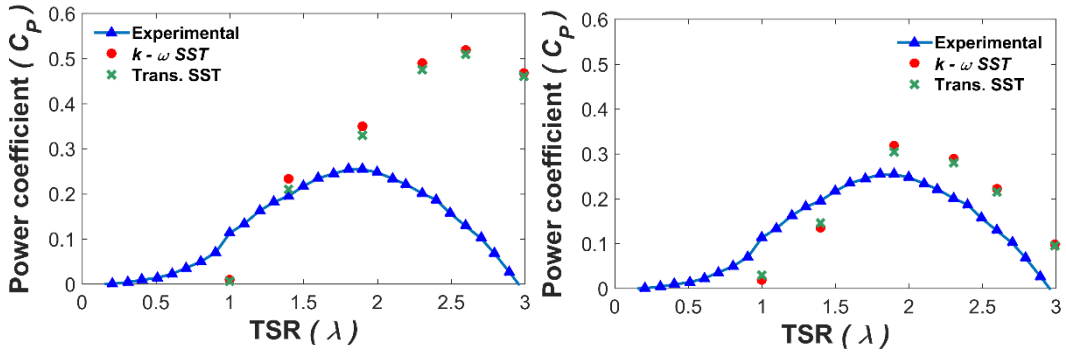

Figure 6.9: Comparison between 2D modelled and measured C_P for (a) *High Blockage model* and (b) *Low Blockage model* using the Transitional SST and the $k-\omega$ SST turbulence models.

Table 6.6: 2D model RMSE for C_P relative to the measured data.

2D model	RMSE (C_P)
Trans. SST High Blockage	0.265
$k-\omega$ SST High Blockage	0.266
Trans. SST Low Blockage	0.057
$k-\omega$ SST Low Blockage	0.061

Figure 6.11 (a) shows the variation in C_m for a single hydrofoil over the course of a full rotation. Output from the *High Blockage* and *Low Blockage* models are presented for a λ value of 1.9. As shown in Figure 6.11 (b), an azimuthal position of 0° corresponds to three o'clock with the turbine rotating anti-clockwise. As would be expected, the vast majority of the turning moment is created from the upstream part of the rotational cycle (40° to 140°). The figure shows the effect of tank blockage with the higher blockage resulting in higher torque being computed during the upstream part of the rotation, thus leading to over-prediction of C_P.

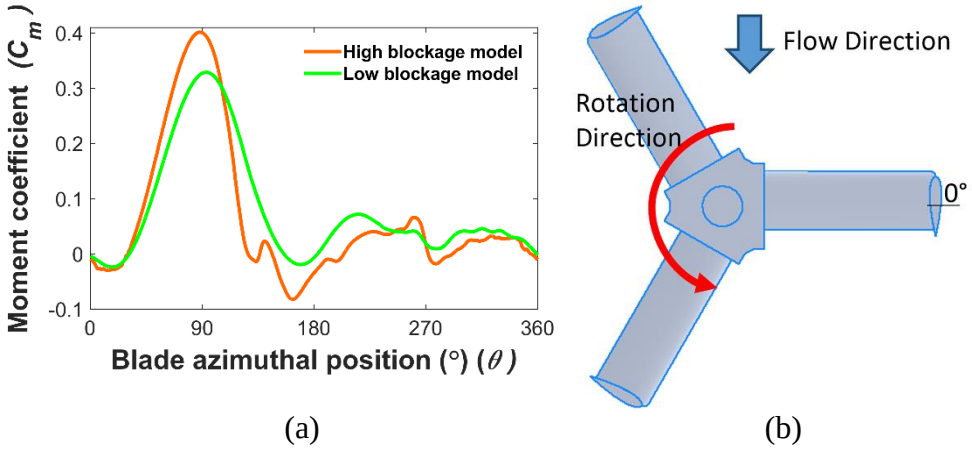

Figure 6.10: (a) Comparison of C_{m} computed over one complete rotation cycle by the high and low blockage models and (b) schematic showing 0^{o} blade azimuth position, flow direction and direction of turbine rotation.

To investigate the difference in performance between the turbulence models, Figure 6.12 presents a comparison of C_{m} output from the Transitional SST and $k-\omega$ SST models for the *low blockage* model. It is clear from the figure that there are two azimuthal regions where noticeable differences in C_{m} can be observed, namely at approximately 140° to 170° and 260° to 270°. The $k-\omega$ SST model computed higher C_{m} values for both of these blade positions. To investigate further, velocity streamline plots were output for a blade azimuthal of 150° (Figure 6.12). The streamline plot from the Transitional SST model (Figure 6.12 (b)) shows the occurrence of detached and reattached flow near the trailing edge of the blade which is not predicted by the $k-\omega$ SST model. This flow detachment suggests the onset of stall, causing lower lift and therefore, lower torque. These images present visual confirmation of one of the often-stated benefits of the Transitional SST model [125,187].

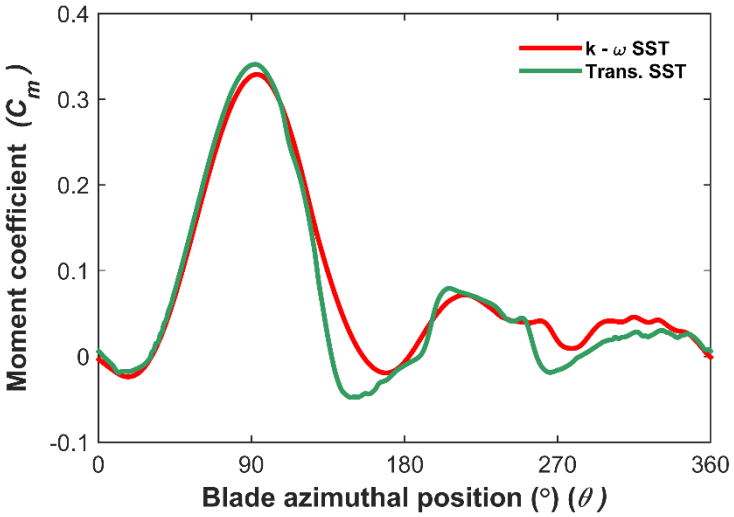

Figure 6.11: Comparison of C_{m} output for a single hydrofoil in the low blockage model for the $k-\omega$ SST and Transitional SST turbulence models.

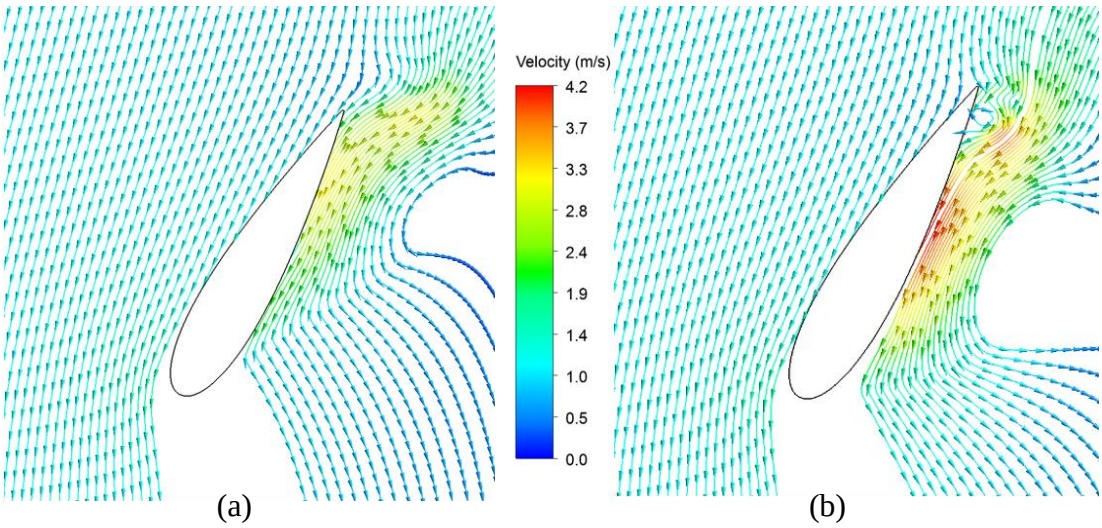

Figure 6.12: Velocity streamline plots for a single hydrofoil at 150° azimuth within the low blockage model for: (a) $k-\omega$ SST and (b) Transitional SST turbulence models.

Figure 6.13 shows normalised velocity contour plots from the 2D *High* and *Low Blockage* models. Figure 6.13 (a) shows that higher blockage results in larger flow acceleration. The velocities at the entrance and at either side of the turbine are higher than in the low blockage case (Figure 6.13 (b)) leading to higher C_{P} values. The higher blockage also affects the near-wake characteristics. The smaller domain width in the high blockage model results in a more constrained flow and therefore a more persistent wake.

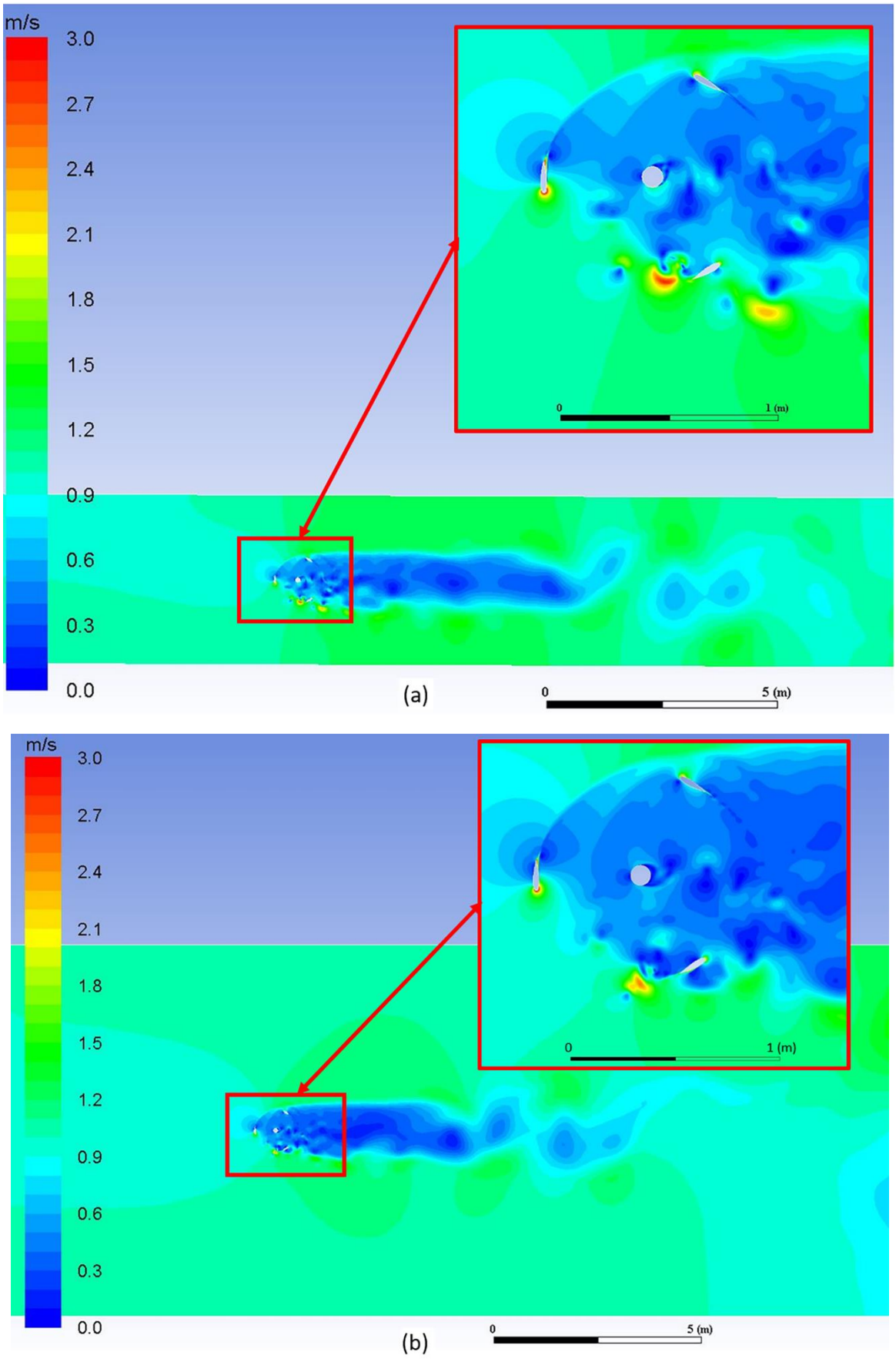

Figure 6.13: Velocity contour plots for (a) *High Blockage* and (b) *Low Blockage* models.

Flow velocities in the near-wake were measured along *Transect B* shown in Figure 6.5. Corresponding instantaneous velocity data was output from the *High Blockage* and *Low Blockage* models. A comparison of measured and modelled along-stream (x-direction) velocities for a λ value of 1.9 is presented in Figure 6.14. The velocities are normalised against the free-stream velocity. Overall, the *Low Blockage* model more accurately reproduces the experimental data. The *High Blockage* model RMSE was 0.204 m/s, while the *Low Blockage* model had an RMSE of 0.128 m/s. There are some peaks and troughs within the modelled data that do not occur in the experimental data. It is believed these discrepancies are caused by differences in the positions of the model and experiment turbulent eddies. While the model data was sampled at discrete time instances, the experimental data were collected over the course of several tows.

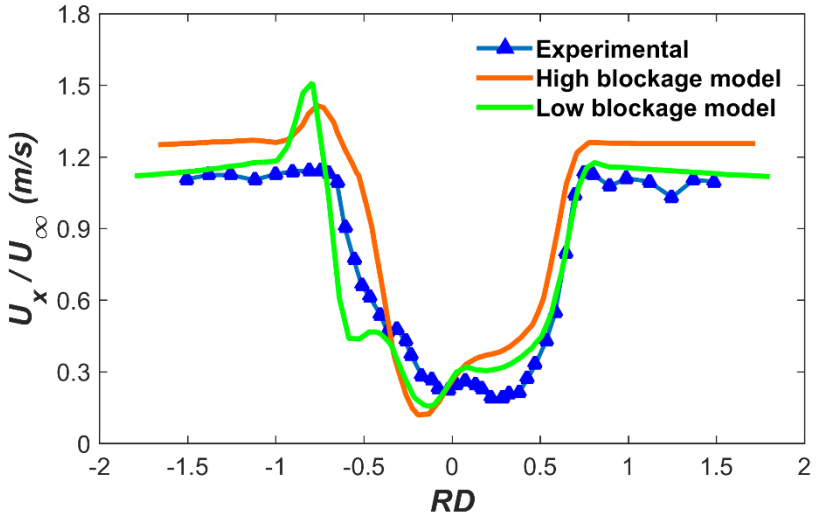

Figure 6.14: Comparison of measured and 2D modelled along-stream velocities for *Transect B*. Velocities are normalised against the free-stream value and distance along the transect is measured from the turbine centre.

To further understand the reasons for the differences between the high and low blockage models, model velocities were also output along *Transect A*, located upstream of the turbine (see Figure 6.5). These data are compared in Figure 6.15. It is clear that flow velocities are noticeably higher in the *High blockage model*. The transect average was 1.020 m/s for the *High blockage model* compared to 0.957 m/s for the *Low blockage model*; a 6.37 % increase on the *Low Blockage* value. Since power is proportional to velocity cubed, this will have a significant effect on extracted power.

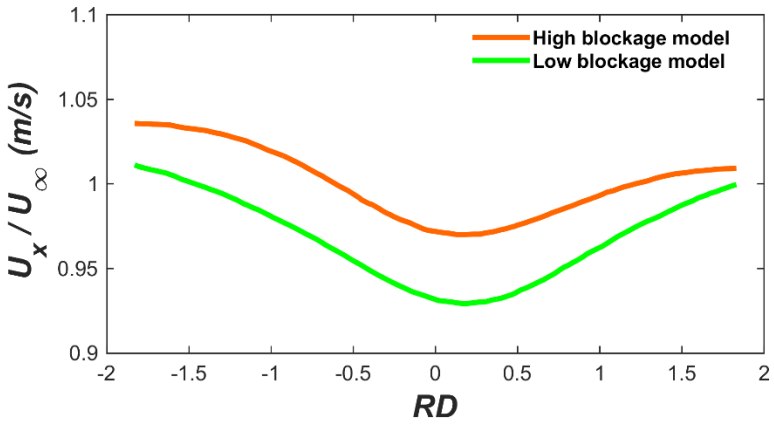

Figure 6.15: Normalised along-stream velocities output from the 2D models along *Transect A* upstream of the turbine.

6.6 Sensitivity Studies

Two sensitivity studies were carried out using the 2D models to study the effects of (1) rotating domain diameter (RDD) and (2) inlet and outlet values for T_I and TVR. The sensitivity studies were conducted using the *Low blockage* model. Figure 6.16 shows the effect of RDD on modelled power coefficient for different λ values. Clearly, there is an effect of RDD on predicted C_P at lower λ values; this is attributed to the fact that angle of attack varies dramatically at low λ values, with large flow separations occurring. A small diameter domain could curtail these flow features. The results of the inlet turbulence parameterisation study are presented in Figure 6.17. They show that the model is not overly sensitive to inlet specifications of T_I and TVR but predicted device power is seen to decrease marginally with increasing T_I and TVR.

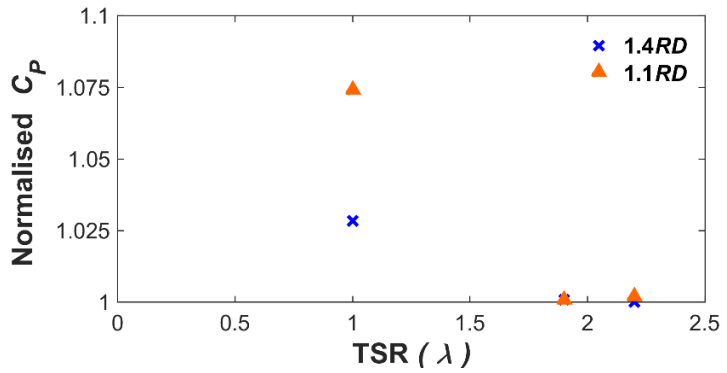

Figure 6.16: Graph of C_P computed by models with rotating domains of 1.1 RD and 1.4 RD normalised against those from the 2 RD model as a function of λ.

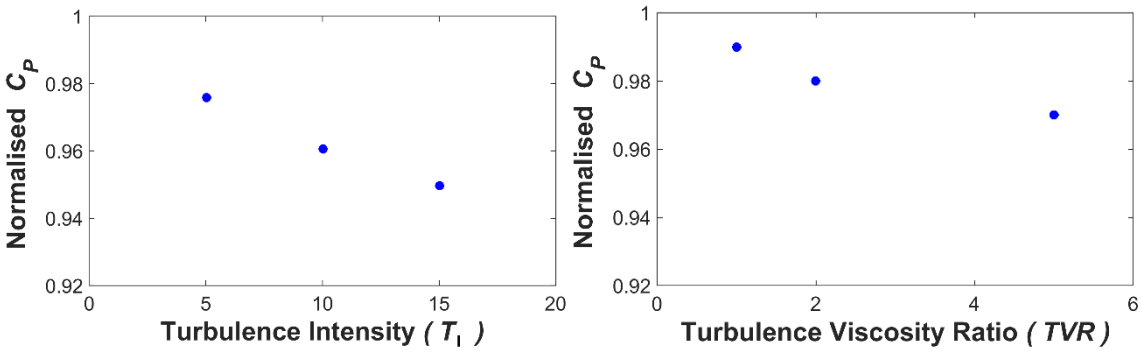

(a) (b)

Figure 6.17: Graphs of C_P computed by models with different inlet boundary values for (a) T_I and (b) TVR, normalised against those achieved with T_I= 1 % and TVR = 0.2.

6.7 3D Model Results.

Similar to the 2D case, 3D model accuracy was evaluated by comparing the modelled and experimental turbine power curves. Figure 6.19 compares measured C_P with corresponding model values predicted using the Transitional SST and $k-\omega$ SST turbulence models. It can be seen that the model accuracy was much improved over the 2D performance. Both turbulence models predicted the peak performance (C_{Pmax}) within 5 % of the measured value and both predicted this to occur at a λ value of 1.9 which concurs with the experimental data. In general, both models behaved similarly, slightly underestimating the turbine performance at λ values less than the optimum and overestimating performance for higher λ values. The Transitional SST model performs better than the $k-\omega$ SST model. The Transitional SST model data had a RMSE of 0.028, while the $k-\omega$ SST model data had a value of 0.035.

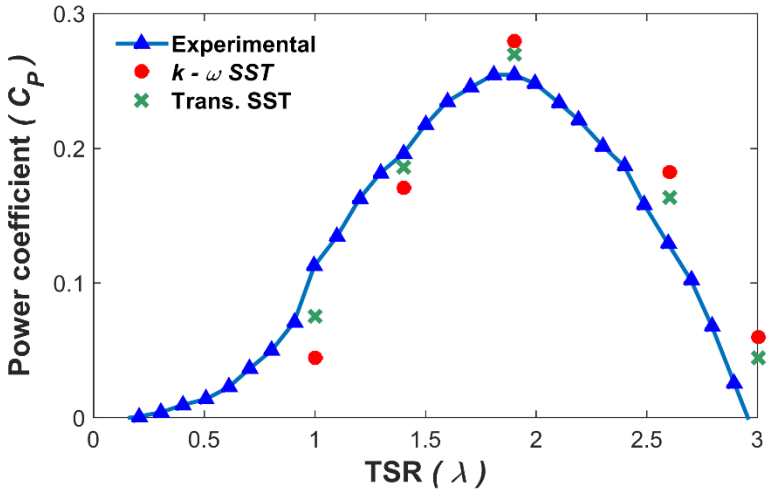

Figure 6.18: Comparison between experimentally measured C_P and those output from 3D models using two different SST turbulence models.

The improved power performance prediction of the 3D model in comparison to the 2D model also manifested itself in improved agreement in downstream velocities. Figure 6.19 shows a comparison of the modelled and measured velocities for a λ value of 1.9. Both of the 3D models accurately reproduce the bypass velocities outside of the wake. Both models also give good correlation relative to the experimental data inside the wake, but the Transitional SST model outperforms the $k-\omega$ SST model here. The Transitional SST model had a RMSE of 0.067 m/s while the $k-\omega$ SST model had a value of 0.079 m/s, relative to the measured data.

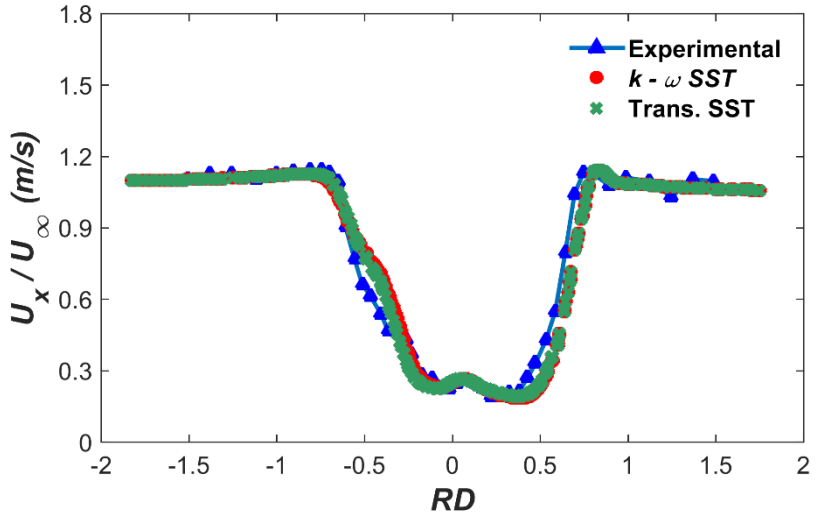

Figure 6.19: Comparison of measured and 3D modelled normalised near-wake velocities distributions along Transect B for a λ value of 1.9.

Presented in Figure 6.20 is a comparison of measured turbulent kinetic energy levels against corresponding values outputted from the 3D models along the same transect as the near-wake velocities (see Figure 6.5). As expected, turbulent kinetic energy levels are highest at the extremities of the turbine due to the shedding of eddy vortices from the blades. At this extreme near-field location (just 1.5 RD downstream of the turbine centre), low levels of turbulent kinetic energy would be expected in the middle of the wake before increasing downstream due to turbulent mixing of the wake and the bypass flow. Once again, the Transitional SST model is the more accurate turbulence model. Excluding the outlier in the experimental data at RD = 0.45, the RMSE values for the Transitional SST and $k-\omega$ SST models are 0.012 m^2/s^2 and 0.015 m^2/s^2 respectively.

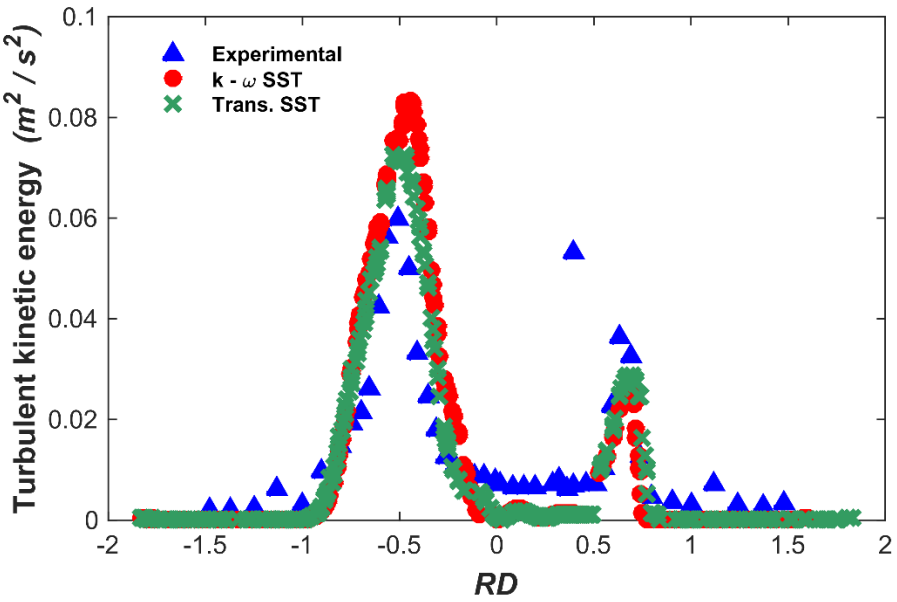

Figure 6.20: CFD model comparison to experimental data for turbulent kinetic energy.

Figure 6.21 shows velocity contour plots of a horizontal sectional plane at mid-turbine through the centre of the turbine from the Transitional SST model. Comparing this contour plot with those from the 2D models, the velocity immediately upstream, and to either side of the device are most similar to those of the Low Blockage model in Figure 6.13 (b), further confirming the validity of this approach for 2D model blockage correction.

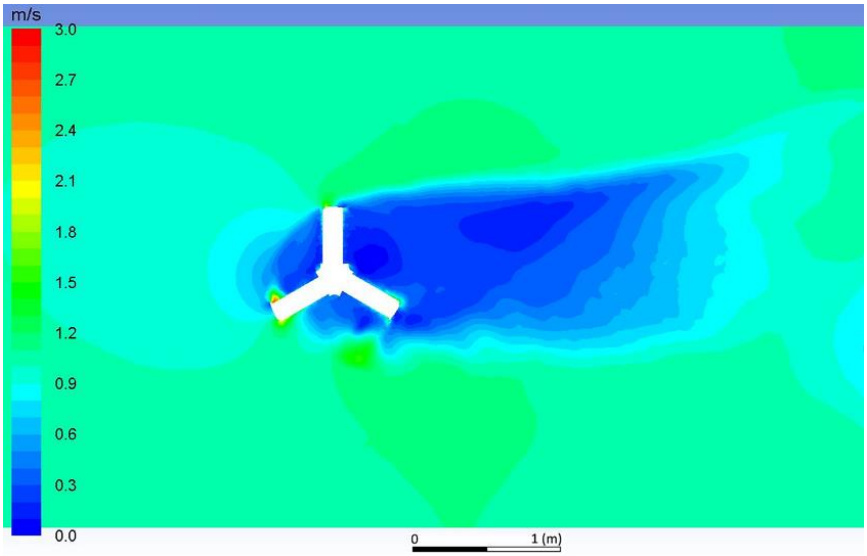

Figure 6.21: CFD predicted velocity contour at a λ value of 1.9 for the Transitional SST model.

6.7.1 Aspects of Turbine Design

Figure 6.22 shows a 3D contour of the vorticity generated by the turbine. It is seen that the large 95 mm diameter shaft shed significant vortices into the path of the oncoming downstream blades, thus potentially reducing the effectiveness of the downstream blades. This demonstrates the importance of shaft sizing in the design process; there is a trade-off between using a larger shaft diameter to give a higher factor of safety for better reliability and using a smaller diameter shaft to reduce incoming flow vorticity on the downstream blades.

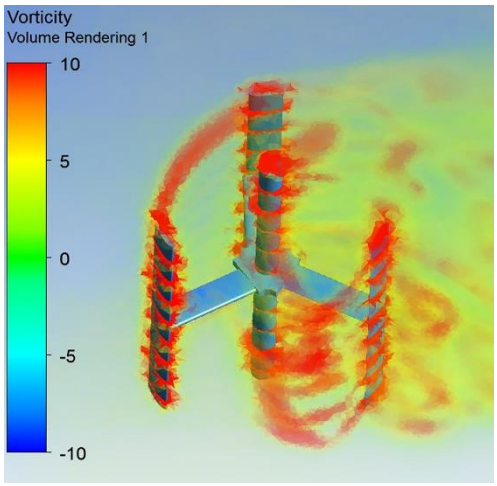

Figure 6.22: 3D vorticity (s^{-1}) contour plot at a λ value of 1.9 showing significant vorticity being distributed onto the path of oncoming downstream blades.

To evaluate the potential effects of the horizontal support struts on turbine performance, an additional 3D model was developed. This model retained the same mesh details and model setup but omitted the struts. The model was run at five different λ values. The C_P results obtained with the struts included were then normalised against the corresponding C_P values obtained without the struts. The resulting normalised C_P curve is shown in Figure 6.23. It is clear that the inclusion of the struts leads to a reduction in C_P with this effect increasing with increasing λ.

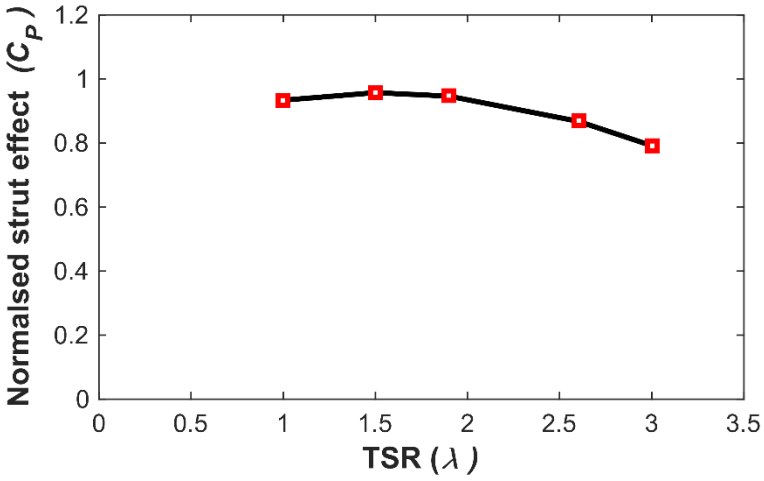

Figure 6.23: Predicted effect of struts on normalised C_P (relative to the case without struts included) on turbine performance.

6.8 Comparison Between 2D and 3D Model Results.

A comparison between the power performance predictions of the 2D blockage-corrected model and the 3D model is presented in Figure 6.24. Even with the improvements in power prediction arising from the blockage correction in the 2D model, the 3D results are clearly more accurate with an RMSE of 0.028 compared to 0.057 for 2D. However, as seen in Table 6.7, this higher level of accuracy comes at the cost of a significant increase in CPU time; the 3D model runtime was over 5.5 times that of the 2D. There is again, a trade-off here in relation to model accuracy versus available computational resources when deciding which modelling approach to use. In some cases, a blockage-corrected 2D model may be of sufficient accuracy for assessment of the effect of design decisions such as shaft sizes, strut design, etc. For example, the inclusion of the struts in the 3D model resulted in a 30 % additional CPU time over an already very high CPU time compared to that of the 2D model.

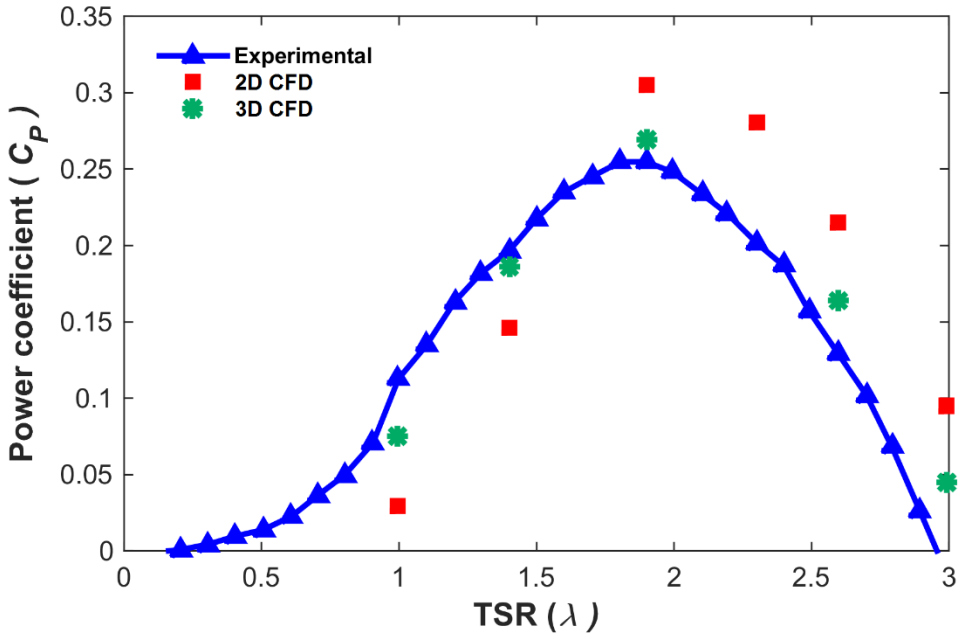

Figure 6.24: Comparison of 3D and 2D Low Blockage model performance for C_P.

Table 6.7: Comparison between runtimes for 2D and 3D CFD models.

Model	CPU Time (hrs.)
2D High Blockage model	3600
2D Low Blockage model	3900
3D model without struts	17500
3D model with struts	23000

6.9 Discussion of Results

The developed 3D CFD model accurately reproduced the measured mechanical performance coefficient of the UNH-RVAT turbine with less than 5 % difference in peak power coefficient. By comparison, the 3D model of Bachant and Wosnik [139] of the same turbine, using the $k-\omega$ SST model, over-predicted the peak performance by 30 %. The higher level of accuracy of the author's is attributed to the rigorous and systematic approach to mesh development, model convergence and sensitivity studies; as well as the validation of the model against both performance and near-wake characteristics. Comparison of model performance to other research is also quite favourable, Zamani *et al.* [159] and Marsh *et al.* [188] over-predicted peak performance by approximately 8 % and 56 %, respectively, both using the $k-\omega$ SST

model while Lei *et al*. [119], also using the $k-\omega$ SST model, under-predicted peak performance by approximately 11 %.

This high level of 3D model accuracy shows that $URANS$ CFD models and the sliding mesh technique can be successfully used in the design and optimisation of VATTs. Accurate wake modelling is vital in identifying optimum distances for placement of downstream turbines to avoid excessive turbulence and/or reduced power availability. However, the averaging nature of the URANS equations which results in turbulence dissipation means that the approach may not be suitable for far-field wake characterisation. Successfully validated CFD models can also be integral in the areas of device reliability. Li *et al*. [189] conducted a 2-year experimental study and showed that the natural frequency of a vertical axis tidal turbine can be in the same range as that of the turbulence flow conditions it is subjected to. If this is the case, device resonance is likely, and this may ultimately lead to device failure. Accurate CFD models, such as that presented here, could be used to predict turbulence loads for use in preliminary design checks, including vibration analyses, to improve device reliability and avoid resonance.

The 2D model studies investigated whether blockage contributes to poor model accuracy and over-prediction of the power performance in particular. The blockage in a 2D model of a turbine in a constrained flow will be higher than the actual 3D value. In this study, the 2D model without blockage correction significantly over-predicted the turbine mechanical performance coefficient, yielding an average RMSE of >0.26. When corrected for blockage, the model's performance was notably more accurate, with an average RMSE value in the region of 0.05. Comparing the two model's predictions for peak power performance, the uncorrected model over-predicted the maximum power coefficient by approximately 100 % compared to an approximate 20 % over-prediction by the corrected model. In this instance, blockage, therefore, accounted for 80 % of the model over-prediction. The study proves that blockage does cause over-prediction of power performance in 2D models and that they can be corrected for blockage effects, by extending the lateral domain width to give the equivalent 3D blockage. Correcting for blockage also gave better predictions of both the bypass velocities and near-wake velocities. The RMSE in downstream

modelled velocities was reduced from 0.2 m/s to 0.12 m/s when blockage was corrected.

The 2D study on the effect of the size of the rotating domain (sliding mesh) diameter showed that model performance can be adversely affected by the size of the rotating domain, this effect is more noticeable at lower λ values. Larger diameter domains of at least 1.5 times the rotor diameter are required at lower tip speed ratios to avoid incurring excessive errors. At higher λ values (>1.9 in this research), one can use a smaller rotating domain without significantly affecting the model accuracy.

The effect of the turbulence models on model performance was more apparent in the turbine near-wake velocities than the power performance. It is thought that this may be the result of some flow reattachment to the hydrofoil that is being modelled by the Transitional SST but which the $k-\omega$ SST model is incapable of doing. The close similarity of the 3D near-wake velocity contour plot with the corresponding 2D plot from the blockage corrected model, particularly upstream and to either side of the device, provides further confirmation that the 2D blockage correction approach is valid.

In comparison with the accuracy of the BEMT model of the UNH-RVAT from Chapter 5, the CFD models are clearly more accurate. Although the BEMT model over-predicted peak performance by 27 %, compared with 20 % for the 2D CFD model, the phase shift in the BEMT results means there is a significant disparity in the accuracy of the two models. The BEMT RMSE value for the power curve was 0.121 compared to 0.057 for the blockage corrected 2D model and 0.028 for the 3D model.

In summary, if model accuracy is paramount, it is recommended that 3D models are used. If not, then 2D models that account for blockage may be attractive as a device evaluation tool due to their significantly lower computation costs. The potential saving can be demonstrated by comparing the CPU runtimes of 22,000 CPU hours for the 3D model with struts to 3,900 CPU hours for the blockage corrected 2D model.

6.10 Chapter Summary

A number of 2D and 3D CFD models of a vertical axis tidal turbine were developed to reproduce experimental test data. A 2D model blockage correction approach was assessed, in which the correct level of blockage is achieved by extending the width of the 2D model domain. A rigorous approach to model development was employed involving detailed convergence and sensitivity studies and extensive validation of both power performance and near-wake characteristics. The main conclusions of this research are as follows.

- 2D CFD models can be corrected for blockage by extending the domain width to give a blockage value equivalent to the correct value in three dimensions. By doing so, one can achieve a reasonable level of accuracy, but if accuracy is paramount, it is recommended that 3D models are used.

- Model accuracy can be sensitive to the choice of the size of the rotating domain but is dependent on the λ values. To avoid these effects, a domain diameter of 1.5 times the turbine rotor diameter is recommended. Model performance is much less sensitive to domain size at higher λ values (>1.5), therefore smaller rotating domains can be used to reduce computation costs if required.

- The rigorous model development approach resulted in a highly accurate 3D model. This proves that URANS CFD models can give sufficient levels of accuracy for turbine design without the need for the development of higher order, and much more computationally expensive, CFD methods like LES and DES.

- The accuracy of the models presented in this chapter, particularly 3D, have shown that the sliding mesh approach is suitable for modelling the performance and near-wake velocity deficits of vertical axis tidal turbines. The sliding mesh approach was therefore utilised in the development of a model of the GKinetic device presented in Chapter 7.

Chapter 7. Development and Assessment of a 2D CFD Model of the GKinetic VATT.

This chapter has been published in the peer-reviewed Journal of Ocean Engineering and Marine Energy. as:

Mannion, B., McCormack, V., Leen, S. B., and Nash, S., 2019, "A CFD Investigation of a Variable-Pitch Vertical Axis Hydrokinetic Turbine with Incorporated Flow Acceleration," Journal of Ocean Engineering and Marine Energy; doi:10.1007/s40722-019-00130-1

The 2D CFD model development and validation presented in this chapter has been published in a peer-reviewed conference paper presented at International Conference on Offshore Mechanics and Arctic Engineering (OMAE2018), Madrid, Spain, June 17–22, 2018. The full reference is:

Mannion B, Leen S B, McCormack V, Nash S. Numerical Modelling of a Variable-Pitch, Vertical Axis Tidal Turbine Incorporating Flow Acceleration. ASME. International Conference on Offshore Mechanics and Arctic Engineering, Volume 7A: Ocean Engineering: V07AT06A030. doi:10.1115/OMAE2018-77100.

7.1 Introduction

This chapter presents the development of a 2D transient CFD model of the GKinetic turbine using a nested sliding mesh technique. The model includes the flow accelerating bluff body and variable pitching blades, with the latter controlled during simulations via a user-defined function (UDF). The developments are based on CFD modelling recommendations and best practice identified from the literature, as well as the validated modelling techniques presented in Chapter 6 of this thesis. The model is used to simulate the 1:20 scale experimental tests conducted in a recirculating flume (Chapter 4). The predicted performance is validated by comparison with measured data for mechanical power and near-wake velocities. The converged and experimentally validated model is used to investigate various aspects of the current device setup including the number of blades on the turbines, the benefits of variable versus fixed pitch blades, shaft sizing, the location of the turbine relative to the bluff body and the effect of blade chord-length. Each of the design cases is assessed in

relation to mechanical power performance.

7.2 Model Development

In order to model the variable-pitching blades of the GKinetic turbine, a nested sliding mesh approach was proposed, where each blade was resolved in its own sliding mesh. These sliding meshes were then embedded in a larger sliding mesh simulating the rotation of the turbine. A schematic of the model setup is shown in Figure 7.1. The following sections describe the development of the nested sliding mesh model including the mesh geometry, domain extents, implementation of the variable-pitching and mesh/time convergence studies. The dimensions of the CFD model were the same as the 1:20 scale device tested at the IFREMER recirculating flume (shown in Figure 7.2), with the exception of the 2D blockage correction of the flume. The 1:20 scale experimental results from Chapter 4 were used to validate the model. Although the testing was conducted at a range of flow speeds, model development and validation runs were limited to flow speeds of 0.7 m/s and 1.1 m/s. Table 7.1 presents a summary of the key dimensions of the CFD model developed.

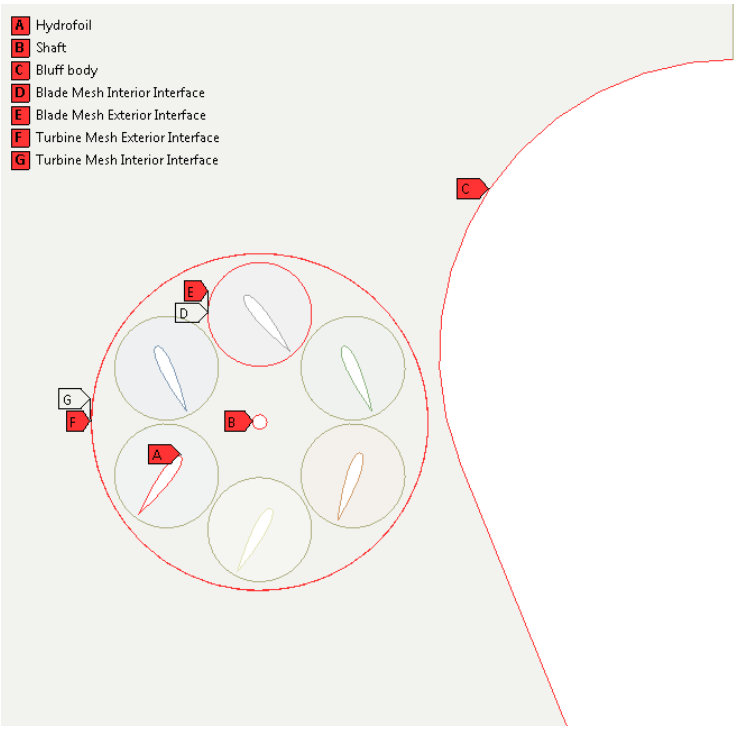

Figure 7.1: Schematic showing the arrangement of the model meshes with key components identified.

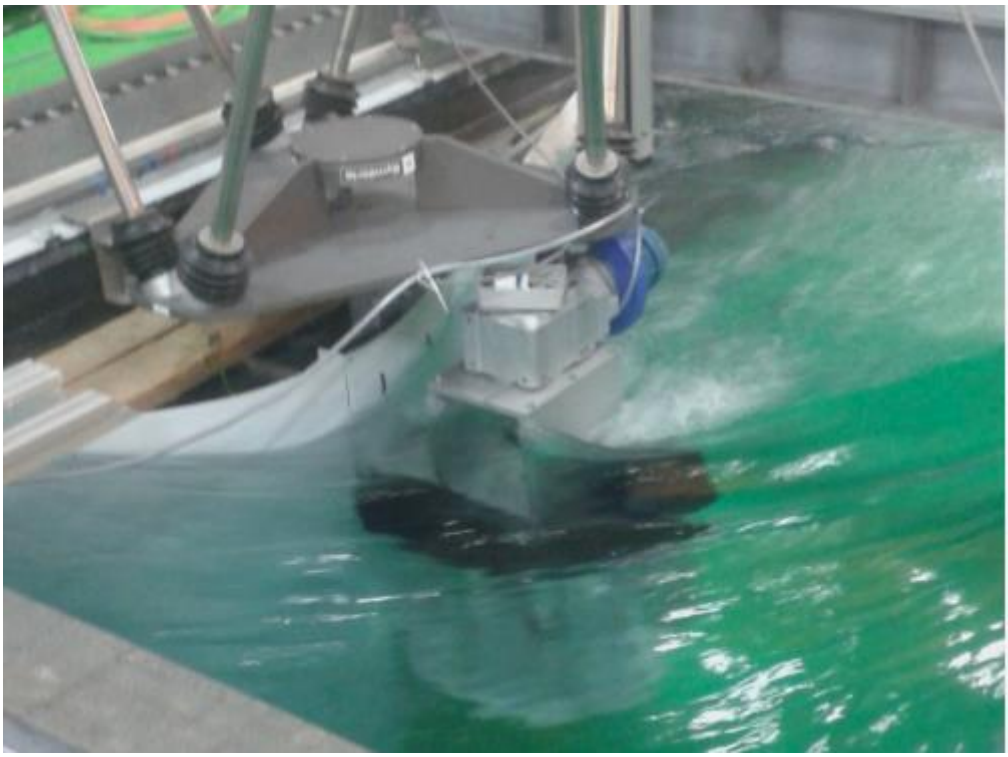

Figure 7.2: Image of the 1:20 scale device being tested in IFREMER's flume tank, with turbine positioned at mid-depth.

Table 7.1: Key details and dimensions of the 1:20 scale device and associated CFD model domain details.

Description	Value
Turbine diameter (D)	0.6 m
Blade rotating mesh diameter	0.29 m
Turbine rotating mesh diameter	0.9 m
Blade profile type	NACA 0018
c	0.2 m
L_B	0.667 m
N_B	6
Bluff body radius (BBR)	0.82 m
Bluff body length (BBL)	3 m

7.2.1 Mesh Geometry

The CFD mesh was developed using ANSYS Workbench Meshing and predominately consists of unstructured triangular elements with quadrilateral elements at the walls. As shown in Figure 7.1, the model contains seven nested meshes in total. The outermost domain is static and contains the half-bluff body. The large outer sliding mesh, measuring 0.9 m in diameter, represents the turbine, which has a diameter of 0.6 m. Nested within the turbine sliding mesh are six smaller sliding meshes of 0.29 m diameter, each of which contains one of the individual blades of 0.2 m chord-length. Figure 7.3 (a) shows the mesh for the full turbine, which is more refined closer to the hydrofoil walls; Figure 7.3 (b) displays the full width of the static mesh where the size of the device in relation to the size of the domain is visible. Figure 7.4 shows an image of the mesh around one of the hydrofoils. The 35 quad element inflation layers (with a growth rate of 1.2) used adjacent to the foil walls are visible in the figure.

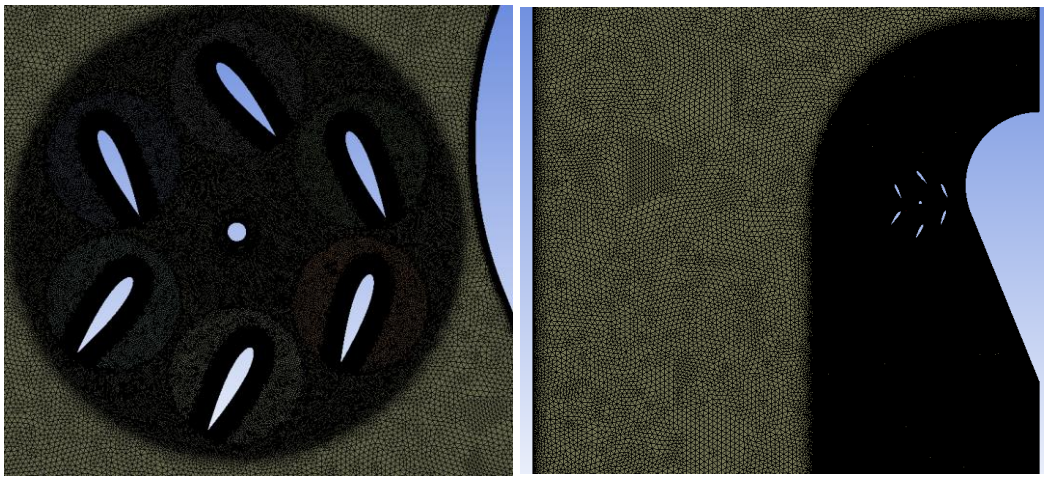

(a) (b)

Figure 7.3: Mesh showing (a) around the turbine and (b) far field.

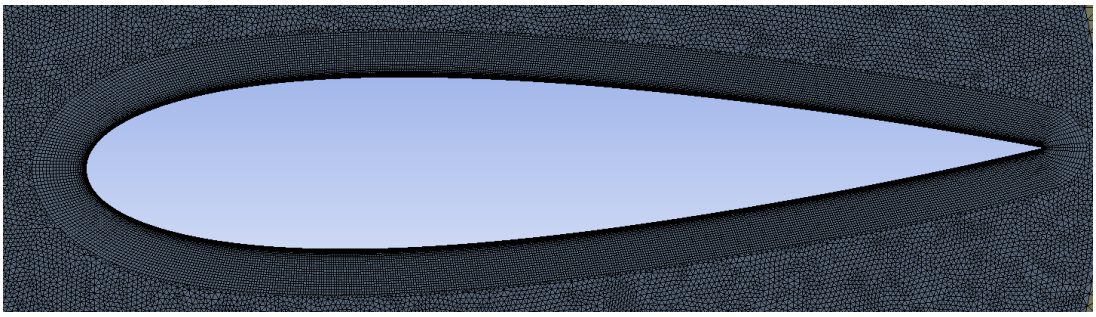

Figure 7.4: Mesh around hydrofoil with 35 quad inflation layers visible.

It was shown in Chapter 6, that while CFD model results of the UNH-RVAT were sensitive to the turbine sliding mesh size, the effects were negligible once the diameter of the turbine rotating mesh was greater than 1.5 times the turbine diameter. In the present study, the sizes of the sliding meshes were restricted by the dimensional constraints of the device setup. As can be seen in Figure 7.3 (a), the presence of the bluff body (i.e. a wall boundary) next to the turbine restricted the turbine mesh size, while the chord-length and the locations of neighbouring blades restricted the size of the blade meshes. In both cases, however, the sliding mesh diameter was 1.5 times the turbine / chord-length diameter. Turbulence intensity was set at 5 % to be reflective of that present in the experimental testing. The lateral walls of the tank were considered as no-slip boundary walls.

7.3 Domain Extents

A 2D model which retains the same domain extent as a test setup presents a higher blockage ratio than the test. As was shown in Chapter 6, this higher blockage of the 2D model can lead to performance over-prediction, particularly in the case where blockage in the test set-up was high, to begin with. It was also shown in Chapter 6 that 2D model blockage errors can be corrected by extending the width of the 2D model domain to give the same blockage ratio as the test setup. This correction approach is implemented here; such that the width of the domain is extended from the tank width of 4 m to 5.633 m (Figure 7.5), to reproduce the correct blockage ratio of 0.25. The model domain extends 10 m upstream and 40 m downstream of the device.

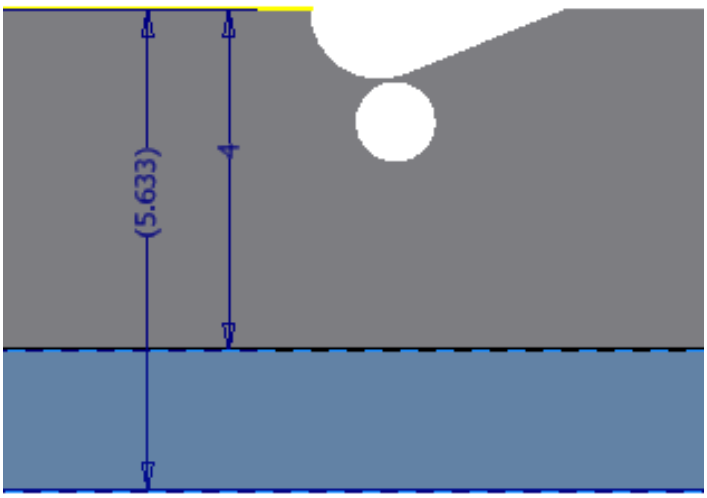

Figure 7.5: Schematic showing widening of model domain from 4 m to 5.633 m implemented according to our blockage correction approach of Chapter 6.

7.3.1 Blade Pitch Control

To incorporate variable-pitching into the CFD model, the motion of the sliding meshes containing the blades had to be controlled. Each blade follows the same pitching profile within each turbine rotation (see Figure 7.6). Mathematical expressions were developed to represent the pitching of the blades at each azimuthal position. A UDF written in the C programming language was used to control the motion of the individual blade domains and is able to account for different turbine rotational velocities. The model was implemented on a Linux 48 node cluster.

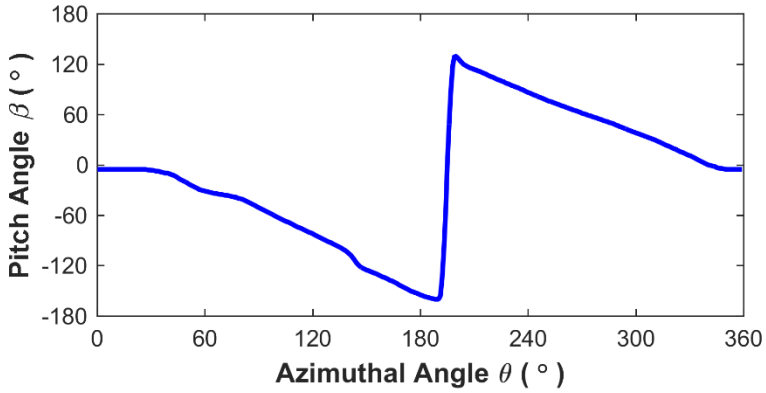

Figure 7.6: Variation in blade pitch angle over the duration of full turbine rotation.

7.3.2 Mesh Convergence Study

The mesh sensitivity study required the development of several different meshes of varying densities which are listed in Table 7.2. As is seen in the table, the method of increasing the mesh densities was to increase the number of nodes along the edges of the hydrofoils (identified as “A” in Figure 7.1). The number of elements along the domain interface edges was increased by increasing the number of divisions. The edges on both sides of the domain were selected to ensure the elements on either side of the interface corresponded; the interfaces are shown in Figure 7.1 as D and E for the blade meshes and F and G for the outer turbine mesh. Face sizing was also adjusted when mesh refinement was required. The numbers of quadrilateral layers used in the blade meshes are also given in the table; a growth rate of 1.2 was used.

Table 7.2: Mesh parameters for sensitivity analysis.

	No. of nodes around hydrofoil	No. of Quad layers	No. of divisions (Turbine interface)	No. of divisions (Blade interface)
M1	400	20	200	200
M2	550	25	400	250
M3	700	35	600	300
M4	850	35	800	350
M5	1000	35	1000	400

Figure 7.7 presents the performance of the five meshes for predicted turbine torque. The Richardson extrapolation was used to calculate the 'exact solution' torque from the simulation results. It is clear that mesh M4 was the most suitable, as it provides a converged solution (within 1 % of the final Richardson's extrapolation value in Table 7.3, with the difference between modelled and extrapolated torque values presented) whilst minimising the computational cost. More specific spatial details of the M4 mesh are presented in Table 7.4. As y^+will change with each azimuthal orientation of the hydrofoil, Figure 7.8 shows the variation of average and maximum y^+ evaluated over the duration of a full rotation are ≤ 1 and therefore, within the recommendations for the applied turbulence models.

Table 7.3: Mesh refinement convergence determined with Richardson's extrapolation.

	No. of mesh elements ($\mathbf{x10^6}$)	Modelled Torque (Nm)	Richardson's Value	Difference in Torque
M1	0.5	240.47	141.25	-70.24%
M2	0.75	194.92	141.25	-37.99%
M3	0.9	162.07	141.25	-14.74%
M4	1.1	142.26	141.25	-0.72%
M5	1.3	141.10	141.25	0.11%

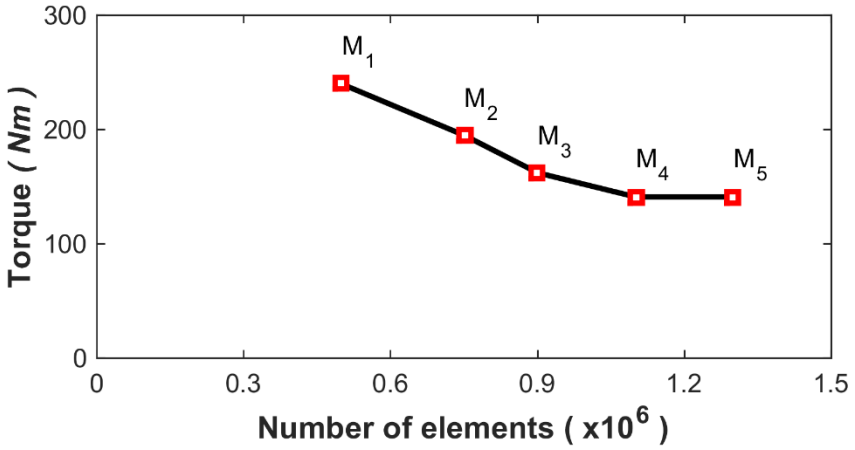

Figure 7.7: Mesh convergence study, showing M4 mesh as optimum for the model.

Table 7.4: Details of converged mesh M4.

Description	Value
Average skewness	0.0059
Max skewness	0.81
Average quality	0.86
Max aspect ratio	65
Max y^+	1.06
Number of elements	1.1 x 10^6

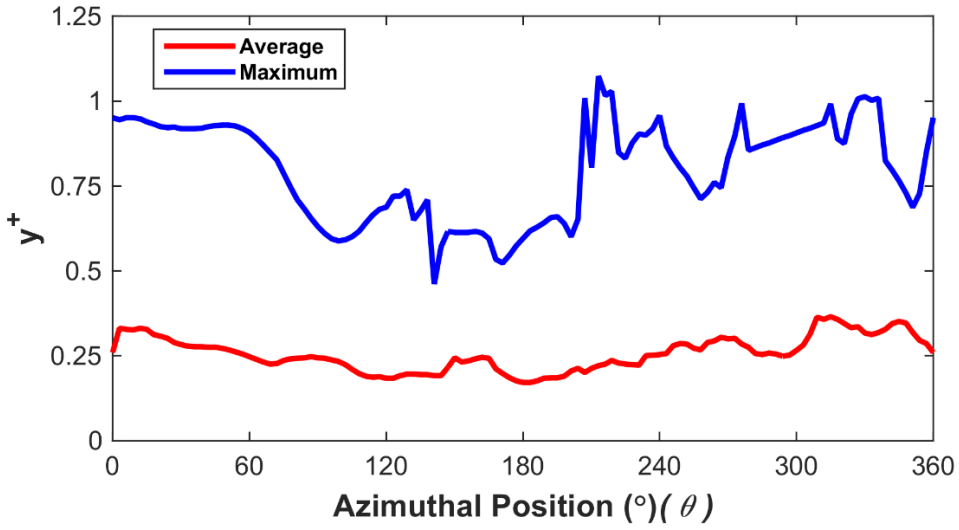

Figure 7.8: Average and maximum y^+ evaluated over the duration of a full rotation.

7.3.3 Solution Convergence

Similarly, as was the case in Chapter 6, the model solution is achieved in three stages. First, a MRF, steady-state approach with 1st order discretization schemes are run for 10,000 iterations. Upon completion of this stage, the model changes to transient mode and *mesh motion* and continues with the 1st order schemes until torque has reached a quasi-periodic state. At this stage, the model is changed to 2nd order schemes for the remainder of the calculation. As before, the COUPLED solver was used throughout.

The criterion used for the number of rotations required for a converged solution was that the difference between average torque values for successive rotations, $\Delta\bar{Q}$, should be less 0.1 %; this criterion was based on recommendations by Balduzzi *et al*. [142]. Table 7.5 shows that 14 rotations were required for this criterion to be met.

Table 7.5: Number of rotations required for convergence

Turbine Rotation	Torque (Nm)
1	260
4	155
8	143.7
13	141. 35
14	141.22

7.3.4 Temporal Convergence Study

A time-dependence study was carried out for a range of model time-steps. Balduzzi *et al*. [142] showed that smaller time-steps are required for turbine simulations involving lower λ values. The lowest λ value of 0.15 was, therefore, chosen for the time convergence study as the most conservative case. The model was run using a number of different time-steps and torque was again compared across simulations. A graph of the results (torque values averaged over a full rotation) is presented in Figure 7.9. It is clear from the figure that the model requires a small time-step in order to obtain an independent solution. This is most likely due to the complexity of the model, with highly variable flows modelled using seven moving meshes, and at very high spatial resolutions. Based on the study, a time-step equivalent to 0.2 azimuthal degrees per

time-step ($°/\Delta t$) was identified as optimum for this λ value and was used across all λ values.

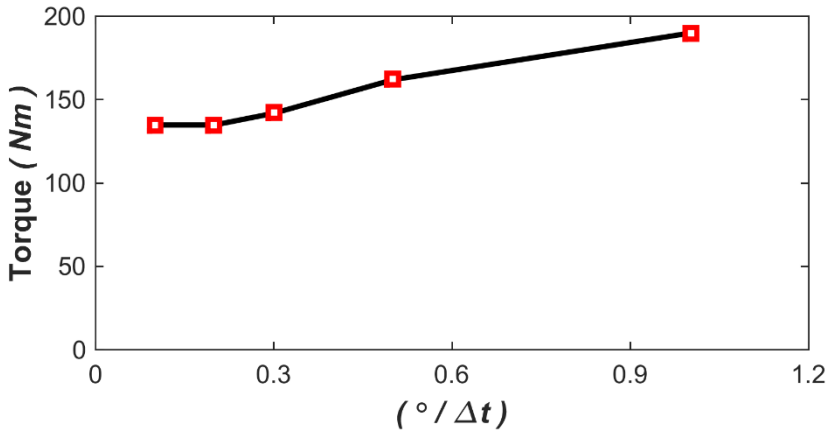

Figure 7.9: The time-step study (torque values averaged over a full rotation), showing optimum time step representing 0.2^{o} per time step.

7.3.5 Design Investigation Study

The validated model was used to investigate the effects of design decisions on device performance. The CFD results from the current device setup (Figure 7.10 (a)) are used as a baseline against which all other device setups are compared. The following design decisions are investigated.

1. Turbine position: the present turbine location relative to the static parts of the device was chosen based on experimental studies of flow acceleration around the bluff body [190], which found that maximum localised flow acceleration occurred at the widest point of the bluff body. To investigate whether this is indeed the optimum position for the turbine, two models are used where the turbine is moved downstream from its present position by 100 mm and 200 mm.

2. Shaft diameter: It is well understood that larger diameter shafts generate more turbulence and vorticity than smaller diameter shafts [176]. As the current 1:20 scale device uses a 40 mm diameter shaft, additional analyses for shaft diameters of 15 mm and 80 mm were investigated.

3. Blade pitching: The effects of variable pitching blades were assessed by simulating the same device, but with fixed 0° pitch blades (Figure 7.10 (b)). To assess the effects of the number of blades; a 3-bladed device was modelled for both variable pitch blades (Figure 7.10 (c)) and fixed 0° pitch blades (Figure 7.10 (d)). A 3-bladed turbine was chosen for comparison as a small number of blades (usually 2 or 3) is more typical of VATS.

4. Hydrofoil chord-length: a model consisting of 0.15 m chord-length hydrofoils is compared with the current 0.2 m chord-length hydrofoils. Both models use NACA 0018 hydrofoils.

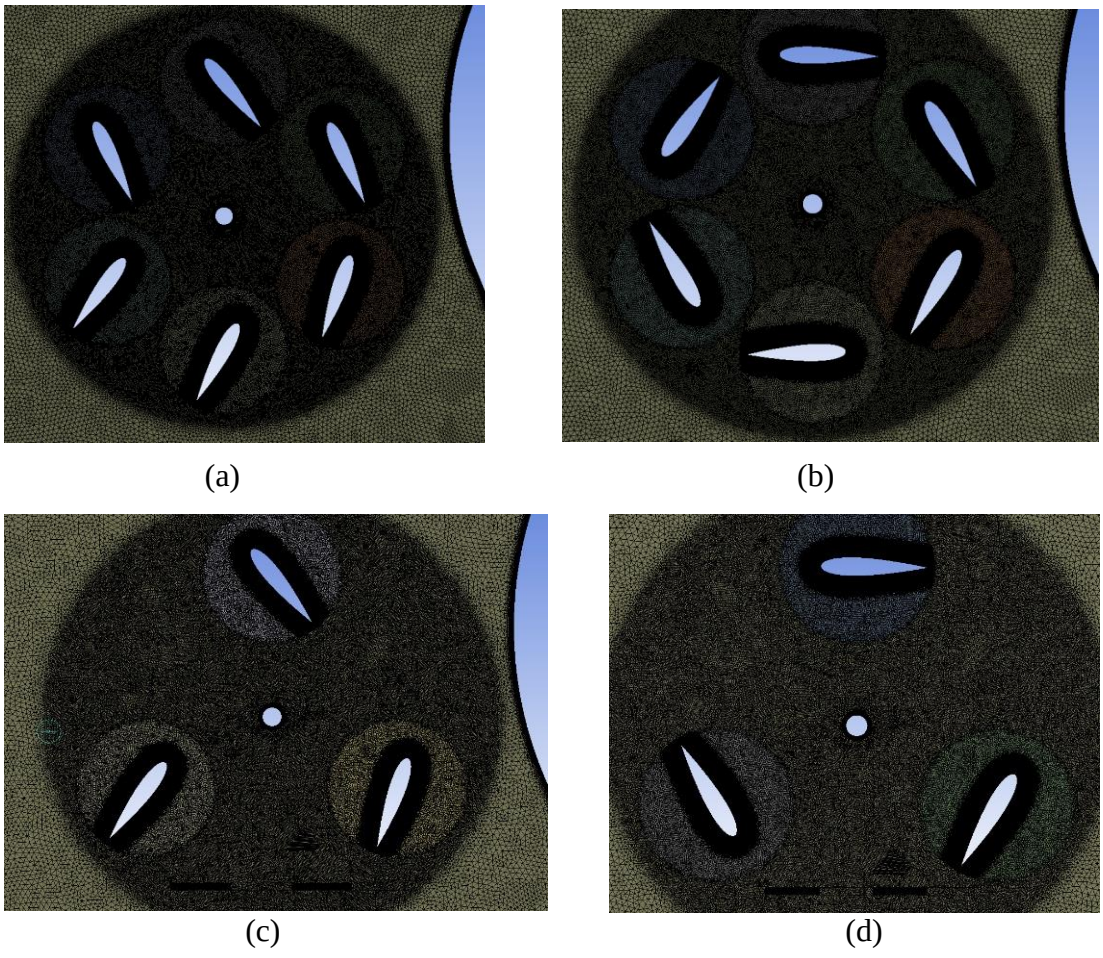

Figure 7.10: Images of meshes used for carrying out investigation of performance for (a) variable pitch baseline model experimental setup, (b) 6-bladed 0^{o} fixed pitched (c) 3-bladed variable pitched and (d) 3-bladed 0^{o} fixed pitched.

7.4 Model Validation

Model-predicted power coefficients and downstream flow velocities are presented in this section and compared with measured experimental data for model validation. Two sets of model results are presented, to compare model performance for the Transitional and $k-\omega$ SST turbulence models.

7.4.1 Model Validation for Power Coefficient

Power performance of the turbine is assessed using the power coefficient, C_P. A common method for calculation of C_P from CFD simulations uses the average moment coefficient ($\overline{C_m}$) over one complete rotation, multiplied by λ. For cases where the free-stream velocity is accelerated before entering the turbine, as in this work, an alternative approach is required. Instead, the torque is output after the completion of each time-step and averaged over the last complete rotation of the simulation. This average torque is then multiplied by the angular velocity of the turbine to give the mechanical power. C_P is subsequently calculated as the ratio of the mechanical power to the available power, where the velocities used in the calculation are determined far upstream. Figure 7.11 presents a comparison of modelled C_P versus λ (for the two different turbulence models) with the corresponding measured data for a free-stream flow speed of 1.1 m/s.

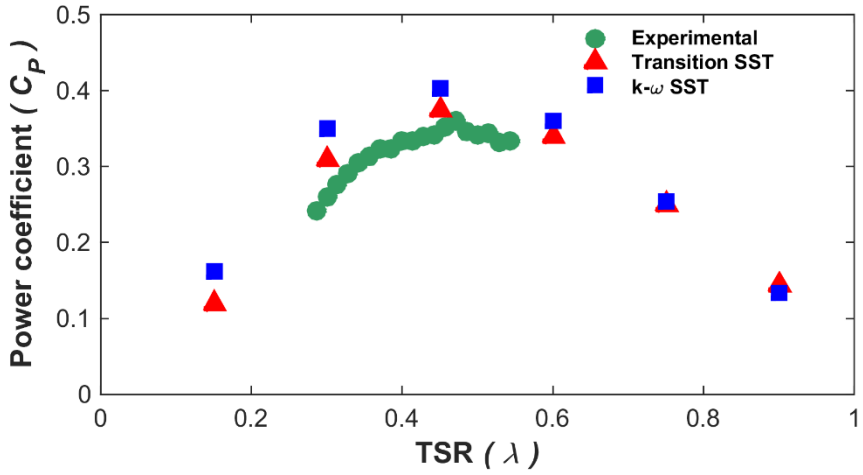

Figure 7.11: Power curve (with rotational speed controlled) comparison between experimental and CFD at a free-stream flow speed of 1.1 m/s.

It can be seen that both models performed well in predicting C_{Pmax} and the overall trend of the power curve. The test data recorded a C_{Pmax} of 0.35 at a λ value of 0.46 and both CFD models predicted the C_{Pmax} to occur at a λ equal to 0.45. The results from the Transitional SST model are more accurate than those from the $k-\omega$ SST model. For C_{Pmax}, the difference in modelled and measured values was just 5.7 % for the Transitional SST model, while the difference was 14 % for the $k-\omega$ SST model. The more accurate Transitional SST model was also subsequently assessed for a free-stream flow speed of 0.7 m/s. Figure 7.12 shows the comparison of the modelled and measured power curves for this flow speed (U_∞ equal to 0.7 m/s). The model is accurate to within 10 % for C_{Pmax} and the general trends are again in agreement.

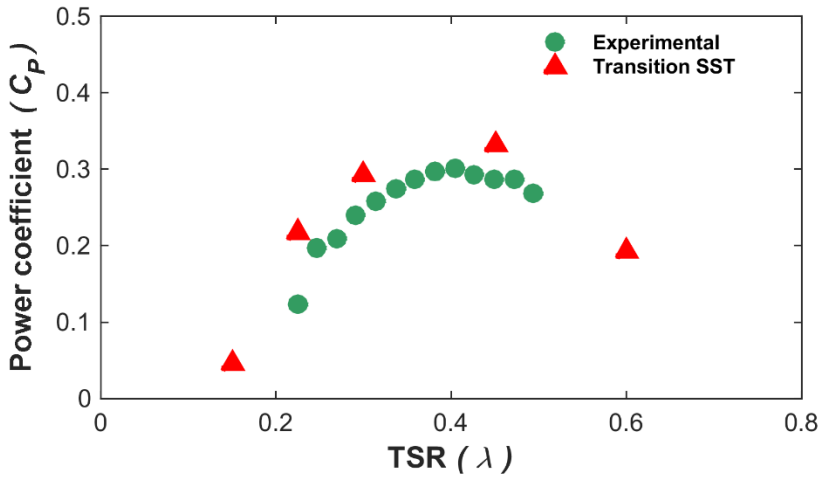

Figure 7.12: Power curve comparison between experimental and CFD at a free-stream flow speed of 0.7 m/s.

Figure 7.13 and Figure 7.14 present velocity contour plots (at U_∞ equal to 1.1 m/s). after 14 rotations from the two different turbulence model simulations. The two plots clearly show the complexity of the flow through and around the device. The flow acceleration, blade pitching and high solidity of the device are some of the reasons why such a complex flow is formed.

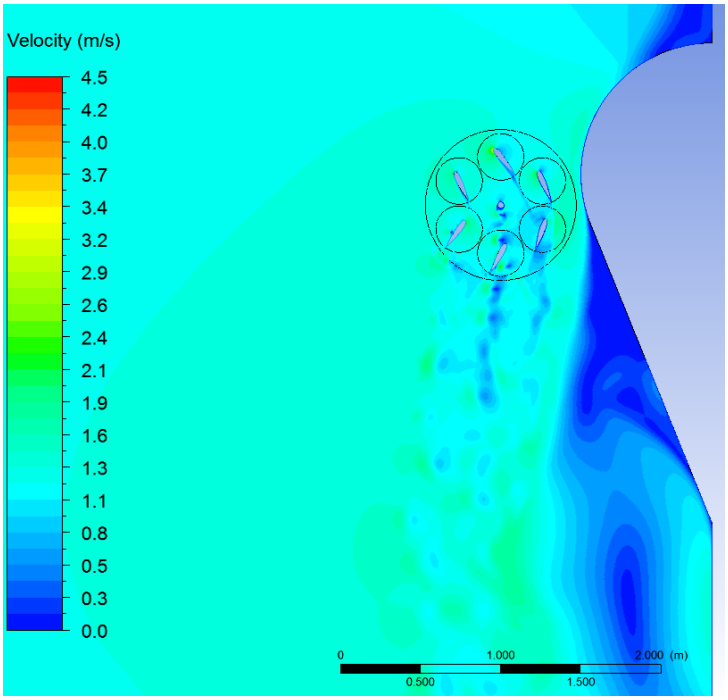

Figure 7.13: Transitional SST velocity contour map around the device at 1.1 m/s.

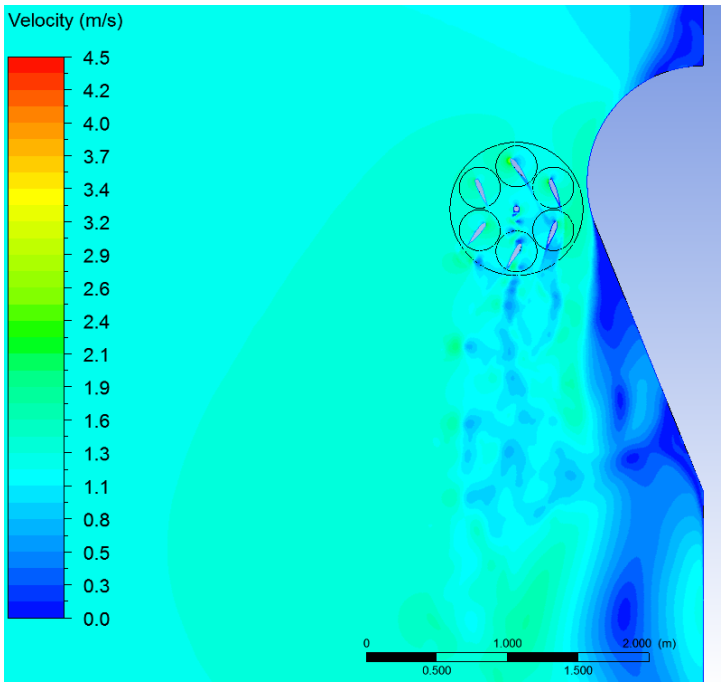

Figure 7.14: $k-\omega$ SST velocity contour map around the device at 1.1 m/s.

Figure 7.15 presents a comparison of the results when the 2D CFD model was corrected and uncorrected for blockage. In the uncorrected model, the lateral width of the domain was reflective of the experimental setup but resulted in much higher blockage factor than in reality. The CFD corrected results are identical to those

presented in Figure 7.11, for the experimental and Transitional SST model. The uncorrected results are shown to overestimate the experimentally determined C_{Pmax} by over 60 %, and the optimum λ value is seen to be three times that of the measured value.

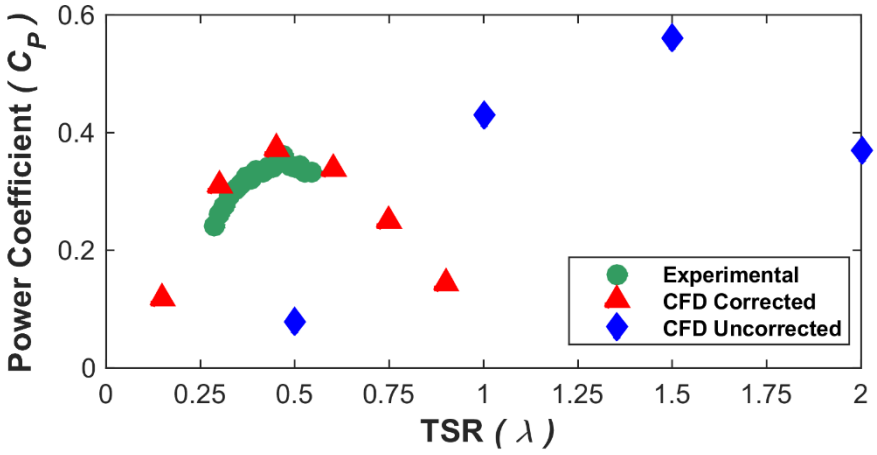

Figure 7.15: Transitional SST CFD model showing variation in blockage corrected and uncorrected results at 1.1 m/s, and compared to experimental results of the same flow speed.

7.4.2 Model Validation for Downstream Velocities

The LDV velocities measured at mid-turbine depth for the 1:20 scale device in Chapter 4, are presented here in the form of a velocity vector plot in Figure 7.16. Velocities are clearly reduced in the near-wake of the turbine and flow reversal due to the generation of turbulent eddies can also be observed adjacent to the bluff body.

By way of further model validation, modelled velocities (at U_∞ equal to 0.8 m/s) are compared with the measured data along transects A-A and B-B in Figure 7.17 and Figure 7.18, respectively. The Transitional SST model is again shown to be most accurate. Both of the model datasets contain some velocity fluctuations not present in the measured data, but the fluctuations are of much lower magnitudes in the Transitional SST model. Given the complexity of the downstream flows shown in Figure 7.13 and Figure 7.14, the level of agreement achieved by the Transitional SST model is very encouraging. The model accurately predicts both the reductions in near-wake velocities and the flow reversal due to the presence of the turbulent eddies. Table 7.6 presents RMSE values for the near-wake velocity data, predicted by the two turbulence models, relative to the measured LDV data. RMSEs are significantly lower for the Transitional SST model.

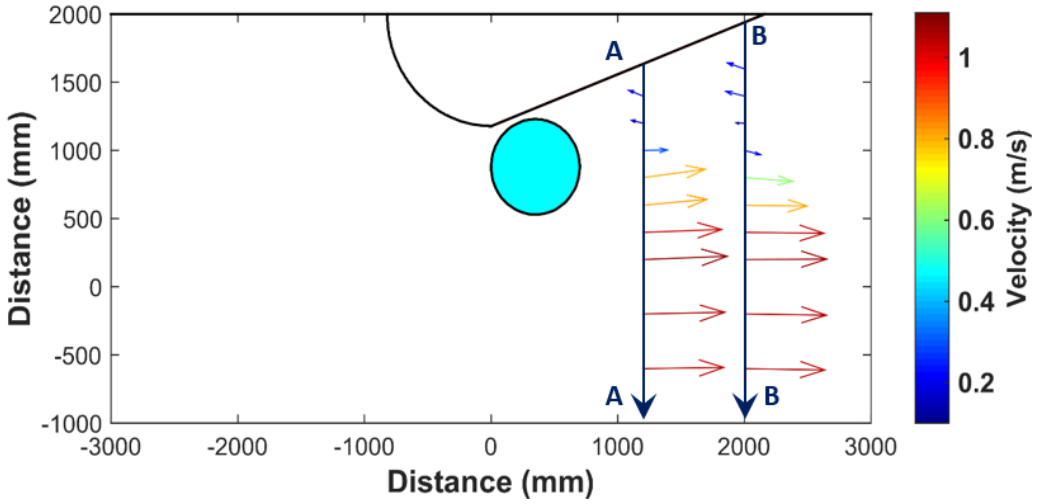

Figure 7.16: Vector plot of LDV experimental flow data for transects A-A and B-B.

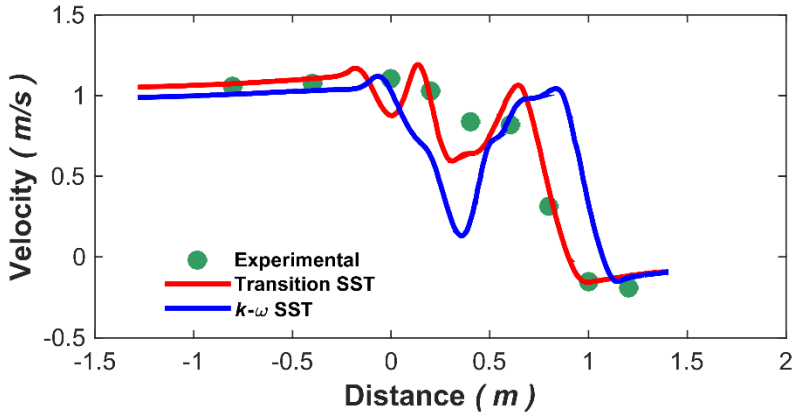

Figure 7.17: Velocity comparison between the SST turbulence models and experimental data along transect A-A

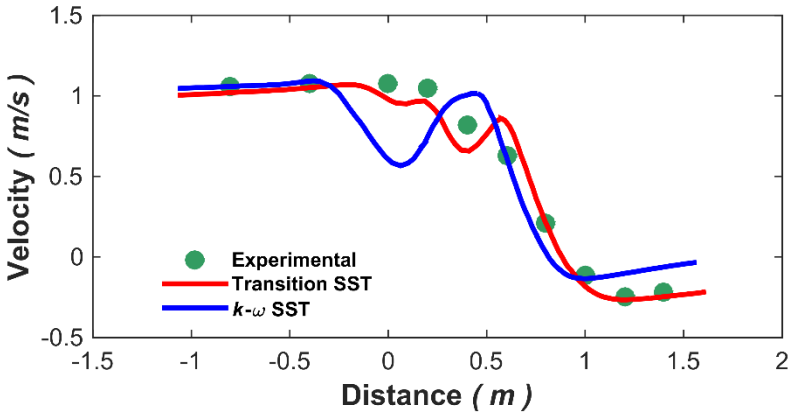

Figure 7.18: Velocity comparison between SST models and experimental data along transect B-B

Table 7.6: RMSE values for predicted velocity data along transects A-A and B-B

	Transitional SST RMSE (m/s)	$k-\omega$ SST RMSE (m/s)
Transect A-A	0.13	0.38
Transect B-B	0.10	0.21

Contours of the turbulent kinetic energy for each of the SST turbulence models are presented in Figure 7.19. The more chaotic distribution of k predicted by the $k-\omega$ SST model is consistent with the larger velocity fluctuations observed for this model in Figure 7.17 and Figure 7.18.

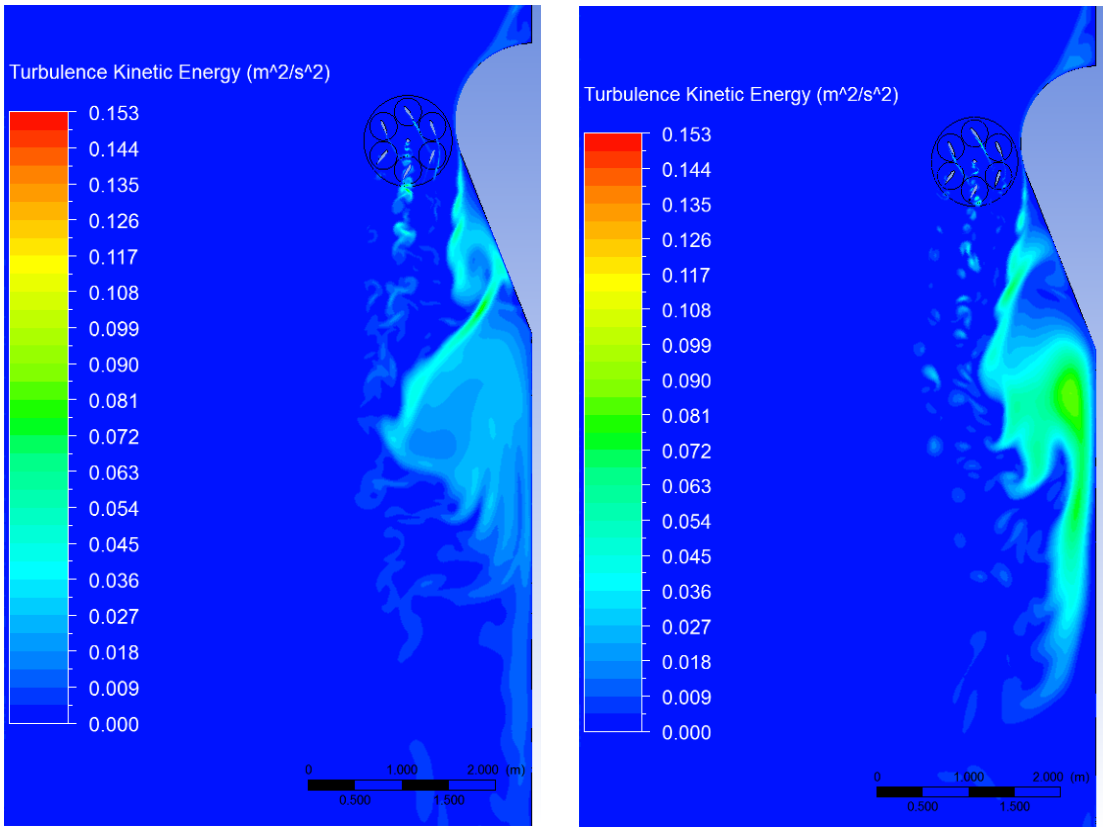

(a) (b)

Figure 7.19: Contour plots for turbulence kinetic energy from (a) Transitional SST, and (b) $k-\omega$ SST models.

Figure 7.20 shows how the averaging nature of the URANS equations dissipates the specified boundary condition for turbulence intensity (5 %) at the inlet. The GKinetic device was positioned 10 m downstream from the inlet. Therefore, the actual value for the turbulence intensity at the turbine was approximately 3 %. As was discussed in the literature review of Chapter 2, a study by Mycek *et al.* [58] showed that turbulence intensity has little to no impact on mechanical performance but does affect the wake length. This is significant as it shows that URANS models are only suitable for modelling near-field wakes and not far-field wakes.

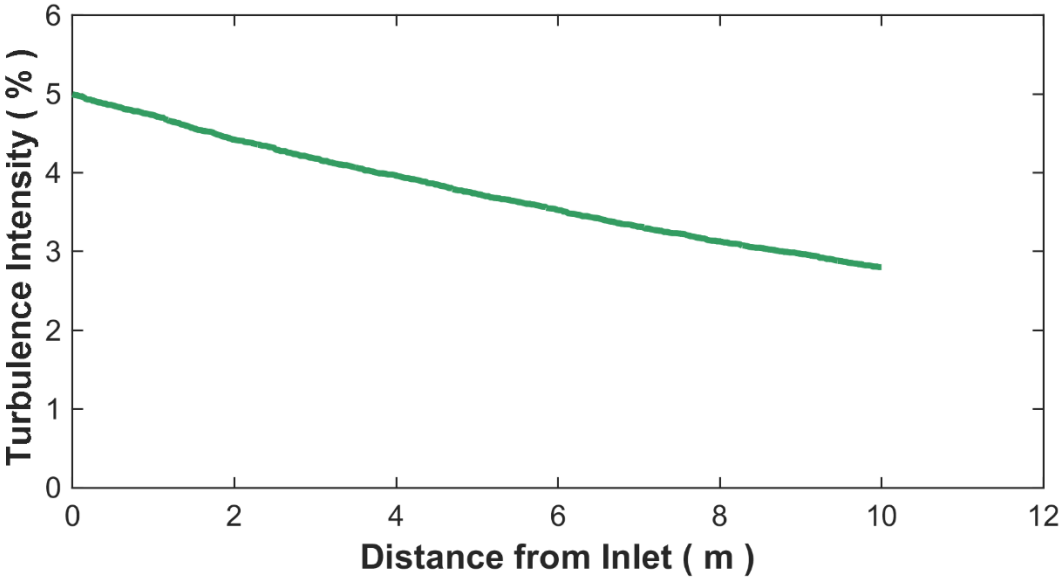

Figure 7.20: Dissipation of turbulence intensity from the upstream boundary to the turbine inlet located 10 m downstream of the boundary.

7.5 Design Investigation Study Results

The results of the convergence studies and model performance validation confirmed that the model was sufficiently accurate for design study purposes. The following sections present the results of the design investigation study, all of which were produced using the Transitional SST model at 1.1 m/s free-stream flow speed. The baseline results used for comparison are the Transitional SST model results from Figure 7.11.

7.5.1 Turbine Position

In the current design set-up, the turbine is positioned at the widest point of the bluff body. This position was determined from an experimental study of flow around a 1:40 scale bluff body conducted in a tidal basin [190] which found that the greatest localised acceleration occurred here. Obviously, the flow around the bluff body will be different from the turbine in place. To determine whether the turbine is in the optimum position, two additional simulations were conducted, with the turbine moved 100 mm and 200 mm downstream; the thinking being that moving the turbine downstream might allow for more flow acceleration to develop before the flow reached the turbine inlet.

Figure 7.21 compares the C_P values for the new turbine positions with those from the turbine in its current position (the baseline case). The baseline case is seen to produce the highest C_P; C_{Pmax} is 6.5 % and 12 % lower for the 100 mm and 200 mm downstream positions, respectively. Figure 7.22 compares velocity contour maps for the three cases. Although there are subtle differences between each case, there is no discernable difference in the entrance flows and it is not possible to definitively conclude why the performance reduces on moving the turbine; one possible explanation is that the present cam control history for each pitch angle which is used in the CFD model via a UDF is designed for the current turbine position and is not optimal for the other cases. It is also possible that there's more space between the turbine and the bluff body.

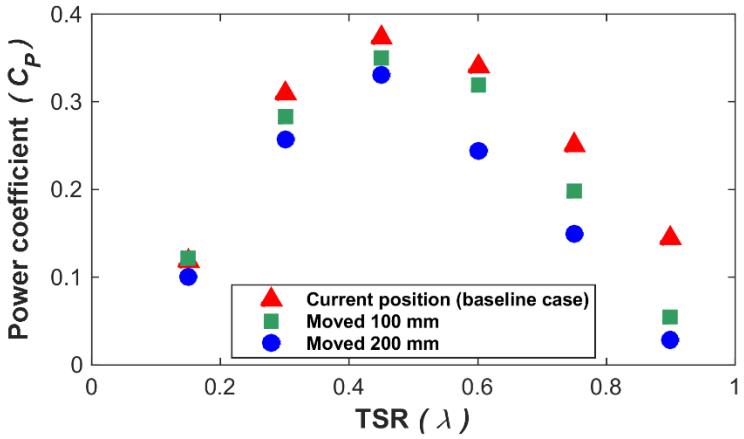

Figure 7.21: Comparison of power curves for three different turbine positions.

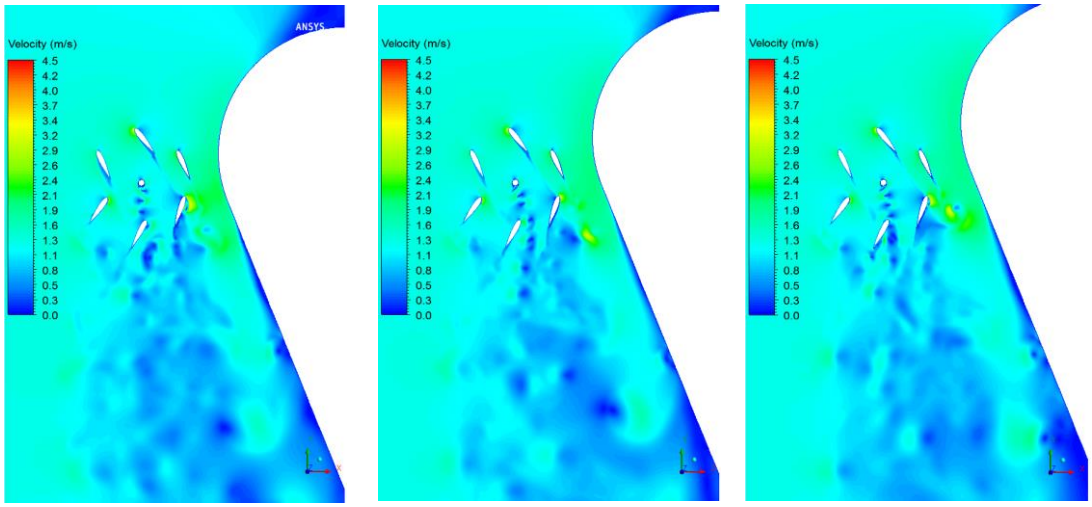

Figure 7.22: Velocity contour plots for different turbine positions behind the widest part of the bluff body for shifted positions of (a) 0 mm (b) 100 mm and (c) 200 mm, relative to static parts.

7.5.2 Shaft Diameter

For VATs, larger turbine shafts create increased turbulence and vorticity on the incoming flow for the downstream blades. The current device uses a shaft of 40 mm diameter. To determine the effect of shaft size, additional model simulations were carried out for shaft diameters of 15 mm and 80 mm. Figure 7.23 compares the resulting $C_{\mathrm{P}max}$ values with that of the current design (baseline case). As expected, use of the 15 mm shaft results in the highest $C_{\mathrm{P}max}$, while the 80 mm gives the lowest. Use of the largest 80 mm shaft results in a 10 % reduction in $C_{\mathrm{P}max}$ compared to the smallest 15 mm shaft. Figure 7.24 presents contour maps of velocities in the vicinity of the turbine for the three design cases. For the 15 mm case, the shaft wake is quite confined in width but as the shaft diameter increases, it can be seen that the vortex street generated by the shaft spreads over an increasingly wider region, thereby impacting on more of the downstream blades and enhancing their parasitic nature to device performance.

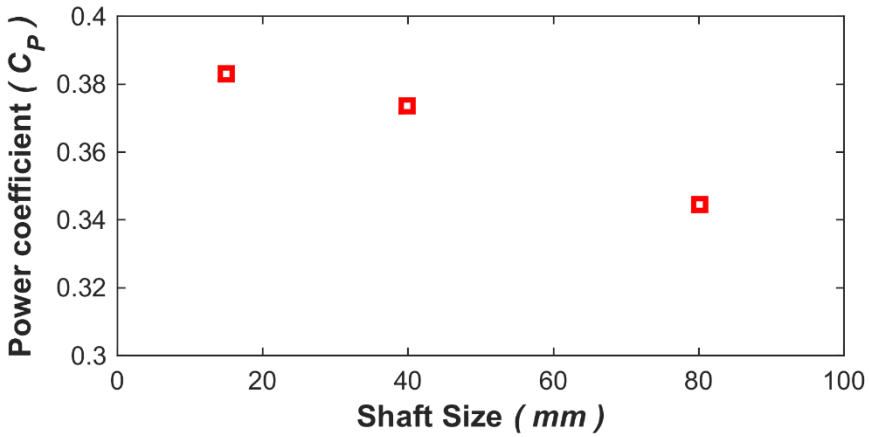

Figure 7.23: Power performance coefficient for turbine against turbine shaft diameter.

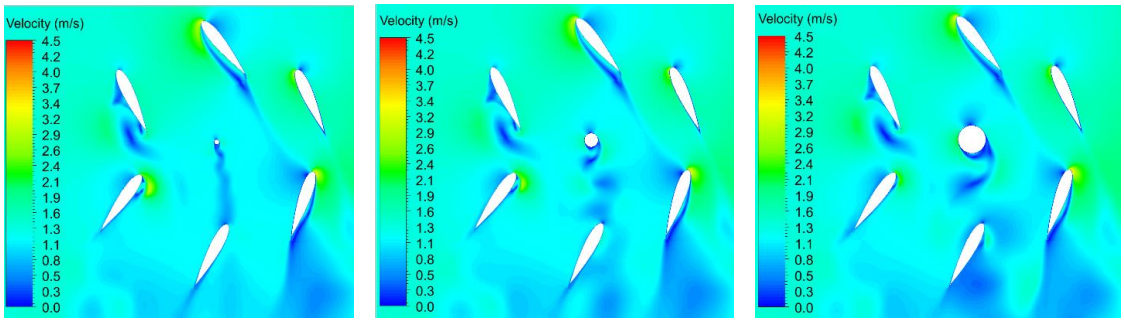

(a) (b) (c)

Figure 7.24: Velocity contour maps for different turbine shaft diameters: (a) 15 mm, (b) 40 mm (baseline case) and (c) 80 mm.

7.5.3 Blade Pitching and Number of Blades

The benefit of the pitching blades with regard to power performance was investigated using an additional simulation where the turbine was modelled with 0^o fixed pitch blades. The effect of device solidity was also investigated by replacing the 6-blade turbine with a 3-blade turbine for both the variable and fixed pitch scenarios. The variable-pitch control specified for the 3-blade turbine was the same as that used for the current 6-blade turbine. Figure 7.25 compares the power curves for these cases. The current 6-blade variable-pitch setup is again, denoted as the baseline case.

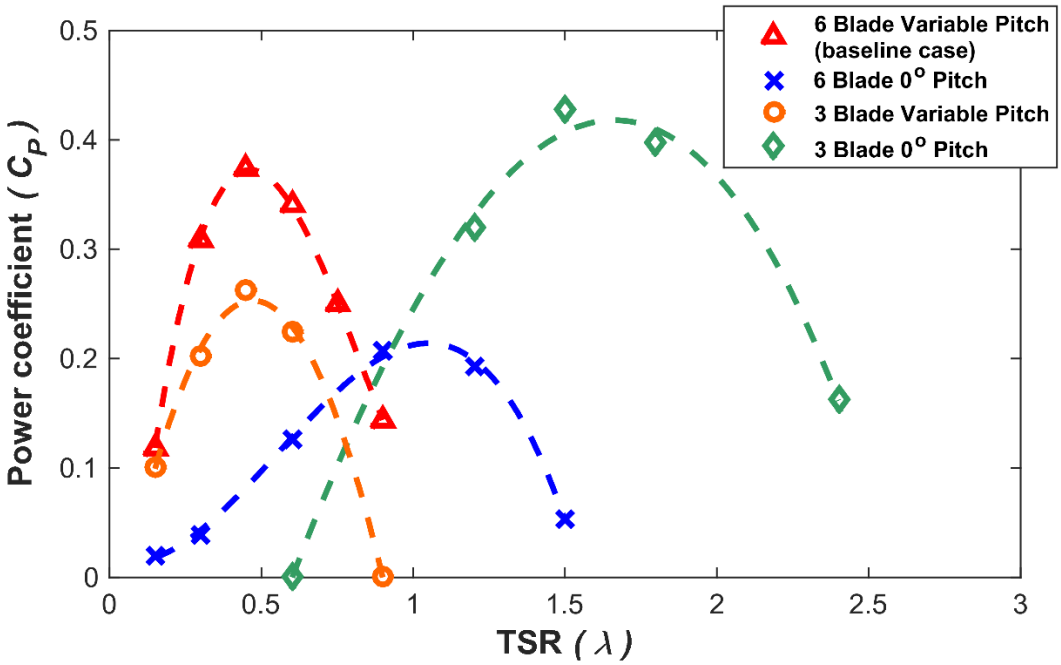

Figure 7.25: Comparison of modelled power curves for 3 and 6-bladed turbines with variable-pitching blades and 0^o fixed pitch blades.

Comparison of the 6-blade variable-pitch baseline case and the 6-blade 0^o fixed pitch case shows the beneficial effect of the variable-pitch regime; it results in an increase in C_{Pmax} from 0.21 to 0.37 and significantly reduces the optimum λ value for C_{Pmax} from 0.9 to 0.45. The 3-blade variable-pitch case shows significantly lower performance than the 6-blade case (C_{Pmax} of 0.26 compared to 0.37). This may be due to the fact that the blade pitch control scheme had been optimised for C_{Pmax} to be achieved at a low λ value, while the 3-bladed turbine will necessarily have a higher optimum λ value. By comparison, the 3-blade 0^o fixed pitch case achieves approximately 0.05 higher C_{Pmax} than the baseline case, although at a much higher optimum λ value (1.7 versus 0.45), and achieves a C_{Pmax} value 76 % higher than its 6-bladed counterpart.

Figure 7.26 to Figure 7.29 present velocity contour and vector plots for the four different design cases at their relevant optimum λ value. Comparing Figure 7.26 (6-blade, variable-pitch) and Figure 7.27 (6-blade, fixed pitch), it is clear that the high solidity of the 6-blade 0^o fixed pitch turbine causes a significant blockage. The bulk of the flow is directed around the turbine, without any beneficial blade interactions, resulting in lower power performance. This is also demonstrated by the very low

velocities inside the turbine in the vector plot of Figure 7.27 (b). The directions of the vectors show that the majority of the flow is passing around the turbine, rather than through it, as a result of the excessive turbine solidity.

Comparing the 3-blade variable-pitch case of Figure 7.28 to those of the 6-blade variable-pitch baseline case (Figure 7.26), the instantaneous velocities immediately around the hydrofoils are seen to be quite similar; however, the contour maps show very different near-wakes. The area of high velocity immediately downstream of the 3-blade case suggests little power extraction from the flow on the right side of the turbine. Some of the flow seems to pass through without interacting with the blades. This is also where the highest inlet velocities are experienced. Much of the available power is, therefore, being lost and power extraction is lower.

Comparing the velocity plots of the 3-blade 0^o fixed pitch case in Figure 7.29 to those of the baseline 6-blade variable-pitch case of Figure 7.26, it can be seen that the peak velocities of the 3-blade 0^o fixed pitch case are significantly higher than those of the 6-blade baseline case; this is likely due to the fact that the optimum λ value of the former is also much higher. While the power performances of the two cases are similar, the velocity deficits in the near-wake of the 3-blade 0^o fixed case are more significant than those of the baseline case and could be significant in terms of the proximity of downstream devices in array deployments.

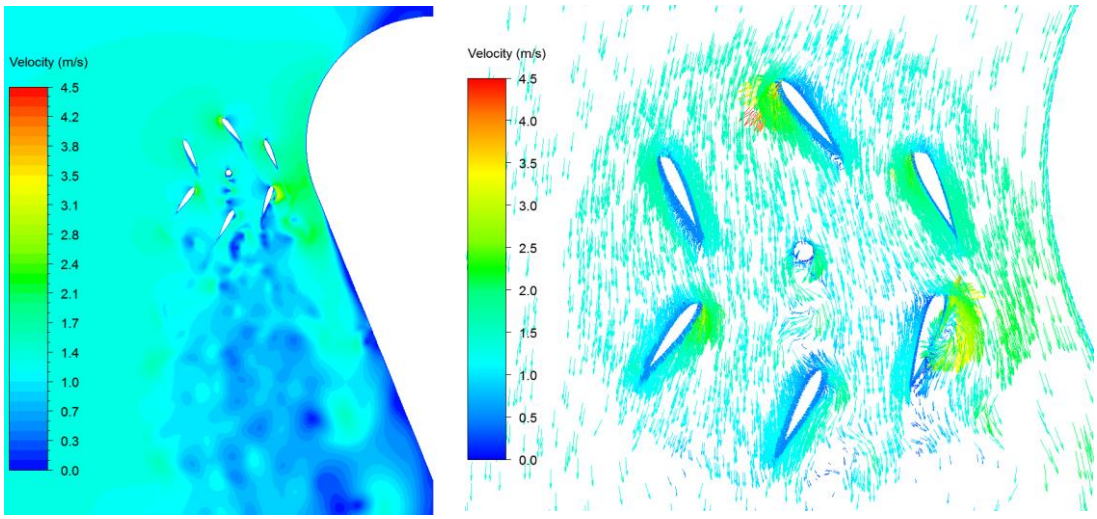

(a) (b)

Figure 7.26: Velocity plot of variable pitch baseline case for (a) contour and (b) vector plot at optimum λ value of 0.45.

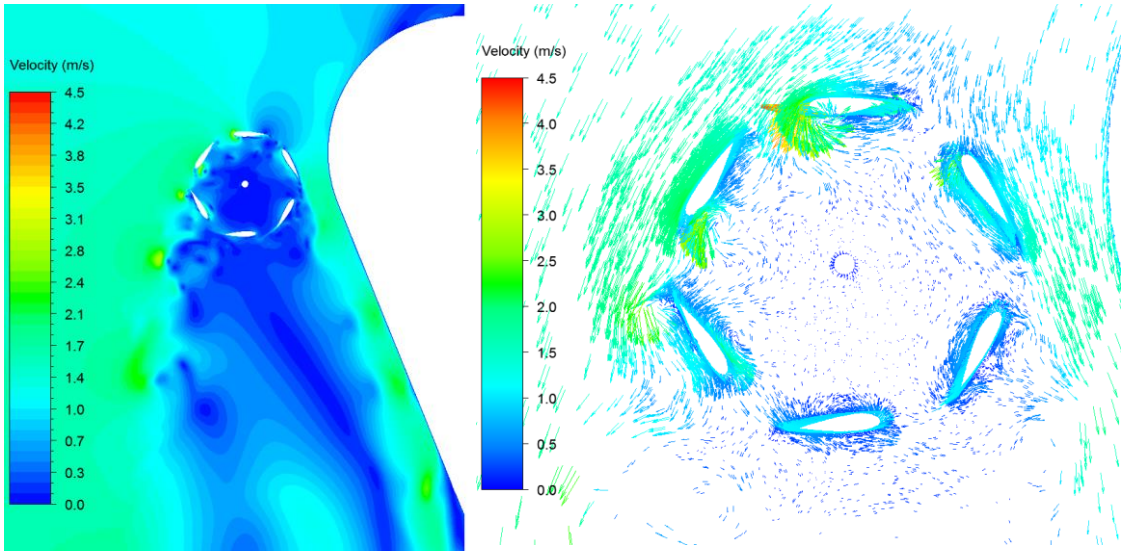

(a) (b)

Figure 7.27: Velocity plot of 6-bladed 0^{o} fixed pitch case for (a) contour and (b) vector plot at optimum λ value of 0.9.

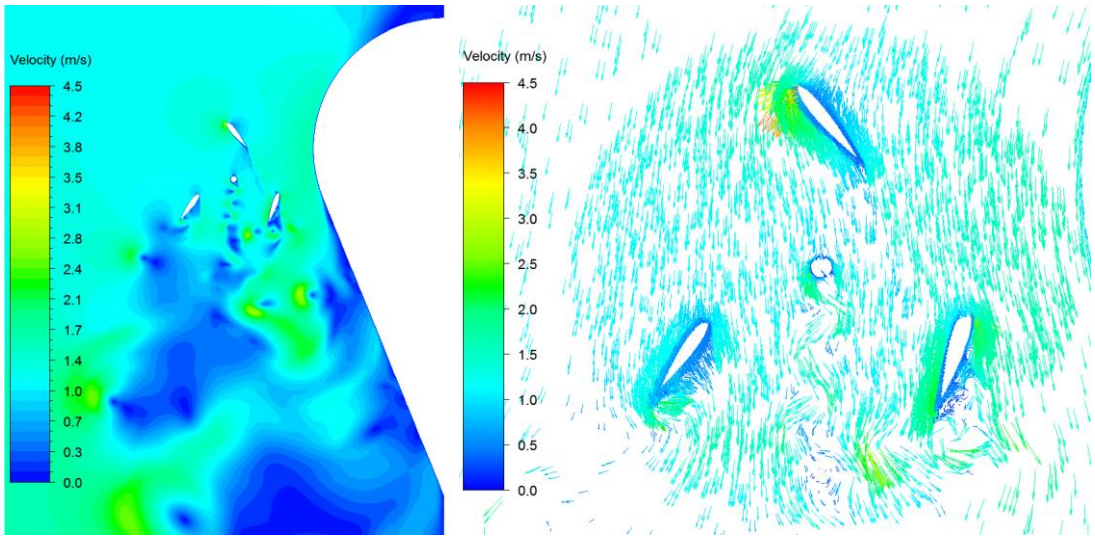

(a) (b)

Figure 7.28: Velocity plot of the 3-bladed variable-pitch case for (a) contour and (b) vector plot at optimum λ value of 0.45.

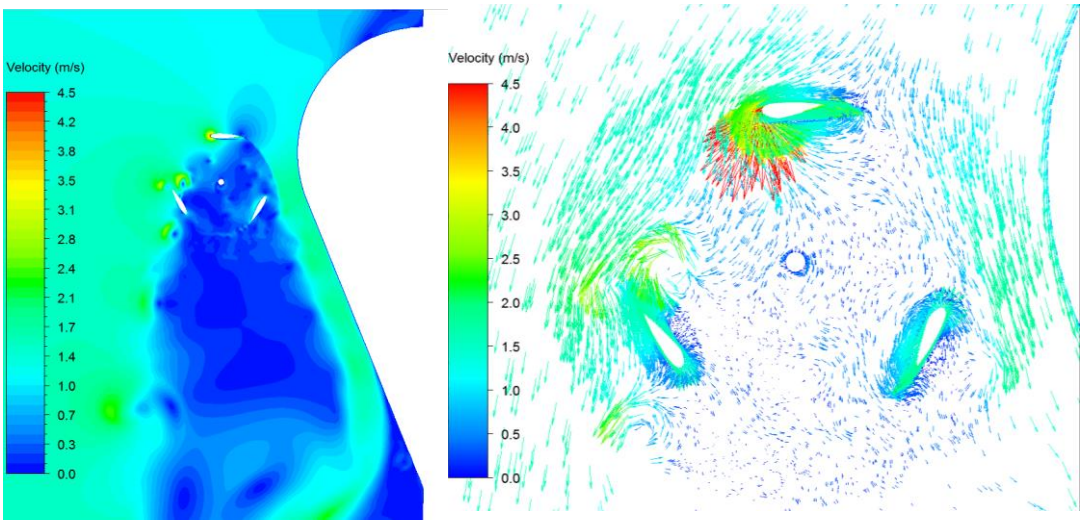

(a) (b)

Figure 7.29: Velocity plot of 3-bladed 0^{o} fixed pitch case for (a) contour and (b) vector plot at optimum λ value of 1.5.

7.5.4 Effect of Chord-length

An investigation was conducted to determine the effect of a shorter chord-length (0.15 m versus the current baseline case 0.2 m) on device performance. It was hypothesised that a shorter chord would reduce the solidity of the device and, therefore, reducing turbine blockage of the flow. Figure 7.30 presents a comparison of the power curves for both cases. The baseline case with the longer chord achieves a higher performance throughout the λ range. Use of the 0.15 m chord results in a 10.5 % reduction in $C_{\mathrm{P}max}$. Figure 7.31 presents velocity contour maps (at a λ value of 0.45) from the 0.2 m chord and 0.15 m chord models, denoted in the figure as (a) and (b), respectively. Unfortunately, the contour maps do not exhibit any dissimilarities that could explain the difference in C_{P}; however, at this λ value, there is only a 4 % difference in C_{P} between the two cases.

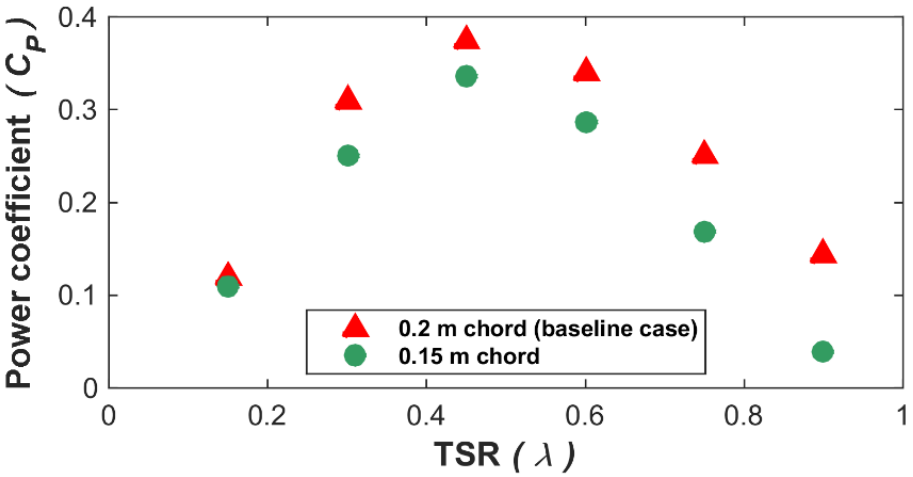

Figure 7.30: Comparison of turbine performance for two different hydrofoil chord-lengths.

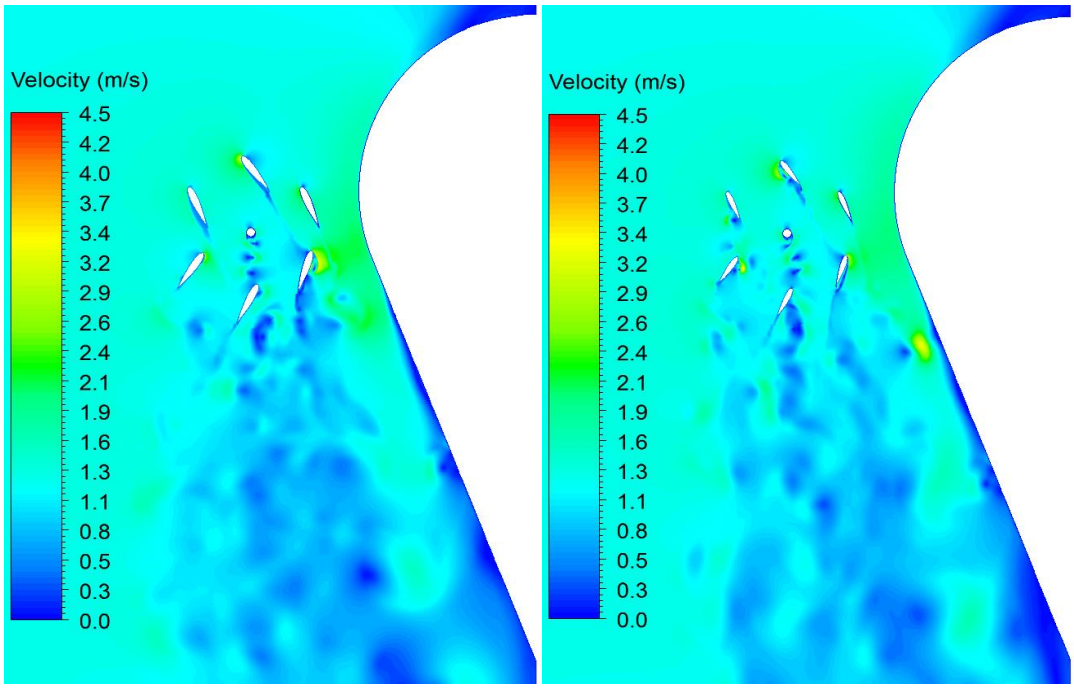

(a) (b)

Figure 7.31: Turbine consisting of hydrofoils with chord-lengths of length (a) 0.2 m and (b) 0.15 m.

7.6 Discussion of Results

The sliding mesh technique for mesh motion has been utilised to facilitate nested sliding meshes and enable CFD modelling and assessment of a novel tidal turbine. The model mesh contains a total of eight different domains including seven rotating domains. Independent blade pitching has been incorporated into the model via a UDF

to control the rotation of the blade meshes. This UDF enables the blades to pitch precisely in the same manner as in the scale experimentally tested device. This modelling approach could be applied to other variable-pitch turbines and also various other types of turbomachinery.

A mesh and time-step independent solution were achieved through the use of sensitivity studies and the Richardson extrapolation. As mentioned, it was not possible to carry out a sensitivity study on the domain diameter sizing. Previous studies [191,192] have shown that results can be affected by the size of the rotating domain relative to the turbine diameter; these studies recommend a rotating domain of at least 1.5 times the turbine diameter for accurate results. In the current research, a rotating domain of precisely 1.5 times the turbine diameter was used, and acceptable agreement between the experimental and model data was achieved.

The CFD-predicted power coefficients correlate closely with the experimental test data, particularly in the case of the Transitional SST turbulence model. Previous published 2D CFD models attribute over-prediction of turbine performance to blade tip end effects and a higher blockage ratio [193]. When blockage was unaccounted for, $C_{\mathrm{P}max}$ prediction was overestimated by over 60 %, and the optimum λ value was three times the measured value.

When comparing the modelled velocities with the LDV measured velocities, in general, the Transitional SST model outperformed the $k-\omega$ SST model. It is thought that this is due to the superior abilities of the Transitional SST model in modelling the transition phase from laminar to turbulent flow. The transitional SST model is therefore recommended for future use in the CFD modelling of vertical axis tidal turbines. However, it was also shown that the averaging nature of the URANS equations dissipates the turbulence intensity specified at the inlet prior to reaching the turbine inlet 10 m downstream. This is significant as it shows that URANS models are only suitable for modelling near-wakes and not far-field wakes. In order to properly characterise the far-field downstream wake, higher order models such as DES and LES would be required as well as far-field wake experimental data for validation. Due to the high computational costs associated with DES and LES, this may be prohibitive with the current level of computational resources.

Several design investigations were conducted using the validated model. Investigation of the positioning of the turbine relative to the bluff body suggests that the current turbine position is optimal. When the turbine was positioned further downstream, performance dropped off. Investigation of shaft sizing confirmed, as expected, that larger shafts are detrimental to turbine performance. A trade-off is, therefore, necessary in regards to selection of the optimum shaft diameter; one must choose between greater structural integrity (stiffness and strength) on the one hand and better power performance on the other hand.

Investigation of variable versus fixed pitch design cases showed that including a pitching regime has had a positive effect on the device performance for the 6-blade case with $C_{\mathrm{P}max}$ being 60 % greater compared to a 0^{o} fixed pitch device and occurring at a lower λ value. The current blade pitch control regime had been optimised for $C_{\mathrm{P}max}$ to be achieved at a low λ value (less than 0.5). As a result, the 3-blade variable-pitch case had insufficient interaction with the flow at this low rotational speed, and significantly lower performance was observed. A different pitch control scheme would be required to properly assess the benefits of the 3-blade case.

The 3-blade 0^{o} fixed pitched case achieved a $C_{\mathrm{P}max}$ that was 5 % higher than that of the 6-blade variable-pitch case thus potentially showing it be a more preferred design. In addition to the improved performance, there would also be lower manufacturing and maintenance costs associated with a 3-bladed fixed pitch device due to the lower number of blades and omission of a pitch control mechanism. However, the optimum rotational velocity of the 3-blade case is more than three times higher than that of the 6-blade variable-pitch case; this is significant in relation to environmental impacts since, lower operating λ values are more environmentally desirable as they reduce the risk of fish and/or animal strikes. The downstream velocity contour maps of the near-wake show that the 3-blade case results in higher velocity deficits and therefore, a more persistent wake. This is significant in relation to the potential proximity of downstream devices in an array.

The results from the blade chord-length investigation showed a 50 mm shorter blade chord-length resulted in a lower $C_{\mathrm{P}max}$ value ($\Delta C_{\mathrm{P}max}$ = 0.04). As was shown in Chapter 6, vertical axis turbines extract the majority of power in approximately the

first 140^o of azimuthal rotation. The shorter chord-length means less blade surface area to interact with with the flow as the blade is passing through this critical region at the upstream end of the turbine, resulting in lower overall turbine performance. This area is also where the highest flow accelerations are observed for the current device; it is therefore, paramount that high blade-flow interactions occur in this region without causing excessive flow retardation and blockage.

7.7 Chapter Summary

A 2D CFD model of a novel vertical axis turbine has been developed, successfully incorporating the key design aspects of flow acceleration and blade pitch control. This was achieved via a complex nested sliding mesh technique to allow independent rotation of the turbine and pitching of the blades. The blade mesh motion is controlled through a user-defined function to represent the blade pitch control of each of the six blades independently. A methodology for achieving a mesh and time-independent solution was presented. The following conclusions are drawn from this chapter's results:

- The Transitional SST model is the more suitable turbulence model for CFD modelling of vertical axis turbines. It was shown to be more accurate than the $k-\omega$ SST model for both performance prediction and near-wake characterisation.
- Strict convergence criteria must be employed if accurate, and completely independent (both temporally and spatially) results are to be obtained from CFD turbine models. An average torque difference of $\Delta\bar{Q}<0.1$ % between one rotation and the next is recommended for convergence criterion as it was shown to produce accurate model results.
- The detailed nested sliding mesh approach developed here could be adopted for other CFD studies of variable-pitch turbines or turbomachinery with complex moving parts.
- Model investigation of the different design cases has confirmed that implementing blade pitch control has had a positive effect on device performance (for a 6-blade case) in the present design compared with the use of a similarly fixed pitch turbine. Pitch control can also be utilised to reduce

the operating λ value of the device where there are environmental concerns while maintaining good performance.

Chapter 8. Summary and Conclusions

8.1 Introduction

The GKinetic turbine comprises a central bluff body which accelerates the entrance flows into two variable pitch VATTs located on either side of the bluff body. Both the flow acceleration and the variable pitching blades are novel aspects of the device. The primary aims of this research were to experimentally evaluate the performance of the GKinetic turbine, and subsequently use this test data to aid the development of a CFD model for prediction of device performance. In the process, the research developed a computationally low-cost (BEMT) and high-cost (CFD) power performance models suitable for more standard VATTs and assessed their levels of accuracy. The research also developed a nested sliding mesh technique which can be used generally for variable pitch VATs or other turbo-machinery involving multiple moving parts.

This chapter summarises and discusses the main findings of the work (Section 8.2) before overall thesis conclusions (Section 8.3) and presenting the recommendations for future studies (Section 8.4).

8.2 Chapter Summaries

This section gives a brief summary of the main results of Chapters 4 to 7.

8.2.1 Chapter 4: Experimental Testing of the GKinetic Turbine

Scale experimental tests are important stages in the development of a viable commercial-scale tidal energy device as they provide crucial information on device performance and rich datasets for validation of numerical models. Chapter 4 presented the methodology and results from scale experimental testing of the GKinetic vertical axis tidal turbine at 1:40, 1:20 and 1:10 scales.

The 1:20 scale testing allowed the study of the flow accelerating capacity of the bluff body. Although a previous study had shown that the bluff body could accelerate the flow velocity by a factor of 2, maximum acceleration measured in the 1:20 scale experiments was 1.6 times free-stream. However, CFD modelling of the 1:20 scale device proved that the flow acceleration was hampered by the boundary layer produced by the concrete tank wall which significantly reduced the free-stream

velocities upstream of the bluff body. When the effect of wall friction was removed, the CFD model showed that accelerations did indeed reach a factor of 2.

The 1:20 scale modelling allowed the development of a series of power curves relating mechanical power coefficient to tip speed ratio. Peak efficiencies of 40 % were recorded, but it should be noted that the blockage in the tank was high at 25 %. Unfortunately, there is currently no accepted method of correcting VATT test results for blockage and so this was not possible. Increasing channel blockage leads to higher levels of power extraction than would occur for lower blockage levels; thus, the measured power coefficients are likely a little high. However, this is balanced by the fact that these were achieved with lower levels of acceleration (factor of 1.6 instead of 2). The research found the optimum λ for the turbines was in the region of 0.45 to 0.55. This is important information as the operation of the device will involve controlling the turbine rotation speed to ensure optimum λ values. Measured power coefficients and near-wake velocities from the tests were subsequently used for validation of a developed CFD model presented in Chapter 7.

The power performance results from the 1:10 scale testing were a little disappointing. The maximum and average peak mechanical efficiency across all 1:10 scale tows were 0.27 and 0.135, respectively. Some of the reasons considered to have contributed to the poor performance include device instabilities whilst under tow, problems with the power control system which caused variation in turbine rotational speed, therefore, suboptimal angles of attack blades. However, the 1:10 scale testing established a towing facility for larger scale experimental tow testing of tidal turbines. The facility is planned to be further utilised by GKinetic for future testing of their device and could facilitate other large devices, which are not yet ready for full-scale deployment and the harsh conditions associated with such sites.

8.2.2 Chapter 5: Development and Assessment of a BEMT Model for VATS

Chapter 5 presented the development of a BEMT model to predict the performance of both low and high solidity VAT rotors. While the model was developed for VATTs, it is also applicable to VAWTs.

The model uses a graphical approach for determining induction factors. To the author's knowledge, this is the first time this approach has been applied to vertical axis tidal turbines. This is significant because the traditional iterative approach used in BEMT models for low solidity turbines is not usable for high solidity turbines. For a VAT, Reynolds number can vary significantly around the azimuthal rotation, and the developed BEMT model captures this by recalculating Reynolds numbers for each location and for every potential induction factor. Correction factors for flow expansion, finite aspect ratio and dynamic stall are implemented in the model and can be switched on and off for simulations.

The model shows an acceptable level of accuracy for an early stage evaluation tool. The model reproduced measured $C_{\mathrm{P}max}$ values to within 6.4 % for a low solidity case and to within 27 % for a high solidity case. The corrective approach which had the greatest effect on model accuracy was the inclusion of the dynamic stall model. It's inclusion reduced the RMSE values for the modelled power curve from 0.079 to 0.054 for the low solidity case and from from 0.155 to 0.137 for the high solidity case.

8.2.3 Chapter 6: Development and Assessment of 2D/3D CFD Models for VATTs.

The literature review revealed that the sliding mesh technique is predominantly used in CFD models of VATs. Prior to its application to the complex GKinetic device, the suitability of the technique was assessed for modelling of a standard VATT. Chapter 6 presented the development of 2D and 3D CFD models of the UNH RVAT – a 3-bladed VATT.

The developed 3D model was shown to accurately reproduce the shape and phase of the power curve with less than 5 % difference in $C_{\mathrm{P}max}$. The 3D model was also able to accurately reproduce the turbine near-wake velocities with RMSE values in the region of 0.067 m/s. The high level of accuracy of the 3D model was attributed to the rigorous and systematic approach to mesh development, model convergence and sensitivity studies.

As expected from the finding of the literature review, 2D model accuracy was quite

poor of VATTs in confined flow. Other studies have attributed 2D model inaccuracy to the higher blockage of a 2D model versus a 3D, but this has never been proven. This research showed 2D power over-prediction is indeed partly due to higher blockage levels. This can be corrected for by extending the model domain width to match the channel blockage of the experiment setup or 3D model. The uncorrected 2D model significantly over-predicted C_P values, with an average RMSE in excess of 0.26. However, the blockage-corrected model produced much more accurate C_P predictions with an average RMSE in the region of 0.05. In this instance, blockage therefore accounted for 80 % of the model over-prediction. Correcting for blockage also gave better predictions of both bypass velocities and near-wake velocities.

In comparison with the accuracy of the BEMT model of the UNH-RVAT from Chapter 5, the CFD models are clearly more accurate. Although the BEMT model over-predicted peak performance by 27 %, compared with 20 % for the 2D CFD model, the phase shift in the BEMT results means there is a significant disparity in the accuracy of the two models. The BEMT RMSE value for the power curve was 0.121 compared to 0.057 for the blockage corrected 2D model and 0.028 for the 3D model.

8.2.4 Chapter 7: Development and Assessment of a 2D CFD Model of the GKinetic VATT.

Chapter 7 presented the development of a 2D model of the variable pitch GKinetic device. The 1:20 scale experimental results from Chapter 4 were used to assess model accuracy. The blockage correction approach tested in Chapter 6 was also incorporated into the model. The sliding mesh technique for mesh motion was utilised to facilitate nesting sliding meshes which allow the blades to pitch along their rotational paths independently of the turbine rotation. The final mesh contained eight different domains including the 6 ‘blade’ sliding meshes which are nested within the ‘turbine’ sliding mesh which, in turn, sits with an outer static mesh. The blade pitching was incorporated by using a user-defined function to control the rotation of the blade meshes.

The model was used to simulate the 1:20 scale half-device that was tested in the IFREMER recirculating flume. Given the complexity of the model, a very high

accuracy of the model data compared with experimental data was achieved. The CFD-predicted C_P values agreed closely with the test data of Chapter 4. For C_{Pmax}, the difference in modelled and measured values was just 5.7 % for the Transitional SST model; this difference was 14 % for the $k-\omega$ SST model. When comparing the modelled and experimentally measured near-wake velocities, again, the Transitional SST model was shown to be most accurate, with RMSEs of the order of 0.1 m/s compared to RMSEs of 0.2 to 0.4 m/s for the $k-\omega$ SST model.

The model was used to investigate the effects of aspects of the device design on power performance. A comparison of the performance of a fixed pitch turbine with the current variable pitch design showed that variable pitching increased the power coefficient by 0.11. Another interesting result showed that a 3-bladed fixed pitch turbine operating at higher rotating speeds gave slightly higher performance levels (0.05 increase in C_{Pmax}) than the current 6-blade variable pitch case. Although this design would reduce the manufacture and maintenance costs of the device, the higher rotational speeds would increase the risk of fish or animal strikes.

8.3 Conclusions

The following overall conclusions are drawn from the research:

- There are a limited number of tidal locations globally with peak tidal stream speeds in excess of 2 m/s; the figure that is generally quoted as the minimum requirement for tidal turbines to be economically viable. By accelerating the free-stream flows, devices such as the GKinetic turbine can operate in less energetic tidal currents, or even in rivers thereby significantly increasing the number of potential deployment sites and routes to market.

- Scale model experimental testing is critical to the successful development of an efficient and economically viable tidal energy device. Experimental testing allows for the determination of key device parameters, such as mechanical performance and drag coefficients, as well as turbine wake deficits. Obtaining experimental test data in controlled environments is key for informing and validating numerical models. However, laboratory testing of turbines is

expensive and suitable facilities are relatively scarce, particularly for intermediate sized devices (1:10 to 1:4). Field testing is even more expensive and is further hampered by the difficulties of working in a highly dynamic marine environment, a fact realised all too well by the recent liquidation of OpenHydro. The testing programme implemented in this research established a towing facility for intermediate and larger scale tidal turbines. The financial costs associated with upscaling devices can be kept to a minimum by completing optimisation studies, as much as possible, at smaller scales; however, this is not always possible and numerical models can play an important role here.

- Numerical models are of vital importance to the development process of commercial-scale tidal devices and offer a cost-effective alternative to experimental testing for assessment and optimisation of prototypes at any scale. There are drawbacks with numerical modelling in that, they do require some experimental test data for validation purposes and they cannot completely account for all real word conditions. Numerical modelling and experimental testing should be used to inform each other and reduce the risk associated with moving to larger scale devices. Numerical models can be validated against measured data from small scale physical model experiments and once accuracy has been ensured, models can then be developed of larger scale prototypes prior to their construction. BEMT models can be used in the first instance, to estimate the performance of devices and determine blade forces to inform structural design. CFD models can then be used to inform the progression plan for larger scale devices, in particular with a view to optimisation of the hydrodynamic performance of the device or investigating aspects of the design. The experimentally validated CFD model of the GKinetic turbine developed as part of this research was used to investigate several alternative design iterations of the device. Therefore, keeping the requirement for experimental testing and the financial risk associated with progression to larger scales to a minimum.

- BEMT models can be used to inform the early stage design process for VATTs. The research has shown that it is possible to evaluate the performance of both low and high solidity devices by incorporating the graphical approach for determining axial induction factors by McIntosh *et al*. [44]; by comparison, the more commonly used iterative method cannot be used at all for such high solidity turbines. The developed model was reasonably accurate for low solidity turbines but less accurate for high solidity turbines. In general, BEMT model accuracy can be improved by implementing corrective approaches for flow expansion, finite aspect ratio, and dynamic stall.

- The rigorous CFD model development approach resulted in a highly accurate 3D model. This proves that URANS CFD models can give sufficient levels of accuracy for VAT design without the need for the development of higher order, and much more computationally expensive CFD methods like large eddy simulation (LES) models. However, it was shown that the averaging nature of the URANS can lead to dissipation of turbulence which would lead to an underestimation of far-field wake length. Proper characterisation of the far-field wake length is especially important for array analysis.

- Overprediction of turbine power performance is a common problem with 2D CFD models of VATTs and has been attributed to the higher blockage of a 2D model. The research has shown that 2D models can be corrected for blockage by extending the domain width to give a blockage value equivalent to the true 3D value. By doing so, one can achieve a reasonable level of accuracy, but if accuracy is paramount, it is recommended that 3D models are used.

- The accuracy of CFD sliding mesh models is sensitive to the choice of size of the rotating domain. For the VATs modelled here, the extent of sensitivity is dependent on the λ value. To avoid these effects, a domain diameter of 1.5 times the turbine rotor diameter is recommended. Model performance is much less sensitive to domain size at higher λ values (>1.5); therefore, smaller rotating domains can be used to reduce computation costs at these rotation speeds.

- In addition to the well-documented benefits of variable pitching, such as overcoming start-up torque issues and optimising blade angle of attack, the research has shown that implementing blade pitch control has had a positive effect on the performance of the 6-bladed VATT studied compared with that of a similarly fixed pitch turbine. Research results also showed that pitch control had the effect of reducing the operating λ value of the device while maintaining, or improving, the power performance; this is significant with regard to potential environmental impacts of the device as slower rotation speeds mean lower risks of fish or animal strikes.

8.4 Recommendations for Future Work

The work presented here provides a comprehensive investigation into the performance of vertical axis tidal turbines. During the course of this work, several opportunities for further study were identified. This section identifies a number of potential areas for further study.

- **3D CFD model to assess 3D flow and coupled with a solid mechanics model to assess fluid-structure interaction.**

The 2D blockage-corrected model of the GKinetic turbine was able to predict the performance of the device relatively accurately. However, a 2D model is unable to account for three-dimensional flow effects. A 3D CFD model would allow for further study of the device. One example is with regards to the shape, positioning and depth of the bluff body for which accurate modelling of the three-dimensional flow field is important. A 3D model is a natural progression of the current research as the developed CFD methodology and the UDF which controls the variable pitching of the blades can be readily applied to a 3D model. The model could subsequently be coupled with a solid mechanics model for fluid-structure interaction to structurally appraise the current blade design and propose new alternatives.

- **Investigation into far-field characterisation abilities of URANS models.**

Although shown to be highly accurate at modelling near-wake effects in this research, further investigation of the far-wake prediction capabilities of URANS models is recommended. It was shown in this research that the averaging nature of URANS models leads to the dissipation of turbulence and in turn leads to an underestimation of wake length. Further investigation is needed including acquisition of far-wake experimental data in order to properly characterise the far-field wake of turbines. Such an analysis would likely involve more computationally expensive CFD modelling methods such as DES. While current levels of computational resources may deem any such analysis prohibitive, it may be possible in the near future.

- **Development of a BEMT model to account for accelerated flow and variable pitching of the GKinetic device.**

Basic BEMT theory assumes non-rotating flows and all-encompassing stream-tubes and this is where an issue arises for the GKinetic turbine. The presence of the flow accelerating bluff body affects the angle at which the inlet flow reaches the turbine and so the flow is non-uniform. The author believes it may be possible to redefine all BEMT model equations to align the inlet plane for the BEMT model with the velocity distribution of the bluff body. The angle of attack equation would require redefinition to account for any variation in flow angle from the bluff body, as well as account for the variable pitch. CFD models of the bluff body (without turbine) at all required flow speeds would be required to investigate variation in flow angle. This could be efficiently conducted in 2D and would be relatively computationally inexpensive. This would ensure that the correct free-stream angles were incorporated into the model.

- **Improvement of the BEMT model for high solidity VATs.**

It is possible that the BEMT model for the presented high solidity case could potentially be further improved by incorporating a more complex dynamic stall model, such as a Leishmann-Beddoes, or similar. Additionally, a different aerofoil characteristic database to that of the one used in this research (Shedahl and Klimas), could further enhance accuracy. A comprehensive CFD study, possibly using LES or DES for a large range of aerofoils, angles of attack and Reynolds numbers, could be

carried out. Extensive model verification and validation would be paramount, to ensure confidence and reliability in the data.

- **Development of an accurate blockage correction methodology for VATs**

With the recent rise in research in vertical axis tidal turbines, there is a need for the development of a methodology for correcting scale experimental test results for blockage effects. It is anticipated that any corrective method would be based on estimating the unconfined thrust coefficient, which has been shown to be accurate for horizontal axis turbines and, subsequently correcting other parameters accordingly. Development of such a method that can accurately correct for blockage and accurately replicate unconfined flow physics would be no mean feat. An accurate methodology to correct for VATT blockage would be invaluable to the tidal industry. Again, comprehensive validation on any such method would be of vital importance to give accuracy assurance.

References

[1] Agreement, P., 2015, "United Nations Framework Convention on Climate Change," Paris, France.

[2] BP, 2017, *BP Statistical Review of World Energy 2017*.

[3] Kulovesi, K., Morgera, E., and Muñoz, M., 2011, "Environmental Integration and Multi-Faceted International Dimensions of EU Law: Unpacking the EU's 2009 Climate and Energy Package," Common Market Law Review, **48**(3), pp. 829–891.

[4] Myers, D. E., 1995, "GRAVITATIONAL EFFECTS OF THE PERIOD OF HIGH TIDES AND," **13**(4), pp. 529–532.

[5] O'Doherty, T., O'Doherty, D. M., and Mason-Jones, A., 2017, "Tidal Energy Technology," *Wave and Tidal Energy*, pp. 105–150.

[6] "TURBINE: FRANCIS TURBINE AND KAPLAN PROPELLER TURBINE" [Online]. Available: https://kids.britannica.com/students/assembly/view/53475. [Accessed: 14-Apr-2018].

[7] Ben Elghali, S. E., Benbouzid, M. E. H., and Charpentier, J.-F., 2010, "Modelling and Control of a Marine Current Turbine-Driven Doubly Fed Induction Generator," IET Renewable Power Generation, **4**(1), p. 1.

[8] Andritz Hydro Hammerfest, "ANDRITZ HYDRO Hammerfest" [Online]. Available: http://www.andritzhydrohammerfest.co.uk/references/. [Accessed: 01-Feb-2017].

[9] "EMEC: European Marine Energy Centre." [Online]. Available: http://www.emec.org.uk. [Accessed: 19-May-2016].

[10] Laws, N. D., and Epps, B. P., 2016, "Hydrokinetic Energy Conversion: Technology, Research, and Outlook," Renewable and Sustainable Energy Reviews, **57**, pp. 1245–1259.

[11] Zhou, Z., Benbouzid, M., Charpentier, J.-F., Scuiller, F., and Tang, T., 2017, "Developments in Large Marine Current Turbine Technologies – A Review," Renewable and Sustainable Energy Reviews, **71**(December 2016), pp. 852–858.

[12] Allsop, S., Peyrard, C., Thies, P. R., Boulougouris, E., and Harrison, G. P., 2017, "Hydrodynamic Analysis of a Ducted, Open Centre Tidal Stream Turbine Using Blade Element Momentum Theory," Ocean Engineering, **141**(June), pp. 531–542.

[13] ALLO, J. C., and DHOMÉ, D., 2017, "FROM REAL SCALE DEMONSTRATION TO TIDAL TURBINE PILOT POWER PLANT IN THE FROMVEUR STRAIT," Proceedings of the 12th European Wave and Tidal Energy Conference 27th Aug -1st Sept 2017, Cork, Ireland, pp. 1–5.

[14] Desplanque, C., and Mossman, D. J., 2004, "Tides and Their Seminal Impact on the Geology , Geography , History , and Socio-Economics of the Bay of Fundy , Eastern Canada," **130**, pp. 1–65.

[15] Brown, C. E., 2002, *World Energy Resources*, Springer.

[16] Rajgor, G., 2016, "Tidal Developments Power Forward," Renewable Energy Focus, **17**(4), pp. 147–149.

[17] SEAI, 2008, *Tidal & Current Energy Resources in Ireland*.

[18] Eirgrid and SONI, 2015, *Generation Capacity Statement 2015-2024*.

[19] "Science Foundation Ireland" [Online]. Available: http://www.sfi.ie/about-us/about-sfi/. [Accessed: 10-Jul-2017].

[20] Nash, S., Nagle, D., Phoenix, A., and Gannon, R., 2013, *Experimental Analysis for the Design of a Prototype Flow Acceleration Device*.

[21] Fraenkel, P. L., 2002, "Power from Marine Currents," Proceedings of the Institution of Mechanical Engineers, Part A: Journal of Power and Energy, **216**(1), pp. 1–14.

[22] Greenblatt, D., Ben-Harav, A., and Mueller-Vahl, H., 2014, "Dynamic Stall Control on a Vertical-Axis Wind Turbine Using Plasma Actuators," AIAA Journal, **52**(2), pp. 456–462.

[23] Singh, M. A., Biswas, A., and Misra, R. D., 2015, "Investigation of Self-Starting and High Rotor Solidity on the Performance of a Three S1210 Blade H-Type Darrieus Rotor," Renewable Energy, **76**, pp. 381–387.

[24] Dabiri, J. O., 2011, "Potential Order-of-Magnitude Enhancement of Wind Farm Power Density via Counter-Rotating Vertical-Axis Wind Turbine Arrays," Journal of Renewable and Sustainable Energy, **3**(4).

[25] Soraghan, C. E., Leithead, W. E., Feuchtwang, J., and Yue, H., 2013, "Double Multiple Streamtube Model for Variable Pitch Vertical Axis Wind Turbines," 31st AIAA Applied Aerodynamics Conference, pp. 1–12.

[26] Tahani, M., Babayan, N., Mehrnia, S., and Shadmehri, M., 2016, "A Novel Heuristic Method for Optimization of Straight Blade Vertical Axis Wind Turbine," Energy Conversion and Management, **127**, pp. 461–476.

[27] White, F., 2010, "Fluid Mechanics," McGraw-Hill,New York, p. 862.

[28] Leishman, J. G., 2002, "Challenges in Modelling the Unsteady Aerodynamics of Wind Turbines," Wind Energy, **5**(2–3), pp. 85–132.

[29] Anderson, J. D., 1989, *Introduction to Flight*, New York: McGraw-Hill.

[30] Leishman, J. G., 2006, *Principles of Helicopter Aerrodynamics*, Cambridge University Press.

[31] Ahmadi-Baloutaki, M., Carriveau, R., and Ting, D. S. K., 2016, "A Wind Tunnel Study on the Aerodynamic Interaction of Vertical Axis Wind Turbines

in Array Configurations," Renewable Energy, **96**, pp. 904–913.

[32] Ahmedov, A., and Ebrahimi, K. M., 2017, "Numerical Modelling of an H-Type Darrieus Wind Turbine Performance under Turbulent Wind," American Journal of Energy Research, **5**(3), pp. 63–78.

[33] Ahmed, U., Apsley, D. D., Afgan, I., Stallard, T., and Stansby, P. K., 2017, "Fluctuating Loads on a Tidal Turbine Due to Velocity Shear and Turbulence: Comparison of CFD with Field Data," Renewable Energy, **112**, pp. 235–246.

[34] Sheldahl, R. E., and Klimas, P. C., 1981, "Aerodynamic Characteristics of Seven Symmetrical Airfoil Sections through 180-Degree Angle of Attack for Use in Aerodynamic Analysis of Vertical Axis Wind Turbines. Technical Report SAND80-2114, Sandia National Laboratories," Technical SAND80-2114, Sandia National Laboratories.

[35] Mccroskey, W. J., 1982, "Unsteady Airfoils," Annual Review of Fluid Mechanics, pp. 285–311.

[36] McCroskey, W. J., 1981, "The Phenomenon of Dynamic Stall," NASA Technical Memorandum 81264, pp. 1–28.

[37] Tsang, K. K. Y., So, R. M. C., Leung, R. C. K., and Wang, X. Q., 2008, "Dynamic Stall Behavior from Unsteady Force Measurements," Journal of Fluids and Structures, **24**(1), pp. 129–150.

[38] Larsen, J. W., Nielsen, S. R. K., and Krenk, S., 2007, "Dynamic Stall Model for Wind Turbine Airfoils," Journal of Fluids and Structures, **23**(7), pp. 959–982.

[39] Gormont, R. E., 1973, *A Mathematical Model of Unsteady Aerodynamics and Radial Flow for Application to Helicopter Rotors*.

[40] Leishman, J. G., and Beddoes, T. S., 1989, "A Semi-Empirical Model for Dynamic Stall," Journal of the American Helicopter Society, **34**(3), pp. 3–17.

[41] Øye, S., 1991, *Dynamic Stall Simulated as Time Lag of Separation*.

[42] Hansen, M. H., Gaunaa, M., and Madsen, H. a, 2004, "A Beddoes-Leishman Type Dynamic Stall Model in State-Space and Indicial Formulations," Riso National Laboratory, (Ris{ø}-R-1354(EN)), pp. 7–35.

[43] Dyachuk, E., and Goude, A., 2015, "Simulating Dynamic Stall Effects for Vertical Axis Wind Turbines Applying a Double Multiple Streamtube Model," Energies, **8**(2), pp. 1353–1372.

[44] McIntosh, S. C., Babinsky, H., and Bertenyi, T., 2009, "Convergence Failure and Stall Hysteresis in Actuator-Disk Momentum Models Applied to Vertical Axis Wind Turbines," Journal of Solar Energy Engineering, **131**(3), p. 034502.

[45] Eppler, R., and Somers, D. M., 1980, *A Computer Program for the Design and Analysis of Low-Speed Airfoils*.

[46] Antheaume, S., Maître, T., and Achard, J. L., 2008, "Hydraulic Darrieus

Turbines Efficiency for Free Fluid Flow Conditions versus Power Farms Conditions," Renewable Energy, **33**(10), pp. 2186–2198.

[47] Klimas, P. C., French, R. E., Laboratories., S. N., States., U., and Energy., D. of, 1980, *A User's Manual for the Vertical Axis Wind Turbine Performance Computer Code DARTER*, Sandia National Laboratories, Albuquerque, N.M.

[48] Wosnik, M., Bachant, P., Neary, V. S., and Murphy, A. W., 2016, "Evaluation of Design & Analysis Code , CACTUS , for Predicting Cross-Flow Hydrokinetic Turbine Performance," (September).

[49] Sanyer, W. E., 2011, "The Development of a Wind Turbine for Residential Use," A thesis submitted to the Graduate Faculty of North Carolina State University.

[50] Ashwill, T. D., 1992, *Measured Data for the Sandia 34-Meter Vertical Axis Wind Turbine*.

[51] Worstell, M. H., 1978, *Aerodynamic Performance of the 17 Meter Diameter Darrieus Wind Turbine*.

[52] Sheldahl, R. E., Klimas, P., and Feltz, L., 1980, "Aerodynamic Performance of a 5-Metre- Diameter Darrieus Turbine With Extruded Aluminum NACA-0015 Blades," Sandia Laboratories.

[53] Blackwell, B. F., Sheldahl, R. E., and Feltz, L. V, 1976, *Wind Tunnel Performance Data for the Darrieus Wind Turbine with NACA 0012 Blades*.

[54] Bahaj, A. S., Blunden, L., and Anwar, and A. A., *University of Southampton. OES IA Annex II Task 2.2 Tidal Energy Development Protocol, Report from BERR for the OES-IA.*

[55] McCombes, T., Johnstone, C. M., Holmes, B., Myers, L. E., Bahaj, A. S., and Kofoed, J. P., 2010, "Best Practice for Tank Testing of Small Marine Energy Devices," EquiMar Project, pp. 1–48.

[56] IEC, 2013, *PD IEC / TS 62600-200 : 2013 BSI Standards Publication Marine Energy — Wave , Tidal and Other Water Current Converters Energy Converters — Power Performance*.

[57] Gaurier, B., Germain, G., Facq, J. V., Johnstone, C. M., Grant, A. D., Day, A. H., Nixon, E., Di Felice, F., and Costanzo, M., 2015, "Tidal Energy 'Round Robin' Tests Comparisons between Towing Tank and Circulating Tank Results," International Journal of Marine Energy, **12**, pp. 87–109.

[58] Mycek, P., Gaurier, B., Germain, G., Pinon, G., and Rivoalen, E., 2014, "Experimental Study of the Turbulence Intensity Effects on Marine Current Turbines Behaviour. Part II: Two Interacting Turbines," Renewable Energy, **68**, pp. 876–892.

[59] Rolland, S. A., Thatcher, M., Newton, W., Williams, A. J., Croft, T. N., Gethin, D. T., and Cross, M., 2013, "Benchmark Experiments for Simulations of a Vertical Axis Wind Turbine," Applied Energy, **111**, pp. 1183–1194.

[60] Fraenkel, P., 2010, “Practical Tidal Turbine Design Considerations : A Review of Technical Alternatives and Key Design Decisions Leading to the Development of the SeaGen 1 . 2MW Tidal Turbine,” Ocean Power Fluid Machinery Seminar, 19 October 2010, London, pp. 1–19.

[61] Ladokun, L. L., Ajao, K. R., and Sule, B. F., 2013, “Hydrokinetic Energy Conversion Systems : Prospects and Challenges in Nigerian Hydrological Setting,” Nigerian Journal of Technology, **32**(3), pp. 538–549.

[62] Shiono, M., Suzuki, K., and Kiho, S., 2000, “An Experimental Study of the Characteristics of a Darrieus Turbine for Tidal Power Generation,” Electrical Engineering in Japan, **132**(3), pp. 38–47.

[63] Coiro, D. P., Marco, a De, Nicolosi, F., Melone, S., and Montella, F., 2005, “Dynamic Behaviour of the Patented Kobold Tidal Current Turbine : Numerical and Experimental Aspects,” Acta Polytechnica, **45**(3), pp. 77–84.

[64] Birjandi, A. H., Bibeau, E. L., Chatoorgoon, V., and Kumar, A., 2013, “Power Measurement of Hydrokinetic Turbines with Free-Surface and Blockage Effect,” Ocean Engineering, **69**, pp. 9–17.

[65] Bachant, P., and Wosnik, M., 2016, “Effects of Reynolds Number on the Energy Conversion and Near-Wake Dynamics of a High Solidity Vertical-Axis Cross-Flow Turbine,” *Energies*.

[66] Lissaman, P. B. ., 1983, “Low Reynolds Number Airfoils,” Fluid Mechanics, pp. 3–6.

[67] Bachant, P., Wosnik, M., Gunawan, B., and Neary, V. S., 2016, “Experimental Study of a Reference Model Vertical-Axis Cross-Flow Turbine,” PLoS ONE, **11**(9), pp. 1–20.

[68] Bachant, P., and Wosnik, M., 2015, “Performance Measurements of Cylindrical- and Spherical-Helical Cross-Flow Marine Hydrokinetic Turbines, with Estimates of Exergy Efficiency,” Renewable Energy, **74**, pp. 318–325.

[69] Kirke, B. K., and Lazauskas, L., 1991, “Enhancing the Performance of Vertical Axis Wind Turbine Using a Simple Variable Pitch System,” Wind Engineering, **15**(4), pp. 187–195.

[70] Jain, P., and Abhishek, A., 2016, “Performance Prediction and Fundamental Understanding of Small Scale Vertical Axis Wind Turbine with Variable Amplitude Blade Pitching,” Renewable Energy, **97**, pp. 97–113.

[71] Gazzano, R., Marini, M., and Satta, A., 2010, “Performance Calculation for a Vertical Axis Wind Turbine with Variable Blade Pitch,” International Journal of Heat and Technology, **28**(2), pp. 147–153.

[72] Ponta, F. L., Seminara, J. J., and Otero, a. D., 2007, “On the Aerodynamics of Variable-Geometry Oval-Trajectory Darrieus Wind Turbines,” Renewable Energy, **32**(1), pp. 35–56.

[73] Kirke, B., 2016, “Tests on Two Small Variable Pitch Cross Flow Hydrokinetic Turbines,” Energy for Sustainable Development, **31**, pp. 185–193.

[74] Xue-wei, Z., Shu-qi, W., Feng, W., Liang, Z., and Qi-hu, S., 2012, "THE HYDRODYNAMIC CHARACTERISTICS OF FREE VARIABLE- PITCH VERTICAL AXIS TIDAL TURBINE *," Journal of Hydrodynamics, **24**(6), pp. 834–839.

[75] Pawsey, N. C. K., 2002, "Development and Evaluation of Passive Variable-Pitch Vertical Axis Wind Turbines," School of Mechanical and Manufacturing Engineering, **PhD**(November).

[76] Jing, F., Sheng, Q., and Zhang, L., 2014, "Experimental Research on Tidal Current Vertical Axis Turbine with Variable-Pitch Blades," Ocean Engineering, **88**, pp. 228–241.

[77] Somoano, M., and Huera-Huarte, F. J., 2018, "The Dead Band in the Performance of Cross-Flow Turbines: Effects of Reynolds Number and Blade Pitch," Energy Conversion and Management, **172**(June), pp. 277–284.

[78] Zhang, X. W., Wang, S. Q., Wang, F., Zhang, L., and Sheng, Q. H., 2012, "The Hydrodynamic Characteristics of Free Variable-Pitch Vertical Axis Tidal Turbine," Journal of Hydrodynamics, **24**(6), pp. 834–839.

[79] Aggarwal, A., Mishra, D., Chandramouli, V., and Rani, S., 2016, "Optimization of Vertical Axis Wind Turbine on Individual Blade Pitch Control," Journal of Chemical and Pharmaceutical Sciences, **9**(4), pp. 2644–2646.

[80] Graf, W. H., and Yulistiyanto, B., 1998, "Experiments on Flow around a Cylinder; the Velocity and Vorticity Fields," Journal of Hydraulic Research, **36**(4), pp. 637–653.

[81] Roddier, D., Cermelli, C., and Aubault, A., 2007, "Electrical Power Generation by Tidal Flow Acceleration," *26th International Conference on Offshore Mechanics and Arctic Engineering OMAE2007, June 10-15, 2007, San Diego, California, USA*, pp. 1–6.

[82] Gerrard, J. H., 1966, "The Mechanics of the Formation Region of Vortices behind Bluff Bodies," Journal of Fluid Mechanics, **25**(02), p. 401.

[83] Golecha, K., Eldho, T. I., and Prabhu, S. V., 2011, "Influence of the Deflector Plate on the Performance of Modified Savonius Water Turbine," Applied Energy, **88**(9), pp. 3207–3217.

[84] Shaughnessy, B. M., and Probert, S. D., 1992, "Partially-Blocked Savonius Rotor," Applied Energy, **43**(4), pp. 239–249.

[85] Kim, D., and Gharib, M., 2013, "Efficiency Improvement of Straight-Bladed Vertical-Axis Wind Turbines with an Upstream Deflector," Journal of Wind Engineering and Industrial Aerodynamics, **115**, pp. 48–52.

[86] McAdam, R. A., Houlsby, G. T., Oldfield, M. L. G., and McCulloch, M. D., 2010, "Experimental Testing of the Transverse Horizontal Axis Water Turbine," IET Renewable Power Generation, **4**(6), p. 510.

[87] Ohya, Y., and Karasudani, T., 2010, "A Shrouded Wind Turbine Generating High Output Power with Wind-Lens Technology," Energies, **3**(4), pp. 634–649.

[88] Jin, X., Wang, Y., Ju, W., He, J., and Xie, S., 2018, "Investigation into Parameter Influence of Upstream Deflector on Vertical Axis Wind Turbines Output Power via Three-Dimensional CFD Simulation," Renewable Energy, **115**, pp. 41–53.

[89] Harries, T., Kwan, A., Brammer, J., and Falconer, R., 2016, "Physical Testing of Performance Characteristics of a Novel Drag-Driven Vertical Axis Tidal Stream Turbine; With Comparisons to a Conventional Savonius," International Journal of Marine Energy, **14**, pp. 215–228.

[90] Werle, M. J., 2010, "Wind Turbine Wall-Blockage Performance Corrections," Journal of Propulsion and Power, **26**(6), pp. 1317–1321.

[91] A., P., and JJ., H., 1966, *Low-Speed Wind Tunnel Testing.*, New York, NY, John Wiley & Sons.

[92] Bahaj, a. S. S., Molland, a. F. F., Chaplin, J. R. R., and Batten, W. M. J. M. J., 2007, "Power and Thrust Measurements of Marine Current Turbines under Various Hydrodynamic Flow Conditions in a Cavitation Tunnel and a Towing Tank," Renewable Energy, **32**(3), pp. 407–426.

[93] Cavagnaro, R.; Polagye, B., "An Evaluation of Blockage Corrections for a Helical Cross-Flow Turbine," *Proceedings of the 3rd Oxford Tidal Energy Workshop, Oxford, UK, 7–8 April 2014.*

[94] Dossena, V., Persico, G., Paradiso, B., Battisti, L., Dell'Anna, S., Brighenti, A., and Benini, E., 2015, "An Experimental Study of the Aerodynamics and Performance of a Vertical Axis Wind Turbine in a Confined and Unconfined Environment," Journal of Energy Resources Technology, **137**(5), p. 051207.

[95] Ponta, F. L., and Jacovkis, P. M., 2001, "A Vortex Model for Darrieus Turbine Using Finite Element Techniques," Renewable Energy, **24**(1), pp. 1–18.

[96] Strickland, J. H., Webster, B. T., and Nguyen, T., 1979, "A Vortex Model of the Darrieus Turbine: An Analytical and Experimental Study," Journal of Fluids Engineering, **101**(4), p. 500.

[97] Li, Y., and Calisal, S. M., 2010, "Three-Dimensional Effects and Arm Effects on Modeling a Vertical Axis Tidal Current Turbine," Renewable Energy, **35**(10), pp. 2325–2334.

[98] Templin, R. J., 1974, "Aerodynamic Performance Theory for the NRC Vertical-Axis Wind Turbine," NASA STI/Recon Technical Report N 76:16618, **76**, p. 16618.

[99] Li, Y., and Çalışal, S. M., 2010, "A Discrete Vortex Method for Simulating a Stand-Alone Tidal-Current Turbine: Modeling and Validation," Journal of Offshore Mechanics and Arctic Engineering, **132**(3), p. 031102.

[100] H. Glauert, 1926, "The Elements of Airfoil and Airscrew Theory," p. 243.

[101] Strickland, J., 1975, "The Darrieus Turbine, A Performance Prediction Method Using Multiple Stream Tubes," Sandia Laboratories, SAND, (SAND75-0431).

[102] Paraschivoiu, I., 1988, "Double-Multiple Streamtube Model for Studying VAWT's," Journal of Propulsion and Power, **4**(4), pp. 370–378.

[103] Read, S., and Sharpe, D. J., 1980, "An Extended Multiple Streamtube Theory for Vertical Axis Wind Turbines," *Wind Energy Workshop*, Cranfield, pp. 65–72.

[104] Paraschivoiu, I., 1982, "Aerodynamic Loads and Performance of the Darrieus Rotor," Journal of Energy, **6**(6), pp. 406–412.

[105] Klimas, P. C., and Sheldahl, R. E., 1978, "Four Aerodynamic Prediction Schemes for Vertical-Axis: A Compendium SAND78-0014. 1978."

[106] Paraschivoiu, I., Delclaux, F., Fraunié, P., and Béguier, C., 1983, "Aerodynamic Analysis of the Darrieus Wind Turbines Including Secondary Effects," Journal of Energy, **7**(5), pp. 416–422.

[107] Gupta, S., and Leishman, J. G., 2005, "Comparison of Momentum and Vortex Methods for the Aerodynamic Analysis of Wind Turbines," 43rd AIAA Aerospace Sciences Meeting and Exhibit, **AIAA 2005**-(January), pp. 1–24.

[108] Freris, L. L., 1990, *Wind Energy Conversion Systems*, Prentice Hall, New York.

[109] Paraschivoiu, I., Fraunie, P., and Beguier, C., 1985, "Streamtube Expansion Effects on the Darrieus Wind Turbine," Journal of Propulsion and Power, **1**(2), pp. 150–155.

[110] Paraschivoiu, I., 2002, *Wind Turbine Design with Emphasis on Darrieus Concept*, Polytechnic international Press.

[111] Massé, B., 1981, "Description de Deux Programmes d'ordinateur Pour Le Calcul Des Performance et Des Charges Aérodynamiques Pour Les Éoliennes à Axe Vertical," Institut de Recherche de l'Hydro, **IREQ-2379**.

[112] Berg, D. E., 1983, "Improved Double-Multiple Streamtube Model for the Darrieus-Type Vertical-Axis Wind Turbine," United States.

[113] Beddoes, T. S., 1983, "Representation of Airfoil Behaviour," Vertica, **7**(2), pp. 183–197.

[114] Abbott, I. H., and Von Doenhoff, A. E., 1959, *Theory of Wing Sections: Including a Summary of Airfoil Data*.

[115] Viterna, L., and D. Corrigan, R., 1981, "Fixed Pitch Rotor Performance of Large Horizontal Axis Wind Turbines," *DOE/NASA Workshop on Large Horizontal Axis Wind Turbines*, Cleveland, OH.

[116] Castelli, M. R., Fedrigo, A., and Benini, E., 2012, "Effect of Dynamic Stall, Finite Aspect Ratio and Streamtube Expansion on VAWT Performance Prediction Using the BE-M Model," World Academy of Science, Engineering and Technology, **68**(8), pp. 426–438.

[117] Soraghan, C. E., 2014, "Aerodynamic Modelling and Control of Vertical Axis Wind Turbines."

[118] Shamsoddin, S., and Porté-Agel, F., 2014, "Large Eddy Simulation of Vertical Axis Wind Turbine Wakes," Energies, **7**(2), pp. 890–912.

[119] Lei, H., Zhou, D., Bao, Y., Li, Y., and Han, Z., 2017, "Three-Dimensional Improved Delayed Detached Eddy Simulation of a Two-Bladed Vertical Axis Wind Turbine," Energy Conversion and Management, **133**, pp. 235–248.

[120] Stergiannis, N., Lacor, C., Beeck, J. V, and Donnelly, R., 2016, "CFD Modelling Approaches against Single Wind Turbine Wake Measurements Using RANS," Journal of Physics: Conference Series, **753**, p. 032062.

[121] Zanette, J., Imbault, D., and Tourabi, a., 2010, "A Design Methodology for Cross Flow Water Turbines," Renewable Energy, **35**(5), pp. 997–1009.

[122] Ghosh, A., Biswas, A., Sharma, K. K., and Gupta, R., 2015, "Computational Analysis of Flow Physics of a Combined Three Bladed Darrieus Savonius Wind Rotor," Journal of the Energy Institute, **88**(4), pp. 425–437.

[123] Gupta, R., and Biswas, A., 2010, "Computational Fluid Dynamics Analysis of a Twisted Three-Bladed H-Darrieus Rotor," Journal of Renewable and Sustainable Energy, **2**(4).

[124] Mohamed, M. H., 2013, "Impacts of Solidity and Hybrid System in Small Wind Turbines Performance," Energy, **57**, pp. 495–504.

[125] Lanzafame, R., Mauro, S., and Messina, M., 2014, "2D CFD Modeling of H-Darrieus Wind Turbines Using a Transition Turbulence Model," Energy Procedia, **45**, pp. 131–140.

[126] Balduzzi, F., Bianchini, A., Ferrara, G., and Ferrari, L., 2016, "Dimensionless Numbers for the Assessment of Mesh and Timestep Requirements in CFD Simulations of Darrieus Wind Turbines," Energy, **97**, pp. 246–261.

[127] Almohammadi, K. M., Ingham, D. B., Ma, L., and Pourkashanian, M., 2012, "CFD Sensitivity Analysis of a Straight-Blade Vertical Axis Wind Turbine," Wind Engineering, **36**(5), pp. 571–588.

[128] Biadgo, a M., Simonović, a, Komarov, D., and Stupar, S., 2013, "Numerical and Analytical Investigation of Vertical Axis Wind Turbine," FME Transactions, **41**(1), pp. 49–58.

[129] Howell, R., Qin, N., Edwards, J., and Durrani, N., 2010, "Wind Tunnel and Numerical Study of a Small Vertical Axis Wind Turbine," Renewable Energy, **35**(2), pp. 412–422.

[130] Lain, S., and Osorio, C., 2010, "Simulation and Evaluation of a Straight-Bladed Darrieus-Type Cross Flow Marine Turbine," Journal of Scientific and Industrial Research, **69**(12), pp. 906–912.

[131] Korobenko, a., Hsu, M.-C., Akkerman, I., and Bazilevs, Y., 2013, "Aerodynamic Simulation of Vertical-Axis Wind Turbines," Journal of Applied Mechanics, **81**(February), p. 021011.

[132] Lee, N. J., Kim, I. C., Kim, C. G., Hyun, B. S., and Lee, Y. H., 2015,

"Performance Study on a Counter-Rotating Tidal Current Turbine by CFD and Model Experimentation," Renewable Energy, **79**(1), pp. 122–126.

[133] Spalart, P. R., Allmaras, S. R., and Reno, J., 1992, "A One-Equatlon Turbulence Model for Aerodynamic Flows Boeing Commercial Airplane Group 30th Aerospace Sciences," AIAA paper 1992-0439.

[134] Launder, B. E., and Spalding, D. B., 1974, "The Numerical Computation of Turbulent Flows," Computer Methods in Applied Mechanics and Engineering, **3**(2), pp. 269–289.

[135] Wilcox, D. C., 1988, "Reassessment of the Scale-Determining Equation for Advanced Turbulence Models," AIAA Journal, **26**(11), pp. 1299–1310.

[136] Menter, F. R., 1994, "2-Equation Eddy-Visocity Turbulence Models for Engineering Applications," Aiaa Journal, **32**(8), pp. 1598–1605.

[137] Menter, F. R., Langtry, R. B., Likki, S. R., Suzen, Y. B., Huang, P. G., and Volker, S., 2006, "A Correlation-Based Transition Model Using Local Variables - Part I: Model Formulation," Journal of Turbomachinery, **128**(3), p. 413.

[138] ANSYS Fluent 17.1 theory guide, 2016, *ANSYS Fluent 17.1 Theory Guide*.

[139] Bachant, P., and Wosnik, M., 2016, "Modeling the Near-Wake of a Vertical-Axis Cross-Flow Turbine with 2-D and 3-D RANS," Journal of Renewable and Sustainable Energy, **8**(5).

[140] Raciti Castelli, M., Englaro, A., and Benini, E., 2011, "The Darrieus Wind Turbine: Proposal for a New Performance Prediction Model Based on CFD," Energy, **36**(8), pp. 4919–4934.

[141] Trivellato, F., and Raciti Castelli, M., 2014, "On the Courant-Friedrichs-Lewy Criterion of Rotating Grids in 2D Vertical-Axis Wind Turbine Analysis," Renewable Energy, **62**, pp. 53–62.

[142] Balduzzi, F., Bianchini, A., Maleci, R., Ferrara, G., and Ferrari, L., 2016, "Critical Issues in the CFD Simulation of Darrieus Wind Turbines," Renewable Energy, **85**, pp. 419–435.

[143] Maître, T., Amet, E., and Pellone, C., 2013, "Modeling of the Flow in a Darrieus Water Turbine: Wall Grid Refinement Analysis and Comparison with Experiments," Renewable Energy, **51**, pp. 497–512.

[144] Ferreira, C. J. S., Bijl, H., Bussel, G. Van, and Kuik, G. Van, 2007, "Simulating Dynamic Stall in a 2D VAWT: Modeling Strategy, Verification and Validation with Particle Image Velocimetry Data," Journal of Physics: Conference Series, **75**, p. 012023.

[145] Almohammadi, K. M., Ingham, D. B., Ma, L., and Pourkashanian, M., 2015, "Modeling Dynamic Stall of a Straight Blade Vertical Axis Wind Turbine," Journal of Fluids and Structures, **57**.

[146] Wang, S., Ingham, D. B., Ma, L., Pourkashanian, M., and Tao, Z., 2010,

"Numerical Investigations on Dynamic Stall of Low Reynolds Number Flow around Oscillating Airfoils," Computers and Fluids, **39**(9), pp. 1529–1541.

[147] Mohamed, M. H., 2012, "Performance Investigation of H-Rotor Darrieus Turbine with New Airfoil Shapes," Energy, **47**(1), pp. 522–530.

[148] Rolland, S. a. A., Thatcher, M., Ellis, R., Gaurier, B., Croft, T. N. N., and Cross, M., 2015, "Performance Assessment of a Vertical Axis Turbine in a Marine Current Flume Tank and CFD Modelling," International Journal of Marine Energy, **12**, pp. 35–45.

[149] Velasco, D., López Mejia, O., and Laín, S., 2017, "Numerical Simulations of Active Flow Control with Synthetic Jets in a Darrieus Turbine," Renewable Energy, **113**, pp. 129–140.

[150] Almohammadi, K. M., Ingham, D. B., Ma, L., and Pourkashan, M., 2013, "Computational Fluid Dynamics (CFD) Mesh Independency Techniques for a Straight Blade Vertical Axis Wind Turbine," Energy, **58**, pp. 483–493.

[151] Rossetti, A., and Pavesi, G., 2013, "Comparison of Different Numerical Approaches to the Study of the H-Darrieus Turbines Start-Up," Renewable Energy, **50**, pp. 7–19.

[152] Simão Ferreira, C. J., van Zuijlen, A., Bijl, H., van Bussel, G., and van Kuik, G., 2010, "Simulating Dynamic Stall in a Two-Dimensional Vertical-Axis Wind Turbine: Verification and Validation with Particle Image Velocimetry Data," Wind Energy, **13**(1), pp. 1–17.

[153] Chatterjee, P., and Laoulache, R. N., 2013, "Performance Modeling of Ducted Vertical Axis Turbine Using Computational Fluid Dynamics," Marine Technology Society Journal, **47**(4), pp. 36–44.

[154] Lam, H. F., and Peng, H. Y., 2016, "Study of Wake Characteristics of a Vertical Axis Wind Turbine by Two- and Three-Dimensional Computational Fluid Dynamics Simulations," Renewable Energy, **90**, pp. 386–398.

[155] Ghasemian, M., and Nejat, A., 2015, "Aero-Acoustics Prediction of a Vertical Axis Wind Turbine Using Large Eddy Simulation and Acoustic Analogy," Energy, **88**, pp. 711–717.

[156] Orlandi, A., Collu, M., Zanforlin, S., and Shires, A., 2015, "3D URANS Analysis of a Vertical Axis Wind Turbine in Skewed Flows," Journal of Wind Engineering and Industrial Aerodynamics, **147**, pp. 77–84.

[157] Zamani, M., Maghrebi, M. J., and Varedi, S. R., 2016, "Starting Torque Improvement Using J-Shaped Straight-Bladed Darrieus Vertical Axis Wind Turbine by Means of Numerical Simulation," Renewable Energy, **95**, pp. 109–126.

[158] Marsh, P., Ranmuthugala, D., Penesis, I., and Thomas, G., 2015, "Three-Dimensional Numerical Simulations of Straight-Bladed Vertical Axis Tidal Turbines Investigating Power Output, Torque Ripple and Mounting Forces," Renewable Energy, **83**, pp. 67–77.

[159] Zamani, M., Nazari, S., Moshizi, S. A., and Maghrebi, M. J., 2016, "Three Dimensional Simulation of J-Shaped Darrieus Vertical Axis Wind Turbine," Energy, **116**, pp. 1243–1255.

[160] Li, C., Zhu, S., Xu, Y.-L., and Xiao, Y., 2013, "2.5D Large Eddy Simulation of Vertical Axis Wind Turbine in Consideration of High Angle of Attack Flow," Renewable Energy, **51**, pp. 317–330.

[161] Lam, H. F. F., and Peng, H. Y. Y., 2016, "Study of Wake Characteristics of a Vertical Axis Wind Turbine by Two- and Three-Dimensional Computational Fluid Dynamics Simulations," Renewable Energy, **90**, pp. 386–398.

[162] Alaimo, A., Esposito, A., Messineo, A., Orlando, C., and Tumino, D., 2015, "3D CFD Analysis of a Vertical Axis Wind Turbine," Energies, **8**(4), pp. 3013–3033.

[163] Delafin, P. L., Nishino, T., Kolios, A., and Wang, L., 2017, "Comparison of Low-Order Aerodynamic Models and RANS CFD for Full Scale 3D Vertical Axis Wind Turbines," Renewable Energy, **109**, pp. 564–575.

[164] Boudreau, M., and Dumas, G., 2015, "Wake Analysis of Various Hydrokinetic Turbine Technologies through Numerical Simulations," 62nd CASI Aeronautics Conference and AGM 3rd GARDN Conference, pp. 1–16.

[165] Chowdhury, A. M., Akimoto, H., and Hara, Y., 2016, "Comparative CFD Analysis of Vertical Axis Wind Turbine in Upright and Tilted Configuration," Renewable Energy, **85**, pp. 327–337.

[166] Le, T. Q., Lee, K. S., Park, J. S., and Ko, J. H., 2014, "Flow-Driven Rotor Simulation of Vertical Axis Tidal Turbines: A Comparison of Helical and Straight Blades," International Journal of Naval Architecture and Ocean Engineering, **6**(2), pp. 257–268.

[167] Bhargav, M. M. S. R. S., Ratna Kishore, V., and Laxman, V., 2016, "Influence of Fluctuating Wind Conditions on Vertical Axis Wind Turbine Using a Three Dimensional CFD Model," Journal of Wind Engineering and Industrial Aerodynamics, **158**(October), pp. 98–108.

[168] Subramanian, A., Yogesh, S. A., Sivanandan, H., Giri, A., Vasudevan, M., Mugundhan, V., and Velamati, R. K., 2017, "Effect of Airfoil and Solidity on Performance of Small Scale Vertical Axis Wind Turbine Using Three Dimensional CFD Model," Energy, **133**, pp. 179–190.

[169] Wilcox, D. C., 2006, *Turbulence Modeling for CFD (Third Edition)*.

[170] Menter, F. R., Kuntz, M., and Langtry, R., 2003, "Ten Years of Industrial Experience with the SST Turbulence Model," Turbulence Heat and Mass Transfer 4, **4**, pp. 625–632.

[171] Langtry, R. B., and Menter, F. R., 2009, "Correlation-Based Transition Modeling for Unstructured Parallelized Computational Fluid Dynamics Codes," AIAA Journal, **47**(12), pp. 2894–2906.

[172] Schlichting, D. H., and Gersten, K., 1979, *Boundary-Layer Theory*.

[173] AIAA_G-077, 1998, “Guide for the Verification and Validation of Computational Fluid Dynamics Simulations (AIAA G-077-1998(2002)),” **1998**.

[174] Versteeg, H. K., and Malalasekera, W., 1995, “An Introduction to Computational Fluid Dynamics - The Finite Volume Method,” Fluid flow handbook. McGraw-Hill …, p. 267.

[175] IFREMER, “IFREMER” [Online]. Available: https://wwz.ifremer.fr. [Accessed: 10-Nov-2014].

[176] Sumer, B. M., and Fredsoe, J., 2006, *Hydrodynamics Around Cylindrical Structures*, World Scientific Pub.

[177] Nortek, 2015, “NORTEK Comprehensive Manual - Principles of Operation,” p. 142.

[178] New Energy Corporation, 2015, “EnCurrent Hydro Turbines 5 and 10 KW Specifications,” pp. 1–2 [Online]. Available: http://www.newenergycorp.ca/Portals/0/documents/datasheets/ENC.005.010.DataSheet.pdf.

[179] Betz, A., 1926, *Wind-Energie und ihre Ausnutzung durch Windmühlen.*, Vandenhoeck & Ruprecht, Göttingen.

[180] Ferreira, C. S., 2009, “The near Wake of the VAWT 2D and 3D Views of the VAWT Aerodynamics,” Delft University of Technology.

[181] Burton, T., Jenkins, N., Sharpe, D., and Bossanyi, E., 2001, *Wind Energy Handbook*.

[182] Lewis, M., Neill, S. P., Robins, P., Hashemi, M. R., and Ward, S., 2017, “Characteristics of the Velocity Profile at Tidal-Stream Energy Sites,” Renewable Energy, **114**, pp. 258–272.

[183] McIntosh, S. C., 2009, “Wind Energy for the Built Environment,” PQDT - UK Ireland, (May).

[184] Masson, C., Leclerc, C., and Paraschivoiu, I., 1998, “Appropriate Dynamic-Stall Models for Performance,” International Journal of Rotating Machinery, **4**(2), pp. 129–139.

[185] Mays, I., Morgan, M., Anderson, M., and Powles, S., 1990, “Experience with the VAWT 850 Demonstration Project,” *European Community Wind Energy Conference 1990*, Madrid, Spain, pp. 482–487.

[186] McLaren, K., 2011, “A Numerical and Experimental Study of Unsteady Loading of High Solidity Vertical Axis Wind Turbines,” pp. 206–215.

[187] Rezaeiha, A., Kalkman, I., and Blocken, B., 2017, “Effect of Pitch Angle on Power Performance and Aerodynamics of a Vertical Axis Wind Turbine,” Applied Energy, **197**, pp. 132–150.

[188] Marsh, P., Ranmuthugala, D., Penesis, I., and Thomas, G., 2012, “Three

Dimensional Numerical Simulations of a Straight-Bladed Vertical Axis Tidal Turbine," 18th Australasian Fluid Mechanics Conference, **USB**(December), pp. 1–4.

[189] Li, Y., Yi, J.-H., Song, H., Wang, Q., Yang, Z., Kelley, N. D., and Lee, K.-S., 2014, "On the Natural Frequency of Tidal Current Power Systems—A Discussion of Sea Testing," Applied Physics Letters, **105**(2), p. 23902.

[190] Mannion, B., McCormack, V., Kennedy, C., Leen, S. B., and Nash, S., 2018, "An Experimental Study of a Flow-Accelerating Hydrokinetic Device," Proceedings of the Institution of Mechanical Engineers, Part A: Journal of Power and Energy, p. 095765091877262.

[191] Castelli, M. R., Ardizzon, G., Battisti, L., Benini, E., and Pavesi, G., 2010, "Modeling Strategy and Numerical Validation for a Darrieus Vertical Axis Micro-Wind Turbine," Proceedings of the ASME 2010 International Mechanical Engineering Congress & Exposition IMECE2010, pp. 1–10.

[192] Mannion, B., Leen, S. B., and Nash, S., 2018, "A Two and Three-Dimensional CFD Investigation into Performance Prediction and Wake Characterisation of a Vertical Axis Turbine," Journal of Renewable and Sustainable Energy, **10**(3), p. 34503.

[193] Bianchini, A., Balduzzi, F., Bachant, P., Ferrara, G., and Ferrari, L., 2017, "Effectiveness of Two-Dimensional CFD Simulations for Darrieus VAWTs: A Combined Numerical and Experimental Assessment," Energy Conversion and Management, **136**, pp. 318–328.

[194] Yang, L. J., 2003, "Wear Coefficient Equation for Aluminium-Based Matrix Composites against Steel Disc," Wear, **255**(1–6), pp. 579–592.

[195] Trethewey, K. R., and Chamberlain, J., 1995, *Corrosion for Science and Engineering, Second Edition*, NACE International, Houston, TX (United States), United States.

Appendix A: Design Analysis of 1:10 Scale GKinetic Device

Appendix A. Design Analysis of 1:10 Scale GKinetic Device

A.1 Introduction

Following the 1:10 scale testing of the GKinetic VATT in Limerick Dock, a visual inspection of the prototype revealed a number of turbine design issues that were suspected of adversely affecting the performance of the device. The most significant of these, wear and movement at connection points of the main central shaft of the turbines and the six blade shafts.

This chapter presents the structural analysis of the current designs and proposes redesigns, including their justification, where redesigns were deemed necessary. Section A.2 presents problem identification and discusses the key design issues to be addressed. Section A.3 presents the analysis of the current flawed designs and possible new designs with a comparison of performance in terms of stress reduction and deflection minimisation. Section A.4 presents the design recommendations based on the design analysis undertaken, in the form of conclusions.

A.2 Problem Identification

The following subsections present the discussion of the specific design issues identified and analysed following testing of the 1:10 scale device at Limerick Dock. A general schematic of one of the GKinetic turbines is shown in Figure A.1.

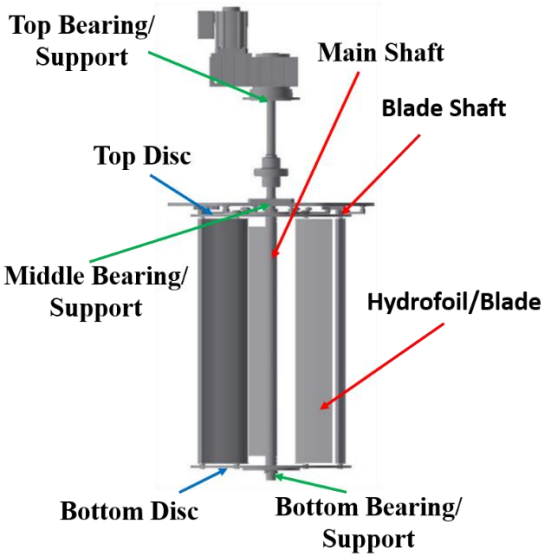

Figure A.1: Schematic of one of the turbines tested at 1:10 scale, with components of interest to this analysis identified.

A.2.1. Sizing of the Main Turbine Shaft

The main shafts of the turbines of the 1:10 scale device had a diameter of 0.05 m. However, there was minimal structural analysis of the device conducted during its design and this shaft diameter was considered excessive. The CFD modelling of the GKinetic turbine in Chapter 7 showed that the sizing of the main turbine shaft can impact on power performance through the generation of vorticity. It was, therefore, proposed to analyse the main shaft in order to determine the optimum shaft diameter. Under-sizing the shaft could cause it to shear or suffer severe bending depending on the hydrodynamic loading, whereas oversizing the shaft could adversely affect power performance, as was shown. Material selection for the shaft was also investigated taking into account metal properties such as yield strength, ultimate tensile strength and corrosion resistance.

A.2.2. Wear and Movement at Main Shaft/Hub Connections

The main shaft on the GKinetic turbine connects the top and bottom discs of the turbine, which in turn hold each of the six blades in position. The shaft also transfers torque from the turbine into the generator. Figure A.2 shows the connection between the main shaft and the top disc and hub. Wear of the main shaft was observed at Marker "1" in the figure, primarily within the keyway connection between the hub and shaft which is designed to prevent movement between the hub and shaft. As can be clearly seen in Figure A.3, the wear occurred on the shoulders of the central shaft which had been squared on two sides to resist movement. This rounding of the shaft's corners allowed movement of the shaft under hydrodynamic loading which would likely have resulted in displacement and misalignment of the shaft, and thus energy loss. Wear occurred at both the top and bottom shaft/hub connections. The benefit of including a middle support bearing between the turbine and generator was assessed. A redesign of the main shaft and cam arm connections was proposed. Determination of the wear volume was used as a method for comparing the old and new designs.

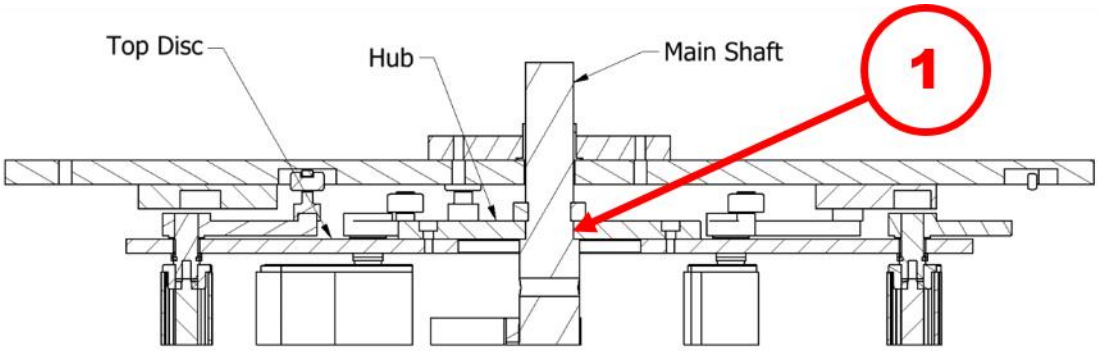

Figure A.2: Cross-sectional schematic through Top disc connection to the main shaft

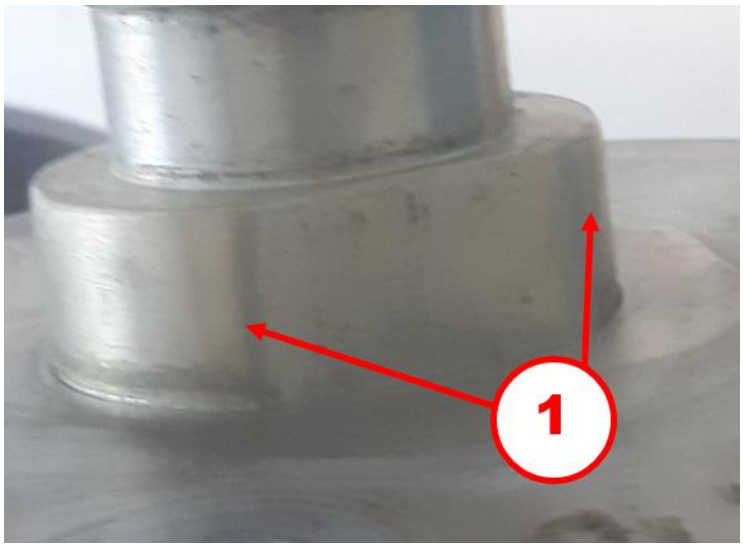

Figure A.3: Image of wear on the main shaft

A.2.3. Wear and Movement at Blade Shaft/Cam Arm Connections

Wear of the blade shafts, similar to the main shaft was observed as the same design was used. The location of the wear was at the connection between the cam follower arm and the blade shaft indicated by Marker "2" in Figure A.4. Figure A.5 shows the wear on the corners of the squared shaft. This was not an isolated incident as it occurred on all 12 blade shaft connections (6 blades by 2 turbines). The wear likely occurred as the same key connection method was used with the two sides of the round shaft squared to resist undesirable movement between components.

The wear and resulting movement of the blade shafts may have been exacerbated by the design of the blade shaft which consisted of short top and bottom shafts attached

to the blade end caps rather than a single shaft running the length of the blade. It was hypothesized that lack of blade rigidity, which resulted in significant blade deflections, contributed to the amount of movement at the cam arm connections and augmented the wear issue. The cam arm serves two purposes in the function of the design, one being to hold the blade in position and the other to pitch the blade according to the positioning of the follower in the track. Additionally, the use of two stub shafts instead of one continuous shaft, running the full length of the blade was suspected of contributing to misalignment between these components (two shafts and blade) and the discs. The wear and resulting movement of the blade would have meant blade pitch was not always optimum which could, in turn, have resulted in the loss of efficiency. The current design and a proposed redesign to reduce wear and movement of the blade shaft were compared by determining the wear volume of each design.

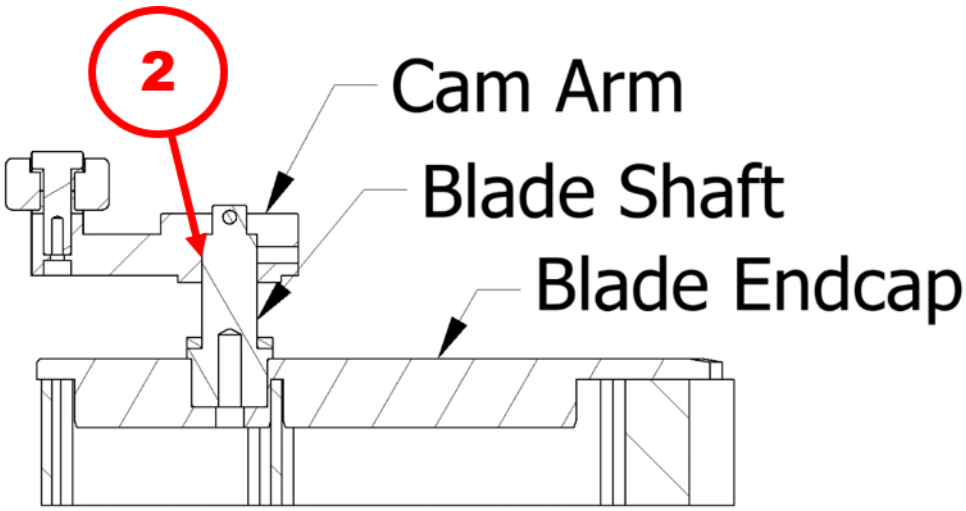

Figure A.4: Cross-sectional schematic through the blade shaft to cam arm connection

Figure A.5: Image showing wear on the blade shaft, particularly at the corners.

A.2.4. Flange Design

In addition to the main shaft and blade shaft design issues, the turbine developers were also interested in the design of a flange that would couple the main turbine shaft to the hub, as an alternative design option. The inclusion of this flange coupling would eliminate the necessity for a redesign for the shaft-hub connection used in the 1:10 scale prototype. However, both scenarios are considered.

A.3 Analysis of Existing and Proposed New Designs.

A.3.1. Sizing of the Main Shaft

Determination of the appropriate sizing of the main shaft required establishing the shear and bending stresses which the shaft would be subjected to. The torsional shear stress was deduced from the rated power of the turbine operating at its peak efficiency (i.e. optimum λ). The bending stress was determined from the drag coefficient at a rated flow speed of 2.5 m/s. From these stresses, the max principal and in-plane stresses and subsequently Von Mises stresses were determined. These stresses were then compared to allowable stresses for different materials, to allow determination of a minimum allowable shaft diameter based on specified factors of safety. The proposed shaft diameters then underwent a final check for the likelihood of resonance.

A.3.1.1. Shear Stress Analysis

The appropriate shaft size was determined for a turbine with a rated mechanical power of 10 kW (this was the rated capacity of the 1:10 scale device). The first step of this analysis was the determination of the forces acting on the shaft. It was decided to determine the torque (Q) on the shaft from the rated mechanical power of the device according to $P_{mech} = Q\Omega$. As the turbine has a rated mechanical power of 10 kW, it is logical to assume the main shaft transmits all this power into the generator. It was assumed that the rated power was achieved at the optimum λ value. The experimental testing presented in Chapter 4 showed that the optimum λ value was 0.55. This was used to determine the corresponding angular rotational velocity, Ω, and the torque on the shaft was subsequently determined. Values for known and computed parameters are shown in Table A.1. Once the torque was determined, the torsional shear stress in the shaft, τ_0, was calculated using the expression:

$$\tau_0 = \frac{Qr}{J} \tag{A.1}$$

where r is the shaft radius and J is the second polar moment of area (defined previously in Chapter 4).

The relationship of the yield strength of a material in tension to that in shear is dependent on the failure criteria applied, The Tresca criterion states that yield strength in shear, τ_Y , is 50 % of that in tension, whereas, Von Mises states it is 57 %. As the Tresca criterion is more conservative, it is used as part of this analysis.

$$\tau_Y = 0.5\sigma_Y \tag{A.2}$$

Table A.1 sets out the material properties and device specification values used in subsequent calculations. The results of these calculations are set out in Table A.2.

Table A.1: Known and computed variables used in shear stress calculations.

Variable	Value
Turbine radius (R)	0.3 (m)
Blade length (L_B).	1.33 m
Blade chord length (c)	0.2 m
Shaft Diameter (d)	0.05 (m)
Rated Power (P_{mech})	10 (kW)
Freestream velocity (U_∞)	2.5 (m/s)
Re_c	500 $x10^3$
TSR (λ)	0.55
Rotational velocity (Ω)	4.58 (rad/s)
Polar moment of inertia (J)	6.13 x10^{-7} (m^4)
Torque (Q)	1090 (Nm)

Table A.2: Calculated values of induced and yield shear stresses.

Variable	Value
τ_0	44.861 (MPa)
τ_Y	120.000 (MPa)

A.3.1.2. Bending Analysis

To determine the bending stress on the main shaft, the drag force, F_D, was first calculated using the drag coefficient of 0.83 determined from the 1:10 scale testing in Limerick Dock and the drag force formula, previously defined. Table A.3 provides the variable values that were used to determine the drag force on the device, with a total drag force value of 9.4 kN determined for the full device.

Table A.3: Known variables used in determining bending stress

Variable	Value
Water Density (ρ)	998 kg/m^3
Free-stream velocity (U_∞)	2.5 m/s
Full Device area (A)	3.63 m^2
Drag coefficient (C_D)	0.83
Shaft Diameter (d)	0.05 m
Distance to neutral fibres (y)	0.025 mm
Shaft Length (L)	2.3 m
Yield Strength (σ_Y)	240 MPa
6082 T6 Young's modulus E	70 GPa

The total device drag load was assumed to be distributed evenly between the two turbines (i.e. 4.7 kN acting on each turbine). This is again taking the more conservative approach that all of that force is being taken by the turbines since it is ignoring the portion that will be taken by the bluff body. The main shaft of either turbine was considered to experience this load as two-point loads of equal magnitude acting at the

points where the top and bottom hubs connect to the shaft, as shown in Figure A.6. Initial analysis considered the system as being supported at either end only; however, subsequent analysis will show that this design is not recommended. This analysis was requested by turbine developers to determine the necessity of a central support bearing. Static beam theory was used to produce: free body, shear force and bending moment diagrams (shown in Figure A.7, Figure A.8 and Figure A.9 respectively), from which the maximum bending moment ($M_{\max}$) was determined. The maximum bending stress (σ_0) was calculated via the flexure formula as:

$$\sigma_0 = \frac{M_{\max} y}{I} \tag{A.3}$$

where y is the distance to the neutral fibres ($d/2$ for a circular cross-section) and I is defined as:

$$I = \frac{\pi d^4}{64} \tag{A.4}$$

For the case where there is no central support bearing in place, seen in Figure A.6 and Table A.4, the maximum bending moment that occurs is 1.314 kNm.

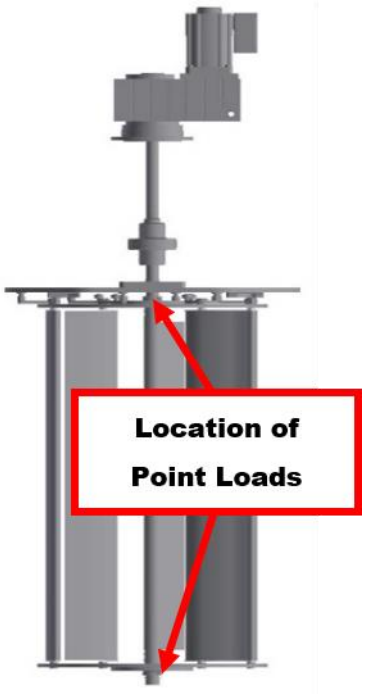

Figure A.6: Positioning of point loads relative to turbine representative of drag

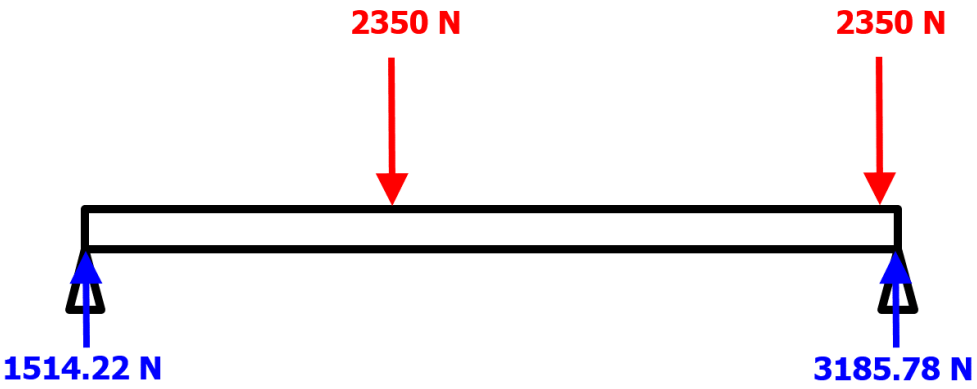

Figure A.7: Free body diagram of the shaft with no central support bearing.

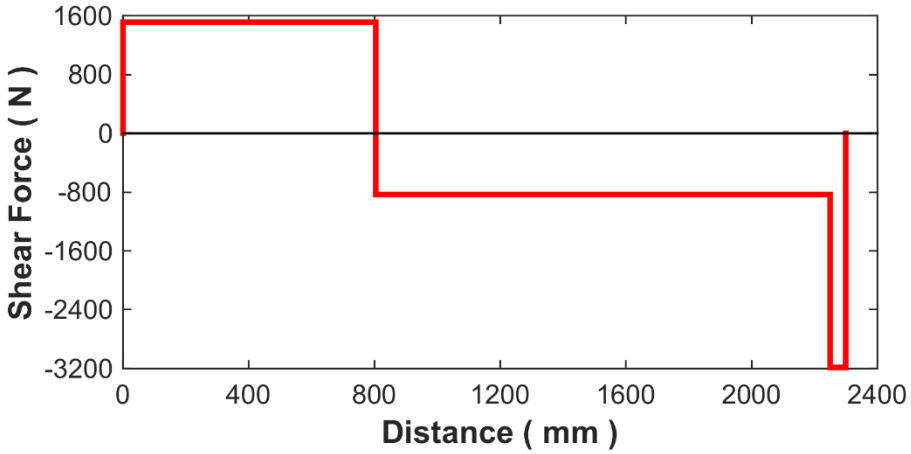

Figure A.8: Shear force diagram of the shaft with no central support bearing.

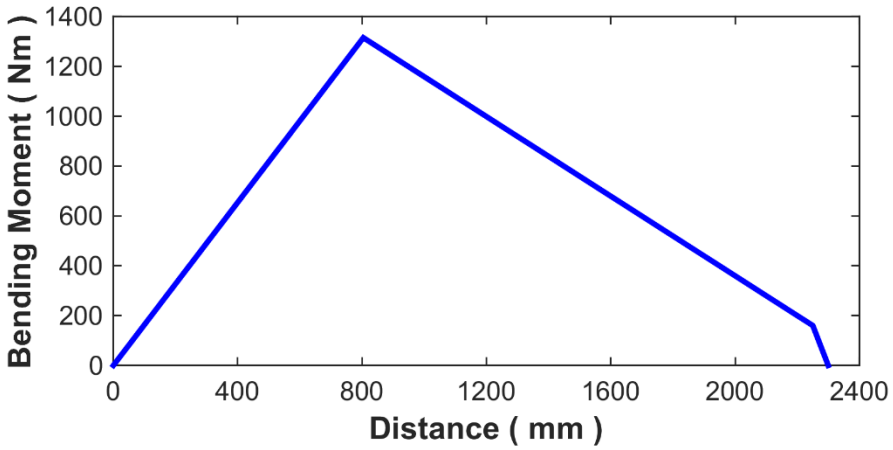

Figure A.9: Bending moment diagram of the shaft with no central support bearing.

Table A.4: Computed variables for bending stress analysis of the case without a central support bearing.

Variable	Value
Total Drag, F_D	9.4 (kN)
Drag per turbine	4.7 (kN)
F	2.35 (kN)
R_1	1.514 (kN)
R_2	3.185 (kN)
I	3.068E-07 m^4
M_{max}	1.314 (kNm)
σ_0	11 (MPa)

In the second case analysed, a central support bearing is positioned between the generator and turbine, located inside a housing at the top disc. A free body diagram of this system is shown in Figure A.10 and the bending moment diagram of this setup is shown in Figure A.11 Table A.5 lists the reaction forces acting on the system, denoted R_1, R_2, and R_3 from left to right, and the maximum bending moment and bending stress. Negative values denote direction. A maximum bending moment of 135 Nm occurs; this is almost a full order of magnitude lower compared to the case without a central support bearing. It is, therefore, strongly recommended that the central bearing is included in future designs. In all of the following analyses in this chapter, it is assumed this bearing support is included in the design.

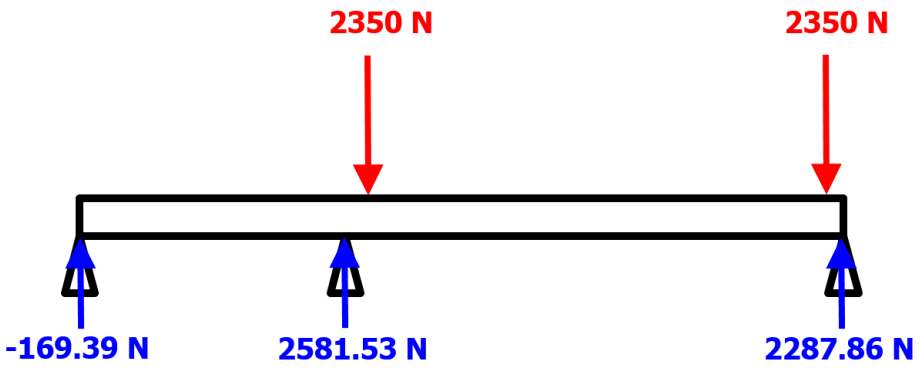

Figure A.10: Free body diagram of the shaft with central bearing included.

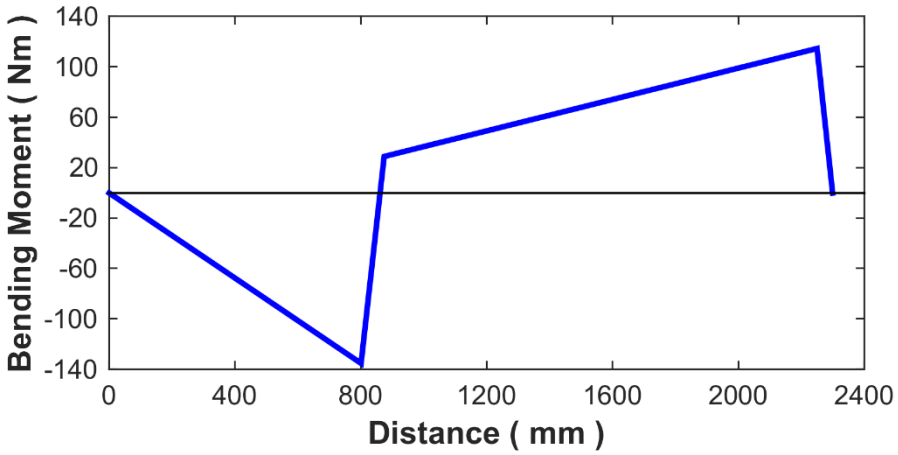

Figure A.11: Bending moment diagram of the shaft with central support bearing included.

Table A.5: Details of bending stress analysis for the case with central support bearing in place.

Variable	Value
R_1	-0.169 (kN)
R_2	2.581 (kN)
R_3	2.287 (kN)
$M_{\max}$	-0.135 (kNm)
σ_0	107.1 (MPa)

A.3.1.3. Material Properties

The main shafts used in the 1:10 scale testing were made of aluminium 6082 T6. An investigation into alternative materials was carried out. This concentrated on several different grades of stainless steel due to their strength and corrosive resistant attributes. The relevant material properties for strength and corrosion resistance were obtained from the materials software package CES Edupack and are summarised in Table A.6. It is seen that stainless steel is superior to aluminium in all physical property categories.

Table A.6: Comparison of various material properties for strength and corrosion resistance.

Material	Min Yield (MPa)	Min UTS (MPa)	Durability Freshwater	Durability Saltwater
6082 T6	240	280	Excellent	Acceptable
AISI 201	275	655	Excellent	Excellent
AISI 304	205	510	Excellent	Excellent
AISI 309	205	515	Excellent	Excellent
AISI 314	327	515	Excellent	Excellent
AISI 316	205	515	Excellent	Excellent

A.3.1.4. Determining the Optimum Shaft Diameter

Static analysis was used to calculate the induced stresses and a comparison of these stresses with the material properties then allowed correct sizing of the shaft. It is important to note that this approach does not account for fatigue; the turbine developers were only interested in static analysis and, therefore, fatigue analysis was omitted. The inclusion of fatigue would require further analysis and would generally result in an increase in the minimum shaft diameter. The two main stress components that were used for determining the minimum shaft diameter under static analysis were the bending stress and the shear stress caused by the bending moment and torque (shown in Table A.7), respectively.

Table A.7: Summary of values required to determine stresses

Variable	Value (Nm)
$M_{\max}$	135
Q	1090

Once the bending stress and shear stress were determined, Mohr's circle analysis was used to determine the maximum in-plane shear stress ($\tau_{\max}$) and the maximum principle stress (σ_1) for a particular shaft diameter. An example of a Mohr's circle is shown in Figure A.12.

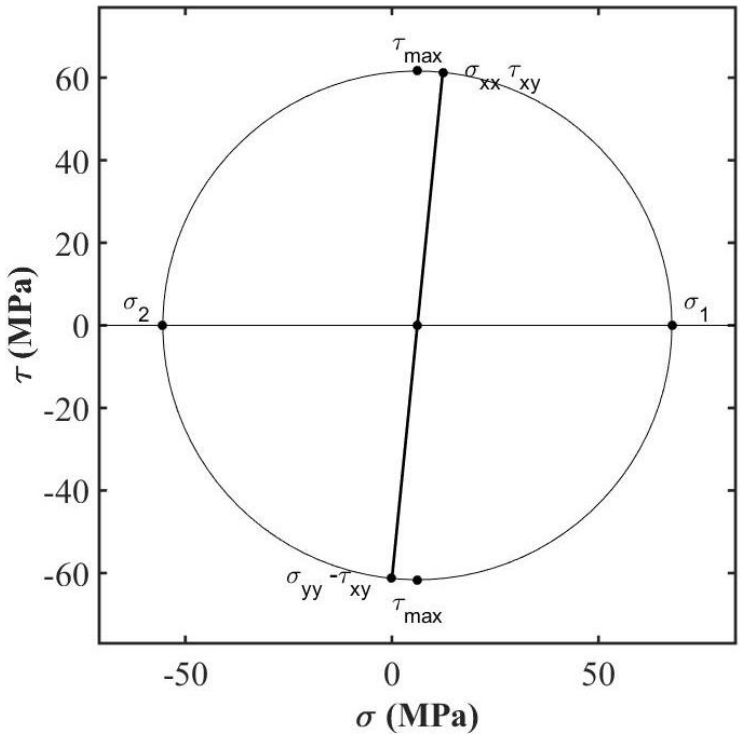

Figure A.12: Mohr's circle with principal stresses and max in-plane shear stresses identified.

Table A.8 summarises the dimensional properties of a selection of different shaft sizes that were assessed. Table A.9 presents the values determined for the bending and shear stresses; the maximum in-plane shear stress ($\tau_{\max}$), maximum principle stresses (σ_1, σ_2) and the Von Mises stress (Equation (A.5)) for the selected shaft diameters.

$$\sigma_{VMS} = \sqrt{{\sigma_1}^2 - \sigma_1\sigma_2 + {\sigma_2}^2} \tag{A.5}$$

Table A.8: Dimensional properties for selection of shaft sizes analysed.

d (m)	***J*** (m^4)	***y*** (m)	***I*** (m^4)
0.025	$3.8\,x10^{-8}$	0.0125	$1.92x10^{-8}$
0.03	$7.9\,x10^{-8}$	0.015	$3.98\,x10^{-8}$
0.035	$1.4\,x10^{-7}$	0.0175	$7.37x10^{-8}$
0.04	$2.5\,x10^{-7}$	0.02	$1.26\,x10^{-7}$
0.045	$4.03\,x10^{-7}$	0.0225	$2.02\,x10^{-7}$
0.05	$6.14\,x10^{-7}$	0.025	$3.07\,x10^{-7}$

Table A.9: Computed stresses for the selection of shaft sizes analysed.

d (m)	τ_0 (Mpa)	σ_0 (Mpa)	τ_{max} (Mpa)	σ_1 (Mpa)	σ_2 (Mpa)	σ_{VMS} (Mpa)
0.025	355.58	88.01	358.29	402.30	-314.29	622.14
0.03	205.78	50.93	207.35	232.81	-181.88	360.04
0.035	129.59	32.07	130.57	146.61	-114.54	226.73
0.04	86.81	21.49	87.47	98.22	-76.73	151.89
0.045	60.97	15.09	61.44	68.98	-53.89	106.68
0.05	44.45	11.00	44.79	50.29	-39.29	77.77

With all of the stress values known, it was possible to determine the minimum allowable shaft diameter for each of the materials assessed based on their properties. Minimum diameters were calculated for two factors of safety (1.5 and 2) and are shown in Table A.10.

Table A.10: Shaft sizing for FOS of 1.5 and 2, for different materials.

	Minimum shaft diameter (mm)					
FOS	6082 T6	AISI 201	AISI 304	AISI 309	AISI 314	AISI 316
1.5	40	38	40	40	36	40
2	44	40	44	44	38	44

An investigation of the effect of shaft sizing on the downstream flow was also conducted by evaluating the Reynolds numbers based on the different shaft diameters. These are shown in Table A.11. The Reynolds numbers for all diameter sizes are in the subcritical flow range and will, therefore, all exhibit the same type of downstream flow pattern. However, as was shown in Chapter 7, the larger shaft sizes exhibit wider vortex streets downstream that can negatively affect turbine performance.

Table A.11: Shaft diameter dependent Reynolds numbers

d (mm)	**44**	**42**	**40**	**38**	**36**
$Re_d\ x10^3$	109	104	99	94	89

A.3.1.5. Critical Speed Analysis

Critical speed analysis was conducted to check for the likelihood of shaft resonance. This was done using Rayleigh's method for lumped masses, where the critical speed ω_i is expressed as:

$$\omega_i = \frac{g \sum W_i y_i}{\sum W_i {y_i}^2} \tag{A.6}$$

where W_i is the weight at the ith location and y_i is the deflection at the ith body location. The natural frequency of the material is taken as the critical speed, at which resonance would occur. Table A.12 shows the natural frequency of the shaft for the shaft diameters identified as possibilities (Table A.10) for the six materials. As these values are much higher than the operating speeds of the shaft, it was concluded that resonance will not be an issue. Based on the analysis presented in this subsection, it is recommended that AISI 314 be used, for it has the highest yield strength.

Table A.12: Critical speeds/natural frequencies for identified shaft diameters.

Diameter $\boldsymbol{d}$ (m)	Natural Frequency $\boldsymbol{\omega_N}$ (rad/s)					
	6082.00	**AISI 201**	**AISI 304**	**AISI 309**	**AISI 314**	**AISI 316**
0.036	164.85	273.73	271.59	275.85	275.85	270.87
0.038	183.67	304.98	302.60	307.35	307.35	301.81
0.040	221.47	352.61	349.47	355.60	355.08	348.50
0.042	224.38	372.57	369.66	375.45	375.45	368.68
0.044	274.70	439.68	435.66	443.49	442.68	434.43

A.3.2. Wear and Movement at Main Shaft/Hub Connections

Schematics of the old and new main shaft-to-hub connections are presented in Figure A.13 showing the points of action of the bearing stresses. The bearing stress was determined using:

$$\sigma = \frac{F_B}{A_c} \tag{A.7}$$

where, A_c is the contact area and is defined as:

$$A_c = Lt \tag{A.8}$$

The bearing force for the old connection is defined as:

$$F_{B_{Old}} = \frac{Q}{2R} \tag{A.9}$$

whereas, the bearing force for the new hex connection is defined as:

$$F_{B_{new}} = \left(\frac{Q}{6R}\right) \sin\gamma \tag{A.10}$$

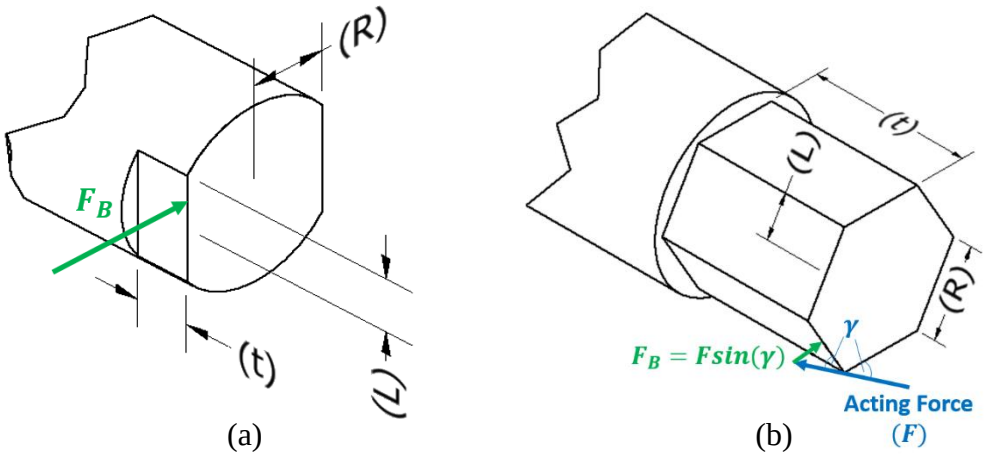

Figure A.13: Schematic showing the location of bearing forces acting on the shaft for (a) old connection and (b) proposed new connection.

Table A.13 and Table A.14 present the known variable values used to calculate bearing stresses for the old and new connections, respectively. It can be seen that for the new design the bearing stress reduces to 39 MPa from 121 MPa for the old design.

Table A.13: Old connection bearing stress analysis details.

Variable	Value
L	0.015 (m)
t	0.015 (m)
Q	1090 (Nm)
R	0.02 (m)
F_B	27.25 (kN)
Bearing Stress (σ)	121.1 (MPa)

Table A.14: New connection bearing stress analysis details.

Variable	Value
L	0.01 (m)
t	0.02 (m)
Angle of Force acting relative to bearing force (γ)	30 (°)
Q	1090 (Nm)
R	0.02 (m)
F_B	7.87 (kN)
Bearing Stress (σ)	39.33 (MPa)

A.3.3. Movement and Wear at Blade Shaft-to-Cam Arm Connections

A.3.3.1. Bearing Stress Analysis

In order to determine the bearing stresses for the cam arm-to-blade shaft connection, an approximation had to be made in order to determine the force that a single blade is subjected to. It had been hoped to adapt the BEMT model of Chapter 5 for application to the GKinetic device to calculate the blade loads but this was not possible in the timeframe of the PhD. Instead, a more fundamental approach was adopted, where the maximum instantaneous torque was determined for a single hydrofoil. To determine the torque acting on a single foil at any given time, appropriate lift and drag coefficients had to be selected from those for the NACA 0018 profile, used in the 1:10 scale device.

The C_{L} and C_{D} values in Table A.15 were selected as the values that would give the highest tangential coefficient [34]. The tangential coefficient is a function of the lift and drag coefficients and was previously defined in Chapter 5. Figure A.14 shows C_{T} plotted versus α. It was identified that the highest tangential coefficient occurred at $\alpha = 14^{o}$.

Table A.15: Hydrofoil properties used to calculate the force on a single blade (taken from Sheldahl and Klimas [34]).

Variable	Value
C_{L}	1.0175
C_{D}	0.0245
α	14^{o}
C_T	0.0245

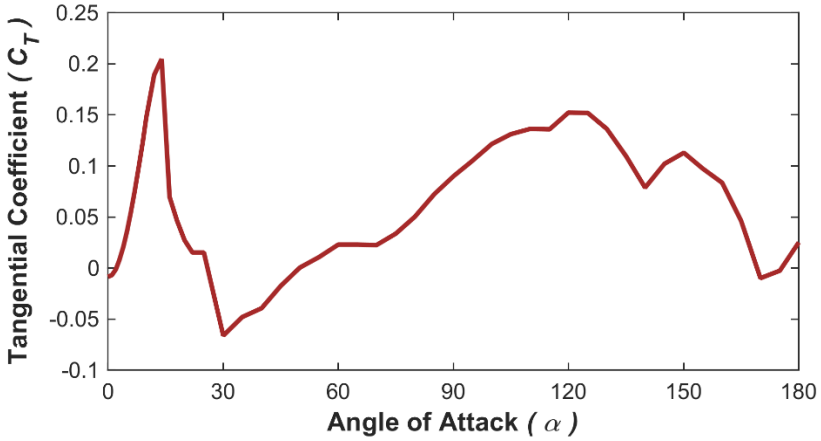

Figure A.14: Tangential coefficient versus angle of attack.

Figure A.15 presents a plot showing variation in angle of attack (α) with blade azimuth position (θ) for λ = 0.55 and assuming an axial induction factor of 0.3. Plots are compared for the variable pitched GKinetic blade with an unpitched blade, i.e. the GKinetic pitching regime has the effect of modifying the unpitched α values. There are several locations for the *pitched* results where the azimuth position of the blade corresponds with an α of 14^{o}. Each of these was investigated to determine the highest value of instantaneous torque.

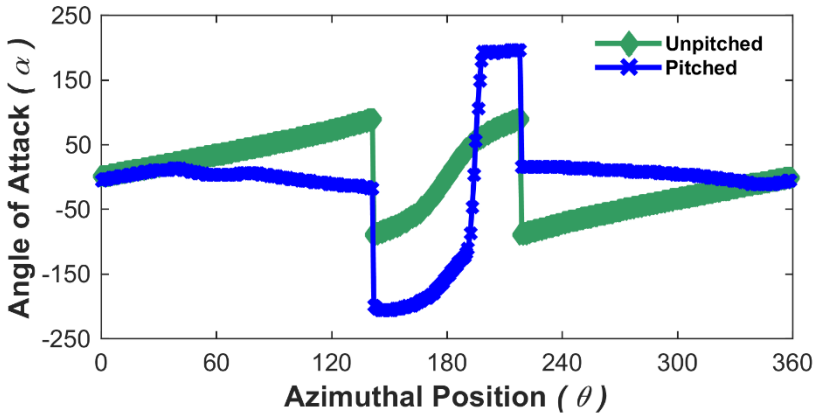

Figure A.15: Angle of attack versus azimuth position for a non-pitched foil and the GKinetic foil.

Instantaneous torque, Q_{i}, on a single foil was determined with the expression:

$$\mathrm{Q_i} = \frac{1}{2}\rho {V_{\mathrm{rel}}}^2 L_{\mathrm{B}} c C_{\mathrm{t}} \tag{A.11}$$

The V_{rel} is in turn determined using Equation (A.12). The axial induction factor in this instance was set to 0 to give the highest possible relative velocity.

$$V_{\mathrm{rel}} = U_{\infty}\sqrt{((1-a)\sin(\theta))^2 + \left((1-a)\cos(\theta) + \lambda\right)^2} \tag{A.12}$$

Table A.16 shows the assumed parameter values used in the torque calculations. Table A.17 shows the instantaneous torque calculated for those azimuth positions that gave a α of 14°.

Table A.16: Water and blade properties

U_{∞} (m/s)	a	λ	ρ (kg/m^3)	L_{B} (m)	c (m)
2.5	0	0.55	998.1	1.33	0.2

Table A.17: Torque and V_{rel} for azimuthal positions corresponding to a α of 14°.

$\boldsymbol{\theta}$ (^{o})	$\boldsymbol{V_{rel}}$ (m/s)	$\boldsymbol{Q_i}$ (Nm)
134	1.83	59.60
135	1.81	58.08
136	1.79	56.59
137	1.76	55.13
138	1.74	53.70
195	1.22	26.57
240	2.17	83.30
241	2.19	85.15
242	2.22	87.02
243	2.24	88.91
244	2.26	90.81
245	2.29	92.73
Max Torque	**-**	**92.73**

The approach used for the main shaft-to-hub connections in Section A.3.2 was also adopted to calculate the bearing stress on the cam arm connections. A schematic of the old connection is shown in Figure A.16, while the new connection is shown in Figure A.17. Table A.18 and Table A.19 show the results for the old and new connections, respectively. Comparing the results of the analyses, the new connection significantly reduces the bearing stress to 7.73 MPa from 118 MPa for the old connection.

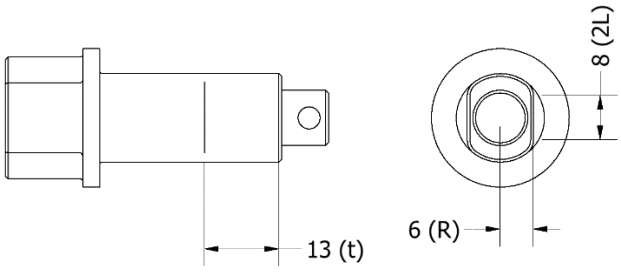

Figure A.16: Front and end elevation of old blade shaft (dimensions in mm).

Table A.18: Bearing stress analysis details for the old cam arm connection

Q (Nm)	L (mm)	t (mm)	R (m)	Ac ($\mathbf{mm^2}$)	F_B (N)	Stress (Mpa)
92.73	4	13	0.006	65	7730	118.88

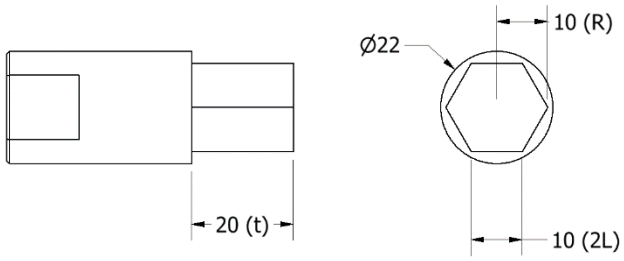

Figure A.17: Partial front elevation and end elevation of the new full-length shaft and hexagonal connection (dimensions in mm).

Table A.19: Bearing stress analysis details for new connection

Q (Nm)	L (mm)	t (mm)	R (m)	Ac ($\mathbf{mm^2}$)	ψ (^{o})	F_B (N)	**Stress** (MPa)
92.73	5	20	0.01	100	30	772.72	7.73

A.3.3.2. Blade Deflection Analysis

As discussed in section A.2.3, it was speculated that excessive blade deflections and the use of stub shafts were contributing to wear and misalignment issues. Finite Element (FE) modelling was carried out using Autodesk Inventor's built-in FE package. Deflection analyses were carried out on the blade for the current design case and the proposed new design case with the full-length shaft and support with the focus being on deflections in the axial and radial directions of the blade. The new design case (shown in Figure A.18) involves running a 22 mm solid shaft through the full length of the blade to increase blade stiffness and thus reduce deflections. Middle support of 40 mm in width was also included to further increase the stiffness. This support could be attached to the shaft in a number of ways, such as by welding, adhesion or a using mechanical fixing. It is not envisaged that this support would interfere with the existing shear web support of the blade (Figure A.19).

(a) (b)

Figure A.18: New blade design showing mid-blade support

Figure A.19: Existing blade cross section showing shear web support.

Figure A.20 and Figure A.21 show the deflection results in planes normal and tangential to the chord-line, respectively, for the current design while Figure A.22 and Figure A.23 show the deflection results for the proposed new design. Clearly, the new design has the effect of reducing deflections in both planes. In Figure A.20, a max normal deflection of 1.463 mm is observed, for the current design compared to 0.6711 in Figure A.22 for the new design, giving a 54 % reduction. In Figure A.21 a max tangential deflection of 0.0982 mm is observed for the current design, compared to 0.0477 in Figure A.23 for the new - a 51 % reduction.

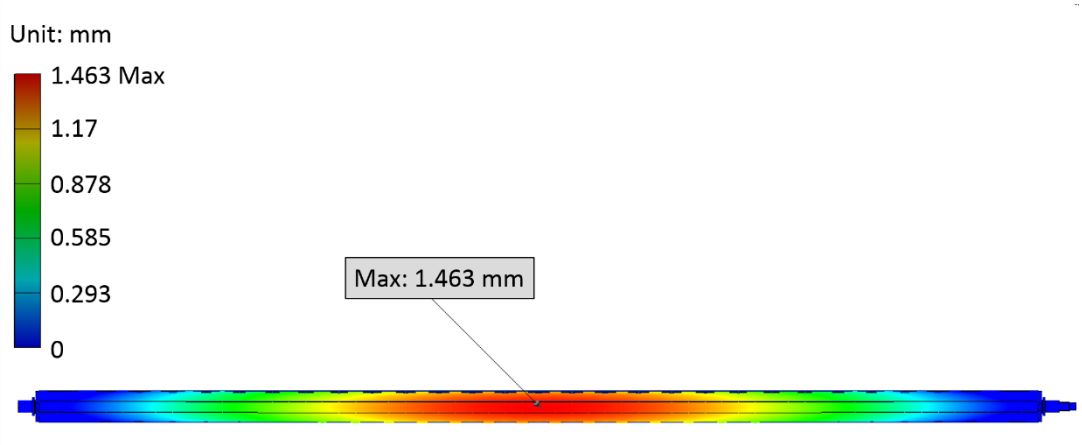

Figure A.20: Deflections in the chord-line normal plane for the current design.

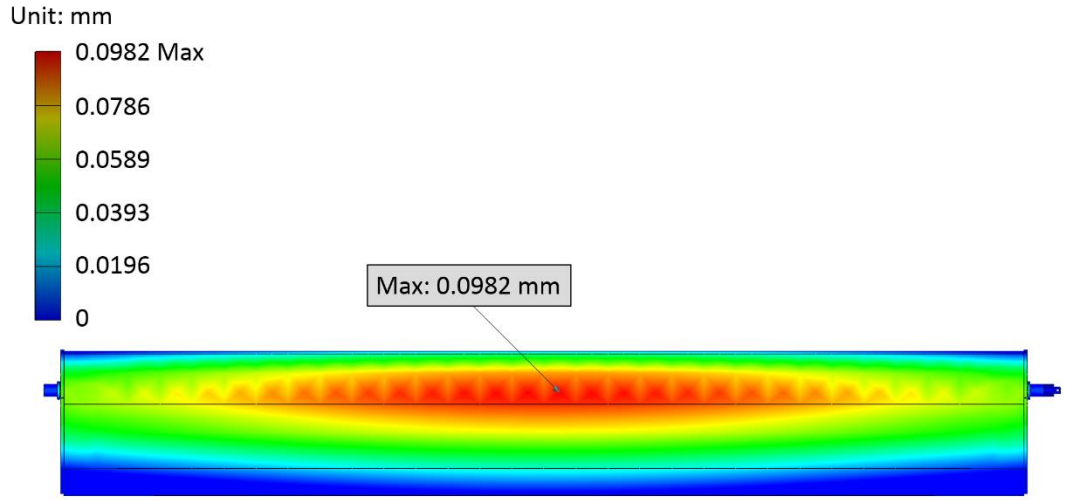

Figure A.21: Deflections in the chord-line tangential plane for the current design.

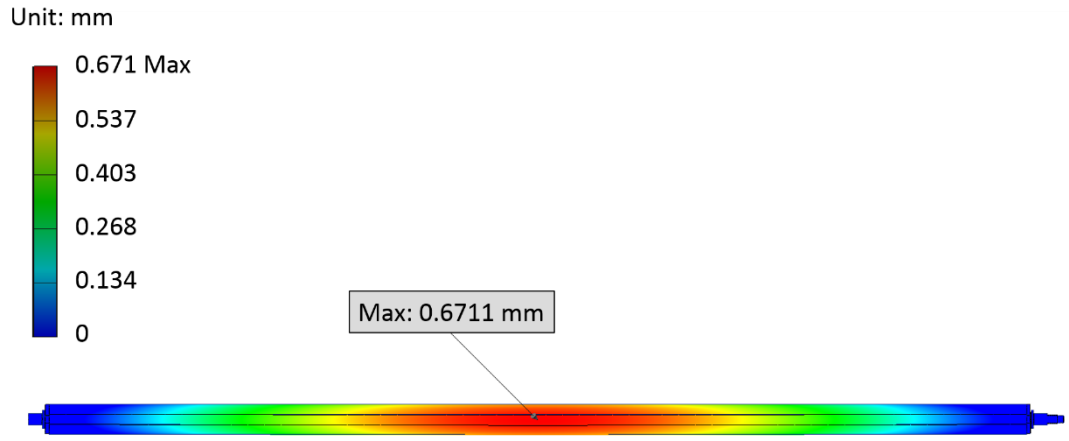

Figure A.22: Deflections in the chord-line normal plane for the new design.

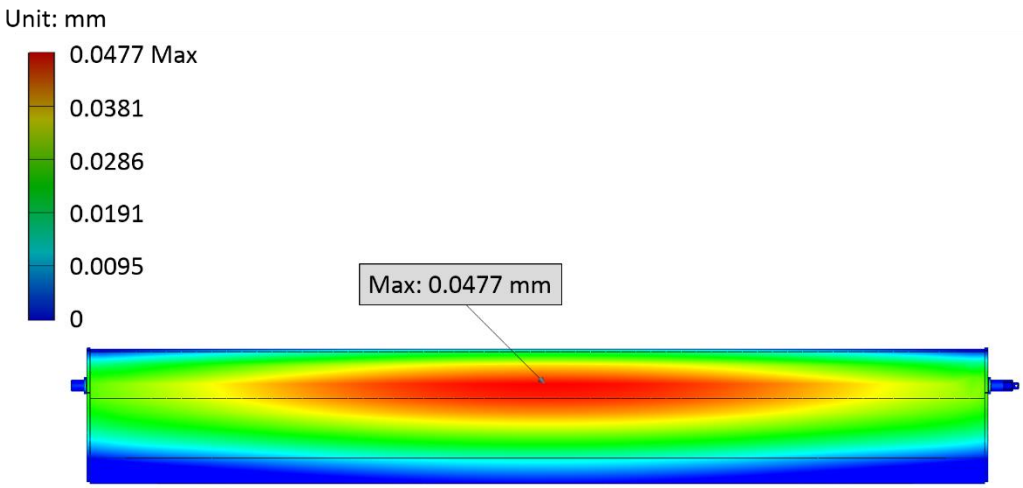

Figure A.23: Deflections in the chord-line tangential plane for the new design.

Figure A.24 and Figure A.25 present a comparison of deflections in the normal and tangential planes, respectively, for the current and new design cases along lines through the points of maximum deflection in Figure A.20 to Figure A.23. In all cases, the max deflection occurs at the blade mid-span; this is as expected since the system is essentially a simply supported beam problem. The figures show that the new design has the effect of reducing deflections by more than 50 % in both planes. Table A.20 compares the values for the maximum deflections for the two design cases extracted from Figure A.24 and Figure A.25. The new design offers a significant improvement, as it significantly reduces deflections and should, therefore, improve alignment and reduce wear.

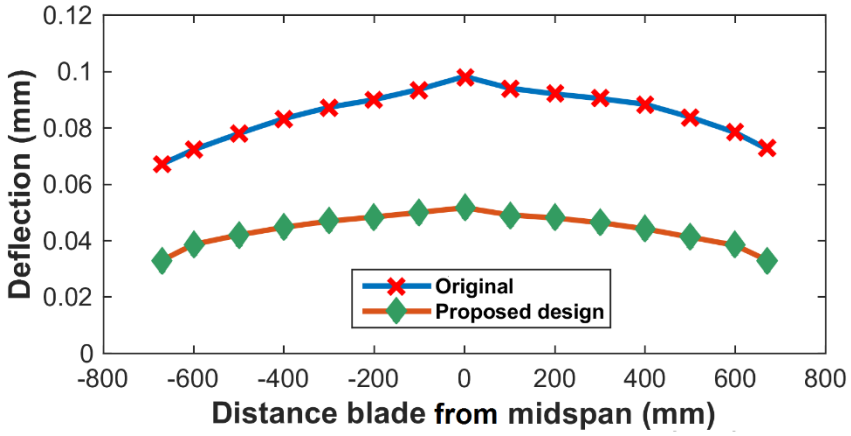

Figure A.24: Comparison plot of deflections in the chord-line normal plane

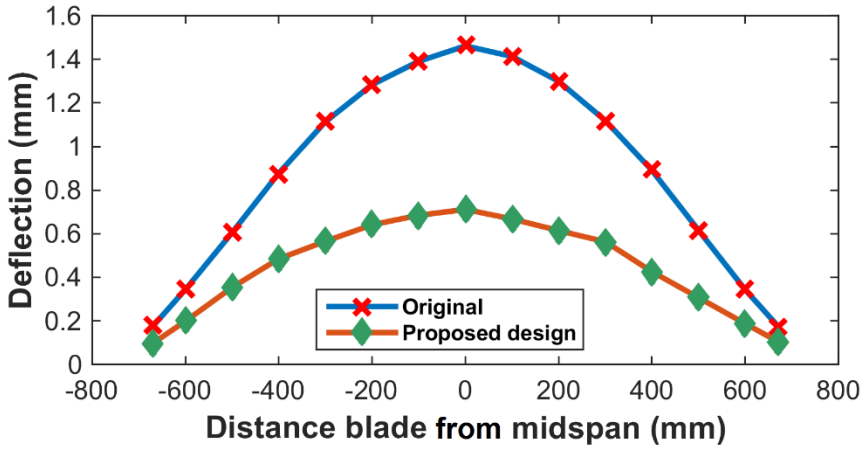

Figure A.25: Comparison plot of deflection in the chord-line tangential plane

Table A.20: Summary of maximum blade deflections for both designs

	Max Normal Deflection (mm)	Max Tangential Deflection (mm)	Normal % difference	Tangential % difference
Original	1.463	0.0982	-	-
Proposed Design	0.671	0.0477	-54.13	- 51.42

A.3.3.3. Redesign of the Blade Shaft-to-Cam Arm Connection.

Changing the blade shaft-to-cam arm connection key from two flattened sides of a circle to a hexagonal shape was shown to significantly reduce the bearing stresses on the connection. Additionally, deflection analysis of the new blade design including a full-length blade shaft showed that deflections could be reduced. Additionally, this would also have the effect of reducing the wear sliding distance and wear volume of the connection. This subsection presents a comparison of the current blade shaft-to-cam arm connections with a proposed new design aimed at further reducing movement and wear at the connections.

The current blade-to-cam arm connection is shown in Figure A.26. As previously shown, this design resulted in significant wear of the blade shaft which is considered to have adversely affected the performance of the device. In the proposed new design

(shown in Figure A.27), the connection is designed to be an interference fit. Additional grub screws could also be added to further restrain movement in the components if high accuracy machining is not possible. Increasing the shaft diameter from 16 to 22 mm increases the torsional strength of the shaft, as well as increasing the contact area, thus reducing the contact stress. Similarly, increasing the length of the connection contact area from 13 mm to 20 mm also has the effect of reducing the contact stress for the same reason. The key benefits of the new design are:

- Stresses will be carried by 6 faces instead of 2.
- Shaft diameter is increased from 16 mm to 22 mm, increasing torsional strength and reducing contact stress.
- The hex shaft runs the full 20 mm thickness of the cam arm instead of 13 mm in the existing design, reducing contact stress.
- Normal load on the surface will be reduced, thus reducing bearing stress and wear rate.
- It requires less machining time compared to splines.

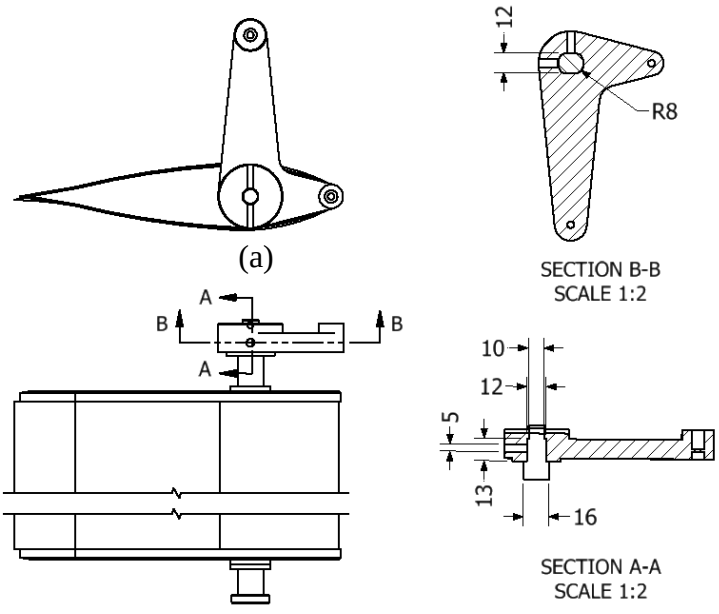

(a) (b) (c)

Figure A.26: Old cam arm to blade shaft connection schematic with (a) plan view, (b) broken partial side elevation and (c) sectional planes A-A and B-B.

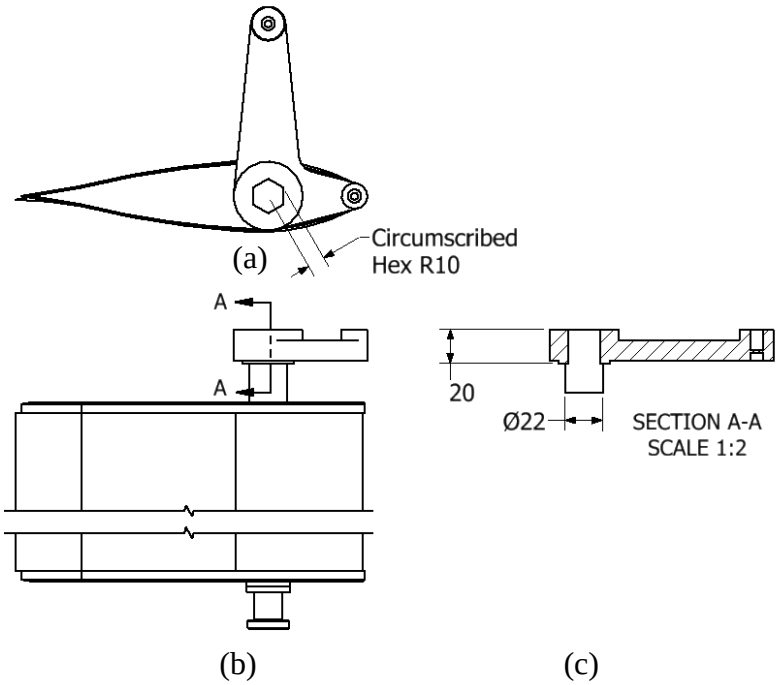

Figure A.27: Proposed new cam arm to blade shaft connection with (a) Plan view, (b) partial side elevation and (c) sectional view through planes A-A.

A.3.3.4. Wear Volume Analysis on Blade Shafts

The primary intention of the new design for the blade-to-cam arm connections was to reduce wear, thus the wear volume of both designs was evaluated. The Archard wear equation was used to determine the wear volume, W:

$$W = K\frac{F_B S}{H} \tag{A.13}$$

where, H, is the material hardness, S, in this instance, is the sliding distance, and K, is the wear coefficient. From the literature [194], a suitable value of $K = 2.5\ x10^{-5}$ was identified for this coefficient. The sliding distance was determined from the deflections due to loading on the blade, previously calculated by the FE model. As can be seen in Figure A.28, the sliding distance can be calculated from trigonometry using the rotational angle due to the deflection, ψ, which can in turn be determined from the blade deflections. The results of the wear volume calculations are shown in Table

A.21. Comparing the designs, it is seen that the new connection reduces the wear volume by a factor of 20 compared to the old connection.

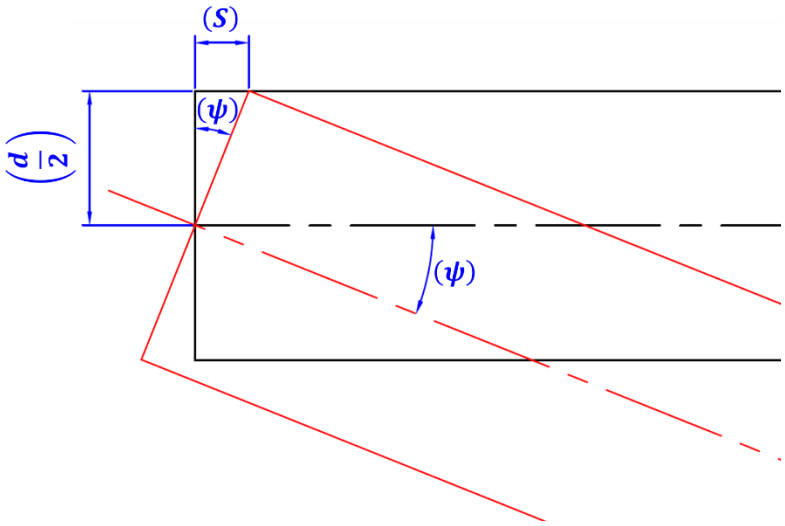

Figure A.28: Schematic showing rotation angle, ψ, and sliding distance, S.

Table A.21: Wear volume analysis results of both designs

	y_{max} (mm)	ψ (°)	S (mm)	d (mm)	K	H (Mpa)	F_B (N)	W mm^3
Old	1.46	0.13	0.02	16	$2.5x10^{-05}$	85.51	7727.25	$3.98x10^{-05}$
New	0.71	0.06	0.01	16	$2.5x10^{-05}$	85.51	772.72	$1.93x10^{-06}$

A.3.4. Flange Design

A schematic of a proposed design for a new flange, to connect the main shaft of the turbine to the discs via a hub, is shown in Figure A.29. Once the gross dimensions of the flange were determined based on the recommendations of Bhandari's "Design of machine elements" [195], it was important to ensure that these dimensions satisfied the required stress criteria.

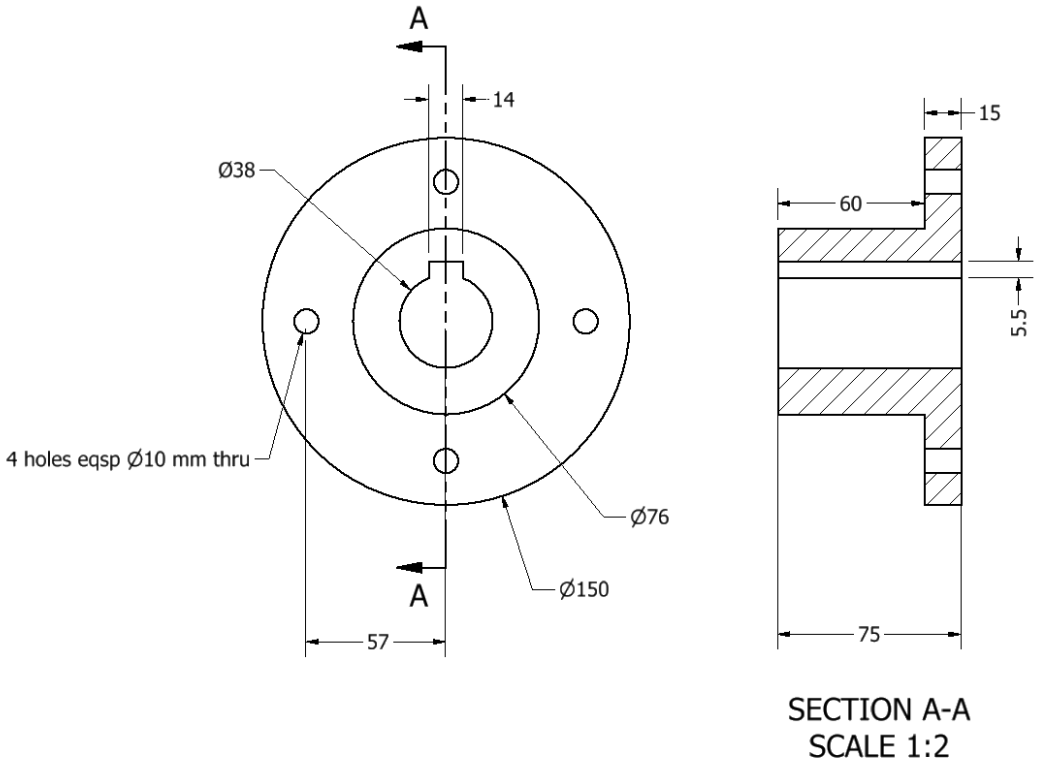

Figure A.29: Proposed new flange design, all dimensions are in mm.

It was assumed that the flange would be made from the same material that was recommended for the shaft (AISI 314 stainless steel) in order to avoid galvanic corrosion of dissimilar metals [195]; this stainless steel has a yield stress of 327 MPa. The hub shear stress was determined using the torsional formula:

$$\tau = \frac{Qr_{\mathrm{h}}}{\mathrm{J}} \tag{A.14}$$

where the polar moment for this flange is determined as:

$$\mathrm{J} = \frac{\pi {D_h}^4 - d^4}{32} \tag{A.15}$$

D_{h} is the hub diameter and has a value of 76 mm as shown in Figure A.29. The variable values used in the hub shear stress calculations are set out in Table A.22. The shear stress was determined to be 12.81 MPa.

Table A.22: Hub shear stress analysis of proposed new flange design

Variable	Value
Q	1090 (Nm)
d	38 (mm)
D_{h}	76 (mm)
r_{h}	38 (mm)
τ	12.81 (MPa)

The shear stress at the connection of the flange and hub is determined using Equation (A.16). The results are shown in Table A.23; shear stress was determined to be 7.6 MPa.

$$\tau = \frac{2Q}{\pi {D_{\mathrm{h}}}^2 t} \tag{A.16}$$

Table A.23: Flange to hub connection shear stress analysis of the proposed design.

Variable	Value
Hub thickness (t)	15 (mm)
τ	7.6 (MPa)

The use of mechanical fixings, such as a key, to affix the flange to the main shaft of the turbine is recommended instead of welding. Failure of a key is usually either by shear or compression. The equation for determining the shear stress in a key is:

$$\tau = \frac{2Q}{d b_{\mathrm{k}} b l_{\mathrm{k}}} \tag{A.17}$$

while the equation for determining the compressive stress in a key is

$$\sigma = \frac{4Q}{d h_{\mathrm{k}} h l_{\mathrm{k}}} \tag{A.18}$$

where, b, l, and, h, refer to breadth, length and height dimensions, respectively, while

the subscript k denotes dimensions for the key. As can be seen in Table A.24, the shear stress was calculated at 51.8 MPa and the compressive stress was 145 MPa.

Table A.24: Stress analysis details for Key connecting flange and shaft.

Variable	Value
b_{k}	14 (mm)
l_{k}	75 (mm)
h_{k}	10 (mm)
τ	51.8 (MPa)
σ	145 (MPa)

The final required analysis was the identification of the bolts to be used. Equation (A.19) determines the allowable stress for the bolts. It was assumed the bolts are also made from AISI 314 stainless, again to avoid galvanic corrosion, which has a yield strength of 327 MPA.

$$\sigma_{\mathrm{allow}} = \frac{\sigma_{\mathrm{Y}}}{\sqrt{3}\, FOS} \tag{A.19}$$

With the allowable stress known, it is possible to determine the required diameter of the bolts, d_{bolt}, according to:

$$d_{\mathrm{bolt}} = \sqrt{\frac{8\, Q}{\pi (BCD) N_{\mathrm{bolt}}\, \sigma_{\mathrm{allow}}}} \tag{A.20}$$

where BCD is the bolt circular diameter and N_{bolt} is the number of bolts used. Finally, the compressive stress in the bolt was determined using:

$$\sigma_{\mathrm{B_{comp}}} = \frac{2\, Q}{(BCD) N_{\mathrm{bolt}} d_{\mathrm{bolt}} t} \tag{A.21}$$

The results of these calculations are shown in Table A.25. If 4 bolts are used, the minimum bolt diameter is 10 mm and the resulting bolt compressive stress would be 32.4 MPa which is well below the yield strength of 327 MPa.

For all of the analyses conducted for the new flange connection, all of the stresses determined were within the material yield limits for AISI stainless steel 314. It can, therefore, be concluded that the proposed flange design is a structurally suitable one.

Table A.25: Details of stress analysis for bolts connecting flange and turbine disc.

Variable	Value
σ_{Y}	327 (MPa)
FOS	3
BCD	114 (mm)
N_{bolt}	4
σ_{allow}	62.9 (MPa)
t	15 (mm)
d_{bolt}	10 (mm)
$\sigma_{\mathrm{B_{comp}}}$	32.4 (MPa)

A.4 Chapter Summary

The conclusions for this chapter take the form of the following design recommendations which are based on the presented structural analyses.

- It is recommended that the main shaft of the turbine be made from AISI 314 stainless steel and accordingly, the minimum shaft diameter should be 38 mm; this would give a factor of safety of 2. This will provide sufficient structural integrity whilst keeping the width and strength of the shaft-induced vortex street to a minimum.

- It is recommended to introduce a 22 mm interior shaft to run the full length of the blade and include a central support for this shaft. This will make the blade more rigid and reduce deflections, which will, in turn, reduce wear of the blade connections and improve blade alignment.

- It is recommended to redesign the cam arm-to-blade shaft connections from the current interference fit of two flatted sides to a hexagonal (hex) connection and also to extend the hex connection to run the full thickness of the cam arm, rather than just part of thickness as in the current design. These hex connections should be circumscribed from a 20 mm diameter circle to maximise the contact area and reduce stress.

- At the outset of this study, the turbine developers requested an investigation into the requirement of central support bearing positioned between the generator and turbine, located in a housing at the top disc. The turbine developers had hoped to omit this in order to simplify the assembly process. However, the presented analysis shows that this central support bearing is crucial in order to reduce the bending stresses on the main shaft.

Appendix B: Further Derivations of Fluent Turbulence Models

Appendix B. Further Derivations of Fluent Turbulence Models

The following sections describe the turbulence models discussed in this thesis.

B.1 $k-\varepsilon$ model

The transport equations for k and ε used in the model are:

$$\frac{\partial(\rho k)}{\partial t}+\frac{\partial\left(\rho u_j k\right)}{\partial x_j}=P-\rho\varepsilon+\frac{\partial}{\partial x_j}\left[\left(\mu+\frac{\mu_t}{\sigma_k}\right)\frac{\partial k}{\partial x_j}\right] \tag{B.1}$$

$$\frac{\partial(\rho\varepsilon)}{\partial t}+\frac{\partial\left(\rho u_j \varepsilon\right)}{\partial x_j}=C_{\varepsilon 1}\frac{\varepsilon}{k}P-C_{\varepsilon 2}\,\frac{\rho\varepsilon^2}{k}+\frac{\partial}{\partial x_j}\left[\left(\mu+\frac{\mu_t}{\sigma_\varepsilon}\right)\frac{\partial \varepsilon}{\partial x_j}\right] \tag{B.2}$$

The production term P, is:

$$P=\tau_{ij}\frac{\partial u_i}{\partial x_j} \tag{B.3}$$

where τ_{ij} is the specific Reynolds stress tensor defined as:

$$\tau_{ij}=\mu_t\left(2S_{ij}-\frac{2}{3}\frac{\partial u_k}{\partial x_k}\delta_{ij}\right)-\frac{2}{3}\rho k\delta_{ij} \tag{B.4}$$

and the mean strain rate tensor is given by:

$$S_{ij}=\frac{1}{2}\left(\frac{\partial u_i}{\partial x_j}+\frac{\partial u_j}{\partial x_i}\right) \tag{B.5}$$

Turbulent viscosity is modelled as:

$$\mu_t=\rho C_\mu\frac{k^2}{\varepsilon} \tag{B.6}$$

Table B.1: Default recommended constants for the $k-\varepsilon$ model

$\sigma_k=1.0$	$\sigma_\varepsilon=1.3$	$C_\mu=0.09$	$C_{\varepsilon 1}=1.44$	$C_{\varepsilon 2}=1.92$

B.2 $\mathbf{k-\omega}$ model

The standard $k-\omega$ model included in Fluent is the 1998 revision. The 1998 revised model [169] uses the following transport equations for k and it's specific dissipation rate, ω :

$$\frac{\partial(\rho k)}{\partial t}+\frac{\partial\left(\rho u_j k\right)}{\partial x_j}=P-Y_k+\frac{\partial}{\partial x_j}\left[\left(\mu+\frac{\mu_t}{\sigma_k}\right)\frac{\partial \omega}{\partial x_j}\right] \tag{B.7}$$

$$\frac{\partial(\rho \omega)}{\partial t}+\frac{\partial\left(\rho u_j \omega\right)}{\partial x_j}=\frac{\alpha\omega}{k}P-Y_\omega+\frac{\rho\sigma_d}{\omega}\frac{\partial k}{\partial x_j}\frac{\partial \omega}{\partial x_j}+\frac{\partial}{\partial x_j}\left[\left(\mu+\frac{\mu_t}{\sigma_\omega}\right)\frac{\partial \omega}{\partial x_j}\right] \tag{B.8}$$

P is the production term as defined in Equation (B.3)

The eddy viscosity is then determined using:

$$\mu_t=\alpha^*\frac{\rho k}{\omega} \tag{B.9}$$

The α^*coefficient damps the turbulent viscosity causing a low-Reynolds number correction. It is given by:

$$\alpha^*=\alpha_\infty^*\left(\frac{\alpha_0^*+\frac{Re_t}{Re_k}}{1++\frac{Re_t}{Re_k}}\right) \tag{B.10}$$

where,

$$Re_t=\frac{\rho k}{\mu\omega} \tag{B.11}$$

Note that in the high-Reynolds number form of the $k-\omega$ model, $\alpha^*=\alpha_\infty^*=1$.

The dissipation of k is given by:

$$Y_k=\rho\beta^* f_{\beta^*} k\omega \tag{B.12}$$

where,

$$f_{\beta^*} = \begin{cases} 1 & \chi_k \leq 0 \\ \dfrac{1+680\chi_k^2}{1+400\chi_k^2} & \chi_k > 0 \end{cases} \tag{B.13}$$

$$\chi_k \equiv \frac{1}{\omega^3}\left(\frac{\partial k}{\partial x_j}\frac{\partial \omega}{\partial x_j}\right) \tag{B.14}$$

$$\beta^* = \beta_i^*[1+\zeta^*] \tag{B.15}$$

$$\beta_i^* = \beta_\infty^* \frac{\frac{4}{15}+\left(\frac{Re_t}{Re_\beta}\right)^4}{1+\left(\frac{Re_t}{Re_\beta}\right)^4} \tag{B.16}$$

The dissipation of ω is given by:

$$Y_{k\omega} = \rho\beta f_\beta \omega^2 \tag{B.17}$$

where,

$$f_\beta = \frac{1+70\chi_\omega}{1+80\chi_\omega} \tag{B.18}$$

$$\beta = \beta_i\left[1-\frac{\beta_i^*}{\beta_i}\zeta^*\right] \tag{B.19}$$

$$\beta_i^* = \beta_\infty^* \frac{\frac{4}{15}+\left(\frac{Re_t}{Re_\beta}\right)^4}{1+\left(\frac{Re_t}{Re_\beta}\right)^4} \tag{B.20}$$

Table B.2: Closure coefficients appearing in the $\boldsymbol{k-\omega}$ model

$\alpha_\infty^* = 1$	$\alpha_\infty = 0.52$	$\sigma_k = 2.0$	$\beta_\omega^* = 0.09$	$\beta_i = 0.072$
$\alpha_\infty = 0.11$	$R_\beta = 8$	$\sigma_\omega = 2.0$	$R_k = 6$	$R_\omega = 2.95$
$\zeta^* = 1.5$	$\Omega_{ij} = \frac{\partial u_i}{\partial x_j} - \frac{\partial u_j}{\partial x_i}$	$\chi_\omega = \left\lvert\frac{\Omega_{ij}\Omega_{\mathrm{jk}}\hat{S}_{ki}}{(\beta^*\omega)^3}\right\rvert$		

B.3 $k-\omega$ SST model

The model used in Fluent is the later 2003 version of $k-\omega$ SST model. Menter added a blending function, F_1 into the original definitions of the transport equations for k, and ω, and also multiplied the definitions of k and ε by $(1-F_1)$ to give the following transport equations:

$$\frac{\partial(\rho k)}{\partial t}+\frac{\partial\left(\rho u_j k\right)}{\partial x_j}=P_k-D_k+\frac{\partial}{\partial x_j}\left[(\mu+\sigma_k\mu_t)\frac{\partial k}{\partial x_j}\right] \tag{B.21}$$

$$\begin{aligned}\frac{\partial(\rho\omega)}{\partial t}+\frac{\partial\left(\rho u_j\omega\right)}{\partial x_j}&\\ =\alpha\rho S^2\ -\beta\rho\omega^2+\frac{\partial}{\partial x_j}\left[(\mu+\sigma_\omega\mu_t)\frac{\partial\omega}{\partial x_j}\right]+2(1&\\ -F_1)\frac{\rho\sigma_{\omega2}}{\omega}\frac{\partial k}{\partial x_j}\frac{\partial\omega}{\partial x_j}&\end{aligned} \tag{B.22}$$

where,

$$CD_{k\omega}=\max\left(2\rho\sigma_{\omega2}\frac{1}{\omega}\frac{\partial k}{\partial x_i}\frac{\partial\omega}{\partial x_i},10^{-10}\right) \tag{B.23}$$

The blending function F_1 is defined as:

$$F_1=\tanh[arg_1^4] \tag{B.24}$$

where,

$$arg_1=min\left[max\left(\frac{\sqrt{k}}{\beta^*\omega y},\frac{500\mu}{y^2\omega\rho}\right),\frac{4\rho\sigma_{\omega2}k}{CD_{k\omega}y^2}\right]$$

The definitions of P,τ_{ij} and S_{ij} are the same as defined previously.

ϕ_1 is used to represent any constant in the original Wilcox $k-\omega$ model, ϕ_2 any constant from the $k-\varepsilon$ model. While, ϕ is used to denote any constant of the new model. The relationship between all three is defined as:

$$\phi=\phi_1F_1+\phi_2(1-F_1) \tag{B.25}$$

F_1 is equal to zero away from the wall ($k-\varepsilon$ model), and is equal to one inside the boundary layer $k-\omega$ model.

The turbulent eddy viscosity is defined as follows:

$$\mu_t = \frac{\rho a_1 k}{\max(a_1\omega, SF_2)} \tag{B.26}$$

where $S = \sqrt{2S_{ij}S_{ij}}$ is the invariant measure of the strain rate.

F_2 is a second blending function defined as:

$$F_2 = \tanh[arg_2^2] \tag{B.27}$$

with

$$arg_2 = \max\left(2\frac{\sqrt{k}}{\beta^*\omega y}, \frac{500\mu}{\rho y^2 \omega}\right)$$

A limiter is used to prevent the build-up of turbulence in stagnation regions and is defined as:

$$P = \mu_t \frac{\partial U_i}{\partial x_j}\left(\frac{\partial U_i}{\partial x_j} + \frac{\partial U_j}{\partial x_i}\right) \rightarrow P_k = \min(P, 10 \cdot D_k) \tag{B.28}$$

Table B.3: Closure coefficients for the $k-\omega$ *SST* models

$\sigma_{k1} = 0.85$	$\sigma_{\omega 1} = 0.5$	$\beta^* = 0.09$	$\beta_1 = 0.075$
$\beta_2 = 0.0828$	$\beta = \beta_0 f_\beta$	$\sigma_{\omega 2} = 0.856$	$\sigma_{k2} = 1.0$
$\alpha_1 = \frac{5}{9}$	$\alpha_2 = 0.44$	$D_k = \beta^* \rho k \omega$	

B.4 Transitional SST model.

The Transitional SST model sometimes called the $\gamma - Re\theta t$ SST turbulence model or the Langtry-Menter model after the authors/developers [137,171], is a four-equation model that built on the previous SST model work of Menter. The four transport equations of the model are presented below for k, ω, γ and $\overline{Re}_{\theta t}$ respectively:

$$\frac{\partial(\rho k)}{\partial t} + \frac{\partial\left(\rho u_j k\right)}{\partial x_j} = \tilde{P}_k - \widetilde{D}_k + \frac{\partial}{\partial x_j}\left[(\mu + \sigma_k \mu_t)\frac{\partial k}{\partial x_j}\right] \tag{B.29}$$

$$\frac{\partial(\rho\omega)}{\partial t}+\frac{\partial\left(\rho u_j\omega\right)}{\partial x_j} = \frac{\gamma}{\rho\mu_t}P_k-\beta\rho\omega^2+\frac{\partial}{\partial x_j}\left[(\mu+\sigma_\omega\mu_T)\frac{\partial\omega}{\partial x_j}\right]+2(1-F_1)\frac{\rho\sigma_{\omega2}}{\omega}\frac{\partial k}{\partial x_j}\frac{\partial\omega}{\partial x_j} \tag{B.30}$$

$$\frac{\partial(\rho\gamma)}{\partial t}+\frac{\partial(\rho U u_j\gamma)}{\partial x_j}=P_\gamma-E_\gamma+\frac{\partial}{\partial x_j}\left[\left(\mu+\frac{\mu_t}{\sigma_\gamma}\right)\frac{\partial\gamma}{\partial x_j}\right] \tag{B.31}$$

$$\frac{\partial(\rho\overline{Re}_{\theta t})}{\partial t}+\frac{\partial(\rho u_j\overline{Re}_{\theta t})}{\partial x_j}=P_{\theta t}+\frac{\partial}{\partial x_j}\left[\sigma_{\theta t}(\mu+\mu_t)\frac{\partial\overline{Re}_{\theta t}}{\partial x_j}\right] \tag{B.32}$$

Definitions of the terms, τ_{ij}, S_{ij}, ϕ, F_1, arg_1, S, F_2, arg_2, and $CD_{k\omega}$ are the same as previously defined for the $k-w$ SST model.

Instead of using the momentum thickness Reynolds number to trigger a transition, as other transition models do, the current model is based on the strain-rate Reynolds number, as it contains easily calculable variables in a Navier-Stokes code. The strain-rate Reynolds number is defined as:

$$Re_v=\frac{\rho y^2 S}{\mu} \tag{B.33}$$

The intermittency is used to turn on the production term of the turbulent kinetic energy downstream of the transition point in the boundary layer.

The transition source term is defined as:

$$P_{\gamma1}=F_{length}c_{a1}\rho S[\gamma F_{onset}]^{0.5}(1-c_{e1}\gamma) \tag{B.34}$$

This source term was designed to be equal to zero (due to the F_{onset} function) in the laminar boundary layer upstream of transition and active wherever the local strain rate Reynolds number exceeds the local transition onset criteria. The magnitude of the source term is controlled by the transition function F_{length}. The F_{onset} function is used to trigger the intermittency by activating the source term. It is designed to switch

rapidly from a value of zero in a laminar boundary layer to a value of one downstream of the transition onset. It is formulated as a function of the local strain-rate Reynolds number and the turbulent Reynolds number defined as:

$$R_T = \frac{\rho k}{\mu \omega} \tag{B.35}$$

The following definitions apply for determining the onset function, F_{onset}

$$F_{onset1} = \frac{Re_v}{2.193\, Re_{\theta c}} \tag{B.36}$$

$$F_{onset2} = \min\left(\max\left(F_{onset1}, {F_{onset1}}^4\right), 2.0\right) \tag{B.37}$$

$$F_{onset3} = \max\left(1 - \left(\frac{R_T}{2.5}\right)^3, 0\right) \tag{B.38}$$

$$F_{onset} = \max(F_{onset2} - F_{onset3}, 0) \tag{B.39}$$

The term $Re_{\theta c}$ as used in the definition of F_{onset1} is considered the location where turbulence starts to grow, whereas $Re_{\theta t}$ is the location where the velocity profile initially starts to deviate from a purely laminar flow.

$$Re_{\theta c} = \mathrm{f}(\overline{Re}_{\theta t}) \tag{B.40}$$

F_{length} is an empirical correlation that controls the length of the transition region. Based on numerical experiments. F_{length} and $Re_{\theta c}$ correlations are a strong function of each other. Iteration is required to obtain good agreement between both correlations

$$F_{length} = F_{length,1}\left(1 - F_{sublayer}\right) + 40 F_{sublayer} \tag{B.41}$$

where,

$$F_{length,1} = \begin{cases} 39.8189 + -(119.27 \times 10^{-4})\overline{Re_{\theta t}} + (132.567 \times 10^{-4})\overline{Re_{\theta t}}^{2}, & \overline{Re_{\theta t}} < 400 \\ 263.404 + -(123.939 \times 10^{-2})\overline{Re_{\theta t}} + (194.548 \times 10^{-5})\overline{Re_{\theta t}}^{2} + -(123.939 \times 10^{-2})\overline{Re_{\theta t}}^{3}, & 400 \leq \overline{Re_{\theta t}} < 596 \\ 0.5 - (3 \times 10^{-4}), & 596 \leq \overline{Re_{\theta t}} < 1200 \\ 0.3188, & 1200 \leq \overline{Re_{\theta t}} \end{cases} \quad \text{(B.42)}$$

$$F_{sublayer} = \mathrm{e}^{\left[-\left(\frac{Re_{\omega}}{200}\right)^{2}\right]} \quad \text{(B.43)}$$

The destruction/relaminarization source term is defined as:

$$E_{\gamma} = c_{a2}\rho\Omega\gamma F_{turb}(c_{e2}\gamma - 1) \quad \text{(B.44)}$$

The term acts as a sink term and ensures that the intermittency remains close to zero in the laminar region and one in the free-stream. The constant in the term controls the strength and ensures the entire expression is smaller than that of the transition source term, P_{γ}. F_{turb} is used to disable the destruction/relaminarisation source outside of the laminar boundary layer or in the viscous sublayer and is defined as:

$$F_{turb} = e^{\left[-\left(\frac{R_T}{4}\right)^{4}\right]} \quad \text{(B.45)}$$

The model developers/ research authors report that in order to capture the laminar and transitional boundary layers, the grid must have a $y^{+} \leq 1$. If the y^{+} is too large, the transition onset location moves upstream with increasing y^{+}.

The transition correlations relate the Reynolds number of transition onset, $Re_{\theta t}$ to the turbulence intensity, T_{I} and other quantities in the free-stream where:

$$Re_{\theta t} = f(T_{\mathrm{I}} \ldots\ldots)_{freestream} \quad \text{(B.46)}$$

It should also be noted that the turbulence intensity can change dramatically within a domain and that implementing an initial global value over the entire flow field is inaccurate. The $\overline{Re}_{\theta t}$ transport equation, can be used to resolve this issue. The basic concept is to treat $Re_{\theta t}$ as a transported scalar quantity. An empirical correlation is then used to calculate $Re_{\theta t}$ in the free-stream and let this value diffuse into the

boundary layer. This transport equation removes the non-logical correlation and converts into a local quantity, which is then used to calculate the transition length, F_{length} and the critical Reynolds number, $Re_{\theta c}$. Outside the boundary layer the term $P_{\theta t}$ is constructed to compel the transported scalar $\overline{Re}_{\theta t}$ to match the local value of $Re_{\theta t}$ and is defined as:

$$P_{\theta t} = c_{\theta t}\frac{\rho}{t}(Re_{\theta t} - \overline{Re_{\theta t}})(1.0 - F_{\theta t}) \tag{B.47}$$

where, t, is a time scale and is included for dimensionality reasons and is:

$$t = \frac{500\mu}{\rho U^2} \tag{B.48}$$

where,

$$U = \sqrt{u^2 + v^2 + w^2}$$

The blending function $F_{\theta t}$ is used to switch off the source term in the boundary layer and allow $\overline{Re}_{\theta t}$ diffuse in from the free-stream. $F_{\theta t}$ is equal to zero in the free-stream and to one in the boundary layer, $F_{\theta t}$ is defined as:

$$F_{\theta t} = min\left[\max\left(F_{wake}\,\mathrm{e}^{\left(-\left(\frac{y}{\delta}\right)^4\right)}, 1.0 - \left(\frac{c_{e2}\gamma - 1}{c_{e2} - 1}\right)^2\right), 1.0\right] \tag{B.49}$$

where,

$$\delta = \frac{375\Omega\mu\overline{Re_{\theta t}}y}{\rho U^2} \tag{B.50}$$

$$F_{wake} = e^{\left[-\left(\frac{Re_\omega}{1\times10^5}\right)^2\right]} \tag{B.51}$$

$$Re_\omega = \frac{\rho\omega y^2}{\mu} \tag{B.52}$$

F_{wake} ensures that the blending function is not active in the wake regions downstream of the aerofoil/hydrofoil or blade/wing. The boundary condition for $Re_{\theta t}$ at a wall is zero flux and at the inlet is calculated for an empirical correlation based on the inlet turbulence intensity.

The model developers realised the model consistently predicted the turbulent reattachment location too far downstream. They assumed this was due to the turbulent kinetic energy in the separating shear layer being smaller at lower free-stream turbulence intensities. As a result, it takes longer for k to cause the boundary layer to reattach. To correct this, a modification to the transition model was introduced that allows k to grow rapidly once the laminar boundary layer separates. The modification has been formulated so that it has a negligible effect on the predictions for attached transition or fully turbulent flow. The modification for separation-induced transition is given by:

$$\gamma_{sep} = \min(\mathrm{s}_1 max\left[0, \left(\frac{R_{ev}}{3.235\, Re_{\theta c}}\right) - 1\right](F_{reattach}, 2)F_{\theta t} \tag{B.53}$$

where,

$$\gamma_{eff} = \max(\gamma, \gamma_{sep}) \tag{B.54}$$

$$F_{reattach} = e^{\left[-\left(\frac{R_T}{20}\right)^4\right]} \tag{B.55}$$

The function $F_{reattach}$ disables the modification once the viscosity ratio is large enough for reattachment to occur.

$Re_{\theta t}$ is another empirical correlation, it is the transition onset and defined as:

$$Re_{\theta t} = \begin{cases} (1173.51 - 589.428T_{\mathrm{I}} + 0.2196T_{\mathrm{I}}^{-2})F(\lambda_\theta), & T_{\mathrm{I}} \leq 1.3 \\ (331.50\,(T_{\mathrm{I}} - 0.5658)^{-0.671})F(\lambda_\theta), & T_{\mathrm{I}} \leq 1.3 \end{cases} \tag{B.56}$$

where,

$$F(\lambda_\theta) = \begin{cases} 1 + [12.986\lambda_\theta + 12.986\lambda_\theta^2 + 12.986\lambda_\theta^3]\,\mathrm{e}^{\left(-\frac{T_{\mathrm{I}}}{1.5}^{1.5}\right)}, & \lambda_\theta \leq 0 \\ 1 + 0.275[1 - \exp(-35.0\lambda_\theta)]\,\mathrm{e}^{\left(-\frac{T_{\mathrm{I}}}{0.5}^{1.5}\right)}, & \lambda_\theta > 0 \end{cases} \tag{B.57}$$

with Thwaites' pressure gradient coefficient defined as:

$$\lambda_\theta = \frac{\rho\theta_t^2}{\mu}\frac{dU}{ds} \tag{B.58}$$

The third and final empirical correlation in the model $Re_{\theta c}$, it is the point where the model is activated in order to match both, $Re_{\theta t}$ and F_{length}

$$Re_{\theta c} = \begin{cases} [(-396.035\times10^{-2}) + (10120.656\times10^{-4})\overline{Re_{\theta t}} + \left(-868.10\times10^{-6}\overline{Re_{\theta t}}^{2}\right) \\ +(696.506\times10^{-6})\overline{Re_{\theta t}}^{3} + (-174.105\times10^{-12})\overline{Re_{\theta t}}^{4}\,] & \overline{Re_{\theta t}} \le 1870, \\ \left[\overline{Re_{\theta t}} - \left(593.11 + 0.483(\overline{Re_{\theta t}} - 1870)\right)\right] & \overline{Re_{\theta t}} > 1870 \end{cases} \tag{B.59}$$

The model developers+ report that for numerical robustness, the acceleration parameters, the turbulence intensity, and the empirical correlation should be limited as follows:

$$-0.1 \le \lambda_\theta \le 0.1 \quad T_{\mathrm{I}} \ge 0.027 \quad Re_{\theta t} \ge 20$$

Table B.4: The Transition SST model specific coefficients

$C_{a1} = 2.0$	$C_{a2} = 0.06$	$C_{e1} = 1.0$	$C_{e2} = 50$	a_1 =0.31
$C_{\theta t} = 0.03$	$s_1 = 2.0$	$\sigma_f = 1.0$	$\sigma_{\theta t} = 2.0$	

Note all other coefficients are taken from the $k-\omega$ SST model.

The turbulent eddy viscosity is defined as follows:

$$\mu_t = \min\left[\frac{\rho k}{\omega}; \frac{a_1\rho k}{SF_2}\right] \tag{B.60}$$

A modification has also been made to the production term, P_k, and the destruction term, D_k, of the turbulent kinetic energy equation from the $k-\omega$ SST model, in that effective intermittency, γ_{eff} was added in order to control the source terms in the k-equation as follows:

$$\tilde{P}_k = \gamma_{eff} P_k$$
$$\widetilde{D}_k = \min(\max(\gamma_{eff}, 0.1), 1.0) D_k \quad \text{(B.61)}$$

The final modification to the $k-\omega$ SST model was a change in the blending function F_1 used to switch between the $k-\omega$ and $k-\varepsilon$ models. It was identified that in the centre of the laminar boundary layer F_1 could potentially switch from 1.0 to 0.0. This is not desirable, as the $k-\omega$ model must be active in the laminar and transitional boundary layers. The solution was to redefine F_1 in terms of a blending function that will always be equal to 1.0 in a laminar boundary layer. The modified blending function is defined as:

$$F_1 = \max(F_{1orig}, F_3) \quad \text{(B.62)}$$

where

$$F_3 = \mathrm{e}^{\left[-\left(\frac{R_y}{120}\right)^8\right]} \quad \text{(B.63)}$$

and,

$$R_y = \frac{\rho y \sqrt{k}}{\mu} \quad \text{(B.64)}$$

The function F_{1orig} is the original blending function from the SST turbulence model.

Appendix C: 1:10 Experimental Performance Result Tables.

Appendix C 1:10 Scale Experimental Performance

The following sections present tables of time-averaged efficiencies for each turbine. It should be noted that in the tables, a Versalog (Versa.) efficiency of 0* means that strain gauge data was not available at that time. Presented in Section A.1. is the performance results evaluated using ADCP data. However, in the results presented in Section A.2, ADCP data was unavailable and instead, the tow speed from the winch was used to evaluate performance.

C.1 1:10 Scale Device Performance Evaluated using ADCP Data.

Date	Tow	Time (mins)	Vel Mag (m/s)	T1 RPM	% Eff. Versa T1	% Eff. PLC T1	T2 RPM	% Eff. Versa T2	% Eff. PLC T2
30-8-17	Tow1	1	1.11	25.12	8.55	1	25.56	8.64	1.15
30-8-17	Tow1	2	1.15	23.14	8.78	3.02	23.68	8.94	2.77
30-8-17	Tow1	3	1.12	21.53	9.53	3.72	21.9	10.58	4.15
30-8-17	Tow1	4	1.11	20.14	10.76	6.8	21.03	12.48	4.87
30-8-17	Tow1	5	1.14	19.11	10.49	7.47	20.21	12.98	6.6

Date	Tow	Time (mins)	Vel Mag (m/s)	T1 RPM	% Eff. Versa T1	% Eff. PLC T1	T2 RPM	% Eff. Versa T2	% Eff. PLC T2
30-8-17	Tow2	1	1.11	24.68	9.05	2.3	25	9.18	0.78
30-8-17	Tow2	2	1.15	21.78	9.76	3.7	22.12	10.29	4.03
30-8-17	Tow2	3	1.12	19.69	10.73	5.83	19.8	10.76	5.15
30-8-17	Tow2	4	1.11	18.11	11.85	6.67	18.23	12.47	6.31
30-8-17	Tow2	5	1.14	17.36	11.68	7.39	17.36	11.67	8.08
30-8-17	Tow2	6	0.98	15.95	12.48	8.89	16.02	12.7	9.02

Date	Tow	Time (mins)	Vel Mag (m/s)	T1 RPM	% Eff. Versa T1	% Eff. PLC T1	T2 RPM	% Eff. Versa T2	% Eff. PLC T2
30-8-17	Tow3	1	1.18	24.5	7.34	2.54	24.81	6.88	1.11
30-8-17	Tow3	2	1.19	21.96	8.81	3.57	22.25	7.86	4.49
30-8-17	Tow3	3	1.1	18.44	11.43	7.04	18.66	12.55	7.84
30-8-17	Tow3	4	1.08	16.21	13.51	11.09	16.36	13.72	10.18
30-8-17	Tow3	5	1.13	14.41	11.62	8.79	14.5	11.8	8.17

Date	Tow	Time (mins)	Vel Mag (m/s)	T1 RPM	% Eff. Versa T1	% Eff. PLC T1	T2 RPM	% Eff. Versa T2	% Eff. PLC T2
30-8-17	Tow4	1	1.16	23.81	7.23	2.82	24.69	6.89	1.92
30-8-17	Tow4	2	1.15	20.28	8.57	4.81	21.16	9.42	4.03
30-8-17	Tow4	3	1.07	17.41	12.17	8.21	17.91	12.26	8.18
30-8-17	Tow4	4	1.12	15.48	10.59	6.86	16.9	12.47	7.63
30-8-17	Tow4	5	1.14	15.99	10.98	7.52	15.98	10.3	7.43

Date	Tow	Time (mins)	Vel Mag (m/s)	T1 RPM	% Eff. Versa T1	% Eff. PLC T1	T2 RPM	% Eff. Versa T2	% Eff. PLC T2
30-8-17	Tow5	1	1.11	25.64	7.85	0.84	25.87	6.18	1.46
30-8-17	Tow5	2	1.09	21.41	10.49	3.63	21.89	10.29	5.91
30-8-17	Tow5	3	1.01	17.92	15.51	10.84	17.96	13.49	7.79
30-8-17	Tow5	4	1.02	17.11	15.35	10.64	17.22	14.2	8.89
30-8-17	Tow5	5	1.03	16.46	15.54	10.45	16.58	14.3	11.08
30-8-17	Tow5	6	0.98	15.79	15.94	11.16	15.72	14.9	11.58

Date	Tow	Time (mins)	Vel Mag (m/s)	T1 RPM	% Eff. Versa T1	% Eff. PLC T1	T2 RPM	% Eff. Versa T2	% Eff. PLC T2
30-8-17	Tow6	1	1.16	24.41	7.24	2.18	24.74	5.79	2.31
30-8-17	Tow6	2	1.16	21.31	7.9	3.54	21.74	6.95	3.85
30-8-17	Tow6	3	1.08	18.1	11.5	7.19	18.32	11.09	8.23
30-8-17	Tow6	4	1.09	16.07	12.21	8.79	16.42	11.31	8.4
30-8-17	Tow6	5	1.18	14.43	10.21	7.47	14.51	8.9	7.92

Date	Tow	Time (mins)	Vel Mag (m/s)	T1 RPM	% Eff. Versa T1	% Eff. PLC T1	T2 RPM	% Eff. Versa T2	% Eff. PLC T2
30-8-17	Tow7	1	1.04	18.57	14.09	8.6	18.61	12.51	7.86
30-8-17	Tow7	2	1.12	17.75	12.14	7.95	17.79	11.18	7.87
30-8-17	Tow7	3	1.1	17.5	12.98	8.2	17.45	11.6	10.25
30-8-17	Tow7	4	1.06	17.03	12.72	7.68	17.15	11.38	7.22
30-8-17	Tow7	5	1.09	16.75	12.15	7.43	16.73	10.12	8.05
30-8-17	Tow7	6	1.03	16.28	12.38	8.03	16.23	10.28	8.27

Date	Tow	Time (mins)	Vel Mag (m/s)	T1 RPM	% Eff. Versa T1	% Eff. PLC T1	T2 RPM	% Eff. Versa T2	% Eff. PLC T2
30-8-17	Tow8	1	1.19	22.21	9.11	3.34	22.8	8.17	2.51
30-8-17	Tow8	2	1.15	17.89	15.34	7.55	18.15	12	7.9
30-8-17	Tow8	3	1.06	16.44	20.14	10.96	16.51	15.59	11.28
30-8-17	Tow8	4	1.08	16.16	17.42	9.03	16.2	13.4	9.66
30-8-17	Tow8	5	1.13	15.77	14.82	8.04	15.8	11.28	7.9

Date	Tow	Time (mins)	Vel Mag (m/s)	T1 RPM	% Eff. Versa T1	% Eff. PLC T1	T2 RPM	% Eff. Versa T2	% Eff. PLC T2
30-8-17	Tow9	1	1.16	20.55	10.53	4.37	21.27	8.32	4.18
30-8-17	Tow9	2	1.18	15.51	13.59	7.63	15.83	10.22	8.28
30-8-17	Tow9	3	1.19	15.28	14.74	8.64	15.32	10.17	8.57
30-8-17	Tow9	4	1.15	14.91	16.08	9	14.99	11.74	9.3
30-8-17	Tow9	5	1.2	14.63	13.75	6.97	14.72	9.49	8.07
30-8-17	Tow9	6	1.09	13.02	14.62	8.57	13.02	9.43	7.46

Date	Tow	Time (mins)	Vel Mag (m/s)	T1 RPM	% Eff. Versa T1	% Eff. PLC T1	T2 RPM	% Eff. Versa T2	% Eff. PLC T2
30-8-17	Tow10	1	1.2	21.79	9.1	3.32	22.53	7.12	1.98
30-8-17	Tow10	2	1.23	17.19	12.03	6.67	17.69	9.28	6.8
30-8-17	Tow10	3	1.14	13.55	15.2	8.81	13.49	10.74	9.47
30-8-17	Tow10	4	1.09	13.26	17.7	10.33	13.25	12.57	10.3
30-8-17	Tow10	5	1.16	12.92	14.43	8.49	12.97	10.46	8.46
30-8-17	Tow10	6	1.08	12.66	14.76	8.73	12.65	10.52	8.88

Date	Tow	Time (mins)	Vel Mag (m/s)	T1 RPM	% Eff. Versa T1	% Eff. PLC T1	T2 RPM	% Eff. Versa T2	% Eff. PLC T2
30-8-17	Tow11	1	1.17	19.27	7.58	5.76	20.17	5.65	5.61
30-8-17	Tow11	2	1.2	15.77	15.01	7.49	15.81	9.89	8.26
30-8-17	Tow11	3	1.22	8.64	7.13	4.12	15.64	8.95	7.21
30-8-17	Tow11	4	1.17	3.17	3.42	1.98	15.35	7.46	9.1
30-8-17	Tow11	5	1.19	15.61	15.36	8.76	15.5	9.66	9.29
30-8-17	Tow11	6	1.21	9.99	10.68	8.21	10.08	8.77	5.86

Date	Tow	Time (mins)	Vel Mag (m/s)	T1 RPM	% Eff. Versa T1	% Eff. PLC T1	T2 RPM	% Eff. Versa T2	% Eff. PLC T2
1-9-17	Tow1	1	1.12	22.03	11.89	5.88	23.09	12.18	3.44
1-9-17	Tow1	2	1.19	17.58	13.71	6.39	18.1	11.82	6.93
1-9-17	Tow1	3	1.13	16.39	16.47	8.26	16.62	13.34	8.83
1-9-17	Tow1	4	1.05	16.17	20.43	11.41	16.33	16.78	11.03
1-9-17	Tow1	5	1.03	15.95	21.54	11.12	16.06	17.5	11.76

Date	Tow	Time (mins)	Vel Mag (m/s)	T1 RPM	% Eff. Versa T1	% Eff. PLC T1	T2 RPM	% Eff. Versa T2	% Eff. PLC T2
1-9-17	Tow2	1	1.08	20.38	18.54	7.33	21.42	16.51	6.72
1-9-17	Tow2	2	1.03	16.61	20.9	10.21	16.79	16.33	11.15
1-9-17	Tow2	3	1.05	16.51	20.51	11.1	16.48	16.39	11.26
1-9-17	Tow2	4	1.06	16.17	19.17	10.09	16.14	14.77	10.25
1-9-17	Tow2	5	1.13	15.76	15.32	7.7	15.81	11.91	8.21

Date	Tow	Time (mins)	Vel Mag (m/s)	T1 RPM	% Eff. Versa T1	% Eff. PLC T1	T2 RPM	% Eff. Versa T2	% Eff. PLC T2
1-9-17	Tow3	1	1.15	24	11.15	2.5	24.84	10.33	4.01
1-9-17	Tow3	2	1.17	17.39	13.51	7.63	18.21	11.87	6.51
1-9-17	Tow3	3	1.05	16.33	19.11	10.82	16.42	14.51	10.91
1-9-17	Tow3	4	1.04	16	19.76	10.93	16.06	14.88	10.89
1-9-17	Tow3	5	1.04	15.74	20.16	10.38	15.78	15.08	11.27

Date	Tow	Time (mins)	Vel Mag (m/s)	T1 RPM	% Eff. Versa T1	% Eff. PLC T1	T2 RPM	% Eff. Versa T2	% Eff. PLC T2
1-9-17	Tow4	1	1.37	28.21	10.86	3.98	28.21	8.21	4.87
1-9-17	Tow4	2	1.23	24.23	7.06	1.6	24.84	5.39	1.71
1-9-17	Tow4	3	1.06	20.47	10.93	2.67	20.74	7.47	2.98
1-9-17	Tow4	4	1.02	18.39	11.57	4.22	18.76	8.96	3.75
1-9-17	Tow4	5	0.96	16.63	14.72	5.74	16.82	10.78	6.44

Date	Tow	Time (mins)	Vel Mag (m/s)	T1 RPM	% Eff. Versa T1	% Eff. PLC T1	T2 RPM	% Eff. Versa T2	% Eff. PLC T2
1-9-17	Tow5	1	1.34	28.07	5.73	4.21	28.71	3.73	4.82
1-9-17	Tow5	2	1.26	24.29	9.72	0.1	24.76	6.24	0.14
1-9-17	Tow5	3	1.13	22.37	5.93	0.07	22.76	5.98	0.1

Date	Tow	Time (mins)	Vel Mag (m/s)	T1 RPM	% Eff. Versa T1	% Eff. PLC T1	T2 RPM	% Eff. Versa T2	% Eff. PLC T2
1-9-17	Tow6	1	1.38	27.63	5	1.76	27.62	0*	1.13
1-9-17	Tow6	2	1.21	22.68	5.21	0.08	22.68	0*	0.18
1-9-17	Tow6	3	0.98	21.04	8.18	-0.21	21.48	0*	0.36
1-9-17	Tow6	4	0.97	20.05	8.52	0.6	20.44	0*	0.24
1-9-17	Tow6	5	1.03	18.46	6.15	1.23	18.14	0*	2.25
1-9-17	Tow6	6	0.97	15.61	3.53	2.12	7.55	0*	0

Date	Tow	Time (mins)	Vel Mag (m/s)	T1 RPM	% Eff. Versa T1	% Eff. PLC T1	T2 RPM	% Eff. Versa T2	% Eff. PLC T2
1-9-17	Tow7	1	1.18	24.71	13.17	0.66	24.71	0*	3.91
1-9-17	Tow7	2	0.97	22.24	8.08	0.15	22.24	0*	0.12
1-9-17	Tow7	3	0.93	21.26	9.43	0.35	21.26	0*	0.93
1-9-17	Tow7	4	0.93	20.06	8.66	0.09	20.06	0*	0.32
1-9-17	Tow7	5	0.98	19.06	6.62	0.04	19.06	0*	0.31
1-9-17	Tow7	6	0.86	18.39	7.17	0.5	18.39	0*	0.53

Date	Tow	Time (mins)	Vel Mag (m/s)	T1 RPM	% Eff. Versa T1	% Eff. PLC T1	T2 RPM	% Eff. Versa T2	% Eff. PLC T2
4-9-17	Tow1	1	1.21	28.19	6.12	2.78	28.58	8.07	3.86
4-9-17	Tow1	2	0.94	21.54	5.37	-0.28	22.11	7.16	0.04
4-9-17	Tow1	3	0.87	20.29	6.34	-0.19	20.74	8.36	0.19
4-9-17	Tow1	4	0.83	19.05	6.71	-0.2	19.48	8.94	0.27
4-9-17	Tow1	5	0.86	19.12	5.79	-0.19	19.12	7.8	0.09
4-9-17	Tow1	6	0.83	18.43	6.14	-0.1	18.85	7.94	0.1

Date	Tow	Time (mins)	Vel Mag (m/s)	T1 RPM	% Eff. Versa T1	% Eff. PLC T1	T2 RPM	% Eff. Versa T2	% Eff. PLC T2
4-9-17	Tow2	1	1.24	27.33	9.31	4.17	27.51	0*	4.25
4-9-17	Tow2	2	1.01	25.66	7.03	2.97	25.73	0*	2.73
4-9-17	Tow2	3	0.97	23.73	5.9	-0.2	24.15	0*	0.42
4-9-17	Tow2	4	0.96	22.23	6.55	-0	22.68	0*	0.52
4-9-17	Tow2	5	0.93	20.42	8.81	1.7	20.6	0*	2.69
4-9-17	Tow2	6	0.85	18.56	9.89	2.18	18.66	0*	3.05

Date	Tow	Time (mins)	Vel Mag (m/s)	T1 RPM	% Eff. Versa T1	% Eff. PLC T1	T2 RPM	% Eff. Versa T2	% Eff. PLC T2
4-9-17	Tow3	1	1.24	21.45	14.6	9.24	21.52	0*	9.09
4-9-17	Tow3	2	1.15	21.35	12.05	10.29	21.37	0*	9.25
4-9-17	Tow3	3	1.03	20.63	12.76	8.77	20.51	0*	8.55
4-9-17	Tow3	4	0.97	20.7	9.01	3.55	20.93	0*	2.83

Date	Tow	Time (mins)	Vel Mag (m/s)	T1 RPM	% Eff. Versa T1	% Eff. PLC T1	T2 RPM	% Eff. Versa T2	% Eff. PLC T2
4-9-17	Tow4	1	1.29	20.85	13.67	8.12	20.98	0*	8.49
4-9-17	Tow4	2	1.29	20.88	14.47	12.58	20.86	0*	11.87
4-9-17	Tow4	3	1.28	20.39	14.23	12.45	20.32	0*	11.63
4-9-17	Tow4	4	1.28	20.17	14.31	12.7	20.13	0*	12.07
4-9-17	Tow4	5	1.21	19.85	15.97	12.47	20.01	0*	12.65

Date	Tow	Time (mins)	Vel Mag (m/s)	T1 RPM	% Eff. Versa T1	% Eff. PLC T1	T2 RPM	% Eff. Versa T2	% Eff. PLC T2
4-9-17	Tow5	1	1.27	21.3	12.31	7.92	21.3	0*	7.8
4-9-17	Tow5	2	1.27	21.62	12.53	12.24	21.62	0*	8.85
4-9-17	Tow5	3	1.25	21.62	13.44	12.29	21.62	0*	8.73
4-9-17	Tow5	4	1.24	20.94	13.58	10.08	20.94	0*	11.5
4-9-17	Tow5	5	1.24	20.75	13.71	11.1	20.75	0*	11.68

Date	Tow	Time (mins)	Vel Mag (m/s)	T1 RPM	% Eff. Versa T1	% Eff. PLC T1	T2 RPM	% Eff. Versa T2	% Eff. PLC T2
4-9-17	Tow6	1	1.29	20.21	0	10.97	20.21	13.95	10.67
4-9-17	Tow6	2	1.28	19.82	0	10.62	19.82	15.01	11.57
4-9-17	Tow6	3	1.26	19.48	0	14.08	19.48	15.27	10.89
4-9-17	Tow6	4	1.26	19.27	0	12.62	19.27	14.75	11.95
4-9-17	Tow6	5	1.25	18.93	0	13.14	18.93	15.58	12.32

Date	Tow	Time (mins)	Vel Mag (m/s)	T1 RPM	% Eff. Versa T1	% Eff. PLC T1	T2 RPM	% Eff. Versa T2	% Eff. PLC T2
4-9-17	Tow7	1	1.3	18.91	0*	9.79	18.91	13.77	10.71
4-9-17	Tow7	2	1.28	18.88	0*	12.1	18.88	14.53	11.53
4-9-17	Tow7	3	1.31	18.63	0*	11.48	18.63	14.82	11.82
4-9-17	Tow7	4	1.28	15.22	0*	13.1	15.22	13.34	13.09

Date	Tow	Time (mins)	Vel Mag (m/s)	T1 RPM	% Eff. Versa T1	% Eff. PLC T1	T2 RPM	% Eff. Versa T2	% Eff. PLC T2
6-9-17	Tow1	1	1.5	31.14	4.17	7.24	31.56	12.44	5.95
6-9-17	Tow1	2	1.5	29.97	11.74	10.3	29.96	12.78	10.22
6-9-17	Tow1	3	1.47	28.01	14.03	10.27	28.17	14	10.29
6-9-17	Tow1	4	1.44	27.05	14.96	10.28	26.99	14.38	9.72

Date	Tow	Time (mins)	Vel Mag (m/s)	T1 RPM	% Eff. Versa T1	% Eff. PLC T1	T2 RPM	% Eff. Versa T2	% Eff. PLC T2
6-9-17	Tow2	1	1.52	32.41	7.78	4.9	33.89	9.79	5.28
6-9-17	Tow2	2	1.5	27.01	12.52	10.59	27.1	13.64	11.14
6-9-17	Tow2	3	1.45	25.01	13.24	11.59	25.15	14.78	11.42
Date	Tow	Time (mins)	Vel Mag (m/s)	T1 RPM	% Eff. Versa T1	% Eff. PLC T1	T2 RPM	% Eff. Versa T2	% Eff. PLC T2
6-9-17	Tow3	1	1.51	29.89	10.22	7.85	30.12	11.67	8.04
6-9-17	Tow3	2	1.49	24.21	12.91	12.67	24.57	14.51	11.36
6-9-17	Tow3	3	1.44	22.33	13.9	12.67	22.38	15.58	13.03

Date	Tow	Time (mins)	Vel Mag (m/s)	T1 RPM	% Eff. Versa T1	% Eff. PLC T1	T2 RPM	% Eff. Versa T2	% Eff. PLC T2
6-9-17	Tow4	1	1.5	27.29	12.49	8.34	27.77	14.67	7.86
6-9-17	Tow4	2	1.54	23.83	13.12	11.24	23.79	14.13	10.78
6-9-17	Tow4	3	1.48	23.05	14.2	13.72	23.04	15.6	13.18
6-9-17	Tow4	4	1.45	22.27	14.6	13.52	22.33	15.92	13.46

Date	Tow	Time (mins)	Vel Mag (m/s)	T1 RPM	% Eff. Versa T1	% Eff. PLC T1	T2 RPM	% Eff. Versa T2	% Eff. PLC T2
6-9-17	Tow5	1	1.5	28.08	12.4	8.84	28.46	13.97	7.66
6-9-17	Tow5	2	1.49	24.1	14.14	12.25	24.12	15.3	11.78
6-9-17	Tow5	3	1.46	23.18	14.64	13.8	23.38	16.17	12.92
6-9-17	Tow5	4	1.44	22.65	14.7	13.25	22.63	15.94	13.05

Date	Tow	Time (mins)	Vel Mag (m/s)	T1 RPM	% Eff. Versa T1	% Eff. PLC T1	T2 RPM	% Eff. Versa T2	% Eff. PLC T2
6-9-17	Tow6	1	1.51	27.31	13	9.01	27.85	14.83	8.64
6-9-17	Tow6	2	1.51	23.89	13.53	12.27	24.05	14.66	12.41
6-9-17	Tow6	3	1.47	23.15	14.04	12.01	23.18	15.51	12.75
6-9-17	Tow6	4	1.32	22.43	14.9	12.52	22.43	16.28	12.96

Date	Tow	Time (mins)	Vel Mag (m/s)	T1 RPM	% Eff. Versa T1	% Eff. PLC T1	T2 RPM	% Eff. Versa T2	% Eff. PLC T2
6-9-17	Tow7	1	1.5	27.33	13.11	8.36	27.85	14.59	8.58
6-9-17	Tow7	2	1.52	23.89	13.35	11.82	23.92	14.37	11.78
6-9-17	Tow7	3	1.47	23.03	14.17	12.94	23.03	14.56	12.37
6-9-17	Tow7	4	1.45	22.38	14.63	12.64	22.49	15.56	13.35

Date	Tow	Time (mins)	Vel Mag (m/s)	T1 RPM	% Eff. Versa T1	% Eff. PLC T1	T2 RPM	% Eff. Versa T2	% Eff. PLC T2
6-9-17	Tow8	1	1.64	36.88	8.17	5.99	37.17	9.05	5.3
6-9-17	Tow8	2	1.61	32.56	11.03	7.98	33.4	12.53	8.96
6-9-17	Tow8	3	1.6	29.14	12.2	10.42	29.94	13.92	11.42

Date	Tow	Time (mins)	Vel Mag (m/s)	T1 RPM	% Eff. Versa T1	% Eff. PLC T1	T2 RPM	% Eff. Versa T2	% Eff. PLC T2
6-9-17	Tow9	1	1.64	31.85	10.98	7.45	32.3	11.95	9.03
6-9-17	Tow9	2	1.61	28.98	13.99	12.7	29.03	14.37	12.04
6-9-17	Tow9	3	1.6	26.88	14.36	12.64	26.99	14.96	12.99

Date	Tow	Time (mins)	Vel Mag (m/s)	T1 RPM	% Eff. Versa T1	% Eff. PLC T1	T2 RPM	% Eff. Versa T2	% Eff. PLC T2
15-9-17	Tow1	1	0.69	9.63	14.73	5.19	9.61	15.09	7.01
15-9-17	Tow1	2	0.68	9.54	13.56	4	9.53	13.85	5.09
15-9-17	Tow1	3	0.67	9.53	12.73	2.64	9.54	13.49	4.79
15-9-17	Tow1	4	0.66	9.53	13.14	2.87	9.53	13.65	3.08
15-9-17	Tow1	5	0.66	9.53	12.27	1.54	9.54	13.61	2.61
15-9-17	Tow1	6	0.65	9.5	12.2	2.02	9.52	13.9	3.43
15-9-17	Tow1	7	0.66	9.54	11.77	2.59	9.59	13.64	3.79
15-9-17	Tow1	8	0.66	9.54	13.26	2.49	9.56	14.44	4.35
15-9-17	Tow1	9	0.67	9.5	14.15	3.06	9.49	14.2	5.81

Date	Tow	Time (mins)	Vel Mag (m/s)	T1 RPM	% Eff. Versa T1	% Eff. PLC T1	T2 RPM	% Eff. Versa T2	% Eff. PLC T2
15-9-17	Tow2	1	0.71	8.14	12.79	4.84	8.43	14.35	6.5
15-9-17	Tow2	2	0.67	10.03	13.68	3.87	10.07	15.36	4.4
15-9-17	Tow2	3	0.66	10.04	12.93	2.75	10.07	11.29	3.69
15-9-17	Tow2	4	0.66	10.09	12.12	2.67	10.06	11.17	3.9
15-9-17	Tow2	5	0.66	10	12.76	1.78	10.06	11.32	2.96
15-9-17	Tow2	6	0.67	10	10.04	1.64	10.03	10.61	2.25
15-9-17	Tow2	7	0.67	10.06	10.88	1.68	10.03	10.79	2.34
15-9-17	Tow2	8	0.66	8.73	10.17	1.45	8.68	9.08	2.32

Date	Tow	Time (mins)	Vel Mag (m/s)	T1 RPM	% Eff. Versa T1	% Eff. PLC T1	T2 RPM	% Eff. Versa T2	% Eff. PLC T2
15-9-17	Tow3	1	0.66	9.67	13.36	2.45	9.91	14.18	3.71
15-9-17	Tow3	2	0.66	10.43	12.92	1.34	10.56	13.5	2.9
15-9-17	Tow3	3	0.66	10.46	11.69	1.04	10.56	12.47	1.62
15-9-17	Tow3	4	0.65	10.43	11.37	1.39	10.52	12.64	1.6
15-9-17	Tow3	5	0.65	10.38	11.95	1.51	10.51	12.64	1.7
15-9-17	Tow3	6	0.64	10.48	11.62	0.71	10.52	13.15	1.62
15-9-17	Tow3	7	0.65	10.35	11.32	0.57	10.51	12.31	2.29
15-9-17	Tow3	8	0.64	10.44	11.53	1.38	10.49	12.69	0.98
15-9-17	Tow3	9	0.64	10.45	12.09	1.89	10.53	12.66	1.37

Date	Tow	Time (mins)	Vel Mag (m/s)	T1 RPM	% Eff. Versa T1	% Eff. PLC T1	T2 RPM	% Eff. Versa T2	% Eff. PLC T2
15-9-17	Tow4	1	0.85	9.48	10.95	5.17	9.52	11.15	6.35
15-9-17	Tow4	2	0.84	12.68	14.18	8.84	12.55	14.78	8.45
15-9-17	Tow4	3	0.83	12.56	14.18	7.37	12.59	15.48	9.51
15-9-17	Tow4	4	0.83	12.5	13.42	6.58	12.6	14.74	8.23
15-9-17	Tow4	5	0.84	12.65	13.24	8.56	12.62	14.45	7.35
15-9-17	Tow4	6	0.85	12.67	13.35	8.62	12.57	14.22	7.69
15-9-17	Tow4	7	0.82	12.64	13.79	8.79	12.49	15.07	8.76

Date	Tow	Time (mins)	Vel Mag (m/s)	T1 RPM	% Eff. Versa T1	% Eff. PLC T1	T2 RPM	% Eff. Versa T2	% Eff. PLC T2
18-9-17	Tow1	1	0.89	10.72	12.11	5.6	11.03	13.14	7.52
18-9-17	Tow1	2	0.88	13.08	14.5	7.44	13.11	15.43	8.77
18-9-17	Tow1	3	0.87	13.12	14.19	6.58	13.07	14.55	7.05
18-9-17	Tow1	4	0.87	13.16	14.8	7.2	13.07	14.54	7.73
18-9-17	Tow1	5	0.87	13.07	14.39	6.96	13.13	15.35	7.75
18-9-17	Tow1	6	0.88	13.1	14.32	6.87	13.08	15.14	7.47
18-9-17	Tow1	7	0.82	13.11	14.47	7.26	13.16	15.73	7.82

Date	Tow	Time (mins)	Vel Mag (m/s)	T1 RPM	% Eff. Versa T1	% Eff. PLC T1	T2 RPM	% Eff. Versa T2	% Eff. PLC T2
18-9-17	Tow2	1	0.88	13.31	14.13	7.95	13.24	14.11	6.6
18-9-17	Tow2	2	0.86	13.54	13.9	7.7	13.54	14	5.18
18-9-17	Tow2	3	0.85	13.6	13.79	6.37	13.6	14.21	4.5
18-9-17	Tow2	4	0.84	13.58	14.21	2.16	13.7	14.28	6.02
18-9-17	Tow2	5	0.85	13.75	14.04	6.08	13.69	14.41	8.02
18-9-17	Tow2	6	0.85	13.63	13.6	7.78	13.63	14	8.5
18-9-17	Tow2	7	0.85	13.59	14.07	7.09	13.55	14.04	7.6

Date	Tow	Time (mins)	Vel Mag (m/s)	T1 RPM	% Eff. Versa T1	% Eff. PLC T1	T2 RPM	% Eff. Versa T2	% Eff. PLC T2
18-9-17	Tow3	1	1.04	15.26	14.48	9.87	15.63	15.26	10.02
18-9-17	Tow3	2	1.04	15.1	14.25	10.42	15.08	15.15	10.7
18-9-17	Tow3	3	1.03	15.15	14.6	10.57	15.09	14.69	10.81
18-9-17	Tow3	4	1.03	15.09	14.83	9.88	15.09	15.11	11.16
18-9-17	Tow3	5	1.03	15.06	14.14	9.94	15.09	15.02	10.54
18-9-17	Tow3	6	0.95	14.09	14.34	9.62	14.08	15.94	11.02

Date	Tow	Time (mins)	Vel Mag (m/s)	T1 RPM	% Eff. Versa T1	% Eff. PLC T1	T2 RPM	% Eff. Versa T2	% Eff. PLC T2
18-9-17	Tow4	1	1.25	18.18	13.52	10.67	18.2	14.47	10.65
18-9-17	Tow4	2	1.25	18.16	14.96	12.82	18.19	16.27	12.57
18-9-17	Tow4	3	1.24	18.14	14.81	11.79	18.21	15.47	12.95
18-9-17	Tow4	4	1.24	18.18	14.97	12.57	18.18	15.8	12.59

Date	Tow	Time (mins)	Vel Mag (m/s)	T1 RPM	% Eff. Versa T1	% Eff. PLC T1	T2 RPM	% Eff. Versa T2	% Eff. PLC T2
18-9-17	Tow5	1	1.45	23.47	14.29	10.01	23.47	16.28	10.02
18-9-17	Tow5	2	1.44	23.35	14.71	12.55	23.48	16.64	13.1
18-9-17	Tow5	3	1.44	23.38	14.24	12.84	23.46	15.85	12.71
18-9-17	Tow5	4	1.32	23.53	15.02	12.67	23.4	16.24	12.93

Date	Tow	Time (mins)	Vel Mag (m/s)	T1 RPM	% Eff. Versa T1	% Eff. PLC T1	T2 RPM	% Eff. Versa T2	% Eff. PLC T2
18-9-17	Tow6	1	1.62	25.91	11.77	9.41	26.02	13.34	8.83
18-9-17	Tow6	2	1.62	26.16	15.82	13.4	26.14	16.28	13.53
18-9-17	Tow6	3	1.46	26.28	16.69	14.17	26.2	17.91	14.98

Date	Tow	Time (mins)	Vel Mag (m/s)	T1 RPM	% Eff. Versa T1	% Eff. PLC T1	T2 RPM	% Eff. Versa T2	% Eff. PLC T2
18-9-17	Tow7	1	1.77	25.87	12.04	10.55	26.12	13.81	10
18-9-17	Tow7	2	1.74	26.13	15.49	14.51	26.18	17.1	14.5
18-9-17	Tow7	3	1.61	26.24	17.05	15.91	26.22	19.65	15.03

Date	Tow	Time (mins)	Vel Mag (m/s)	T1 RPM	% Eff. Versa T1	% Eff. PLC T1	T2 RPM	% Eff. Versa T2	% Eff. PLC T2
19-9-17	Tow1	1	0.88	13.08	15.44	6.66	13.08	15.99	8.44
19-9-17	Tow1	2	0.82	13.12	16.6	8.03	13.1	17.15	9.42

Date	Tow	Time (mins)	Vel Mag (m/s)	T1 RPM	% Eff. Versa T1	% Eff. PLC T1	T2 RPM	% Eff. Versa T2	% Eff. PLC T2
20-9-17	Tow1	1	0.67	7.82	0*	1.43	7.93	10.42	5.36
20-9-17	Tow1	2	0.66	9.43	0*	0.56	9.47	11.59	2.74
20-9-17	Tow1	3	0.67	9.43	0*	1.2	9.5	11.15	3.14
20-9-17	Tow1	4	0.65	9.18	0*	0.46	9.51	11.48	2.31
20-9-17	Tow1	5	0.65	9.08	0*	0.4	9.51	11.12	1.73
20-9-17	Tow1	6	0.66	9.06	0*	0.6	9.52	10.18	1.44
20-9-17	Tow1	7	0.55	5.47	0*	0.53	5.59	9.53	0.32
20-9-17	Tow1	8	0.66	6.32	0*	0.31	5.99	7.28	1.93
20-9-17	Tow1	9	0.62	9.52	0*	0.82	9.52	12.93	2.92
20-9-17	Tow1	10	0.56	6.07	0*	0.2	6.27	8.04	0.72

Date	Tow	Time (mins)	Vel Mag (m/s)	T1 RPM	% Eff. Versa T1	% Eff. PLC T1	T2 RPM	% Eff. Versa T2	% Eff. PLC T2
20-9-17	Tow2	1	0.67	9.1	0*	3.84	9.61	15	4.79
20-9-17	Tow2	2	0.65	9.86	0*	0.9	9.97	11.61	2.79
20-9-17	Tow2	3	0.66	9.68	0*	0.37	9.93	10.76	0.97
20-9-17	Tow2	4	0.65	9.28	0*	0.15	9.91	11.07	0.95
20-9-17	Tow2	5	0.64	9.62	0*	0.06	9.95	11.65	1.74
20-9-17	Tow2	6	0.64	9.87	0*	0.06	9.97	11.64	0.79
20-9-17	Tow2	7	0.66	9.73	0*	0.25	9.88	10.86	1.94
20-9-17	Tow2	8	0.65	9.78	0*	0.09	9.92	11.97	1.11
20-9-17	Tow2	9	0.61	9.75	0*	1.3	9.98	12.3	1.34

Date	Tow	Time (mins)	Vel Mag (m/s)	T1 RPM	% Eff. Versa T1	% Eff. PLC T1	T2 RPM	% Eff. Versa T2	% Eff. PLC T2
20-9-17	Tow3	1	0.65	7.46	0*	1.24	7.68	9.68	2.01
20-9-17	Tow3	2	0.66	10.26	0*	0.68	10.41	11.44	1.14
20-9-17	Tow3	3	0.67	10.14	0*	0.23	10.44	10.59	1.33
20-9-17	Tow3	4	0.66	10.29	0*	0.05	10.45	11.07	1.12
20-9-17	Tow3	5	0.67	10.24	0*	0.17	10.43	10.77	0.68
20-9-17	Tow3	6	0.68	10.32	0*	0.34	10.55	10.59	1.86
20-9-17	Tow3	7	0.67	10.32	0*	0.75	10.52	11.02	0.91
20-9-17	Tow3	8	0.65	10.14	0*	0.56	10.43	11.38	0.62
20-9-17	Tow3	9	0.62	10.29	0*	0.3	10.36	11.74	0.89

Date	Tow	Time (mins)	Vel Mag (m/s)	T1 RPM	% Eff. Versa T1	% Eff. PLC T1	T2 RPM	% Eff. Versa T2	% Eff. PLC T2
20-9-17	Tow4	1	0.84	10.83	0*	2.75	10.9	10.41	4.6
20-9-17	Tow4	2	0.86	12.6	0*	4.62	12.62	12.73	6.59
20-9-17	Tow4	3	0.85	12.49	0*	4.89	12.57	12.87	6.43
20-9-17	Tow4	4	0.85	12.54	0*	5.09	12.47	12.21	6.09
20-9-17	Tow4	5	0.83	12.75	0*	7.99	12.68	13.21	9.48
20-9-17	Tow4	6	0.85	12.62	0*	5.34	12.6	11.96	6
20-9-17	Tow4	7	0.80	12.62	0*	6.62	12.55	14.45	7.82

Date	Tow	Time (mins)	Vel Mag (m/s)	T1 RPM	% Eff. Versa T1	% Eff. PLC T1	T2 RPM	% Eff. Versa T2	% Eff. PLC T2
20-9-17	Tow5	1	0.84	11.85	0*	6.17	11.83	13.35	8.21
20-9-17	Tow5	2	0.87	13.15	0*	6.51	13.08	13.3	6.95
20-9-17	Tow5	3	0.86	13.13	0*	5.68	13.12	13.09	7.16
20-9-17	Tow5	4	0.85	13.13	0*	6.89	13.18	13.65	7.44
20-9-17	Tow5	5	0.84	13.12	0*	5.33	13.15	13.38	7.59
20-9-17	Tow5	6	0.85	13.1	0*	5.1	13.08	12.23	6.51
20-9-17	Tow5	7	0.81	13.05	0*	6.11	13.13	14.24	6.88

Date	Tow	Time (mins)	Vel Mag (m/s)	T1 RPM	% Eff. Versa T1	% Eff. PLC T1	T2 RPM	% Eff. Versa T2	% Eff. PLC T2
20-9-17	Tow6	1	0.84	10.94	0*	3.89	11.23	11.29	6.35
20-9-17	Tow6	2	0.83	13.7	0*	1.85	13.6	13.23	4.9
20-9-17	Tow6	3	0.84	13.7	0*	6.31	13.67	13.38	4.63
20-9-17	Tow6	4	0.85	13.56	0*	5.65	13.67	12.93	7.97
20-9-17	Tow6	5	0.84	13.61	0*	5.62	13.62	12.79	9.27
20-9-17	Tow6	6	0.83	13.54	0*	1.93	13.54	12.54	6.64
20-9-17	Tow6	7	0.78	13.69	0*	4.65	13.66	14.34	4.7

Date	Tow	Time (mins)	Vel Mag (m/s)	T1 RPM	% Eff. Versa T1	% Eff. PLC T1	T2 RPM	% Eff. Versa T2	% Eff. PLC T2
20-9-17	Tow7	1	1.02	13.25	0*	8.52	13.07	12.57	9.08
20-9-17	Tow7	2	1.02	14.54	0*	9.89	14.62	14.92	11.48
20-9-17	Tow7	3	1.01	14.61	0*	9.81	14.6	15.18	11.1
20-9-17	Tow7	4	0.99	14.53	0*	10.29	14.67	16.03	11.28
20-9-17	Tow7	5	0.99	14.63	0*	10.62	14.57	15.85	11.29
20-9-17	Tow7	6	0.94	14.62	0*	11.94	14.55	16.78	11.53

Date	Tow	Time (mins)	Vel Mag (m/s)	T1 RPM	% Eff. Versa T1	% Eff. PLC T1	T2 RPM	% Eff. Versa T2	% Eff. PLC T2
20-9-17	Tow8	1	1.01	13.93	0*	9.78	13.77	14.72	11.48
20-9-17	Tow8	2	1.01	15.08	0*	10.41	15.09	15.39	12.39
20-9-17	Tow8	3	1.01	15.05	0*	9.42	15.11	14.53	11.61
20-9-17	Tow8	4	1	15.11	0*	10.05	14.99	15.08	12.02
20-9-17	Tow8	5	1	15.13	0*	9.36	15.11	14.52	11.37
20-9-17	Tow8	6	0.95	15.11	0*	9.57	15.07	15.29	11.14

Date	Tow	Time (mins)	Vel Mag (m/s)	T1 RPM	% Eff. Versa T1	% Eff. PLC T1	T2 RPM	% Eff. Versa T2	% Eff. PLC T2
20-9-17	Tow9	1	1.01	14.35	0*	8.34	14.29	14.95	10.11
20-9-17	Tow9	2	1.01	15.69	0*	9.43	15.69	15.47	10.52
20-9-17	Tow9	3	1	15.61	0*	11.72	15.57	15.24	11.48
20-9-17	Tow9	4	1.01	15.47	0*	8.8	15.52	14.99	9.06
20-9-17	Tow9	5	1.02	15.62	0*	8.91	15.66	14.32	9.6
20-9-17	Tow9	6	0.969	15.61	0*	9.86	15.58	14.75	10.37

Date	Tow	Time (mins)	Vel Mag (m/s)	T1 RPM	% Eff. Versa T1	% Eff. PLC T1	T2 RPM	% Eff. Versa T2	% Eff. PLC T2
20-9-17	Tow10	1	1.22	17.58	0*	9.33	17.52	13.92	9.95
20-9-17	Tow10	2	1.44	17.71	0*	7.11	17.68	9.35	7.76
20-9-17	Tow10	3	1.36	17.67	0*	12.44	17.7	14.99	12.72
20-9-17	Tow10	4	1.29	17.72	0*	14.37	17.76	16.57	13.88

Date	Tow	Time (mins)	Vel Mag (m/s)	T1 RPM	% Eff. Versa T1	% Eff. PLC T1	T2 RPM	% Eff. Versa T2	% Eff. PLC T2
20-9-17	Tow11	1	1.58	26.24	0*	11.41	26.34	14.38	10.52
20-9-17	Tow11	2	1.58	26.59	0*	15.14	26.31	18.14	14.57
20-9-17	Tow11	3	1.51	29.36	0*	16.69	29.24	19.31	15.06

Date	Tow	Time (mins)	Vel Mag (m/s)	T1 RPM	% Eff. Versa T1	% Eff. PLC T1	T2 RPM	% Eff. Versa T2	% Eff. PLC T2
21-9-17	Tow1	1	1.16	20.04	12.99	11	20	12.85	12.78
21-9-17	Tow1	2	1.21	19	15.68	11.14	18.97	15.83	12.71
21-9-17	Tow1	3	1.2	19	15.75	11.76	19.01	16.15	13.01
21-9-17	Tow1	4	1.2	18.99	15.37	12.26	19.01	16.42	13.17

Date	Tow	Time (mins)	Vel Mag (m/s)	T1 RPM	% Eff. Versa T1	% Eff. PLC T1	T2 RPM	% Eff. Versa T2	% Eff. PLC T2
21-9-17	Tow2	1	1.24	18.12	14.07	11.15	18.58	15.02	11.98
21-9-17	Tow2	2	1.23	19.29	15.54	13.64	19.24	17.15	13.31
21-9-17	Tow2	3	1.22	19.19	14.88	11.91	19.25	16.61	11.75
21-9-17	Tow2	4	1.23	19.35	14.05	10.63	19.36	15.27	11.3
21-9-17	Tow2	5	1.16	19.33	15.61	12.25	19.22	16.61	12.23

Date	Tow	Time (mins)	Vel Mag (m/s)	T1 RPM	% Eff. Versa T1	% Eff. PLC T1	T2 RPM	% Eff. Versa T2	% Eff. PLC T2
21-9-17	Tow3	1	1.25	17.69	12.12	9.12	17.91	13.06	9.74
21-9-17	Tow3	2	1.25	19.59	14.54	10.93	19.6	14.49	12.1
21-9-17	Tow3	3	1.24	19.55	14.93	10.5	19.59	15.13	12.58
21-9-17	Tow3	4	1.24	19.56	14.99	10.21	19.62	14.45	12.16
21-9-17	Tow3	5	1.17	19.61	15.09	11.57	19.55	16.24	12.22

Date	Tow	Time (mins)	Vel Mag (m/s)	T1 RPM	% Eff. Versa T1	% Eff. PLC T1	T2 RPM	% Eff. Versa T2	% Eff. PLC T2
21-9-17	Tow4	1	1.26	18.03	13.22	9.12	18.16	13.65	8.86
21-9-17	Tow4	2	1.25	19.92	14.01	12.07	19.9	15.21	12.26
21-9-17	Tow4	3	1.25	19.87	15.48	11.77	19.92	15.89	11.68
21-9-17	Tow4	4	1.25	19.93	13.46	12.05	19.93	15.75	12.19
21-9-17	Tow4	5	1.18	19.94	16.69	12.05	19.96	15.59	12.11

Date	Tow	Time (mins)	Vel Mag (m/s)	T1 RPM	% Eff. Versa T1	% Eff. PLC T1	T2 RPM	% Eff. Versa T2	% Eff. PLC T2
21-9-17	Tow5	1	1.27	19.82	12.04	8.34	19.81	11.7	8.58
21-9-17	Tow5	2	1.28	20.23	12.83	10.11	20.23	14.32	10.36
21-9-17	Tow5	3	1.29	20.22	12.11	9.99	20.26	13.28	9.62
21-9-17	Tow5	4	1.24	20.19	14.78	11.68	20.24	15.18	11.57
21-9-17	Tow5	5	1.17	20.22	15.49	11.88	20.22	16.59	12.51

Date	Tow	Time (mins)	Vel Mag (m/s)	T1 RPM	% Eff. Versa T1	% Eff. PLC T1	T2 RPM	% Eff. Versa T2	% Eff. PLC T2
21-9-17	Tow6	1	1.25	18.58	12.96	9.03	18.59	13.75	9.19
21-9-17	Tow6	2	1.22	20.52	14.63	12.69	20.54	16.23	11.93
21-9-17	Tow6	3	1.23	20.59	14.73	12.03	20.61	16.23	11.97
21-9-17	Tow6	4	1.23	20.51	15.07	11.64	20.52	16.05	12.54
21-9-17	Tow6	5	1.16	20.55	15.95	12.41	20.48	16.63	12.8

Date	Tow	Time (mins)	Vel Mag (m/s)	T1 RPM	% Eff. Versa T1	% Eff. PLC T1	T2 RPM	% Eff. Versa T2	% Eff. PLC T2
21-9-17	Tow7	1	1.27	19.09	13.28	8.61	18.87	13.64	9.05
21-9-17	Tow7	2	1.27	20.87	12.79	9.73	20.85	13.82	10.27
21-9-17	Tow7	3	1.21	20.89	13.73	11.17	20.8	14.49	11.25
21-9-17	Tow7	4	1.25	20.79	12.86	9.55	20.75	13.69	9.49
21-9-17	Tow7	5	1.18	20.85	14.5	12.93	20.85	15.73	12.2

Date	Tow	Time (mins)	Vel Mag (m/s)	T1 RPM	% Eff. Versa T1	% Eff. PLC T1	T2 RPM	% Eff. Versa T2	% Eff. PLC T2
21-9-17	Tow8	1	1.27	18.52	11.22	7.93	18.6	11.41	8.04
21-9-17	Tow8	2	1.26	21.08	13.93	9.94	21.1	14.35	11.45
21-9-17	Tow8	3	1.21	21.1	14.69	10.11	21.22	14.14	11.45
21-9-17	Tow8	4	1.21	21.21	14.05	10.71	21.19	14.05	10.15
21-9-17	Tow8	5	1.15	21.2	15.08	11.58	21.09	16.21	11.56

Date	Tow	Time (mins)	Vel Mag (m/s)	T1 RPM	% Eff. Versa T1	% Eff. PLC T1	T2 RPM	% Eff. Versa T2	% Eff. PLC T2
21-9-17	Tow9	1	1.26	18.53	10.77	5.35	18.8	10.7	6.7
21-9-17	Tow9	2	1.24	21.56	14.13	12.62	21.57	15.21	11.46
21-9-17	Tow9	3	1.23	21.41	13.73	9.64	21.42	14.94	9
21-9-17	Tow9	4	1.23	21.33	13.07	10.39	21.41	14.18	10.33
21-9-17	Tow9	5	1.18	21.58	15.03	13.05	21.58	16.19	12.11

Date	Tow	Time (mins)	Vel Mag (m/s)	T1 RPM	% Eff. Versa T1	% Eff. PLC T1	T2 RPM	% Eff. Versa T2	% Eff. PLC T2
21-9-17	Tow10	1	1.23	19.29	11.11	6.72	19.52	11.03	7.51
21-9-17	Tow10	2	1.22	21.81	13.81	10.59	21.88	14.6	10.58
21-9-17	Tow10	3	1.21	21.71	13.98	9.54	21.72	15.26	9.61
21-9-17	Tow10	4	1.21	21.81	13.67	10.35	21.8	14.23	10.09
21-9-17	Tow10	5	1.15	21.7	14.65	10.05	21.71	15.75	10.41

Date	Tow	Time (mins)	Vel Mag (m/s)	T1 RPM	% Eff. Versa T1	% Eff. PLC T1	T2 RPM	% Eff. Versa T2	% Eff. PLC T2
22-9-17	Tow1	1	1.28	17.09	11.02	6.37	17.29	11.7	8.67
22-9-17	Tow1	2	1.26	19.4	14.13	10.52	19.29	14.06	11.36
22-9-17	Tow1	3	1.25	19.25	13.89	11.26	19.33	14.87	12.02
22-9-17	Tow1	4	1.24	19.23	14.24	10.09	19.23	15.31	12.16
22-9-17	Tow1	5	1.17	19.41	15.73	13.74	19.31	17.49	12.66

Date	Tow	Time (mins)	Vel Mag (m/s)	T1 RPM	% Eff. Versa T1	% Eff. PLC T1	T2 RPM	% Eff. Versa T2	% Eff. PLC T2
22-9-17	Tow2	1	1.28	14.32	8.87	5.33	14.14	9.06	6.17
22-9-17	Tow2	2	1.27	19.68	14.08	11.11	19.63	14.7	12.26
22-9-17	Tow2	3	1.25	19.6	14.2	11.15	19.65	14.14	12.55
22-9-17	Tow2	4	1.24	19.6	14.23	12.08	19.59	15.77	12.23
22-9-17	Tow2	5	1.17	19.6	14.53	12.38	19.66	17.13	12.66

Date	Tow	Time (mins)	Vel Mag (m/s)	T1 RPM	% Eff. Versa T1	% Eff. PLC T1	T2 RPM	% Eff. Versa T2	% Eff. PLC T2
22-9-17	Tow3	1	1.28	19.89	11.82	10.23	19.74	15.34	10.36
22-9-17	Tow3	2	1.28	19.87	13.74	10.64	19.93	13.72	10.98
22-9-17	Tow3	3	1.24	19.93	12.99	11.58	19.94	16.08	12.03
22-9-17	Tow3	4	1.24	19.91	14.23	11.82	19.91	15.05	11.12
22-9-17	Tow3	5	1.17	19.9	14.16	12.12	19.97	15.95	12.34

Date	Tow	Time (mins)	Vel Mag (m/s)	T1 RPM	% Eff. Versa T1	% Eff. PLC T1	T2 RPM	% Eff. Versa T2	% Eff. PLC T2
22-9-17	Tow4	1	1.24	20.1	11.01	7.9	20.21	11.74	8.02
22-9-17	Tow4	2	1.23	20.22	13.78	11.9	20.21	16.39	11.65
22-9-17	Tow4	3	1.21	20.2	15.48	12.51	20.23	16.19	12.31
22-9-17	Tow4	4	1.23	20.17	13.98	11.24	20.24	14.92	11.54
22-9-17	Tow4	5	1.16	20.24	15.21	12.87	20.2	17.34	13.31

Date	Tow	Time (mins)	Vel Mag (m/s)	T1 RPM	% Eff. Versa T1	% Eff. PLC T1	T2 RPM	% Eff. Versa T2	% Eff. PLC T2
30-8-17	Tow1	1	1.11	25.12	8.55	1	25.56	8.64	1.15
30-8-17	Tow1	2	1.15	23.14	8.78	3.02	23.68	8.94	2.77
30-8-17	Tow1	3	1.12	21.53	9.53	3.72	21.9	10.58	4.15
30-8-17	Tow1	4	1.11	20.14	10.76	6.8	21.03	12.48	4.87
30-8-17	Tow1	5	1.14	19.11	10.49	7.47	20.21	12.98	6.6

Date	Tow	Time (mins)	Vel Mag (m/s)	T1 RPM	% Eff. Versa T1	% Eff. PLC T1	T2 RPM	% Eff. Versa T2	% Eff. PLC T2
30-8-17	Tow2	1	1.11	24.68	9.05	2.3	25	9.18	0.78
30-8-17	Tow2	2	1.15	21.78	9.76	3.7	22.12	10.29	4.03
30-8-17	Tow2	3	1.12	19.69	10.73	5.83	19.8	10.76	5.15
30-8-17	Tow2	4	1.11	18.11	11.85	6.67	18.23	12.47	6.31
30-8-17	Tow2	5	1.14	17.36	11.68	7.39	17.36	11.67	8.08
30-8-17	Tow2	6	0.97	15.95	12.48	7.89	16.02	12.7	8.02

Date	Tow	Time (mins)	Vel Mag (m/s)	T1 RPM	% Eff. Versa T1	% Eff. PLC T1	T2 RPM	% Eff. Versa T2	% Eff. PLC T2
30-8-17	Tow3	1	1.18	24.5	7.34	2.54	24.81	6.88	1.11
30-8-17	Tow3	2	1.19	21.96	8.81	3.57	22.25	7.86	4.49
30-8-17	Tow3	3	1.1	18.44	11.43	7.04	18.66	12.55	7.84
30-8-17	Tow3	4	1.08	16.21	13.51	11.09	16.36	13.72	10.18
30-8-17	Tow3	5	1.13	14.41	11.62	8.79	14.5	11.8	8.17

Date	Tow	Time (mins)	Vel Mag (m/s)	T1 RPM	% Eff. Versa T1	% Eff. PLC T1	T2 RPM	% Eff. Versa T2	% Eff. PLC T2
30-8-17	Tow4	1	1.16	23.81	7.23	2.82	24.69	6.89	1.92
30-8-17	Tow4	2	1.15	20.28	8.57	4.81	21.16	9.42	4.03
30-8-17	Tow4	3	1.07	17.41	12.17	8.21	17.91	12.26	8.18
30-8-17	Tow4	4	1.12	15.48	10.59	6.86	16.9	12.47	7.63
30-8-17	Tow4	5	1.14	15.99	10.98	7.52	15.98	10.3	7.43

Date	Tow	Time (mins)	Vel Mag (m/s)	T1 RPM	% Eff. Versa T1	% Eff. PLC T1	T2 RPM	% Eff. Versa T2	% Eff. PLC T2
30-8-17	Tow5	1	1.11	25.64	7.85	0.84	25.87	6.18	1.46
30-8-17	Tow5	2	1.09	21.41	10.49	3.63	21.89	10.29	5.91
30-8-17	Tow5	3	1.01	17.92	15.51	10.84	17.96	13.49	7.79
30-8-17	Tow5	4	1.02	17.11	15.35	10.64	17.22	14.2	8.89
30-8-17	Tow5	5	1.03	16.46	15.54	10.45	16.58	14.3	11.08
30-8-17	Tow5	6	0.92	15.79	16.94	11.16	15.72	15.2	11.67

Date	Tow	Time (mins)	Vel Mag (m/s)	T1 RPM	% Eff. Versa T1	% Eff. PLC T1	T2 RPM	% Eff. Versa T2	% Eff. PLC T2
30-8-17	Tow6	1	1.16	24.41	7.24	2.18	24.74	5.79	2.31
30-8-17	Tow6	2	1.16	21.31	7.9	3.54	21.74	6.95	3.85
30-8-17	Tow6	3	1.08	18.1	11.5	7.19	18.32	11.09	8.23
30-8-17	Tow6	4	1.09	16.07	12.21	8.79	16.42	11.31	8.4
30-8-17	Tow6	5	1.18	14.43	10.21	7.47	14.51	8.9	7.92

Date	Tow	Time (mins)	Vel Mag (m/s)	T1 RPM	% Eff. Versa T1	% Eff. PLC T1	T2 RPM	% Eff. Versa T2	% Eff. PLC T2
30-8-17	Tow7	1	1.04	18.57	14.09	8.6	18.61	12.51	7.86
30-8-17	Tow7	2	1.12	17.75	12.14	7.95	17.79	11.18	7.87
30-8-17	Tow7	3	1.1	17.5	12.98	8.2	17.45	11.6	8.25
30-8-17	Tow7	4	1.06	17.03	12.72	7.68	17.15	11.38	7.22
30-8-17	Tow7	5	1.09	16.75	12.15	7.43	16.73	10.12	8.05
30-8-17	Tow7	6	0.96	16.28	14.38	8.03	16.23	13.28	9.77

Date	Tow	Time (mins)	Vel Mag (m/s)	T1 RPM	% Eff. Versa T1	% Eff. PLC T1	T2 RPM	% Eff. Versa T2	% Eff. PLC T2
30-8-17	Tow8	1	1.19	22.21	9.11	3.34	22.8	8.17	2.51
30-8-17	Tow8	2	1.15	17.89	15.34	7.55	18.15	12	7.9
30-8-17	Tow8	3	1.06	16.44	20.14	10.96	16.51	15.59	11.28
30-8-17	Tow8	4	1.08	16.16	17.42	9.03	16.2	13.4	9.66
30-8-17	Tow8	5	1.13	15.77	14.82	8.04	15.8	11.28	7.9

Date	Tow	Time (mins)	Vel Mag (m/s)	T1 RPM	% Eff. Versa T1	% Eff. PLC T1	T2 RPM	% Eff. Versa T2	% Eff. PLC T2
30-8-17	Tow9	1	1.16	20.55	10.53	4.37	21.27	8.32	4.18
30-8-17	Tow9	2	1.18	15.51	13.59	7.63	15.83	10.22	8.28
30-8-17	Tow9	3	1.19	15.28	14.74	8.64	15.32	10.17	8.57
30-8-17	Tow9	4	1.15	14.91	16.08	9	14.99	11.74	9.3
30-8-17	Tow9	5	1.2	14.63	13.75	6.97	14.72	9.49	8.07
30-8-17	Tow9	6	0.84	13.02	17.62	10.57	13.02	12.43	7.46

Date	Tow	Time (mins)	Vel Mag (m/s)	T1 RPM	% Eff. Versa T1	% Eff. PLC T1	T2 RPM	% Eff. Versa T2	% Eff. PLC T2
30-8-17	Tow10	1	1.2	21.79	9.1	3.32	22.53	7.12	1.98
30-8-17	Tow10	2	1.23	17.19	12.03	6.67	17.69	9.28	6.8
30-8-17	Tow10	3	1.14	13.55	15.2	8.81	13.49	10.74	9.47
30-8-17	Tow10	4	1.09	13.26	17.7	10.33	13.25	12.57	10.3
30-8-17	Tow10	5	1.16	12.92	14.43	8.49	12.97	10.46	8.46
30-8-17	Tow10	6	0.91	12.66	19.76	11.73	12.65	14.52	11.88

Date	Tow	Time (mins)	Vel Mag (m/s)	T1 RPM	% Eff. Versa T1	% Eff. PLC T1	T2 RPM	% Eff. Versa T2	% Eff. PLC T2
30-8-17	Tow11	1	1.17	19.27	7.58	5.76	20.17	5.65	5.61
30-8-17	Tow11	2	1.2	15.77	15.01	7.49	15.81	9.89	8.26
30-8-17	Tow11	3	1.22	8.64	7.13	4.12	15.64	8.95	7.21
30-8-17	Tow11	4	1.17	3.17	3.42	1.98	15.35	7.46	9.1
30-8-17	Tow11	5	1.19	15.61	15.36	8.76	15.5	9.66	9.29
30-8-17	Tow11	6	0.83	9.99	13.68	8.21	10.08	9.77	5.86

C.2 1:10 Scale Device Performance Evaluated Using Tow Speed

Date	Tow	Time (mins)	Vel Mag (m/s)	T1 RPM	% Eff. Versa T1	% Eff. PLC T1	T2 RPM	% Eff. Versa T2	% Eff. PLC T2
14-8-17	Tow1	1	0.6	4.63	10.2	7.51	4.69	9.25	6.36
14-8-17	Tow1	2	0.6	9.04	19.97	4.24	8.98	17.05	7.76
14-8-17	Tow1	3	0.6	9.03	20.04	4.57	9.06	17.01	8.48
14-8-17	Tow1	4	0.6	9.49	19.11	4.31	9.35	18.15	6.84
14-8-17	Tow1	5	0.6	9.44	19.31	5.51	9.44	16.76	6.86
14-8-17	Tow1	6	0.6	9.61	18.23	5.24	9.67	17.98	3.55
14-8-17	Tow1	7	0.6	9.71	19.41	2.01	9.65	18.82	5.99
14-8-17	Tow1	8	0.6	9.92	19.31	7	9.97	14.87	6.55
14-8-17	Tow1	9	0.6	10.14	16.27	1.77	10.08	16.07	3.3
14-8-17	Tow1	10	0.6	10.42	17.17	2.05	10.45	19.35	2.88

Date	Tow	Time (mins)	Vel Mag (m/s)	T1 RPM	% Eff. Versa T1	% Eff. PLC T1	T2 RPM	% Eff. Versa T2	% Eff. PLC T2
14-8-17	Tow2	1	0.6	7.15	12.69	7.92	7.15	14.83	9.02
14-8-17	Tow2	2	0.6	7.95	17.89	2.77	7.9	14	7.81
14-8-17	Tow2	3	0.6	7.94	19.13	5.68	7.89	15	9.12
14-8-17	Tow2	4	0.6	8.39	19.64	7.64	8.35	18.46	6.12
14-8-17	Tow2	5	0.6	8.45	19.9	6.65	8.38	16.6	8.11
14-8-17	Tow2	6	0.6	8.56	19.4	7.43	8.67	19.99	8.44
14-8-17	Tow2	7	0.6	8.66	20.08	7.58	8.63	18.38	8.26
14-8-17	Tow2	8	0.6	8.88	20.03	5.68	8.85	17.95	7.22
14-8-17	Tow2	9	0.6	9.02	19.08	5.27	9.01	17.18	7.23
14-8-17	Tow2	10	0.6	9.12	20.42	3.38	9.1	16.97	7.92
14-8-17	Tow2	11	0.6	6.35	13.92	13.22	6.27	12.11	7.52

Date	Tow	Time (mins)	Vel Mag (m/s)	T1 RPM	% Eff. Versa T1	% Eff. PLC T1	T2 RPM	% Eff. Versa T2	% Eff. PLC T2
14-8-17	Tow3	1	0.6	0.69	1.38	0.52	1.12	0*	1.04
14-8-17	Tow3	2	0.6	7.61	16.73	2.58	7.05	0*	3.66
14-8-17	Tow3	3	0.6	9.64	20.12	6.68	9.61	0*	11.06
14-8-17	Tow3	4	0.6	9.73	20.19	5.95	9.64	0*	4.66
14-8-17	Tow3	5	0.6	9.87	23.57	7.41	9.9	0*	8.54
14-8-17	Tow3	6	0.6	9.9	21.25	10.03	9.95	0*	9.55
14-8-17	Tow3	7	0.6	9.99	19.22	6.71	9.97	0*	7.92
14-8-17	Tow3	8	0.6	10.17	17.69	3.69	10.17	0*	6.74
14-8-17	Tow3	9	0.6	10.23	16.78	3.22	10.23	0*	3.83
14-8-17	Tow3	10	0.6	10.27	17.88	2.98	10.32	0*	4.55

Date	Tow	Time (mins)	Vel Mag (m/s)	T1 RPM	% Eff. Versa T1	% Eff. PLC T1	T2 RPM	% Eff. Versa T2	% Eff. PLC T2
15-8-17	Tow1	1	0.81	11.27	8.2	8.79	11.4	8.26	10.95
15-8-17	Tow1	2	0.81	10.71	18.49	9.61	10.62	15.7	13.53
15-8-17	Tow1	3	0.81	11.13	18.74	9.4	11.08	16.16	12.74
15-8-17	Tow1	4	0.81	11.39	19.11	5.81	11.32	15.78	9.35
15-8-17	Tow1	5	0.81	11.77	13.64	4.76	11.81	12.54	4.97
15-8-17	Tow1	6	0.81	12.12	10.13	1.11	12.14	10.56	1.48
15-8-17	Tow1	7	0.81	12.41	7.93	2.08	12.39	8.93	2.02
15-8-17	Tow1	8	0.81	9.47	6.62	6.29	9.5	7.02	1.92

Date	Tow	Time (mins)	Vel Mag (m/s)	T1 RPM	% Eff. Versa T1	% Eff. PLC T1	T2 RPM	% Eff. Versa T2	% Eff. PLC T2
16-8-17	Tow3	1	0.62	8.39	19.05	8.1	8.15	17.7	9.81
16-8-17	Tow3	2	0.62	9.19	19.76	4.98	9.2	17.56	6.11
16-8-17	Tow3	3	0.62	9.25	19.27	4.61	9.25	16.52	7.24
16-8-17	Tow3	4	0.62	9.27	17.77	4.83	9.28	16.8	6.74

Date	Tow	Time (mins)	Vel Mag (m/s)	T1 RPM	% Eff. Versa T1	% Eff. PLC T1	T2 RPM	% Eff. Versa T2	% Eff. PLC T2
16-8-17	Tow4	1	0.62	9.02	19.63	6.18	9.04	17.96	8.41
16-8-17	Tow4	2	0.62	9.33	18.87	6.09	9.31	17.73	7.96
16-8-17	Tow4	3	0.62	9.31	19.9	4.84	9.3	16.81	9.21
16-8-17	Tow4	4	0.62	9.33	18.07	4.73	9.3	16.19	5.67

Date	Tow	Time (mins)	Vel Mag (m/s)	T1 RPM	% Eff. Versa T1	% Eff. PLC T1	T2 RPM	% Eff. Versa T2	% Eff. PLC T2
16-8-17	Tow5	1	0.62	9.16	22.75	9.01	9.17	19.56	13.29
16-8-17	Tow5	2	0.62	9.41	21.51	5.9	9.43	17.87	11.35
16-8-17	Tow5	3	0.62	9.46	18.78	5.08	9.43	16.59	7.86
16-8-17	Tow5	4	0.62	9.42	19.47	3.25	9.37	15.62	8.19

Date	Tow	Time (mins)	Vel Mag (m/s)	T1 RPM	% Eff. Versa T1	% Eff. PLC T1	T2 RPM	% Eff. Versa T2	% Eff. PLC T2
18-8-17	Tow1	1	0.68	9.27	12.84	4.96	9.44	12.92	8.09
18-8-17	Tow1	2	0.68	9.5	13.44	2.25	9.55	13.32	5.74
18-8-17	Tow1	3	0.68	9.54	13.55	3.38	9.6	13.76	6.44
18-8-17	Tow1	4	0.68	9.65	12.48	3.73	9.65	14.53	4.89
18-8-17	Tow1	5	0.68	9.62	12.36	5.33	9.71	15.91	5.04
18-8-17	Tow1	6	0.68	9.72	14.32	5.06	9.75	15.23	4.39
18-8-17	Tow1	7	0.68	8.99	12.25	3.48	9.44	12.64	4.11
18-8-17	Tow1	8	0.68	9.85	13.69	2.98	9.9	13.71	5.67
18-8-17	Tow1	9	0.68	9.86	12.04	3.64	9.85	13.52	3.77
18-8-17	Tow1	10	0.68	9.92	13.28	1.85	9.88	13.47	3.84

Date	Tow	Time (mins)	Vel Mag (m/s)	T1 RPM	% Eff. Versa T1	% Eff. PLC T1	T2 RPM	% Eff. Versa T2	% Eff. PLC T2
18-8-17	Tow2	1	0.68	8.67	13.61	2.45	9.04	12.12	6.6
18-8-17	Tow2	2	0.68	9.23	14.7	2.47	9.19	12.08	5.83
18-8-17	Tow2	3	0.68	9.32	14.46	2.49	9.28	13.03	4.5
18-8-17	Tow2	4	0.68	9.31	13.71	2.85	9.33	13.51	5.34
18-8-17	Tow2	5	0.68	9.38	13.39	3.57	9.45	14.13	5.26
18-8-17	Tow2	6	0.68	9.4	14.32	3.34	9.48	13.69	5.56
18-8-17	Tow2	7	0.68	9.51	14.18	2.3	9.49	12.36	4.25
18-8-17	Tow2	8	0.68	9.52	13.08	2.49	9.57	12.16	3.14
18-8-17	Tow2	9	0.68	9.59	13.91	1.97	9.64	12.11	4.55
18-8-17	Tow2	10	0.68	9.55	13.13	2.74	9.53	12.37	3.91
18-8-17	Tow2	11	0.68	9.41	12.92	1.48	8.63	11.21	3.72

Date	Tow	Time (mins)	Vel Mag (m/s)	T1 RPM	% Eff. Versa T1	% Eff. PLC T1	T2 RPM	% Eff. Versa T2	% Eff. PLC T2
18-8-17	Tow3	1	0.64	9.41	12.87	2.56	9.42	14.25	4.03
18-8-17	Tow3	2	0.64	9.64	14.06	3.49	9.69	15.12	7.4
18-8-17	Tow3	3	0.64	9.67	13.1	3.11	9.7	16.06	3.49
18-8-17	Tow3	4	0.64	9.75	12.56	2.22	9.75	15.34	4.13
18-8-17	Tow3	5	0.64	9.74	12.08	4.54	9.71	14.54	2.57
18-8-17	Tow3	6	0.64	9.85	11.92	3.7	9.92	15.76	3.78
18-8-17	Tow3	7	0.64	9.78	13.19	3.33	9.89	16.44	4.48
18-8-17	Tow3	8	0.64	9.92	12.74	3.2	9.97	14.9	2.31
18-8-17	Tow3	9	0.64	9.95	12.96	2.17	9.93	13.83	1.63
18-8-17	Tow3	10	0.64	9.93	12.82	3.08	9.97	16.17	3.4

Date	Tow	Time (mins)	Vel Mag (m/s)	T1 RPM	% Eff. Versa T1	% Eff. PLC T1	T2 RPM	% Eff. Versa T2	% Eff. PLC T2
18-8-17	Tow4	1	0.64	9.1	15.93	3.74	6.67	6.61	3.61
18-8-17	Tow4	2	0.64	9.22	13.9	2.55	9.26	7.71	5.57
18-8-17	Tow4	3	0.64	9.36	13.99	5.14	9.24	7.57	4.73
18-8-17	Tow4	4	0.64	9.3	14.23	4.41	9.37	7.98	4.78
18-8-17	Tow4	5	0.64	9.31	12.17	2.03	9.34	6.04	3.46
18-8-17	Tow4	6	0.64	9.42	12.02	1.94	9.37	5.8	1.83
18-8-17	Tow4	7	0.64	9.4	11.11	1.88	9.36	4.98	2.05
18-8-17	Tow4	8	0.64	9.45	11.44	1.37	9.46	5.28	2.42
18-8-17	Tow4	9	0.64	9.58	12.43	2.41	9.58	6.11	4.32
18-8-17	Tow4	10	0.64	9.48	12.1	1.93	9.55	5.89	2.07
18-8-17	Tow4	11	0.64	9.52	10.93	0.89	9.5	4.75	1.58

Date	Tow	Time (mins)	Vel Mag (m/s)	T1 RPM	% Eff. Versa T1	% Eff. PLC T1	T2 RPM	% Eff. Versa T2	% Eff. PLC T2
18-8-17	Tow5	1	0.6	7.89	10.58	3.08	7.77	11.46	3.02
18-8-17	Tow5	2	0.6	9.6	12.67	1.06	9.67	15.24	3.01
18-8-17	Tow5	3	0.6	9.67	13.15	2.87	9.64	15.24	0.67
18-8-17	Tow5	4	0.6	9.73	13.87	5.04	9.64	17.84	1.31
18-8-17	Tow5	5	0.6	9.83	11.94	1.35	9.68	14.59	1.43
18-8-17	Tow5	6	0.6	9.77	10.85	-0.06	9.44	13.17	0.38
18-8-17	Tow5	7	0.6	8.75	11.39	0.58	8.92	13.09	1.12
18-8-17	Tow5	8	0.6	8.78	12.02	1.38	8.69	14.52	2.12
18-8-17	Tow5	9	0.6	8.79	12.65	3.12	8.76	14.63	3.85
18-8-17	Tow5	10	0.6	8.76	12.96	1.75	8.75	14.32	2.63

Date	Tow	Time (mins)	Vel Mag (m/s)	T1 RPM	% Eff. Versa T1	% Eff. PLC T1	T2 RPM	% Eff. Versa T2	% Eff. PLC T2
24-8-17	Tow1	1	0.83	19.46	10.9	0.25	19.96	8.17	1.09
24-8-17	Tow1	2	0.83	18.56	13.8	2.99	18.6	7.42	5.66
24-8-17	Tow1	3	0.83	17.38	14.49	5.51	17.57	9.41	4.79
24-8-17	Tow1	4	0.83	16.38	17.09	7.94	16.4	11.88	7.96
24-8-17	Tow1	5	0.83	16.11	21.05	10.26	16.07	15.83	12.33

Date	Tow	Time (mins)	Vel Mag (m/s)	T1 RPM	% Eff. Versa T1	% Eff. PLC T1	T2 RPM	% Eff. Versa T2	% Eff. PLC T2
24-8-17	Tow2	1	0.83	15.9	20.3	13.32	16.02	19.41	13.96
24-8-17	Tow2	2	0.83	15.17	19.48	9.69	15.25	19.84	9.28
24-8-17	Tow2	3	0.83	14.54	20.31	13.1	14.64	19.58	13.39
24-8-17	Tow2	4	0.83	14.13	19.95	13.91	13.98	18.84	13.76
24-8-17	Tow2	5	0.83	13.35	19.63	13.69	13.52	17.97	12.82
24-8-17	Tow2	6	0.83	12.94	20.04	11.93	13	17.73	13.83

Date	Tow	Time (mins)	Vel Mag (m/s)	T1 RPM	% Eff. Versa T1	% Eff. PLC T1	T2 RPM	% Eff. Versa T2	% Eff. PLC T2
24-8-17	Tow3	1	0.83	12.82	15.48	12.06	13.38	16.28	12.32
24-8-17	Tow3	2	0.83	12.38	19.31	13.1	12.39	19.06	13.17
24-8-17	Tow3	3	0.83	11.83	17.07	10.98	11.91	16.87	12.72
24-8-17	Tow3	4	0.83	11.69	17.16	13.36	11.74	16.78	11.44
24-8-17	Tow3	5	0.83	11.13	17.03	11.02	11.21	16.57	12.78
24-8-17	Tow3	6	0.83	10.86	17.47	9.97	10.91	14.93	13.17
24-8-17	Tow3	7	0.83	10.57	16.41	12.33	10.54	16.17	10.64

Date	Tow	Time (mins)	Vel Mag (m/s)	T1 RPM	% Eff. Versa T1	% Eff. PLC T1	T2 RPM	% Eff. Versa T2	% Eff. PLC T2
24-8-17	Tow4	1	0.83	12.32	16.35	10	12.47	20.34	10.27
24-8-17	Tow4	2	0.83	9.89	15.36	11.05	9.92	15.16	11.6
24-8-17	Tow4	3	0.83	9.3	13.35	8.91	9.43	12.62	9.37
24-8-17	Tow4	4	0.83	12.26	15.49	8.21	11.84	13.15	9.43
24-8-17	Tow4	5	0.83	14.78	16.32	9.23	14.84	15.28	9.26
24-8-17	Tow4	6	0.83	14.63	17.89	10.42	14.73	17.43	11.52
24-8-17	Tow4	7	0.83	14.58	19.92	12.57	14.49	18.93	11.65

Date	Tow	Time (mins)	Vel Mag (m/s)	T1 RPM	% Eff. Versa T1	% Eff. PLC T1	T2 RPM	% Eff. Versa T2	% Eff. PLC T2
24-8-17	Tow5	1	0.83	14.65	18.45	11.41	15.16	19.78	12.15
24-8-17	Tow5	2	0.83	13.93	18.8	12.24	13.93	19.37	12.4
24-8-17	Tow5	3	0.83	13.54	17.71	10.41	13.63	18.85	11.7
24-8-17	Tow5	4	0.83	13.28	17.93	11.87	13.28	18.22	11.56
24-8-17	Tow5	5	0.83	12.91	17.39	11.17	12.94	18.39	11.18
24-8-17	Tow5	6	0.83	12.72	17.86	11.93	12.66	18.29	12.15
24-8-17	Tow5	7	0.83	12.49	18.35	12.8	12.61	19.18	12.46

Date	Tow	Time (mins)	Vel Mag (m/s)	T1 RPM	% Eff. Versa T1	% Eff. PLC T1	T2 RPM	% Eff. Versa T2	% Eff. PLC T2
24-8-17	Tow6	1	0.83	13.91	0*	11.05	14.18	17.57	12.01
24-8-17	Tow6	2	0.83	11.84	0*	11.69	11.9	16.85	12.08
24-8-17	Tow6	3	0.83	11.46	0*	11.04	11.45	17.09	11.97
24-8-17	Tow6	4	0.83	11.04	0*	10.6	11.12	15.94	12.08
24-8-17	Tow6	5	0.83	10.83	0*	11.38	10.83	16.53	11.5
24-8-17	Tow6	6	0.83	10.15	0*	11.31	10.23	16.59	11.27
24-8-17	Tow6	7	0.83	10.19	0*	11.45	10.29	16.25	11.19

Date	Tow	Time (mins)	Vel Mag (m/s)	T1 RPM	% Eff. Versa T1	% Eff. PLC T1	T2 RPM	% Eff. Versa T2	% Eff. PLC T2
24-8-17	Tow7	1	0.83	36.12	0*	13.97	14.36	22.58	13.86
24-8-17	Tow7	2	0.83	32.76	0*	13.37	13.63	22.96	16.6
24-8-17	Tow7	3	0.83	28.21	0*	11.45	13.45	21.85	13.24
24-8-17	Tow7	4	0.83	33.69	0*	13.58	13.4	22.92	13.13
24-8-17	Tow7	5	0.83	30.58	0*	12	13.26	22.87	13.62
24-8-17	Tow7	6	0.83	34.29	0*	13.55	13.22	24.16	14.16
24-8-17	Tow7	7	0.83	29.45	0*	0	11.13	22.25	13.45

Date	Tow	Time (mins)	Vel Mag (m/s)	T1 RPM	% Eff. Versa T1	% Eff. PLC T1	T2 RPM	% Eff. Versa T2	% Eff. PLC T2
24-8-17	Tow5	1	0.83	14.65	18.45	11.41	15.16	19.78	12.15
24-8-17	Tow5	2	0.83	13.93	18.8	12.24	13.93	19.37	12.4
24-8-17	Tow5	3	0.83	13.54	17.71	10.41	13.63	18.85	11.7
24-8-17	Tow5	4	0.83	13.28	17.93	11.87	13.28	18.22	11.56
24-8-17	Tow5	5	0.83	12.91	17.39	11.17	12.94	18.39	11.18
24-8-17	Tow5	6	0.83	12.72	17.86	11.93	12.66	18.29	12.15
24-8-17	Tow5	7	0.83	12.49	18.35	12.8	12.61	19.18	12.46

Date	Tow	Time (mins)	Vel Mag (m/s)	T1 RPM	% Eff. Versa T1	% Eff. PLC T1	T2 RPM	% Eff. Versa T2	% Eff. PLC T2
7-9-17	Tow1	1	1.6	26.96	12.79	7.14	27.31	13.43	7.3
7-9-17	Tow1	2	1.6	27.76	13.75	11.05	27.78	14.74	11
7-9-17	Tow1	3	1.6	27.79	19.03	16.92	27.89	20.4	16.32
7-9-17	Tow1	4	1.6	27.87	17.41	14.23	27.92	18.96	13.85

Date	Tow	Time (mins)	Vel Mag (m/s)	T1 RPM	% Eff. Versa T1	% Eff. PLC T1	T2 RPM	% Eff. Versa T2	% Eff. PLC T2
7-9-17	Tow2	1	1.4	28.76	14.78	11.88	30.09	17.2	12.7
7-9-17	Tow2	2	1.4	24.16	17.17	13.97	24.35	18.83	14.61
7-9-17	Tow2	3	1.4	23.32	17.8	17.2	23.5	19.63	15.27
7-9-17	Tow2	4	1.4	22.39	17.44	13.93	22.5	19.42	14.52

Date	Tow	Time (mins)	Vel Mag (m/s)	T1 RPM	% Eff. Versa T1	% Eff. PLC T1	T2 RPM	% Eff. Versa T2	% Eff. PLC T2
7-9-17	Tow3	1	1.6	40.86	7.85	10.45	41.05	7.37	10.75
7-9-17	Tow3	2	1.6	36.54	14.36	12.07	37.29	15.88	11.91
7-9-17	Tow3	3	1.6	33.3	13.48	11.12	33.85	15.57	12.9

Date	Tow	Time (mins)	Vel Mag (m/s)	T1 RPM	% Eff. Versa T1	% Eff. PLC T1	T2 RPM	% Eff. Versa T2	% Eff. PLC T2
7-9-17	Tow4	1	1.6	34.12	8.79	9.17	35.33	10.45	8.23
7-9-17	Tow4	2	1.6	28.83	13.57	12.44	29.03	14.58	11.94
7-9-17	Tow4	3	1.6	27.39	15.52	15.05	27.41	17.54	14.22
7-9-17	Tow4	4	1.6	25.33	16.43	15.61	25.62	17.66	13.5

Date	Tow	Time (mins)	Vel Mag (m/s)	T1 RPM	% Eff. Versa T1	% Eff. PLC T1	T2 RPM	% Eff. Versa T2	% Eff. PLC T2
7-9-17	Tow5	1	1.6	34.91	8.4	5.74	36.52	10.12	7.2
7-9-17	Tow5	2	1.6	29.16	15.42	13.28	29.54	16.39	13.95
7-9-17	Tow5	3	1.6	27.15	16.24	14.95	27.41	17.85	15.03
7-9-17	Tow5	4	1.6	24.7	16.09	15.29	25.22	17.87	14.28

Date	Tow	Time (mins)	Vel Mag (m/s)	T1 RPM	% Eff. Versa T1	% Eff. PLC T1	T2 RPM	% Eff. Versa T2	% Eff. PLC T2
7-9-17	Tow6	1	1.6	31.03	11.87	12.94	31.33	12.87	11.44
7-9-17	Tow6	2	1.6	27.83	15.09	12.78	28.15	16.59	12.41
7-9-17	Tow6	3	1.6	25.57	15.77	14.68	25.94	17.41	14.31
7-9-17	Tow6	4	1.6	24.22	16.46	15.64	24.3	17.65	13.6

Date	Tow	Time (mins)	Vel Mag (m/s)	T1 RPM	% Eff. Versa T1	% Eff. PLC T1	T2 RPM	% Eff. Versa T2	% Eff. PLC T2
7-9-17	Tow7	1	1.6	35.51	8.77	6.71	36.34	9.53	5.63
7-9-17	Tow7	2	1.6	29.88	13.41	12.96	31.1	16.99	12.08
7-9-17	Tow7	3	1.6	28.11	15.26	13.42	28.1	16.37	13.64
7-9-17	Tow7	4	1.6	25.82	16.47	14.75	26.41	18.38	14.12

Date	Tow	Time (mins)	Vel Mag (m/s)	T1 RPM	% Eff. Versa T1	% Eff. PLC T1	T2 RPM	% Eff. Versa T2	% Eff. PLC T2
7-9-17	Tow8	1	1.6	41.93	14.83	10.13	41.89	15.48	10.52
7-9-17	Tow8	2	1.6	37.56	18.24	18.89	39.44	23.78	14.94
7-9-17	Tow8	3	1.6	34.39	20.64	20.41	35.2	23.58	19.29

Date	Tow	Time (mins)	Vel Mag (m/s)	T1 RPM	% Eff. Versa T1	% Eff. PLC T1	T2 RPM	% Eff. Versa T2	% Eff. PLC T2
7-9-17	Tow9	1	1.6	31.14	7.68	5.63	31.41	7.82	4.96
7-9-17	Tow9	2	1.6	29.32	10.71	9.48	29.24	11.78	8.66
7-9-17	Tow9	3	1.6	29.48	19.15	18.97	29.55	20.26	20.24
7-9-17	Tow9	4	1.6	29.32	24.97	17.03	29.19	26.85	15.92